

DETERMINATION OF POLYMER FILM DEVELOPMENT THROUGH SURFACE CHARACTERIZATION STUDIES

A Dissertation
Presented to
The Academic Faculty

By

Gregory M. Fike

In Partial Fulfillment
Of the Requirements for the Degree
Doctor of Philosophy in Paper Science and Engineering

School of Chemical and Biomolecular Engineering
Georgia Institute of Technology
May 2005

Copyright © 2005 by Gregory M. Fike

DETERMINATION OF POLYMER FILM DEVELOPMENT THROUGH SURFACE CHARACTERIZATION STUDIES

Approved by:

Dr. Sujit Banerjee, Advisor
School of Chemical and Biomolecular Engineering
Institute of Paper Science and Technology
Georgia Institute of Technology

Dr. Yulin Deng
School of Chemical and Biomolecular Engineering
Institute of Paper Science and Technology
Georgia Institute of Technology

Dr. Dennis Hess
School of Chemical and Biomolecular Engineering
Georgia Institute of Technology

Dr. Timothy Patterson
School of Mechanical Engineering
Institute of Paper Science and Technology
Georgia Institute of Technology

Dr. Preet Singh
School of Materials Science and Engineering
Institute of Paper Science and Technology
Georgia Institute of Technology

Date Approved: March 18, 2005

To my wife, Melissa.

Without you, I would be much less than I am.

ACKNOWLEDGMENT

I have received a tremendous amount of support from many people, which has helped bring me to this point in my life. The successes that I have enjoyed have been the result of having no fear of failure. For this, I must credit my family for their constant support. My mom, dad, sister, brother and grandparents have always provided unquestioned support for me.

When I came to grad school, I was somewhat uncertain about what I wanted to study or how I wanted to do it. There have been many people who have helped me mold my academic career and to a certain extent, my life. I am extremely grateful to my advisor, Sujit Banerjee, for his support over the last six years. His guidance throughout this journey has helped to make it worthwhile and interesting. I must also thank my committee for their input during the development of this project and their critique of this thesis.

Howard Corcoran helped me tremendously in my initial adjustment to life in Atlanta and graduate school. For this and his continued support and advice, I am thankful. Supy Phongikaroon has shared his extensive knowledge with me to advance this project and he has influenced my growth tremendously as an engineer over the last eight years.

Finally I would like to thank all of the friends who have touched both mine and
Melissa's lives during our stay in Atlanta. The memories of this part of our lives will
always be met with a smile and a raised Sweetwater.

TABLE OF CONTENTS

ACKNOWLEDGMENT	iv
LIST OF TABLES	x
LIST OF FIGURES	xiii
LIST OF SYMBOLS AND ABBREVIATIONS	xx
SUMMARY	xxv
CHAPTER 1 – INTRODUCTION.....	1
CHAPTER 2 – BACKGROUND AND LITERATURE REVIEW	4
2.1 STICKIES BACKGROUND	4
2.1.1 <i>Classification of tacky materials</i>	5
2.1.2 <i>Treatment methods used for stickies</i>	8
2.1.3 <i>Deposition on dryer cans</i>	9
2.2 ROLL TREATMENT AND COVERING	11
2.3 DRYER OPERATION	12
2.4 ADHESION.....	16
2.4.1 <i>Contact angle</i>	17
2.4.2 <i>Work of adhesion</i>	19
2.4.3 <i>Tack</i>	21
2.4.4 <i>Autohesion</i>	22
2.4.5 <i>Effects of roughness</i>	23
2.4.6 <i>Adhesion mechanisms</i>	24
2.4.6.1 Mechanical adhesion.....	25
2.4.6.2 Adsorption adhesion	25
2.4.6.3 Diffusion adhesion	27

2.4.6.4	Electrostatic adhesion	28
CHAPTER 3 – THE ROLE OF FILM TOPOLOGY IN TACK.....		29
3.1	INTRODUCTION	29
3.2	SURFACE FREE ENERGY	30
3.2.1	<i>Background and Introduction</i>	30
3.2.2	<i>Interactions</i>	32
3.2.2.1	van der Waals forces	32
3.2.2.2	Polar or acid-base interactions	35
3.2.3	<i>Calculating Surface Energy from Contact Angles</i>	35
3.3	ATOMIC FORCE MICROSCOPY	40
3.3.1	<i>Background and Introduction</i>	40
3.3.2	<i>Fundamental Principles and Measurements</i>	41
3.3.2.1	Modes of Operation	46
3.3.2.2	Roughness Determination	53
3.4	PRESSURE SENSITIVE ADHESIVES	54
3.5	TACK	58
3.5.1	<i>Tack tests</i>	60
3.5.1.1	Rolling ball test	61
3.5.1.2	Loop tack test	62
3.5.1.3	Quick stick test	64
3.5.1.4	Probe tack test	64
3.5.2	<i>Factors influencing tack</i>	69
3.5.2.1	Temperature	69
3.5.2.2	Debonding rate	70
3.5.2.3	Contact time and contact pressure	70

3.5.2.4	Roughness	71
3.5.3	<i>Tack summary</i>	73
3.6	EXPERIMENTAL AND RESULTS	74
3.6.1	<i>Tack and surface energy studies</i>	76
3.6.2	<i>X-ray Photoelectron Spectroscopy (XPS) data</i>	85
3.6.3	<i>AFM studies</i>	85
3.6.4	<i>Thermography studies</i>	92
3.7	CONCLUSIONS	94
CHAPTER 4 – SUBSTRATE DEPENDENCE OF POLYMER FILM TOPOLOGY.....		96
4.1	NON-UNIFORMITY IN METALS	97
4.1.1	<i>Composition of carbon steel</i>	97
4.1.2	<i>Composition of stainless steel</i>	99
4.1.3	<i>Localized heat transfer</i>	100
4.2	SURFACE DRIVEN FLOW	109
4.2.1	<i>Importance of surface driven flow in applications</i>	114
4.2.2	<i>Surface driven flow imaging with IR thermography</i>	115
4.3	SURFACE DRIVEN FLOW EXPERIMENTS.....	121
4.3.1	<i>Calculation of critical thickness</i>	122
4.3.2	<i>Calculation of heat flux</i>	122
4.3.3	<i>Finding film emissivity</i>	124
4.3.4	<i>Calculation of Marangoni numbers</i>	125
4.4	CONCLUSIONS OF HEAT TRANSFER STUDIES	129
CHAPTER 5 – WADS STUDY OF CONTAMINATION ON DRYER CANS.....		131
5.1	INTRODUCTION	131

5.2	DESCRIPTION OF WADS	133
5.3	WADS EXPERIMENTAL RESULTS	136
5.4	WADS SUMMARY	146
5.5	CONCLUSIONS	147
5.6	FUTURE WORK	150
APPENDIX A – AFM DATA		152
APPENDIX B – WADS DATA		172
B.1	SYSTEM CALIBRATION	173
REFERENCES.....		203
VITA.....		223

LIST OF TABLES

Table 2.1: Table of Commonly Used Tack Measurements and the Associated Standards.....	61
Table 3.1: List of Iron Oxides[205]	98
Table 3.2: Chemical composition of 1008 carbon steel.....	99
Table 3.3: Chemical composition of 304L stainless steel.....	100
Table 3.4: Thermal conductivity (k) of carbon steel components and oxides.	101
Table 3.5: ΔT temperatures ($^{\circ}\text{C}$) measured with an IR camera during the heating of coupons.	107
Table 3.6: Heat flux measured at different oven temperatures.	124
Table 3.7: Table of emissivity values of films on various coupons at different oven temperatures.....	125
Table 3.8: Values held constant in Ma number calculation.....	127
Table 4.1: Parameters and ranges for the WADS.	133
Table 4.2: WADS parameters held constant during experiments.....	137
Table 4.3: Work of Adhesion and Peel Point average and standard deviation data for sticky and non-sticky coupons at 40% and 50% solids.	141
Table A.1: AFM roughness data for PSA on carbon steel dried at low temperature.	155
Table A.2: AFM phase shift data for PSA on carbon steel dried at low temperature. ...	155
Table A.3: AFM roughness data for PSA on carbon steel dried at medium temperature.	157
Table A.4: AFM phase shift data for PSA on carbon steel dried at medium temperature.	157
Table A.5: AFM roughness data for PSA on carbon steel dried at high temperature. ...	159
Table A.6: AFM phase shift data for PSA on carbon steel dried at high temperature. ..	159
Table A.7: AFM roughness data for PSA on stainless steel dried at low temperature...	161
Table A.8: AFM phase shift data for PSA on stainless steel dried at low temperature..	161

Table A.9: AFM roughness data for PSA on stainless steel dried at medium temperature.	163
Table A.10: AFM phase shift data for PSA on stainless steel dried at medium temperature.	163
Table A.11: AFM roughness data for PSA on stainless steel dried at high temperature.	165
Table A.12: AFM phase shift data for PSA on stainless steel dried at high temperature.	165
Table A.13: AFM roughness data for PSA on marked stainless steel dried at low temperature.	167
Table A.14: AFM phase shift data for PSA on marked stainless steel dried at low temperature.	167
Table A.15: AFM roughness data for PSA on marked stainless steel dried at medium temperature.	169
Table A.16: AFM phase shift data for PSA on marked stainless steel dried at medium temperature.	169
Table A.17: AFM roughness data for PSA on marked stainless steel dried at high temperature.	171
Table A.18: AFM phase shift data for PSA on marked stainless steel dried at high temperature.	171
Table B.1: WADS data from 40% solids run on a sticky coupon (Experiment #1-21-03).	176
Table B.2: WADS data from 40% solids run on a sticky coupon (Experiment #1-21-04).	178
Table B.3: WADS data from 40% solids run on a sticky coupon (Experiment #1-21-05).	181
Table B.4: WADS data from 40% solids run on a sticky coupon (Experiment #1-21-06).	183
Table B.5: WADS data from 40% solids run on a non-sticky coupon (Experiment #1-22-02).	185
Table B.6: WADS data from 40% solids run on a non-sticky coupon (Experiment #1-22-03).	187
Table B.7: WADS data from 50% solids run on a sticky coupon (Experiment #1-22-05).	190

Table B.8: WADS data from 50% solids run on a sticky coupon (Experiment #1-22-06).	192
Table B.9: WADS data from 50% solids run on a sticky coupon (Experiment #1-22-07).	194
Table B.10: WADS data 50% solids run on a non-sticky coupon (Experiment #1-22-08).	196
Table B.11: WADS data 50% solids run on a non-sticky coupon (Experiment #1-22-09).	198
Table B.12: WADS data 50% solids run on a non-sticky coupon (Experiment #1-22-10).	200
Table B.13: WADS data 50% solids run on a non-sticky coupon (Experiment #1-22-11).	202

LIST OF FIGURES

Figure 2.1: Table of contaminants[11].	5
Figure 2.2: Sources and structures of common adhesives[12].	6
Figure 2.3: Monomer units of polyacrylate and PVAc[23]	7
Figure 2.4: Four phases of drying[40].	13
Figure 2.5: Surface temperatures for a linerboard machine[42].	14
Figure 2.6: CD temperature profile for a linerboard dryer cylinder[40].	15
Figure 2.7: Contact angle definition.	18
Figure 2.8: Common reactions involving a coupling agent[46].	27
Figure 3.1 Diagram describing (a) drop formation on a substrate and (b) film formation on a substrate. Contact angle (θ) is also defined. Adapted from de Gennes[72].	31
Figure 3.2: Simplified schematic of an AFM[123].	41
Figure 3.3: Forces involved in AFM[124].	42
Figure 3.4: The importance of using a high aspect ratio tip. Shown in (a) is the surface deformation and a tip with a low aspect ratio. (b) shows the resulting shape as rendered by the AFM[133].	44
Figure 3.5: Example of how a double tip alters the topography and presents an image that is not an accurate representation of the surface[125].	45
Figure 3.6: Force vs. distance curve showing which forces are considered for each of the three modes of AFM[135].	46
Figure 3.7: Region of the force curve used in contact mode AFM[136].	47
Figure 3.8: Cantilever deflection vs. scanner travel in the vertical direction[120].	49
Figure 3.9: The effect of capillary force on the F_p measured with contact mode AFM[120].	49
Figure 3.10: Region of the force curve used in non-contact mode AFM[142].	50

Figure 3.11: Representation of how the phase and amplitude of oscillation of the cantilever shift when the tip is brought into proximity of the surface[142].	51
Figure 3.12: Diagram of peel test for PSAs[171].	57
Figure 3.13: Diagram of shear test for PSAs[171].	57
Figure 3.14: Diagram of the rolling ball tack test[176].	62
Figure 3.15: Diagram of the loop tack test[171].	63
Figure 3.16. Schematic of a probe tack test[178].	65
Figure 3.17: Schematic of the deformation mechanisms for a conventional PSA during a probe tack test[178].	66
Figure 3.18: Stress-strain curve with optical microscope pictures showing the different stages of the debonding process for an acrylic adhesive[178].	68
Figure 3.19: Adhesive fracture energy as a function of temperature for a generic adhesive[182].	69
Figure 3.20: Adhesion energy as a function of debonding rate[184].	70
Figure 3.21: Role of contact time in adhesive bond energy[183].	71
Figure 3.22: Depiction of the effect of contact pressure on rough and smooth surfaces. 1a shows light pressure on a smooth surface. 1b is light pressure on a rough surface. 2a is high pressure on a smooth surface. 2b is high pressure on a rough surface[188].	72
Figure 3.23: Stress-strain curves for the bonding of a PSA to a steel probe with various levels of roughness[157].	73
Figure 3.24: Film thickness vs. coating rod number to test compatibility of system with coating rods.	76
Figure 3.25: Tack measurements of dry film taken at room temperature of polyacrylate films on stainless steel and carbon steel substrates. The temperature axis refers to the temperature of the oven used to dry the film. Film thickness = 25 μm .	77
Figure 3.26: Tack vs. Curing Temperature for Carbotac on stainless steel and carbon steel. Film thickness = 17 μm .	78
Figure 3.27: Tack vs. Film Thickness for films cured at 105 °C.	78
Figure 3.28: Water Drop Contact Angle vs. Film Thickness for films cured at 105 °C...	79

Figure 3.29: Surface energy components for a polyacrylate adhesive deposited on carbon steel at various curing temperatures.	80
Figure 3.30: Surface energy components for a polyacrylate adhesive deposited on stainless steel at various curing temperatures.	81
Figure 3.31: Non-Polar component of surface energy of a polyacrylate adhesive on carbon steel as a function of film thickness.	82
Figure 3.32: Non-Polar component of surface energy of a polyacrylate adhesive on stainless steel as a function of film thickness.....	83
Figure 3.33: Polar component of surface energy of a polyacrylate adhesive on carbon steel as a function of film thickness.	84
Figure 3.34: Polar component of surface energy of a polyacrylate adhesive on stainless steel as a function of film thickness.....	85
Figure 3.35: RMS roughness values for polyacrylate film on carbon steel and stainless steel at various scan sizes.	87
Figure 3.36: 25 μm phase shift scan of polyacrylate film on stainless steel. Very uniform attractiveness.	88
Figure 3.37: 25 μm phase shift scan of polyacrylate film on carbon steel. Uneven distribution of attractive (dark) material.	89
Figure 3.38: 3-D image of polyacrylate adhesive on carbon steel substrate. The surface contour is the height scan and the color scheme is the phase scan. The horizontal axes are 25 microns and the height ranges from -60 to 60 nm.	90
Figure 3.39: 25 μm^2 AFM height image of a polyacrylate film on carbon steel.	91
Figure 3.40: 1 μm^2 AFM height image of a polyacrylate film on carbon steel.	92
Figure 3.41: COV vs. Time for the drying of a polyacrylate adhesive at 117 °C. The smooth film is on stainless steel and the rough film is on carbon steel.	93
Figure 3.42: COV vs. Time for the drying of a polyacrylate adhesive at 100 °C. The smooth film is on stainless steel and the rough film is on carbon steel.	94
Figure 4.1: Diagram of the coupon described in the heat transfer model.....	103
Figure 4.2: Temperature profile of a coupon containing two elements of low conduction. The feature on the top has a $\lambda_{rc}=0.3$ and the feature on the bottom has a $\lambda_{rc}=0.1$. The graph represents an 8 mm x 8 mm square region of the coupon and the average temperature is 29 °C.....	105

Figure 4.3: Temperature profile of a coupon containing multiple elements of low conduction. The low temperature regions correspond to an equal number of $\lambda_{rc}=0.3$ and $\lambda_{rc}=0.1$ regions. The average temperature is 79 °C.....	106
Figure 4.4: Dependence of ΔT on the size of the lower-conducting features in the metal composite.....	108
Figure 4.5: Optical image of etched carbon steel at 200x magnification. The size bar is 90 μm	109
Figure 4.6: Depiction of surface driven flows.	111
Figure 4.7: Temperature fields measured with IR thermography for evaporating water at various conditions: (a) High heat flux, (b) High heat flux with surfactant, (c) Low heat flux and (d) Low heat flux with surfactant[246]. The temperature scale indicates deviation from the average in °C.....	117
Figure 4.8: Temperature fields at various heat fluxes. The images on the left are clean systems (no surfactant) and the images on the right are systems covered with a monolayer of surfactant[249].	118
Figure 4.9: IR image showing the spread of surfactant on an evaporating water surface. Time between images is 250 milliseconds[250].....	120
Figure 4.10: COV vs. time plot for the drying of acrylate films on stainless steel. The arrows indicate the point at which the plot flattens, which is the time needed to dry the film at a given temperature. The error is within the size of the markers and are less than 0.002.	123
Figure 4.11: Marangoni numbers at various drying temperatures for three coupon types (SS Marked refers to the marked stainless steel coupons).....	127
Figure 4.12: Roughness vs. scan size for three coupons dried at 105 °C.	128
Figure 5.1: Results from the Meinecke study.	132
Figure 5.2: Schematic of the WADS unit.	134
Figure 5.3: Picture of the WADS.....	135
Figure 5.4: Picture of the WADS in operation.	135
Figure 5.5: Tension data for WADS run with 50% solids sheet and sticky coupon.....	138
Figure 5.6: Video capture of a peeling event with a sticky coupon mounted on the WADS and a 50% solids sheet.....	138

Figure 5.7: Work of adhesion (calculated with the average tension values) as a function of incoming paper solids content for experiments on sticky and non-sticky coupons.	139
Figure 5.8: Work of adhesion (calculated with the maximum tension values) as a function of incoming paper solids content for experiments on sticky and non-sticky coupons.	140
Figure 5.9: Work of adhesion vs. peel point.	141
Figure 5.10: Images during the peel event for a 40% solids sheet on a non-sticky coupon.	142
Figure 5.11: Images during the peel event for a 40% solids sheet on a sticky coupon. .	143
Figure 5.12: Images during the peel event for a 50% solids sheet on a sticky coupon, part 1.	144
Figure 5.13: Images during the peel event for a 50% solids sheet on a sticky coupon, part 2.	145
Figure 5.14: Picture of picking on a sticky coupon.	146
Figure 5.15: Picture of picking on a non-sticky coupon.	146
Figure A.1: AFM images of PSA on carbon steel dried at low temperature.	154
Figure A.2: AFM images of PSA on carbon steel dried at medium temperature.	156
Figure A.3: AFM images of PSA on carbon steel dried at high temperature.	158
Figure A.4: AFM images of PSA on stainless steel dried at low temperature.	160
Figure A.5: AFM images of PSA on stainless steel dried at medium temperature.	162
Figure A.6: AFM images of PSA on stainless steel dried at high temperature.	164
Figure A.7: AFM images of PSA on marked stainless steel dried at low temperature. .	166
Figure A.8: AFM images of PSA on marked stainless steel dried at medium temperature.	168
Figure A.9: AFM images of PSA on marked stainless steel dried at high temperature. .	170
Figure B.1: Tension calibration data for WADS.	173
Figure B.2: Tension noise data from WADS.	174

Figure B.3: Peeling images from 40% solids run on a sticky coupon (Experiment #1-21-03).	175
Figure B.4: Tension data from 40% solids run on a sticky coupon (Experiment #1-21-03).....	176
Figure B.5: Peeling images from 40% solids run on a sticky coupon (Experiment #1-21-04).	177
Figure B.6: Tension data from 40% solids run on a sticky coupon (Experiment #1-21-04).....	178
Figure B.7: Peeling images from 40% solids run on a sticky coupon (Experiment #1-21-05), part 1 (continued).....	179
Figure B.8: Peeling images from 40% solids run on a sticky coupon (Experiment #1-21-05), part 2.	180
Figure B.9: Tension data from 40% solids run on a sticky coupon (Experiment #1-21-05).....	181
Figure B.10: Peeling images from 40% solids run on a sticky coupon (Experiment #1-21-06).	182
Figure B.11: Tension data from 40% solids run on a sticky coupon (Experiment #1-21-06).	183
Figure B.12: Peeling images from 40% solids run on a non-sticky coupon (Experiment #1-22-02).....	184
Figure B.13: Tension data from 40% solids run on a non-sticky coupon (Experiment #1-22-02).....	185
Figure B.14: Peeling images from 40% solids run on a non-sticky coupon (Experiment #1-22-03).....	186
Figure B.15: Tension data from 40% solids run on a non-sticky coupon (Experiment #1-22-03).....	187
Figure B.16: Peeling images from 50% solids run on a sticky coupon (Experiment #1-22-05), part 1 (continued).....	188
Figure B.17: Peeling images from 50% solids run on a sticky coupon (Experiment #1-22-05), part 2.	189
Figure B.18: Tension data from 50% solids run on a sticky coupon (Experiment #1-22-05).	190

Figure B.19: Peeling images from 50% solids run on a sticky coupon (Experiment #1-22-06).	191
Figure B.20: Tension data from 50% solids run on a sticky coupon (Experiment #1-22-06).	192
Figure B.21: Peeling images from 50% solids run on a sticky coupon (Experiment #1-22-07).	193
Figure B.22: Tension data from 50% solids run on a sticky coupon (Experiment #1-22-07).	194
Figure B.23: Peeling images from 50% solids run on a non-sticky coupon (Experiment #1-22-08).	195
Figure B.24: Tension data from 50% solids run on a non-sticky coupon (Experiment #1-22-08).	196
Figure B.25: Peeling images from 50% solids run on a non-sticky coupon (Experiment #1-22-09).	197
Figure B.26: Tension data from 50% solids run on a non-sticky coupon (Experiment #1-22-09).	198
Figure B.27: Peeling images from 50% solids run on a non-sticky coupon (Experiment #1-22-10).	199
Figure B.28: Tension data from 50% solids run on a non-sticky coupon (Experiment #1-22-10).	200
Figure B.29: Peeling images from 50% solids run on a non-sticky coupon (Experiment #1-22-11).	201
Figure B.30: Tension data from 50% solids run on a non-sticky coupon (Experiment #1-22-11).	202

LIST OF SYMBOLS AND ABBREVIATIONS

2-D	Two dimensional
AFM	Atomic Force Microscope
α, β	Empirical constants for surface tension calculations
α_i	Polarizability of molecule i
A_o	Free amplitude
A_{sp}	Amplitude set point
c	Speed of light
C	Coulomb
CD	Cross Direction
cm	Centimeter
COV	Coefficient of variation
D	Thickness of the film
ΔG_{ad}	Free energy of adsorption
ΔH_{ad}	Enthalpy of adsorption
DLS	Dynamic Light Scattering
ΔS_{ad}	Entropy of adsorption
ΔT	Temperature difference
Δz	Deflection of the cantilever
E	Exponential (10^{\wedge})
ε	Emissivity
ε_o	Dielectric permittivity
ESCA	Electron Spectroscopy for Chemical Analysis
ϕ	Peel angle in WADS experiments

f	Frequency
F	Force on AFM tip
FE	Finite Element
FIR	Far infrared
FOV	Field of View
F_p	Pull off force
ft	feet
g	Acceleration due to gravity
g	gram
γ	Coefficient of thermal expansion
γ	Surface tension
γ_{ad}	Acceptor-donor component of surface energy
γ_c	Critical surface tension
γ_d	London dispersion component of surface energy
γ^d	Dispersive component of surface energy
γ_e	Electrostatic component of surface energy
γ_h	Hydrogen bonding component of surface energy
γ_i	Induced dipole-dipole component of surface energy
γ_l	Surface tension of the liquid
γ_{lv}	Liquid-vapor interfacial tension
γ^n	Non-dispersive component of surface energy
γ_p	Dipole-dipole component of surface energy
γ_π	Pi bonding component of surface energy
γ_s	Surface tension of the solid
γ_{sl}	Interfacial tension between solid and liquid
γ_{sl}	Solid-liquid interfacial tension

γ_{sv}	Surface energy of a solid
γ_{sv}	Solid-vapor interfacial tension
h	Plank's constant
I	Current
IR	Infrared
J	Joule
k	Spring constant
k	Boltzmann's constant
k	Thermal conductivity
K	Kelvin
kHz	Kilohertz
lb	pound
λ_{Fe}	Thermal conductivity of Iron
λ_i	Thermal conductivity of material i
λ_{max}	Maximum wavelength
λ_{rc}	Relative thermal conductivity
m	meter
m	mass per unit area in WADS experiments
Ma	Marangoni number
MC	Moisture Content
μ_i	Dipole moment of molecule i
min	minute
mJ	Millijoule
mm	Millimeter
μm	Micrometer
MOW	Mixed Office Waste

N	Newton
NDT	Non-Destructive Testing
NIR	Near Infrared
nm	Nanometer
°C	Degrees Celsius
OCC	Old Corrugated Container
°F	Degrees Fahrenheit
ONP	Old Newsprint
P	Power
π	pi = 3.141
PLI	Pound per linear inch (tension)
PSA	Pressure Sensitive Adhesive
psi	Pound per square inch (pressure)
PSTC	Pressure Sensitive Tape Council
θ	Contact angle
q'''	Volumetric heat source
θ_{eq}	Equilibrium contact angle
ρ	Density of the liquid
RMS	Root Mean Square
σ	Stefan-Boltzmann constant
σ	Surface tension
s	Second
SEM	Scanning Electron Microscope
T	Temperature
τ	Surface tension gradient with respect to temperature
T^1	Tension

T_a	Absolute temperature
T_g	Glass transition temperature
V_I	Velocity of sheet in WADS experiments
W	Watt
W^{II}	Work of adhesion for WADS experiments
W_a	Work of adhesion
W_{sl}^a	Work of adhesion between a solid and a liquid
W_R	Resonant frequency
XPS	X-ray Photoelectron Spectroscopy

SUMMARY

The work contained in this thesis stems from a need to better understand how adhesives form films on metal surfaces. Recycled polyacrylate adhesives, known as stickies, are problematic in paper recycling and commonly deposit on dryer can metal surfaces, which leads to finished paper quality problems and reduced drying efficiency. The literature contains limited references to understanding the interactions of stickies in the dryer section and specifically to how adhesive films form on metal surfaces.

Unexpectedly, it was found that when a waterborne polyacrylate adhesive was placed on carbon steel it was not tacky; this was not the case for the same adhesive placed on stainless steel. It was determined that the surface energy, as measured with liquid contact angles, of the adhesive films is significantly different between the two films, with the non-tacky film having a higher surface energy. Atomic force microscopy (AFM) showed that the non-tacky surface has a higher roughness which minimizes the contacting area between the film and a contacting surface.

Analysis of the heating of the carbon steel coupon with infrared (IR) thermography shows a non-uniform temperature profile at the surface. This experimental data is corroborated using a 2-D heat transfer model that incorporates the heat transfer characteristics of the various components of carbon steel. Surface driven flow, or Marangoni convection, can develop from temperature gradients and are known to cause increased roughness in polymer films. IR thermography measurements of the adhesive

film during drying shows larger temperature differences for the films on carbon steel than on stainless steel. These larger temperature differences induce greater Marangoni convection, which result in the rougher surfaces on carbon steel that were measured with AFM.

The effect of lowering the tack of a polyacrylate film has significant impact in the dryer section of a paper machine. This effect was quantified using the Web Adhesion Drying Simulator (WADS), which is a laboratory-scale apparatus that measures the energy required to pull the sheet from a metal surface. By substituting the adhesive-on-stainless steel with the less-sticky adhesive-on-carbon steel surface, the energy required to pull the sheet from the metal surface was reduced significantly and the picking associated with the test was nearly eliminated.

The work here is summarized as follows: The non-uniform heat transfer that develops from the various poor-conducting constituents in carbon steel leads to temperature gradients in the drying polymer film. The temperature gradients drive Marangoni convection, which leads to increased film roughness. This increased roughness ultimately results in a reduction of the adhesive's tack. Understanding the role of the substrate properties on film development can lead to improved efficiency of industrial applications.

CHAPTER 1 – INTRODUCTION

Consumer interest as well as legislation aimed at protecting the environment has caused the paper industry to focus increased attention on the use of recycled fiber to supplement the use of virgin fiber. The use of recycled paper in paper mills has increased drastically in the last decade with a 70% increase in the amount of recycled fiber produced since 1990, and from 1994-1996, ten new de-inking mills opened in the United States[1, 2]. As recycled fiber usage increases, increasing the quality of recycled products will become more important if recycled products are to compete with products made from virgin fiber[3]. Although there are inherent benefits in using recycled fiber, the use of such has introduced increasing levels of metal, plastic, and adhesive contaminants into the papermaking process. The most detrimental of these contaminants is a mixture of adhesives and polymeric substances that are collectively known as stickies.

The nature of stickies makes them difficult to remove from the furnish and they are consequently detrimental to the final product quality. Stickies are hydrophobic, tacky, polymeric materials that are introduced into the papermaking system through a variety of recycled fiber sources. Stickies have specific gravities very similar to the fibers used in papermaking, which makes the stickies virtually transparent to traditional methods of cleaning. It is estimated that stickies cost the paper industry between \$600 and \$700 million a year due to the cost of control methods and lost production[4]. In addition, of the seven recycling mills opened in the United States between 1994-1997, four have closed citing stickies as the main reason for the closure[5].

Deposits of stickies have been known to occur throughout the papermaking process and the resulting problems range from finished product quality reduction to decreased production. Deposition onto the wire and press fabrics has been documented extensively and methods to reduce the problem have been developed with varying degrees of success. Stickies also deposit on the dryer cans as the sheet contacts the metal surface. This can produce a hole in the sheet, and the subsequent build-up of contaminant on the dryer can leads to additional runability problems. Many paper mills operate the first several dryer cans at lower temperatures, in part to reduce the amount of sticking; however, this loss of dryer efficiency can be responsible for lost production if the system is dryer limited.

Once the stickie deposits on the dryer can it spreads to form a film. This spreading is driven by the difference in surface energy between the polymer (low surface energy) and the hot metal surface (high surface energy) and is a primary reason for the preferential deposition of the stickies in the dryer section. The properties of these films can affect the tack of the adhesive layers on the dryer cans. Little work has been documented to describe how these polymer films develop on metal surfaces, which is the focus of the body of work contained here.

Chapter one will present a synopsis of the literature as it relates to stickies and the challenges they pose to the paper industry. The literature is analyzed to highlight areas that are problematic to the industry and to establish a need for the work accomplished here. Also presented are general overviews of topics, such as adhesion and surface energy that are necessary to fully understand much of the presented work.

Chapter two presents the unexpected result of substantially different tack behavior for the same polyacrylate adhesive placed on different metal surfaces. The Atomic Force Microscope (AFM) is a focus in Chapter two where the role of surface topography in adhesive tack is studied. The principles of the AFM are presented to develop sufficient background for the reader and relevant literature is presented to clarify areas related to the relationship between the tack of a surface and the structure of that surface. Additionally, contact angle methods are used to determine surface energies for the different surfaces to further relate tack and surface properties.

Chapter three will discuss the role that substrates play in the formation of adhesive films. Two systems will be compared: a water based polyacrylate adhesive deposited on stainless steel and the same on carbon steel. The role of these substrates in surface driven flow is considered, and the final film properties are related to substrate properties through a heat transfer model and with dimensionless parameters such as the Marangoni number. Also, a novel technique for analysis of infrared thermography data is highlighted and applied to the drying of films on several different surfaces.

Chapter four presents the application of practical results from the more fundamental studies presented in chapters two and three. Chapter four will illustrate the effect of reducing the amount of tack of an adhesive on a dryer can by using a laboratory-scale Web Adhesion Drying Simulator (WADS).

CHAPTER 2 – BACKGROUND AND LITERATURE REVIEW

The literature review begins by discussing stickies—the adhesives introduced into the papermaking process by recycled materials. One focus of this study is the deposition of tacky substances on the dryer cans, therefore some of the operational characteristics of the dryer section will be reviewed. The literature review will conclude with adhesion and a presentation of the mechanisms that are potentially responsible for sticky contaminants adhering to dryer cans.

2.1 Stickies background

Stickies are one of the main obstacles facing the paper industry in its attempt to increase the use of recycled fiber and have been since the 1970s[6-10]. Stickies are introduced through the adhesives and binders that are introduced into the papermaking system from recycled paper. There are three main types of recycled fiber: old newsprint (ONP), mixed office waste (MOW), and old corrugated container (OCC). Each type is responsible for introducing contaminants such as tapes, stickers, binders, staples, dirt and sand. Most of these contaminants are removed throughout the papermaking process, with only the most difficult to remove remaining in the furnish.

2.1.1 Classification of tacky materials

Stickies come from a variety of sources and can be classified in many ways as shown in Figure 2.1. The classes of particular interest are the stickies and the coating binders.

Some of the common stickies are further documented in Figure 2.2, where the chemical compositions are presented.

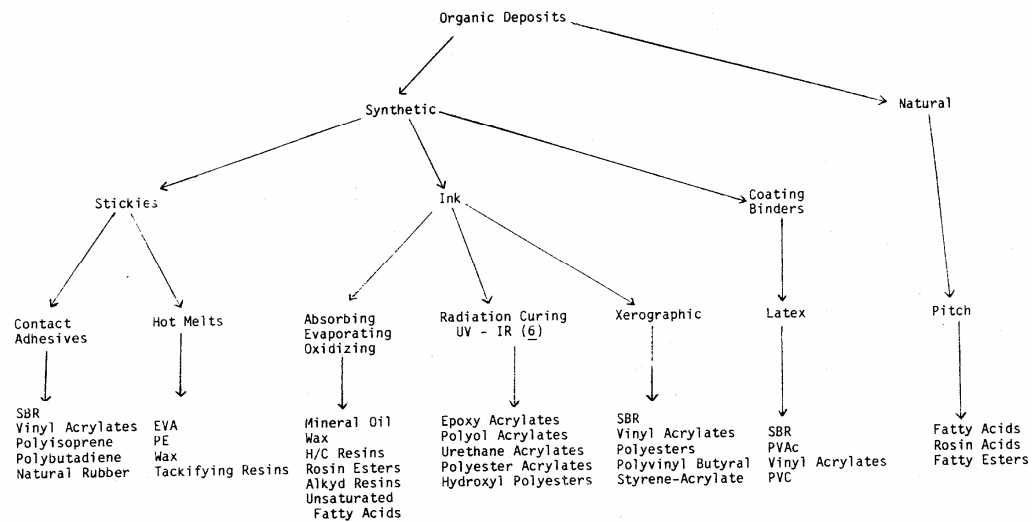


Figure 2.1: Table of contaminants[11].

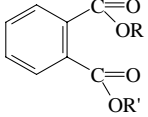
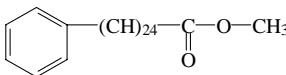
Compound	Source	Typical Structure
Styrene Butadiene	Contact Adhesives Xerographics Coating Latex	$\left(\text{CH}_2 - \underset{\text{C}_6\text{H}_5}{\text{CH}} - \text{CH}_2 - \text{CH} = \text{CH} - \text{CH}_2 \right)_n$
Polyvinyl Acetate	Coating Binder	$\left(\text{CH}_2 - \underset{\text{O}-\text{C}(=\text{O})\text{CH}_3}{\text{CH}} \right)_n$
Polyisoprene	Contact Adhesive	$\left(\text{CH}_2 - \text{CH}_2 - \underset{\text{CH}_3}{\text{CH}} - \text{CH}_2 \right)_n$
Ethylene Vinyl Acetate	Hot Melts	$\left((\text{CH}_2)_2 - \underset{\text{O}-\text{C}(=\text{O})\text{CH}_3}{\text{CH}} \right)_n$
Phthalate Esters	Hot Melts	
Styrene Ester Copolymer	Contact Adhesive	

Figure 2.2: Sources and structures of common adhesives[12].

Most adhesives introduced into the process are removed by equipment designed to eliminate most foreign matter from the pulp stream. The best debris removal systems are able to remove 99% of the debris presented to the process[13]. The process elements typically consist of pressure screens that remove material based on size and cleaners that use a difference in density to separate the heavy and light debris from the pulp mixture. Stickies that are accepted through the pressure screens are smaller than the screen size, typically $< 150 \mu\text{m}$ [6, 13]. The cleaners remove stickies that have densities different from that of the pulp slurry ($\sim 1.0 \text{ g/cm}^3$), which leaves the accepted stickies having densities in

the range of 0.95 – 1.05 g/cm³[6]. Another important characteristic of stickies is their hydrophobicity, which causes the stickies to agglomerate with other hydrophobic materials such as other stickies, pitch and lignin [14].

Several studies of deposits collected from mills have analyzed the composition of the tacky deposits. The results show that the most common materials present in the deposits are polyacrylates and polyvinyl acetates (PVAc)[15-21]. Polyacrylates are typically formed with ester backbones and acrylate end groups, and are tacky at room temperature. PVAc is a typical addition polymer[22]. Both of these compounds share a near-unity specific gravity, which renders them invisible to any cleaning system. In addition, the glass transition temperatures (T_g) of the polymers are below typical operational temperature (acrylate ~ -50 °C, PVAc ~ 30 °C). Above the T_g , the polymers are deformable and are capable of maneuvering through the screen, even if the particle size is larger than the cut in the screen. The monomer units of the two compounds are shown in Figure 2.3.



Figure 2.3: Monomer units of polyacrylate and PVAc[23]

Now that the most common compounds comprising stickies found in the papermaking process have been identified, this review will present some of the most common methods used to treat stickies.

2.1.2 Treatment methods used for stickies

For many years the paper industry has attempted to control the stickies problem using a number of methods. While no universal method has been found to prevent all stickies problems from occurring, several methods have been developed in an effort to reduce the problem and minimize the negative effect stickies have in the papermaking process.

The first method is to remove the adhesives and plastics before they enter the recycling stream. This is most commonly accomplished by having people sort through the recycled material as it continues along a conveyer belt. This method is obviously very labor intensive and the effectiveness is largely dependent on the mixing of the paper and contaminants as well as the capacity of the manpower.

Another common method used to treat stickies is the addition of talc[24-27], to the wet end of the paper machine. Talc contains both hydrophilic and hydrophobic parts. The hydrophobic part associates with the stickie while the hydrophilic part bonds to fibers. Talc can coat the stickie thereby making it less tacky. An added benefit of talc application is the increase of the specific gravity of the talc-stickie combination, which makes the cleaners more effective since the stickie is no longer neutral buoyant. It has been noted however that the ability of talc to bond to the fibers is debatable because analysis of deposits on the paper machine shows that the deposits often contain talc[28].

The use of polymers, such as poly-DADMAC (Diallyldimethyl ammonium chloride) to coagulate stickies and make them larger and potentially easier to remove with pressure

screens is another treatment method[29, 30]. Different polymers can be used to disperse the stickies, which reduces the tendency of these particles to agglomerate and form larger stickies that commonly are problematic.

The final method of treatment discussed here is the application of a cationic polymer that acts as a sacrificial layer that retards the deposition of stickies to a particular surface, most commonly the forming wire[31, 32]. In this application, the polymer coats the forming wire, the stickies bond to the polymer rather than the wire, and the stickies are subsequently removed using wire showers. The bulk of the studies reported in the literature focus on stickie control in the forming and press sections. Few studies have been done on stickie deposition and the reduction of deposition on metal surfaces of dryer cans.

2.1.3 Deposition on dryer cans

The deposition of stickies onto dryer cans is a phenomenon that has garnered little consideration in studies presented in the literature. This is perhaps because the dryer can issues have only recently become more significant due to the success of pacification in the forming and pressing sections. This success has increased the amount of stickies entering the dryer section of the paper machine and increased the likelihood of problems occurring. The problems arising from stickies leaving the sheet of paper and attaching to the dryer cans range from a reduction of the surface quality of the finished sheet to reduced runability and potential downtime from continued buildup of the tacky deposits[33].

A study by Merchant and Banerjee investigated the transfer of macro stickies from a sheet to a hot metal surface under pressure[34]. The variables considered were solids content, temperature, furnish, and control chemicals. The classification method consisted of staining the stickies with Morplas Blue 1003 (a hydrophobic dye) followed by manual counting under a microscope. Several conclusions were drawn from the procedures: more transfer was found with increasing sheet moisture, and pressure sensitive adhesive (PSA) transfer is temperature independent unless the fiber is from a mechanical pulping system and is associated with lignin. Also, talc and polyDADMAC were found to promote retention in the sheet. The presence of lignin is significant because at drying temperatures near 100 °C, the transfer of the stickies to the metal plate greatly increased. This temperature coincides with the T_g of lignin, which is approximately 100 °C. Above the T_g , the bond strength of the stickie-lignin bond will be reduced because the lignin is much more fluid.

In another reported study, Hanecker presented a study on the adsorption of stickies to dryer cans[35]. The procedure involved screening the stickies through a 150 μm screen to remove macro stickies and then classifying the deposition onto metal plates as sheets formed from the pulp/stickie mixture are dried. PSAs containing acrylate as well as PVAc were studied, and qualitative results were presented that show the deposition was less significant at pH values of seven when compared to alkaline conditions. This study only considered pH as a variable and was not designed in a way to provide meaningful deposition data.

The lack of literature regarding both laboratory and real-world studies of stickies in the dryer section points to an interesting research area. There are a number of areas that can be studied including the interactions of stickies during the drying process and studying how the stickies form a bond on the dryer can surfaces. These studies can be extended to develop new methods of pacifying stickies in the dryer section and also to evaluate current techniques used combat the stickies problem.

2.2 Roll treatment and covering

Attempts to mechanically or chemically deter the deposition on dryer cans of stickies have not produced the desired results of reduced picking and deposition, with economical success. Equipment manufactures have attempted to alter roll surface where the deposition has occurred. For instance, press rolls have been fitted with a Teflon coating through a shrink-wrap application that intended to reduce the surface energy of the roll and subsequently reduce the deposition of stickies to the surface[36]. Although the method is effective in reducing build-up, Teflon surfaces are prone to scratching and wear quickly, reducing the efficiency of the method.

In another application of roll coating, the surface of rolls used in coating and size press applications have been covered with a high surface energy coating to increase the wettability of the rolls[37]. Another method was recently presented where the dryer surfaces are covered with a spray of hydrophobic chemical that changes the chemistry of the surface of the roll, thereby reducing the likelihood of deposition[38].

2.3 *Dryer operation*

The purpose of the dryer section of the paper machine is to remove the water remaining in the paper web following dewatering and pressing. Drying is a combination of heat transfer to evaporate the water in the sheet and mass transfer to move the newly formed water vapor away from the sheet. Drying is accomplished using steam-heated cylinders, commonly 2-6 ft in diameter[39]. The paper web is brought into contact with the hot surfaces of the dryer cylinders (or dryer cans) where heat is transferred from the cylinder to the sheet thereby evaporating the water. Figure 2.4 shows the four phases of the drying process.

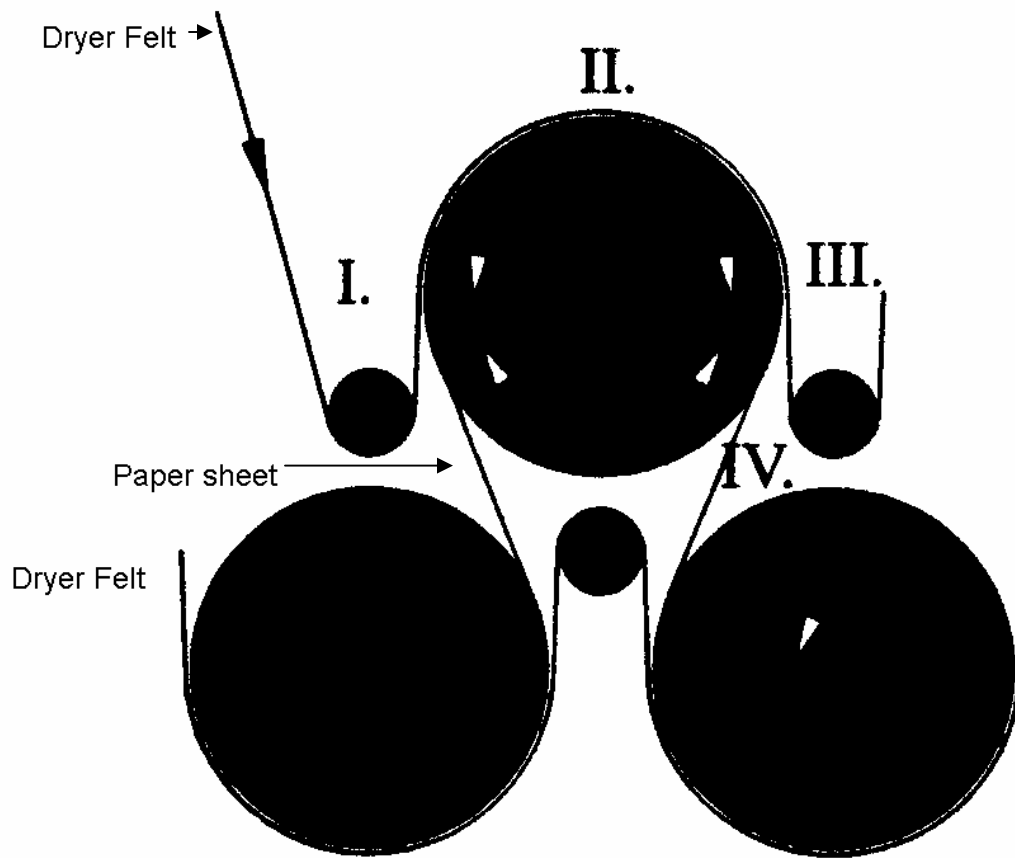


Figure 2.4: Four phases of drying[40].

There are four phases of drying on each dryer can. Phase I is the period when the sheet contacts the cylinder, before the felt applies additional pressure. Phase II is when the sheet is held onto the cylinder with the dryer felt. Phase III is when the felt no longer holds the sheet in place, and phase IV is when the sheet has an open draw until it reaches the next dryer can. The bulk of the heat transfer occurs during phase II when the sheet is in contact with the cylinder and the dryer felt. The bulk of the mass transfer is accomplished in phase IV when the sheet is in the open draw[40].

Steam is used to heat the dryer cylinders to the desired surface temperature. This temperature depends on several variables, most importantly the paper grade. Cylinder surface temperatures for a newsprint machine have been reported to range from 80-100 °C[41]. Surface temperatures for a machine producing 42 lb linerboard are shown in Figure 2.5, where the average temperature of the first cylinders is between 130-145 °C.

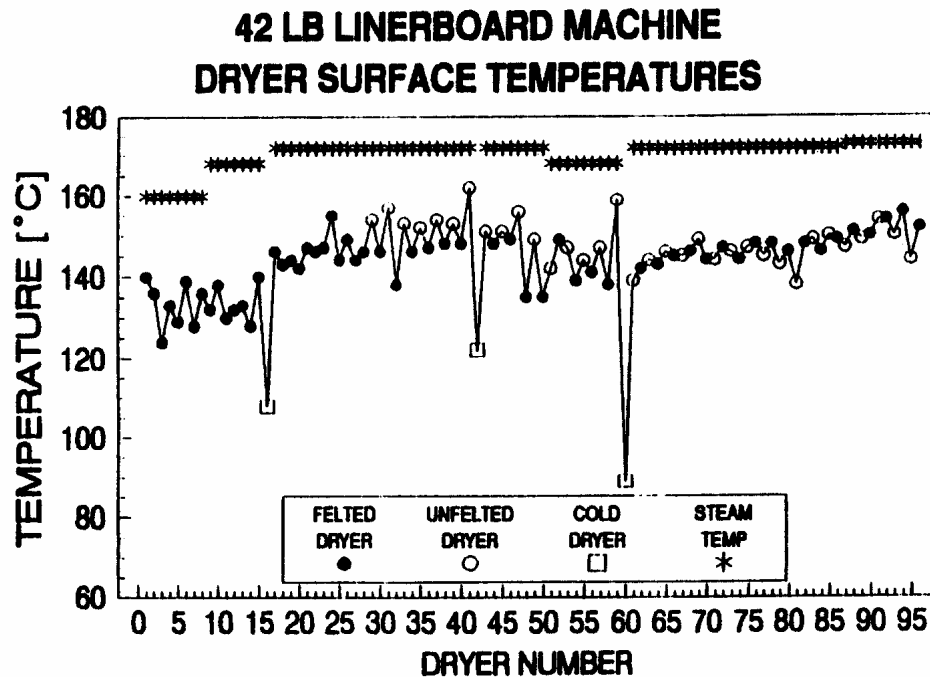


Figure 2.5: Surface temperatures for a linerboard machine[42].

The temperature of the first several dryer cans is typically adjusted to be within 17 °C of the sheet temperature to avoid picking and cockle problems that have been associated with heating the sheet too quickly[43]. Picking occurs when material is pulled from the sheet leaving a surface defect and cockle is blistering or puckering that results from the

sheet drying too quickly. Proper cross-directional (CD) temperature control is necessary to ensure consistent drying of the sheet. The surface temperature should not vary more than 3-5 °C from any position to another on the cylinder[40]. Figure 2.6 shows the CD profile of a cylinder from a linerboard machine that is operating with limited variation.

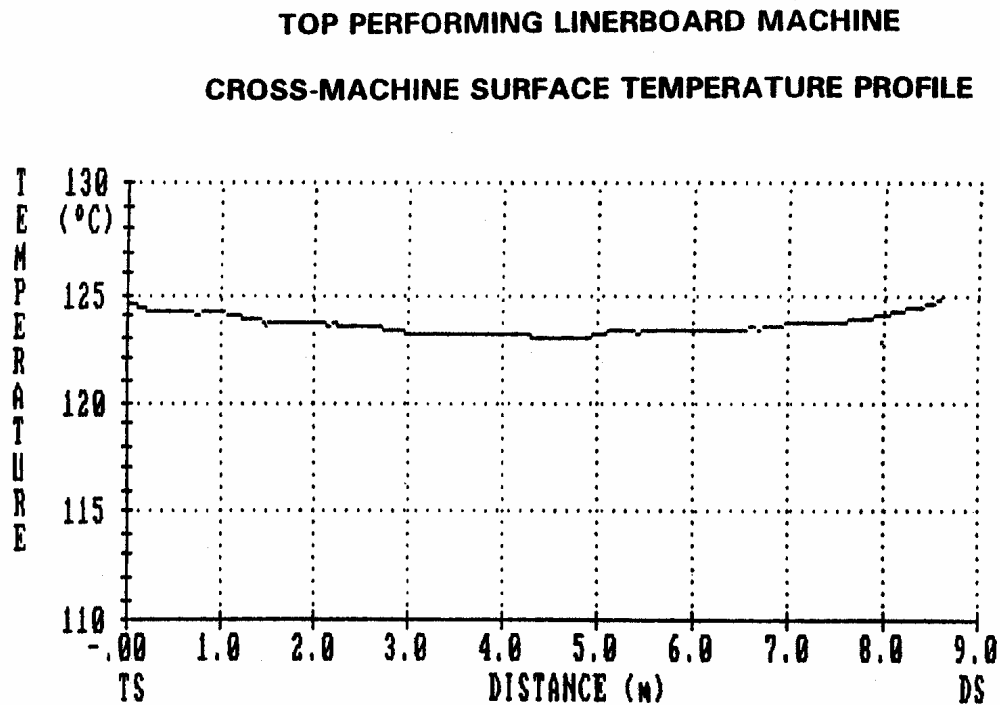


Figure 2.6: CD temperature profile for a linerboard dryer cylinder[40].

The dryer cylinders are typically constructed from cast iron or steel, which are not ideal materials from a conductivity standpoint since the conductivity of both materials is less than copper, for example. These construction materials are chosen because they have lower initial costs and they also meet the strength requirements, which are necessary because the dryer cans contain pressurized steam. Figure 2.4 shows a typical double

felt/two tier design that is common on many types of paper machines. The purpose of the dryer felts, commonly made of nylon or polyester, is to hold the sheet to the dryer surface, support the sheet while it is under tension, and reduce the CD shrinkage of the sheet. The felts are typically operated under tensions below 7.5 pounds per linear inch (PLI)[44]. This tension is used because above this value, the benefit of increased heat transfer is negated by reduced felt life and added wear on the dryer bearings. These conditions impart an operational pressure that ranges from 0.2-0.5 psi on the sheet[44, 45].

The overview of the drying process presented provides background on the operational parameters that potentially affect the transfer of tacky contaminants from the sheet to the dryer cylinders.

2.4 Adhesion

Adhesion is the interaction that occurs between two dissimilar bodies as they are brought into contact[46]. Theories of adhesion remain somewhat poorly developed and adhesion science is largely empirical, mostly depending on previous work to dictate what will be successful for future applications[47]. Therefore, studies must use theory and practical information to determine the mechanisms necessary to provide sufficient bond strength for a particular application. The theory can also provide input about the effects of alternate environments on the adhesive.

Surfaces, when brought into contact, exhibit molecular forces of attraction, which is known as intrinsic adhesion. The molecular forces include: chemical adsorption (covalent and ionic bonds) and physical adsorption (hydrogen bonding, dipole-dipole interactions, and van der Waals' forces). Adsorption, the first step of adhesion, is a thermodynamically derived process. The free energy associated with adsorption, ΔG_{ad} , must be less than zero for the adsorption to occur. The free energy is defined as follows:

$$\Delta G_{ad} = \Delta H_{ad} - T\Delta S_{ad} \quad [1.1]$$

Where ΔG_{ad} is the free energy of adsorption, ΔH_{ad} is the enthalpy of adsorption, ΔS_{ad} is the entropy of adsorption and T is temperature.

When liquid is adsorbed, ΔS_{ad} is always negative, and for adsorption to occur, ΔH_{ad} must also be negative. Physically, there are barriers that will promote or obstruct the adsorption. The surface tension and viscosity of the liquid can reduce the ability of the substance to adsorb on the surface, as can small pockets of gas that produce a pressure gradient away from the surface. Species previously adsorbed on the surface can deter the adsorption if they do not associate well with the adhesive, but if the surface contaminants are attractive to the adhesive, they can promote the adsorption. The application of pressure on the adhesive is yet another factor that promotes the adsorption.

2.4.1 Contact angle

Following the adsorption of the adhesive on the surface, a thermodynamical description can be made of the system. Wetting is another term that is used to describe the spreading

of the adhesive on the surface. Measurement of the contact angle, which characterizes the extent of surface wetting, is shown in Figure 2.7.

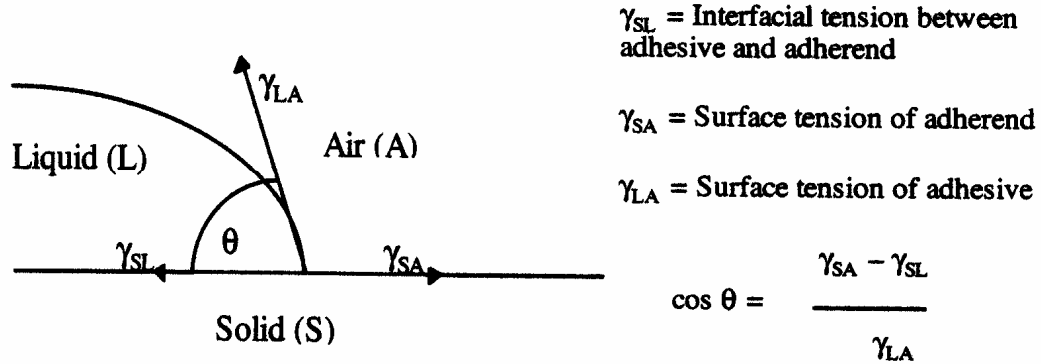


Figure 2.7: Contact angle definition.

(Note: The definition of A for air in the above figure is generalized in the derivations below to v for vapor.)

When the attractive forces between the two substances are low, the contact angle is large and may approach 180° . When the contact angle is near 0° , the liquid will spread and wet the surface. This occurs when the interactions of the liquid with itself are less favorable than the newly formed liquid-solid interactions. The contact angle can be related to the free energies through a geometrical expression known as Young's equation.

$$\gamma_{sv} = \gamma_{sl} + \gamma_{lv} \cos \theta \quad [1.2]$$

The surface tension of liquids (γ_{lv}) is easily measured using contact angle measurements, but the surface energy of the solid (γ_{sv}) is not easily measured. The value of γ_{sv} is approximated by finding the critical surface tension (γ_c). This is accomplished by testing

a series of homologous liquids and extrapolating the results to $\cos \theta = 1$, where the value of the critical surface tension is defined. There are typically different values for liquids that are capable of hydrogen bonding and liquids that do not hydrogen bond. Typically, metals, ceramics, and polar polymers have high values of γ_c while polyolefins and fluorocarbons have low values for γ_c . The contact angle describes the conditions necessary that allow the liquid to wet the surface, and work of adhesion describes the strength of the interactions.

2.4.2 Work of adhesion

In order to quantify the energy associated with an interaction that occurs when a substance is brought into contact with a surface, the principle of work of adhesion has been theorized. Consider the hypothetical condition where θ in Figure 2.7 is 180° .

Equation 1.2 simplifies to:

$$\gamma_{sl} = \gamma_{sv} + \gamma_{lv} \quad [1.3]$$

Equation [1.3] represents a simple ideal expression for the interfacial tension, γ_{sl} that represents the interfacial tension for a system that has no attractive forces between the liquid and solid. In real systems there are attractive forces that reduce the interfacial tension so it is always less than the sum of the solid/vapor and liquid/vapor surface tensions ($\gamma_{sl} < \gamma_{lv} + \gamma_{sv}$). The amount of this reduction is a measure of the strength of the interfacial attraction or work of adhesion (W_a).

$$W_a = \gamma_{sv} + \gamma_{lv} - \gamma_{sl} \quad [1.4]$$

Equation 1.4 is the Dupre equation and physically it means that the work required to separate a liquid and a solid surface is equal to the change in free energy associated with the separation. Combining Young's Equation (Equation 1.2) with Dupre's Equation (Equation 1.4) creates the Young-Dupre Equation that is commonly used as an expression of the work of adhesion.

$$W_a = \gamma_{lv}(1 + \cos \theta) \quad [1.5]$$

Using simple non-polar compounds that wet the surface with a surface tension of, for example, 25 mJ/m², gives a W_a value of 50 mJ/m². Experimental data has shown the work actually required to remove an adhesive from a substrate is 1-10 J/m²[46]. The adhesive dissipates the excess energy as it stretches because of the cohesive strength of the adhesive.

The strength of an adhesive bond is the combination of the molecular bonds associated with the system and the dissipative ability of the adhesive. The molecular bonds consist of London dispersion forces, van der Waals' forces, and others such as hydrogen bonding and dipole-dipole interactions. These bonds are responsible for the threshold strength of the system. Any additional energy that the bond is able to withstand is due to the ability of the adhesive to dissipate energy through elastic deformation. Rheology is the deformation of the substance as it is placed under stress. Adhesives are designed to become stronger as they are placed under stress, which enables them to dissipate large amounts of energy. The adhesives often resist the stresses by crystallizing when subjected to high shear rates.

2.4.3 Tack

The theory of tack is important when dealing with adhesives, particularly PSAs. Tack is the resistance to separation when two substances are momentarily brought together with minimal pressure applied[48]. The surface that the adhesive bonds to is commonly referred to as the adherent[49].

There are three main requirements for a substance to be tacky. First, the substance must wet the surface where it will adhere[50]. Substances that are able to accomplish this are compliant, meaning they are able to conform to the shape of the surface they are placed on. The viscosity of the fluid is the most important factor in determining the conformation potential to the surface[51]. Application of pressure can greatly influence the ability of a substance to comply with a surface. Following the wetting of the surface, the adhesive can interact with the surface.

The second requirement is that the adhesive have attractive interactions with the surface with which it is bonding. Interactions between the adhesive and the substrate include van der Waals' forces, London dispersion forces, dipole-dipole forces and potentially hydrogen bonding. These interactions bring the adhesive and the substrate into intimate contact. With this intimate contact, the strength of the bond is described by work of adhesion, which was discussed previously. Stronger interactions lead to a greater threshold strength of the bond.

The third requirement for a PSA to bond successfully is that it resists flow upon detachment from the surface. This is commonly accomplished by using a polymer that crystallizes when it is introduced to high strain. As the adhesive resists the strain it deforms and dissipates energy that is being applied to the bond. The bond will fail when the strain overwhelms the cohesive strength of the adhesive, or when the adhesive is stressed in a way that limits its ability to deform. Many PSAs are designed to allow removal without leaving material on the surface. These adhesives are designed to have a cohesive strength greater than the bond that is formed. This forces the bond to break, rather than the adhesive.

Many PSAs are modified with tackifiers, which are typically small organic molecules that increase the tacky nature of the adhesive system. The tackifiers increase the ability of adhesives that do not wet or conform well, to flow. This increased flow at low shear rates allows the adhesive to better conform to the surface. A disadvantage of the use of tackifiers is that they potentially reduce the cohesive strength because they could interfere with the bonding sites present in the adhesive.

2.4.4 Autohesion

Autohesion is a process that brings together two surfaces of the same material that are able to bond. Strictly speaking, autohesion describes the association of two identical surfaces, but the theory can be extended to surfaces comprised of similar substances. The principle of autohesion is effective when two similar polymers are brought into contact. The end result of autohesion is a reduction of the total surface area by the elimination of a

surface, which is favorable from a free total surface energy viewpoint[52]. Autohesion begins with contact. This contact can provide a bond if the materials are soft and able to conform to each other. Following the creation of the interface, the polymers can potentially inter-diffuse if the polymers have sufficient mobility, effectively eliminating the interface. The magnitude of the bond formed in an autohesion process is, as expected, larger than a bond based on tack[53]. The ability of polymers to autoadhere is related to the solubility parameter of mixing. Additionally, the diffusion is reduced with higher molecular weight materials, cross-linked polymers, and semi-crystalline, rather than amorphous materials[46].

Adhesion processes involving autohesion are reported to be independent of pressure. The main factor that affects the strength of the autohesion bond of similarly soluble compounds is the extent of contact, or time[46]. Autohesion can enhance the strength of adhesive bonds of similar compounds over the contributions of tack.

2.4.5 Effects of roughness

Although abrasion is a commonly used surface treatment that increases the strength of adhesive bonds, the property of roughness does not affect the strength of bonds[54, 55]. Abrasion is used to remove unwanted contaminants from the surface. These contaminants range from oils and low molecular weight polymers to surface oxides that do not bond well. Abrasion commonly affects the adherent roughness and care is taken to reduce the amount of roughness that is added during any cleaning process.

The wetting of the surface is most affected by changes in roughness of a surface. The roughness may not allow the adhesive to spread to the extent that it would on a smooth surface. The effects of roughness on adhesion are reduced when there is liquid present because the liquid forms a thin layer between the adhesive and the surface, which minimizes the roughness[56]. Additionally, the spreading into a nearly closed pore is limited by pressure build-up inside the pore, which consequently deters the flow[54]. Roughness is also a factor in the debonding mechanisms of PSAs, which will be discussed in detail in Chapter two.

Roughness is a factor in the mechanical adhesion theory of fibrous materials such as cotton, wood and paper. Mechanical interlocking that occurs when the adhesive flows around the fibers and dries can be responsible for significant increases in bond strength over just surface adsorption bonding[57]. However, in cases of adhesion to metal surfaces, increased levels of roughness do not provide additional strength to adhesion bonds.

2.4.6 Adhesion mechanisms

Adhesion can be accomplished and described using four theories or mechanisms. Each of these mechanisms describes separate physical phenomena that work alone or possibly together to provide strength to the adhesive bond. The mechanisms are not completely understood by the adhesives industry. The industry uses mostly empirical data to design new adhesive applications because the current theories are not robust enough to always

predict results of practical problems. The first mechanism, mechanical adhesion, is the oldest and easiest mechanism to visualize.

2.4.6.1 Mechanical adhesion

Mechanical adhesion describes the interaction of adhesive films with fibrous, porous structures such as paper, wood, leather and cotton. The adhesion involves the interlocking of the adhesive with surface irregularities. The process has been described as a “hook and eye” procedure[57, 58]. Simple surface roughness does not provide sufficient irregularities to allow the mechanical interlocking of the adhesive and the surface. The process begins when the adhesive flows into the open pore irregularities of the surface and dries. The drying process ends with the surface and the adhesive entangled, forming an effective bond.

Although mechanical adhesion produces a strong bond, many applications are not suited for adhesives of this type for several reasons. First, surface preparation is not able to alter most surfaces to the extent that mechanical bonding will work well. Also, the adhesives that are used in mechanical bonding are solvent based, which requires them to dry and harden, which is not practical in a number of applications. The following mechanisms have evolved more recently and describe the interactions of many adhesives and the surfaces with which they bond.

2.4.6.2 Adsorption adhesion

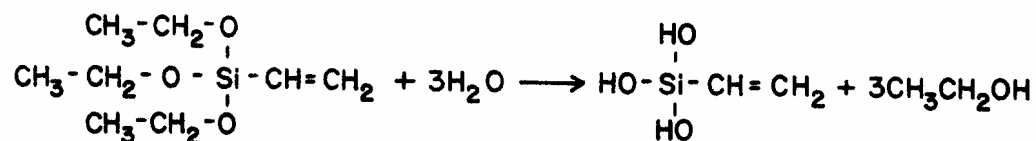
The second mechanism describes the adsorption of the adhesive onto the surface and the interactions that provide the strength to the bond[58]. There are two types of adsorption that are categorized depending on the types of interactions present in the bond: physical

or chemical. Both mechanisms allow for adsorption as described by the work of adhesion. Following the adsorption, each mechanism utilizes alternate methods to increase the bond strength.

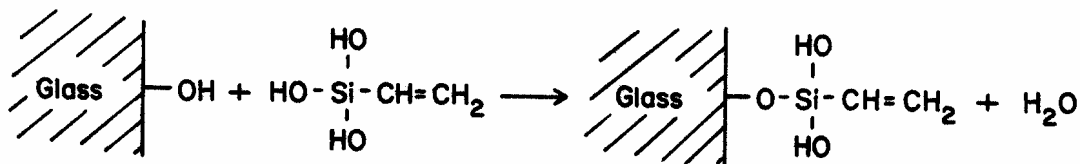
Physical adsorption always utilizes dispersion forces such as van der Waals' forces and potentially uses hydrogen bonds if the adhesive and surface are both polar[59]. Physical adsorption is the mechanism of adhesion for PSA materials, hot melts, and many solvent-based adhesives[51, 58]. Because physical adsorption takes advantage of molecular interactions that are always present, there is always a physical adsorption contribution to adhesion.

The contributions of chemical adsorption are dependent on the chemical nature of surfaces and the adhesive. Chemical adsorption occurs in conjunction with physical adsorption. The bonds produced by chemical adsorption provide additional strength and degradation resistance when compared to just physical bonds. Ionic and covalent bonding is responsible for the additional strength associated with chemical bonds. Adhesives are designed for chemical adsorption by adding coupling agents such as silanes. The silane group enables the adhesive to react with OH^- groups on glass or metal surfaces. The addition of specific groups on the surface typically requires some form of surface preparation that will increase the concentration of OH^- groups available for bonding. Figure 2.8 shows the common reactions that occur in chemical adsorption.

(a) Hydrolysis



(b) Condensation



(c) Coupling

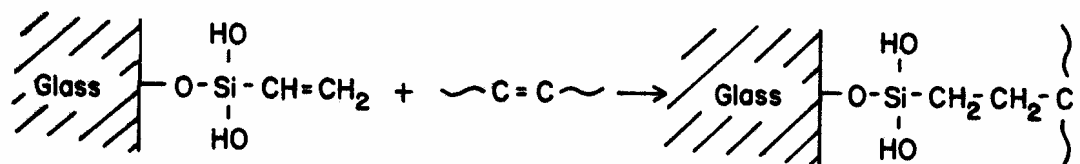


Figure 2.8: Common reactions involving a coupling agent[46].

The bonds associated with chemical adsorption have been reported to increase the threshold strength of adhesion from 1-10 J/m² to 20-100 J/m²[46]. Although the threshold strength is increased dramatically, it is still less than the cohesive strength of most polymers and is still the weak link in the adhesion bond.

2.4.6.3 Diffusion adhesion

The diffusion mechanism describes the situation where the ends of the adhesive polymer are able to diffuse into the substrate and secure themselves in the material[58]. The diffusion is enhanced by the use of solvents that increase the mobility of the polymers during the setting process. The process is only useful in the adhesion of polymers that

allow the adhesive to diffuse across the interface. Therefore, rigid materials with fixed molecules are excluded as substrates for diffusion adhesion.

2.4.6.4 Electrostatic adhesion

The principle of electrostatic adhesion is based on the ability of metals to produce an induced charge when certain polymers are adsorbed on the surface. This charge that produces an electrostatic double layer provides attractive forces in addition to the forces from physical adsorption. The strength of these bonds has not been quantified, but at very short distances it is negligible when compared to dispersion forces[56, 60].

The adhesion mechanisms that describe the bonding of adhesives to surfaces vary in the relative strength of the bonds they produce. Each requires specific material characteristics, although physical adhesion depends on molecular interactions and is always present. There are interactions such as the hydrophobic effect that can help to provide the close contact that is necessary to begin the adhesion process.

The next chapter will expand on these fundamental aspects of adhesion to study and explain the measurement of tack and also introduce several other surface characterization techniques that will be used to explain the phenomena of interest in this thesis.

CHAPTER 3 – THE ROLE OF FILM TOPOLOGY IN TACK

3.1 Introduction

The goal of this chapter is to present and explain an unexpected result that occurred when a common polyacrylate pressure sensitive adhesive formulation (Carbotac® 26171) was dried on different metal surfaces. The tack of the adhesive was noticeably lower for the adhesive dried on 1008 carbon steel, compared to 304L stainless steel. Each film was applied with identical methods that resulted in the same thickness, and each sample was subjected to the same drying conditions.

The result is unexpected since the thickness of the films ($>20\text{ }\mu\text{m}$) is much greater than those of thin films where orientation effects would be expected. The methods used to determine the differences between the films will be chronicled along with descriptions of the relationships between the measured fundamental properties and the observed practical properties of the films.

The background information provided in this chapter will introduce the fundamental concepts necessary to understand surface energy and tack and how each is measured. Additionally, an introduction to AFM is given due to the important role AFM plays in the experimental findings presented here. This information will lead into the experimental and discussion sections where results will be presented to confirm the origin of the unexpected result described above.

3.2 *Surface Free Energy*

3.2.1 Background and Introduction

The study of interfaces between two substances has been of great interest to scientists and technologists for a number of years. A common area of study involves the surface free energy (and its components) that occur between two interacting surfaces. These energies are important in a number of industrial applications including adhesion, coating, deinking, printing; and in other areas including chemistry and biology[61-65]. Interfacial energies are responsible for many of the interactions between two substances and therefore the characterization of these energies is important to understanding and predicting the strength of the interactions. Many of the industrial applications contain interactions between a liquid phase and a solid phase making the characterization of these systems significant. The study of this topic leads to understanding wetting, spreading, bubble-particle and a number of other phenomena that drive the previously mentioned industrial applications.

Perhaps one of the simplest yet most useful and common techniques used to characterize a solid surface is the liquid contact angle. This technique, first developed by Thomas Young in 1805, determines the interaction energy between a liquid and a surface that are within an equilibrium distance[66-71]. The contact angle is the angle produced when a drop of liquid is placed on a solid surface and measured from the solid under the drop to the surface of the drop. The value of the contact angle (typically called θ) is indicative of

the interactions between the surface and the liquid and is a result of a balance of the cohesive energies of the liquid and the adhesive energies of the liquid-solid system. For the case where the work of cohesion between the liquid molecules is greater than the work of adhesion between the liquid and the surface, the liquid will form a drop on the surface with a measurable, finite contact angle. The case is shown and the contact angle is defined in Figure 3.1 illustration a). Spreading, or film formation, will occur in the case where the work of adhesion is greater than the work of cohesion as shown in Figure 3.1 illustration b).

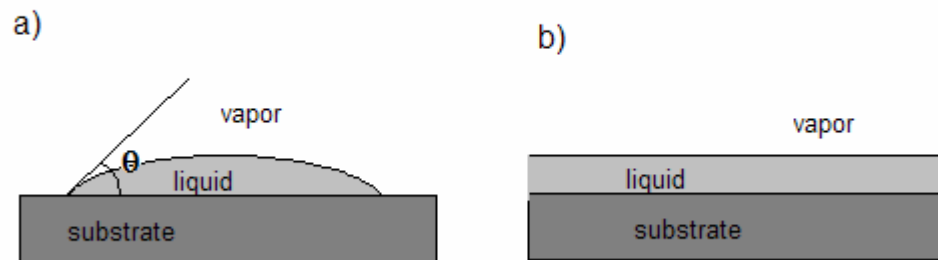


Figure 3.1 Diagram describing (a) drop formation on a substrate and (b) film formation on a substrate. Contact angle (θ) is also defined. Adapted from de Gennes[72].

When water is used as the liquid, the technique becomes a measure of the hydrophobicity of the surface. Surfaces that produce water drops with larger contact angles are more hydrophobic[73-76]. The water drop contact angle results can be combined with the contact angle results from other liquids to calculate the surface free energy (γ_s) of a solid. (This procedure will be developed later in this thesis.) In general, surfaces that have

lower water drop contact angles will have higher surface free energies[77-80]. The review will continue to introduce the forces and interactions commonly discussed with surface energy and then present background information regarding the measurement of these interactions.

3.2.2 Interactions

To facilitate the discussion of interactions between materials, the interactions will be separated into two groups: polar and non-polar (or apolar). Polar and non-polar interactions are also known as non-dispersive and dispersive, respectively. The discussion will begin with the non-polar interactions, often called van der Waals forces since they are present in all systems. These interactions are commonly referred to as Lifshitz-van der Waals interactions. For additional perspective on these interactions, a good review has been done by Yildirim[81].

3.2.2.1 van der Waals forces

The presence of forces between molecules has been studied since the 1870s when van der Waals introduced the concept of a general, attractive force that acts between pairs of neutral atoms to attempt to explain deviations from the ideal gas law in experimental data for gases[82-84].

The van der Waals forces are commonly divided into three groups, each describing a different type of interaction: orientation, induction and dispersion. Of the three, dispersion forces are always present with orientation and/or induction depending on the type of system in question. Because of the constant presence of van der Waals forces, a

number of common phenomena including adhesion, wetting, surface tension and physical adsorption[85] are dependent on van der Waals forces. The three groups of forces will be described next.

First, Keesom described forces that develop from dipole-dipole interactions arising from two molecules with dipoles that orient themselves to attract the other[86]. The energy associated with this interaction is described with the following equation for the total potential energy (V) of attraction of two permanent dipoles in a vacuum, known as the Keesom Equation[87]:

$$V = -\frac{2}{3} \frac{\mu_1^2 \mu_2^2}{(4\pi\epsilon_o)^2 kTr^6} \quad [2.1]$$

In the expression for potential energy, μ_1 and μ_2 are the dipole moments of the molecules; ϵ_o is the dielectric permittivity in vacuo ($8.854 \times 10^{-12} \text{ C}^2\text{J}^{-1}\text{m}^{-1}$); k is the Boltzmann constant ($1.381 \times 10^{-23} \text{ JK}^{-1}$); T is the absolute temperature; and r is the distance between molecules 1 and 2[88]. Of note is the fact that the energy is inversely proportional to the sixth power of the distance between the molecules.

The second interaction was developed by Debye. He suggested that intermolecular forces were caused by the ability of molecules and atoms with a dipole to polarize neighboring molecules and atoms that are neutral[89]. The expression for the potential energy of attraction (V) between a permanent dipole and an induced dipole is called the Debye Equation[87]:

$$V = -\frac{\alpha_2 \mu_1^2 + \alpha_1 \mu_2^2}{(4\pi\epsilon_o)^2 r^6} \quad [2.2]$$

In the expression for potential, α is the polarizability of molecules 1 and 2 and the other symbols are defined as before. As in the Keesom interaction, the Debye potential is inversely proportional to the sixth power of the intermolecular distance.

The final type of interaction included in van der Waals forces is known as London dispersion forces. The London forces are attractive forces between neutral molecules[90, 91]. The potential energy of attraction is given as follows in the London Equation[87]:

$$V = -\frac{3}{2} \frac{\alpha^2 h \nu}{(4\pi\epsilon_o)^2 r^6} \quad [2.3]$$

where, h is Plank's constant (6.626×10^{-34} J*s); ν is the frequency of fluctuation; and all other symbols are as defined previously. Again, London forces are inversely proportional to the sixth power of the intermolecular distance. Because molecules are able to vibrate in three dimensions, the 2 in the above equation becomes a 4[87]. There are a number of other corrections for the London Equation based on the specific properties of the system in question found in the literature on the subject. A good review of these corrections is found in Mahanty and Ninham[92].

To summarize the van der Waals forces, several points must be established. First, the forces act at relatively long ranges (from 0.2 nm up to 10 nm)[85]. Second, although the forces are typically attractive, there are situations when the forces can act as repulsive. An example of this is two macroscopic bodies immersed in a liquid medium[87]. Third, dispersion forces act to bring particles together and to a lesser extent, align them. The

term “dispersion” has nothing to do with the dispersing of particles but with the ability of the forces to disperse light[85, 87]. Finally, the non-additivity of the dispersion force refers to the effect of neighboring atoms or molecules on the interaction between two particles[85, 87].

3.2.2.2 Polar or acid-base interactions

The second type of interaction is polar, or acid-base, which are also called non-dispersive interactions because of the inability of the forces to disperse light when compared to the van der Waals forces. A number of interactions are included under the title “polar,” including H-bonding, all electron-acceptor/electron-donor and Lewis acid/Lewis base[82, 93]. Polar interactions may not be present in a system. The ability to separate the polar and non-polar components of a material, such as water, has proven to be important to analytical techniques designed to measure the surface energy of different surfaces. The next section will discuss this measurement and introduce common techniques used to measure liquid contact angles.

3.2.3 Calculating Surface Energy from Contact Angles

The importance of surface energy in a number of applications has led to measurements to determine the surface energy of a system and its heterogeneity. The surface forces apparatus measures the forces required to remove a very smooth surface away from another surface[94]. The technique is suitable for extremely smooth surfaces, which limits its usefulness as an analytical tool[85, 94].

Contact angle measurements can be performed by a number of techniques, including the du Nouy ring, Wilhelmy plate and sessile drop[62, 68, 85, 94, 95]. There are important considerations when performing contact angle measurements. For instance, when choosing a liquid probe for the measurements that material must have the appropriate polar characteristics and not dissolve the solid material being evaluated[96]. Contact angle measurements can be made using a static drop or a dynamic system. If unstable drops are formed with a static system, it becomes necessary to perform dynamic contact angle measurements. Often with a dynamic system there will be hysteresis, which occurs when the advancing and receding contact angles have differing values. Hysteresis is most commonly found when measuring heterogeneous solids. When present, the advancing contact angle is considered the intrinsic contact angle for the system[61, 97-99].

The contact angle data is commonly related to the surface energy by one of two techniques; both have been developed and used for over 30 years and the first uses an equation of state approach to find surface energy from contact angle data[94, 97, 100, 101]. The second technique is based on the work of Fowkes from 1972 and separates the different components of surface tension to determine the surface energy of a material[68, 98].

Both techniques start with the Young equation that relates the contact angle to the surface tensions of the liquid and the solid:

$$\gamma_{sv} - \gamma_{sl} = \gamma_{lv} \cos \theta_{eq} , \quad [2.4]$$

where θ_{eq} is the equilibrium contact angle as defined in Figure 3.1, γ_{sv} , γ_{sl} and γ_{lv} are the interfacial tension between the solid-vapor, solid-liquid and liquid-vapor, respectively. θ_{eq} and γ_{lv} are found using the contact angle measurement techniques mentioned previously. The common assumption that the equilibrium film pressure is negligible allows the adsorption at the solid-vapor and liquid-vapor interfaces to be neglected. Based on this assumption, $\gamma_{sv} = \gamma_s$ and $\gamma_{lv} = \gamma_l$, where γ_s is the surface tension of the solid and γ_l is the surface tension of the liquid[67, 97]. These assumptions have been confirmed for low-energy surfaces such as polymers[102-104].

The Dupre equation gives the thermodynamic work of adhesion (W_{sl}^a) between a solid and a liquid:

$$W_{sl}^a = \gamma_s + \gamma_l - \gamma_{sl} \quad [2.5]$$

Combining the Young equation and the Dupre equation yields the Young-Dupre equation:

$$W_{sl}^a = \gamma_l (1 + \cos \theta_{eq}) \quad [2.6]$$

Therefore, values for γ_s , γ_{sl} are needed cannot be measured, which is where the “equation of state” and the “Fowkes” techniques appear. First, the equation of state approach will be addressed.

Neumann has been involved with the majority of the work dealing with using the equation of state approach to find γ_{sl} . Two iterations of the equation have occurred. The first, from 1974 was as follows[97]:

$$\gamma_{sl} = \frac{(\sqrt{\gamma_l} - \sqrt{\gamma_s})^2}{1 + 2\alpha\sqrt{\gamma_l\gamma_s}} \quad [2.7]$$

with $\alpha = -0.0075 \text{ m}^2/\text{mJ}$. More recently, the technique has been altered to the following:

$$\gamma_{sl} = \gamma_l + \gamma_s - 2\sqrt{\gamma_l\gamma_s} e^{-\beta(\gamma_l - \gamma_s)^2} \quad [2.8]$$

with $\beta = 0.0001247 \text{ (m}^2/\text{mJ)}^2$. The technique has realized some success due to the empirical nature of the fitting of the constants (α, β) but the thermodynamic basis of the equation has been disputed[105-107].

Fowkes' technique, which has been outlined in several publications, is based on the separation of the different types of interactions that add to the final surface tension[68, 95, 98, 108]. Many of these interactions are described earlier in this review and lead to the following equation:

$$\gamma = \gamma_d + \gamma_i + \gamma_p + \gamma_h + \gamma_\pi + \gamma_{ad} + \gamma_e \quad [2.9]$$

where the subscripts are defined as follows: d – London dispersion forces, i – induced dipole-dipole, p – dipole-dipole, h – hydrogen bonding, π – pi bonding, ad – acceptor-donor and e – electrostatic.

Having introduced the components of the surface tension, the next step is to separate the components into dispersive (non-polar) and non-dispersive (polar) groups, in which case the surface tension is now defined as:

$$\gamma = \gamma^d + \gamma^n, \quad [2.10]$$

where γ^d is the dispersive component of the surface tension and γ^n is the non-dispersive component. By assuming a geometric mixing rule for the components of surface tension, the following is found[63]:

$$\gamma_{sl} = \gamma_s + \gamma_l - 2\sqrt{\gamma_s^d \gamma_l^d} - 2\sqrt{\gamma_s^n \gamma_l^n} \quad [2.11]$$

After inserting the above relation into the Young-Dupre equation (Equation 2.6) and rearranging,

$$\gamma_l \cos \theta_{eq} = -\gamma_l + 2\sqrt{\gamma_s^d \gamma_l^d} + 2\sqrt{\gamma_s^n \gamma_l^n} \quad [2.12]$$

By choosing a non-polar (dispersive) liquid probe ($\gamma_l^n = 0$), the equation can be rearranged, which allows the dispersive component of the solid surface tension to be found from the contact angle and the surface tension of the liquid.

$$\gamma_s^d = \frac{\gamma_l^2 (\cos \theta_{eq} + 1)^2}{4\gamma_l^d} \quad [2.13]$$

After this value is found, another liquid probe can be used to find the contact angle. This probe should have both dispersive and non-dispersive components of surface tension.

Water is a commonly used liquid for this step. The only unknown in Equation 2.13 is γ_s^d , which can be solved for. The total surface energy is then the sum of the dispersive and non-dispersive components: $\gamma = \gamma_s^n + \gamma_s^d$.

Surface energy calculations using contact angle measurements are an efficient way to characterize solid materials, especially low energy polymers, due to the large contact

angles typically formed on the polymers. When combined with other techniques, an accurate assessment of an unknown surface can be made.

3.3 *Atomic Force Microscopy*

3.3.1 Background and Introduction

This review of Atomic Force Microscopy (AFM) will begin with discussions of the development of this technique and its fundamental operating principles. Also, the techniques used to explore the polymer surfaces and examples of the analysis will be presented.

AFM has greatly improved the ability to measure and characterize surface properties of materials at the nano- and micro- scale since it was introduced in 1986 by Binnig *et. al* [109]. AFM has become popular since its invention because of its ability to resolve topographic images and surface characteristics such as hardness and attractiveness from relatively large features (several microns) to atomic levels in a variety of environments[109-113].

The ability of AFM to image surfaces in environments that include vacuum, ambient and fluid and also at a range of temperatures allows the measurement of surface forces and properties of a variety of materials ranging from metals to polymers[114-122].

3.3.2 Fundamental Principles and Measurements

The basic concept of AFM is to position a very sharp tip in close proximity of a surface to measure the deflection of the tip as the forces of the surface act upon the tip. A simplified description of the system is shown in Figure 3.2.

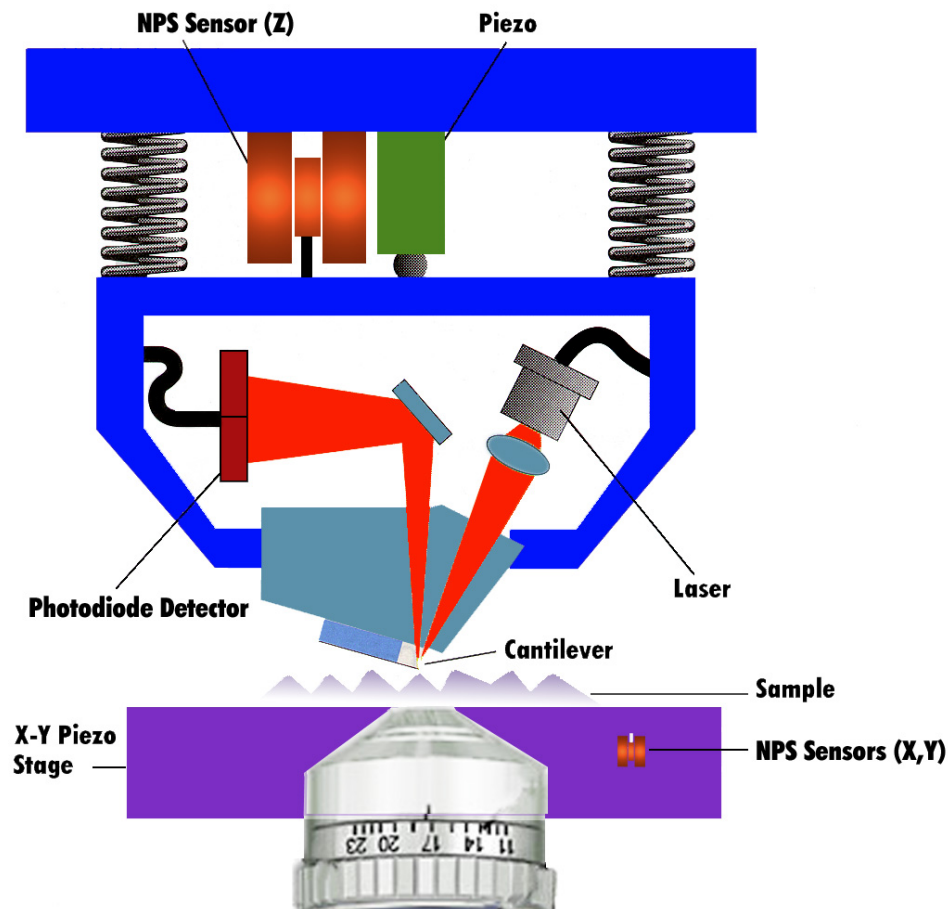


Figure 3.2: Simplified schematic of an AFM[123].

There are a variety of forces resolved with the AFM as the tip moves into close proximity of the surface that is being measured. A summary of the forces and the distance from the surface in the Z-direction where they occur is shown in Figure 3.3[124].

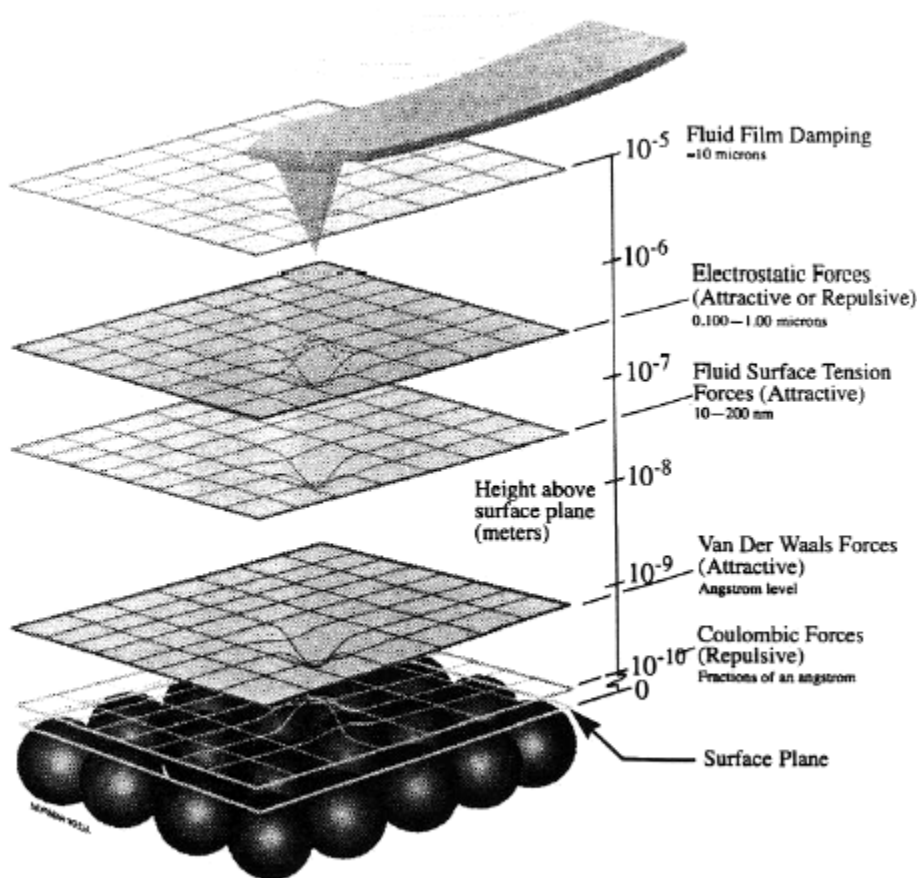


Figure 3.3: Forces involved in AFM[124].

Many of the forces acting upon the tip at distances above the Angstrom level can be altered or eliminated by changing the environment and conditions at which the sample is imaged. For example, the Fluid Surface Tension Forces that are recognized in the range of 10-200 nm can be eliminated by immersing the entire cantilever and tip under a liquid[125, 126]. It is also reasonable to counteract the effects to the Electrostatic Forces that act upon the tip in the 0.1-1.0 μm range by imaging the system in a liquid. This is done by balancing the attractive van der Waals forces with a repulsive double layer force, which is accomplished by changing the ionic strength and/or pH of the aqueous liquid to

manipulate the double layer until its force is repulsive and properly balances the van der Waals forces[127].

The tip, with dimensions in the nanometer (10^{-9} m) range, is mounted on a flexible cantilever beam with a spring constant (k) that can be measured in a number of ways but most commonly with the Sader technique that uses the dimensions of the cantilever and the resonance frequency to calculate k [128, 129]. The cantilever is manufactured with a reflective top side that reflects the laser, which allows determination of the deflection of the cantilever. This deflection data can be converted to force data by applying Hooke's Law ($F=k\Delta z$, where Δz is the deflection of the cantilever) to the deflection data and the spring constant[130].

Tip-cantilever systems can be manufactured from several types of materials: choosing a system depends on the surfaces to be probed and the results desired, which will be discussed later. The materials used to construct the tips can be altered to probe various chemical properties of the sample surface. Coating of the tip by various materials allows flexibility in experimental design. Tips are commonly manufactured using techniques common in integrated circuit manufacture, including lithographic photo-masking and vapor deposition. Tip manufacture itself is a very complicated area and is introduced in a paper by Boisen[131].

The type of sample to be imaged and the information desired from the experiment are important considerations when choosing the type of tip-cantilever system to use for the

study. For example, when imaging soft, delicate materials common in biological systems it is important to use a cantilever that is relatively soft with a low spring constant[125]. AFM users must be cognizant of the effect of tip shape and size on the resultant images found during analysis of a surface. The features that result from the shape and size of the scanning tip are known as artifacts. Artifacts become apparent when the sample has features that are nearly the same size as the tip. The shape of the tip also becomes important when the sample features of interest are nearly the same size as the tip. Figure 3.4 shows the importance of using a high aspect ratio tip[132]. The high aspect ratio tip produces an image much truer to the actual sample and is very important in adhesive modeling through contact mode AFM because it limits the tip-sample interaction to the point of the tip.

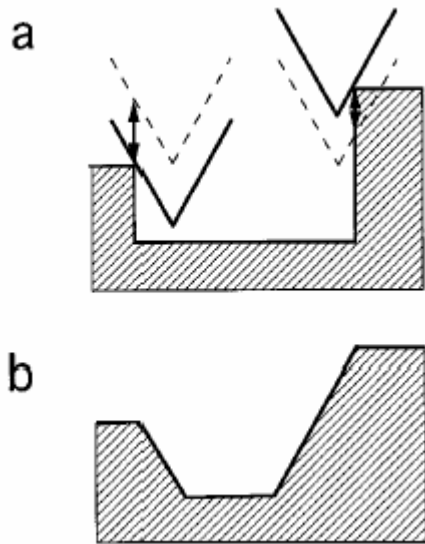


Figure 3.4: The importance of using a high aspect ratio tip. Shown in (a) is the surface deformation and a tip with a low aspect ratio. (b) shows the resulting shape as rendered by the AFM[133].

In addition to artifacts caused by shape effects, several other tip problems can arise that must be considered during analysis of samples with AFM. Depth of field is very limited in AFM. It is limited by the distance a tip extends from the cantilever, typically around 3 μm [125]. Because of this, it is very difficult to image rough samples with peak to valley distances nearing that of the tip height. It must also be noted that during manufacture cantilevers can be inadvertently fabricated with multiple tips. This “double tip” effect can cause images to appear to contain symmetric features similar to what is shown in Figure 3.5, which are typically easy to detect because of the appearance of features in pairs[125]. The most common technique used to characterize the tip attributes is scanning electron microscope (SEM)[134].

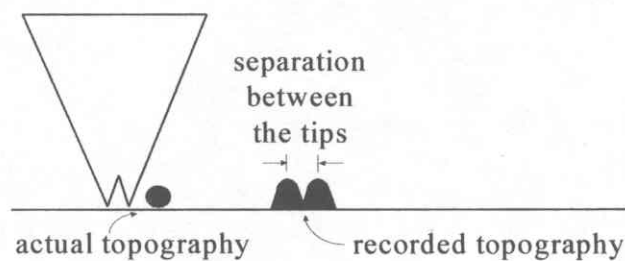


Figure 3.5: Example of how a double tip alters the topography and presents an image that is not an accurate representation of the surface[125].

For the most part, AFM artifacts are easily recognized by an experienced operator[120]. Care must be taken to choose appropriate set points and make proper adjustments as imaging is accomplished on samples with different properties.

3.3.2.1 Modes of Operation

There are three main modes of operation for AFM: contact, non-contact and intermittent-contact. In contact mode the surface is imaged by placing the tip in constant contact with the sample. Non-contact mode brings the tip into very close proximity of the surface without touching it. Intermittent-contact mode, also called tapping mode, operates by vibrating the tip and cantilever and bringing the tip into contact with the sample for very short periods of time. Figure 3.6 shows which forces are used in each of the modes of AFM. Note that tapping mode alternates between attractive and repulsive forces.

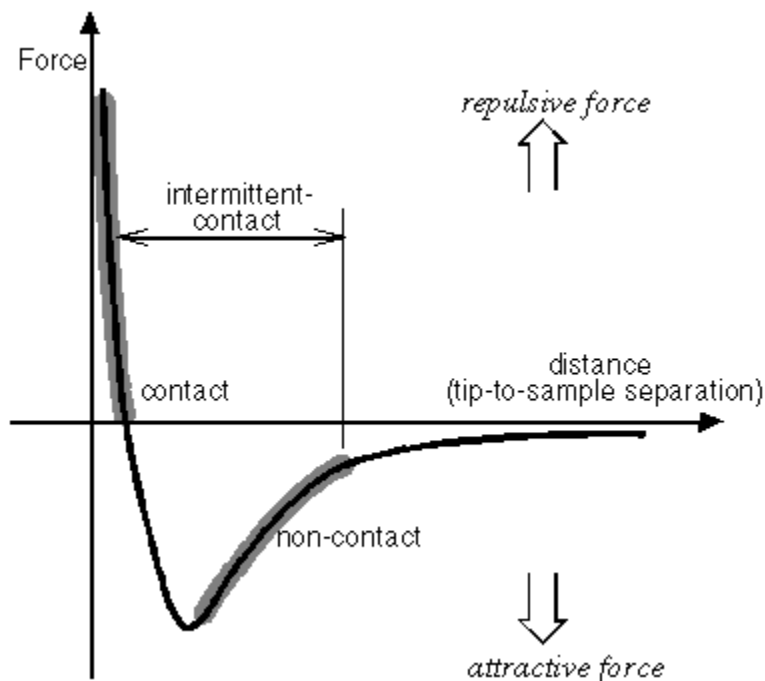


Figure 3.6: Force vs. distance curve showing which forces are considered for each of the three modes of AFM[135].

Scanning of a surface in contact mode AFM is done by lowering the cantilever to the surface thereby bringing the tip to the surface. After the tip contacts the surface the

cantilever is deflected upward by the repulsive force of the interaction, which is a stable interaction. The cantilever is pressed into the surface until the force reaches a set point, which is chosen by the operator and the height information is recorded. This is done a number of times along the surface (typically 512x512) to create a topographic image of the surface. The deflection (or error) image and the lateral tip-sample forces often give an accurate representation of a surface. The deflection image is basically a derivative of the topography image and the lateral forces are a representation of the frictional forces acting between the tip and the surface. Combining the topography images and the lateral force images is effective in exposing areas of the surface that may have varying mechanical or adhesive properties[120].

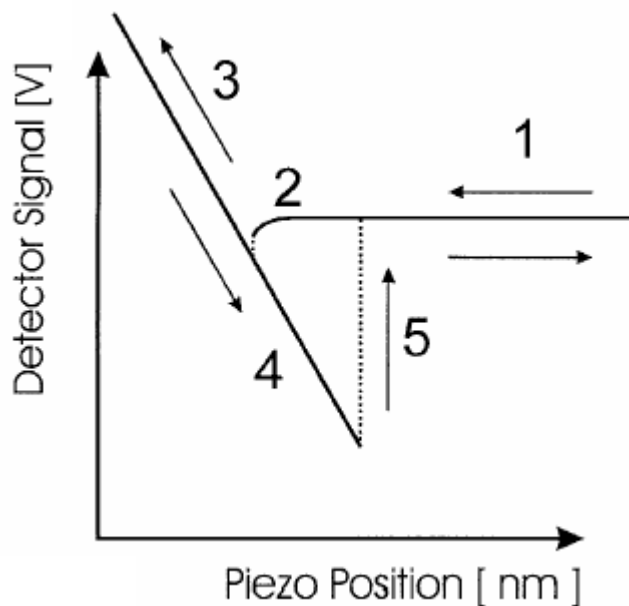


Figure 3.7: Region of the force curve used in contact mode AFM[136].

Figure 3.7 shows an example of a force curve, which is graph of the forces exerted on the tip by the surface as the tip is moved toward and away from the surface. In Figure 3.7 the ordinate is presented as the cantilever deflection in voltage, which is easily converted to force by converting the detector reading to a distance and multiplying by the spring constant of the cantilever as per Hooke's Law[130].

Starting at (1) on the right-hand side of the plot, the tip moves toward the surface until it is affected by long range attractive forces, which cause the tip to “jump in.” This is indicated by the dip in the incoming line at (2). Once the tip is in contact with the surface, the tip is repulsed until the direction of the tip is reversed (3). From this point the tip is pulled away from the surface (4) until it releases from the surface, which occurs at the point in the graph where the line jumps back to the original value (5). The hysteresis in the measurement is due to adhesion of the tip to the surface[137].

Another view of the process is shown in Figure 3.8, which also shows the cantilever position at two positions during the contact mode process. Figure 3.8 does not show the jump in point but otherwise is very similar to the previous image. At position 1 the tip is nearing the surface. At position 2 the tip is in full contact with the surface and at position 3 the tip breaks free from the surface and returns to its original position. The difference between position 3 and position 1 (when converted to Newtons) is called the pull off force (F_p) and is a good measure of adhesion between the tip and the surface. Tips can often be modified to change the chemical characteristics of the sample-tip interaction or to provide a standard surface[138].

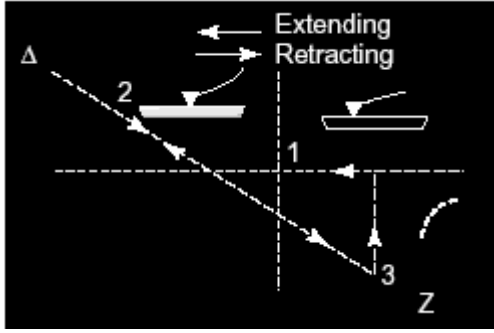


Figure 3.8: Cantilever deflection vs. scanner travel in the vertical direction[120].

Additional consideration must be given to the role of capillary forces due to the very thin layers of water that are inherent on surfaces at ambient conditions. As can be seen in comparing the top image to the lower image in Figure 3.9, the capillary force can significantly increase the F_p and the measured adhesion between the tip and the sample. The capillary force can be reduced by placing the sample and tip system under a liquid, which reduces the F_p by one to two magnitudes[120].

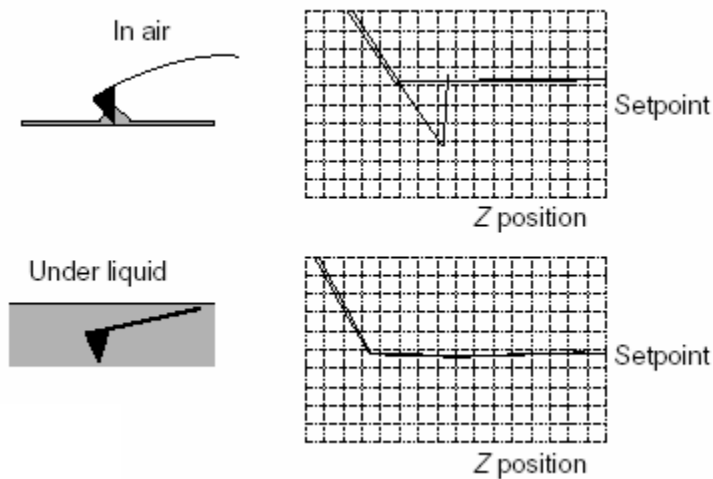


Figure 3.9: The effect of capillary force on the F_p measured with contact mode AFM[120].

The slope of the force curve after the tip has made contact with the surface is potentially useful from a material property standpoint. Information can be gained about the viscoelasticity of the surface material since the slope of the curve is related to the modulus of the material[139-141].

When imaging soft materials such as polymers or components in biological systems, using contact mode AFM could damage the surfaces due to the large pressures exerted on the surfaces by the tip. Magonov has done an extensive review of AFM of polymers and discusses some of the issues specific to polymer systems[120]. A potential way to reduce damage to the sample is to use non-contact AFM. Figure 3.10 shows the area of the force curve that is used in non-contact mode AFM. These forces are the attractive van der Waals' forces shown in Figure 3.3 and they represent an unstable position for the system. This instability, combined with the requirement that the cantilevers be extremely sensitive, makes it difficult to use non-contact mode AFM[142].

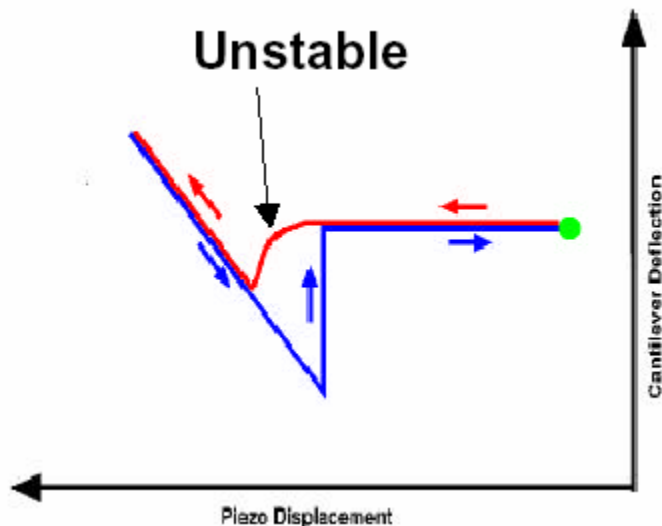


Figure 3.10: Region of the force curve used in non-contact mode AFM[142].

The utility of AFM improved drastically when tapping mode AFM was introduced. In tapping mode the cantilever-tip system is driven at a frequency near the resonance frequency of the cantilever and the tip is brought into contact with the sample. Since the tip is vibrating, it only intermittently contacts the surface, rather than embedding into and damaging a soft sample.

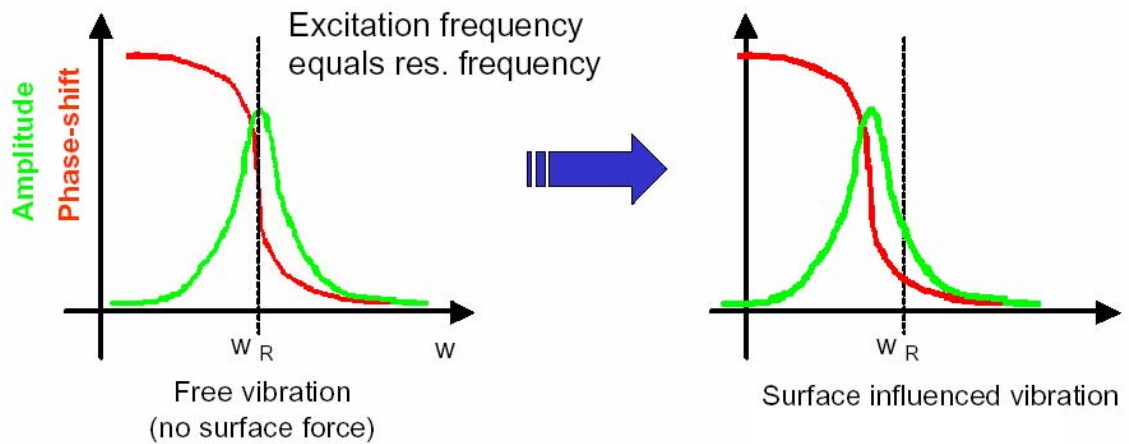


Figure 3.11: Representation of how the phase and amplitude of oscillation of the cantilever shift when the tip is brought into proximity of the surface[142].

As the tip nears the sample and the long-range forces begin to act, the cantilever's phase and amplitude of oscillation will shift. Figure 3.11 shows the original oscillation at the resonant frequency (W_R) and how the phase and amplitude of the oscillation shift when brought near a surface. The phase shift is especially dependent on the dissipative properties of the surface. Attractive forces cause a low-frequency shift in both the phase and amplitude oscillation while repulsive forces cause a high-frequency shift[120, 143].

Not only can tapping mode AFM characterize topology features of a surface but it can also provide insight into the heterogeneity of the attractive regions of the surface[144].

Characterization of the cantilever-tip system is one of the most important considerations in gathering AFM data because conversion of the deflection voltage data requires knowledge of the spring constant. Measurement of the spring constant can be done by a number of techniques and has garnered considerable discussion. Kappl *et al.* have presented a good review of the techniques[136]. Several of the techniques as well as the potential downfalls associated with each will be discussed here.

There have been attempts to calculate the spring constant based on the material properties of the components of the cantilever. The techniques have included using a finite element technique for the calculation and using geometrical parameters of the system[129, 145]. The problems associated with using these techniques arise from the difficulties in manufacturing cantilevers with uniform thickness and in measuring the thickness. Additionally, the topside of many cantilevers is coated with reflective materials to improve the reflection of the laser. This coating also changes the mechanical properties, making theoretical calculation of spring constants very difficult[136].

Due to difficulties in finding the spring constant through theoretical means, many techniques have been developed that utilize experimental values to determine a more accurate spring constant. Several techniques involve applying a force to the cantilever and measuring a variety of properties. The conceptually simple method of adding a

known mass to the cantilever and measuring the deflection due to the mass was first presented by Ducker and Senden[146]. Cleveland *et al.* developed the “added mass method,” which adds different masses to the cantilever and measures how the resonance frequency of the oscillation changes[147]. These different resonance frequencies are related to the spring constant through a plot of added mass vs. $(2\pi f)^{-2}$. A different approach is presented by Butt *et al.* where the cantilever is used to deflect a known pendulum and the deflection of the cantilever is measured[148]. There are also reports of using a second calibrated cantilever to apply a force to the AFM cantilever of interest and measuring the deflection[149-153]. Several of these techniques report accuracies better than 20%; however relatively large forces needed for measurement can cause cantilever damage.

Another technique for calculating the spring constant utilizes the thermal noise present in all objects. Thermal noise produces vibrations of the cantilever that can be measured and related to the spring constant as shown by Hutter and Bechhoefer[154]. Another technique that requires no contact with the cantilever that has proven to be effective is the Sader technique[128]. The Sader technique makes a calculation of the spring constant using the cantilever length, width, resonance frequency and quality factor and is the most commonly employed technique, which is why it is used in this study.

3.3.2.2 Roughness Determination

The tip and cantilever system can be used to scan the surface’s x-y plane to produce a topology map of the height of the sample in either contact or tapping mode. This data can be used to calculate roughness data to characterize the sample. The most common

statistical representation of the roughness is the root mean square (RMS) roughness, which is the standard deviation of all the height data for the image[49, 155-159].

When comparing height data, images of the same scan size must be compared[160].

Image analysis consisting of zeroth or first order flattening is useful to remove sample tilt from uneven sample loading that is often found in AFM images. Additional image analysis can be performed to eliminate image artifacts that develop during imaging.

3.4 *Pressure sensitive adhesives*

Pressure sensitive adhesives (PSA) are also known as permanent-tack adhesives and have a number of characteristics, most notably the ability to form a bond with minimal applied pressure. Additionally, no curing of the adhesive is required for the adhesive to function; there is no chemical reaction between the adherend and adhesive; and there is no loss of solvent during the bonding process[161]. The Pressure Sensitive Tape Council (PSTC) developed a list of characteristics to describe PSAs. PSAs are characterized as adhesives with the following qualities[162]:

1. Aggressive and permanent tack
2. Adhere with no more than finger pressure
3. Require no activation by any energy source
4. Have sufficient ability to hold onto the adherend
5. Have enough cohesive strength to be able to be removed cleanly from the adherend

The composition of PSAs commonly includes tackifiers and plasticizers to depress the glass transition point (T_g) of the polymer system to produce specific adhesive properties[163]. The polymers used in PSAs are above their T_g in the environment in which they are intended for use[164]. Polyacrylates and polyvinyl ethers are unique in that they are inherently pressure sensitive and need minimal additives to act as PSAs[165].

PSAs can be further divided into three general categories based on the specific application, as follows[166]:

1. Removable adhesives like the adhesives used on Post-It® notes by 3M Corporation. These applications require high compliance to allow quick application and low adhesion to ensure removability. Also, the cohesiveness of the adhesive must be strong to allow for complete removal from the adherent.
2. General-purpose or semi-permanent adhesives, which are most commonly associated with office tape and label applications. Moderate compliance and good adhesion is necessary but long-term resistance to environmental exposures is not necessary since the life span of the adhesives is limited.
3. Permanent or semi-structural adhesives are commonly used in applications of floor tile adhesives and other similar situations. High adhesion, high resistance to creep, and good environmental resistance is necessary for these adhesives.

PSAs have recently become more prevalent in manufacturing and building and are becoming more commonplace in situations where adhesives were previously not considered such as replacements for bolts and weld joints. However, some disadvantages limit using PSAs in certain situations such as low peeling and shearing strength, the importance of the adherent's properties (roughness and cleanliness), and the high relative expense[167].

Peel strength, shear strength and tack are used to characterize PSAs and to evaluate their potential uses[162, 167-170]. The basics of these characteristics will be presented along with methods used to test for each. Tack will be presented more completely in a separate section since it is the focus of this work.

Peel strength is measured as described in Figure 3.12 and is most commonly used as a measure of adhesion for pressure sensitive tapes. In the test the substrate is a constant as is the pressure used to apply the tape to the substrate, the rate of removal and the temperature. A peel angle of 90° best simulates the use of tapes in most scenarios but tests are usually accomplished with a peel angle of 180° to ease the experimental setup[171].

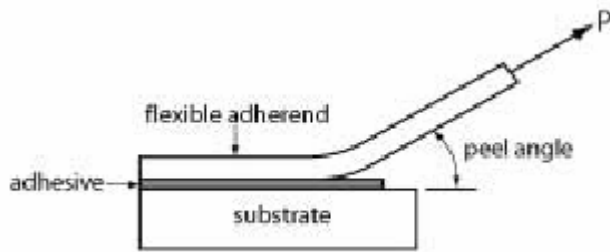


Figure 3.12: Diagram of peel test for PSAs[171].

Testing shear strength of an adhesive is accomplished as shown in Figure 3.13. In this test a weight is applied to the tape after it is attached to a substrate with a given pressure at a constant temperature. Failure in the shear test can occur due to a number of mechanisms, which limits the fundamental understanding that can be gleaned from the test. Often, peeling will contribute to failure during the test and mask true shear failure due to viscous flow of the adhesive[171].

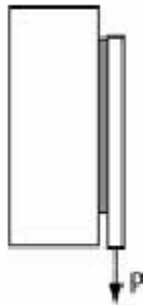


Figure 3.13: Diagram of shear test for PSAs[171].

The peel and shear tests are designed to measure properties specific to tape applications of PSAs (where the adhesive is applied to a paper, cloth or film backing) and the tests are

therefore limited. The property of tack is more fundamental and useful to characterize PSAs and will be reviewed in more depth in the following section.

3.5 Tack

The defining characteristic of a PSA is its tack, which is the quantification of the ability of the adhesive to form a bond with low applied pressure and minimal bond time. It has also been described as the energy needed to separate two objects that are not permanently bonded together[50]. Many factors contribute to the tack of a PSA including the ability of the PSA to wet the adherent, the energy dissipation characteristics of the system and the deterrence to debonding. The specific mechanisms responsible for the development of the adhesive bond have been discussed in Chapter 1. This review will expand the previous discussion by introducing methods used to test tack and also will discuss the factors responsible for debonding and bond failure.

Defining tack is difficult as characterized by the many terms used to describe the same basic phenomena reported in literature associated with the adhesive industry. Other names for tack include: wet grab, quick stick, finger tack, thumb tack, initial adhesion, quick adhesion and wettability[170]. Attempts to formalize the definition have been made by organizations such as the American Society for Testing and Materials (ASTM), which defines tack as “the force required to separate an adherend and an adhesive at the interface shortly after they have been brought rapidly into contact under light load of short duration[170].” This definition leaves significant room for interpretation due to the

ambiguous nature of the duration of contact (short) and the level of contact pressure (light).

To further complicate the understanding of tack, there are several different types of tack, depending on the materials involved and the debonding mechanisms relevant to the systems in question[166].

1. Cohesive tack – the separation process is defined by bulk flow of the materials involved and the tack is therefore dependant on the adhesive's internal resistance to flow[167]. Cohesive tack is applicable in discussions about materials such as printing inks, paints and syrups[172].
2. Adhesive tack – the separation between two materials occurs at the original interface between the two. Adhesive tack describes the adhesion between two dissimilar materials. PSAs typically participate in this type of adhesion during bonding although high temperatures and extreme debonding rates can induce cohesive tack[167]. Removable PSA applications such as Post-It® notes are an example of adhesive tack.
3. Autohesive tack – the bonding and separation of two similar elastomeric materials is described as autohesive tack. Commonly, the materials will exhibit adhesive tack during short contact times and cohesive tack after long contact times. The manufacture of tires is a commonly cited example of processes that involve autohesive tack[167].

The process of measuring tack is highly dependent on the systems under surveillance and the conditions imparted on the materials by the test systems. Some of the methods used to measure tack will be discussed in the following section which will be followed by an introduction to the effects of environmental influences on the measurement of tack.

3.5.1 Tack tests

Perhaps the easiest and most obvious test is the thumb tack test where a technician presses a thumb onto an adhesive and determines the stickiness of the adhesive. Aside from this type of measurement being largely subjective, it is only somewhat applicable among a small number of adhesives. Tests developed since the initial thumb test have improved reproducibility and attempted to standardize the testing and characterization of the tack of PSAs. The large number of tests still in existence indicates that the measurement of tack is not fully understood and that the end use of the adhesive plays a significant role in how the tack should be characterized. The tests described here are commonly referenced tests in the literature about tack measurement and are not meant to be a complete listing of all potential tack tests. A compilation of the commonly used testing standards is adapted from an editorial from Edward Petrie and given in Table 3.1[173].

Table 3.1: Table of Commonly Used Tack Measurements and the Associated Standards.

Organization	Test Method	Common Name	Note
ASTM	D2979	Probe Tack	
ASTM	D3121	Rolling Ball Tack	Identical to PSTC 6
TLMI	LIB 1	Loop Tack	LIB 1 uses a specially designed tester
	LIB 2		LIB 2 uses a modified tensile tester
PSTC	5	Quick Stick	Similar to AFERA 4015
PSTC	6	Rolling Ball Tack	Identical to ASTM3121
FINAT	FTM	Loop Tack	Similar to TLMI methods except uses glass rather than stainless steel as the substrate
AFERA	4015	Quick Stick	Similar to PSTC 5

ASTM - American Society of Testing and Materials

TLMI - Tag and Label Manufacturers Institute

PSTC - Pressure Sensitive Tape Council

FINAT - European Association of the Self-Adhesive, Labeling Industry

AFERA - Association des Fabricants Europeens de Rubans, Auto-Adhesifs

3.5.1.1 Rolling ball test

The rolling ball tack test uses an inclined ramp of a set height and length to accelerate a stainless steel ball down the ramp where it contacts the adhesive as shown in Figure 3.14.

The tack is reported as the length that the ball rolls after contacting the adhesive (d in Figure 3.14) and lower values signify higher tack. This technique is most useful for tape applications but has been shown to not correlate well with application results, especially for water-based systems and systems composed of acrylate based polymers[174, 175].

Additionally, the role of tape backing compliance and adhesive properties such as softness and weight as well as the overall lack of control in the measurement make gleanig fundamental understanding of the adhesion process difficult. Because of this, it is primarily used as a quality control measurement for adhesive tapes[171].

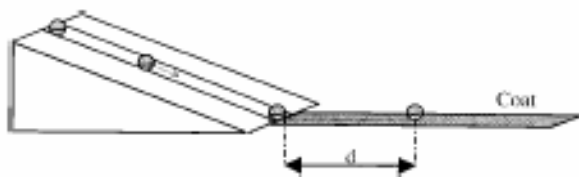


Figure 3.14: Diagram of the rolling ball tack test[176].

3.5.1.2 Loop tack test

The loop tack test is the first of two peel test modifications that have been developed to measure tack. There are two variations to the loop test; the first is for measuring tapes and the other is suited to measuring PSAs and coatings. The only difference between these variations is the location of the adhesive (the loop or the substrate). Obviously in the tape test the adhesive is in the form of a tape. In the second type of test, the film is deposited on a substrate. A schematic for the test is shown in Figure 3.15. Either the tape or a film material is made into a loop and attached to a tensile machine. The loop is then contacted with the substrate (a in Figure 3.15) with a given downward displacement and dwell time. The direction of the machine is then reversed, pulling the loop away from the substrate (b in Figure 3.15). This continues (c -> d in Figure 3.15) until the loop is fully dislodged from the substrate and the adhesive bond is broken. The maximum force measured during the removal is the tack value for the system.

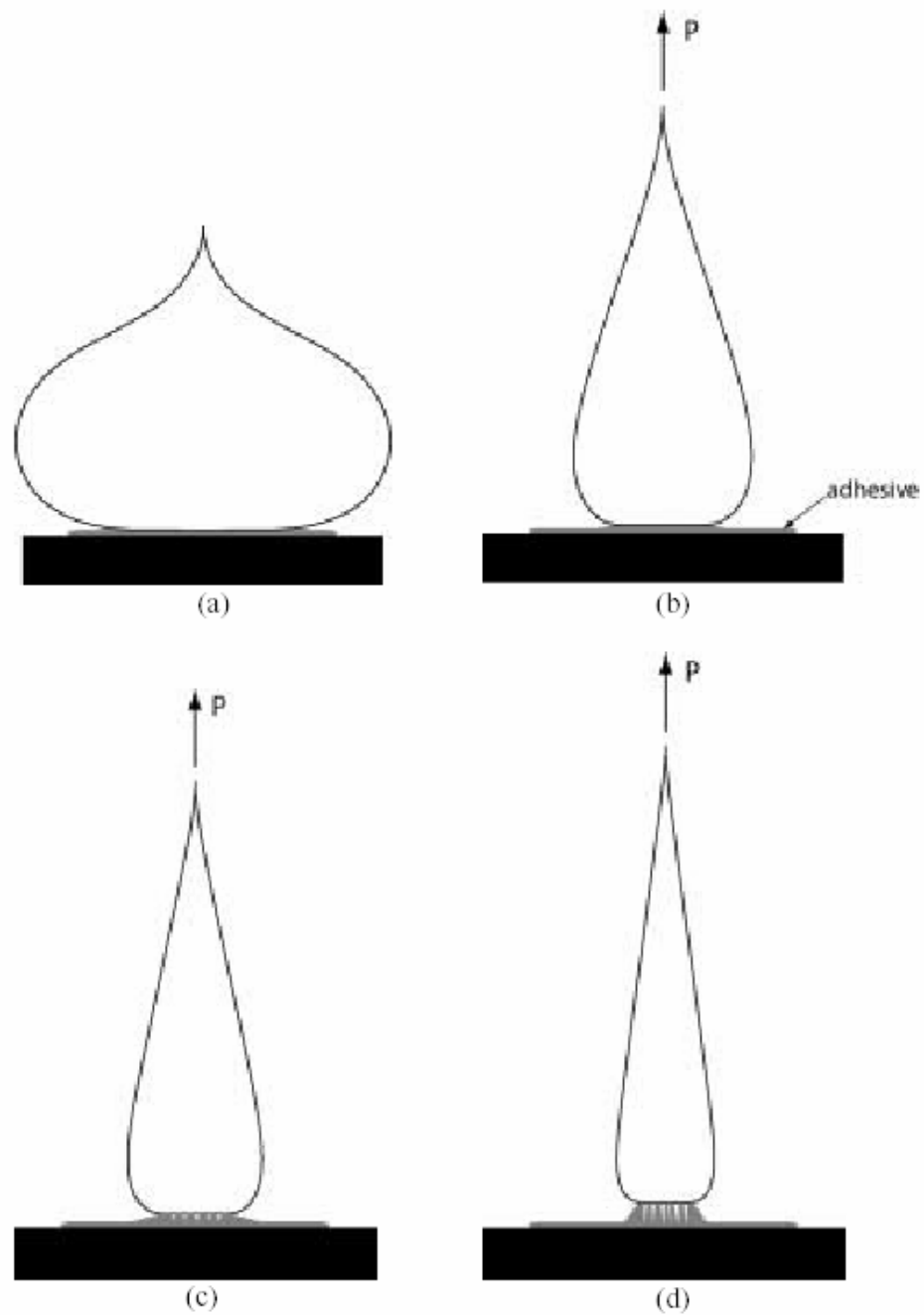


Figure 3.15: Diagram of the loop tack test[171].

There are a number of reported problems with gathering useful data from the loop tack test. Most problems are associated with the choice of material used to make the loop. For instance, with tapes the stiffness of the backing material plays a role in the amount of

pressure used in the compression zone and also in the contact area and peel angles.

Twisting of the loop material also leads to inconsistent contact between the adhesive and loop and ultimately to less reproducible results[166, 171].

3.5.1.3 Quick stick test

In this second modification of the peel test, primarily a test for tapes, the tape is applied to a stainless steel substrate by placing the tape on the surface without adding any additional pressure. The tape is then peeled at a 90° angle while measuring the force necessary for removal. As with the loop tack test, this test is highly dependent on the tape's backing material and the material's effect on the tape's ability to form intimate contact with the substrate.

3.5.1.4 Probe tack test

The final type of tack test to be discussed is the probe tack test. It is also the way tack is measured for the purpose of this study. Probe tack tests are mechanical adaptations of thumb tack tests[177]. In probe tests, the thumb is replaced with a metal probe that is attached to a force gauge. The first probe apparatus was developed by Wetzel but has since been made obsolete by the Polyken Probe Tack Test, which was developed by Hammond of Kendall[169]. The Polyken test significantly improved upon the previous design by increasing the probe size by a factor of 10, thus improving reproducibility. The Polyken technique allows a constant load to be applied to the adhesive-substrate interface and also eliminates the role of backing material as the adhesive is deposited on a metal plate of a specified mass. A diagram of the probe tack test is shown in Figure 3.16.

Similar to the loop tack test, the tack value is defined as the maximum value of the force measured during the debonding phase. Additionally, the area under the force curve is

related to the work of adhesion since the displacement is accomplished at a constant rate[49].

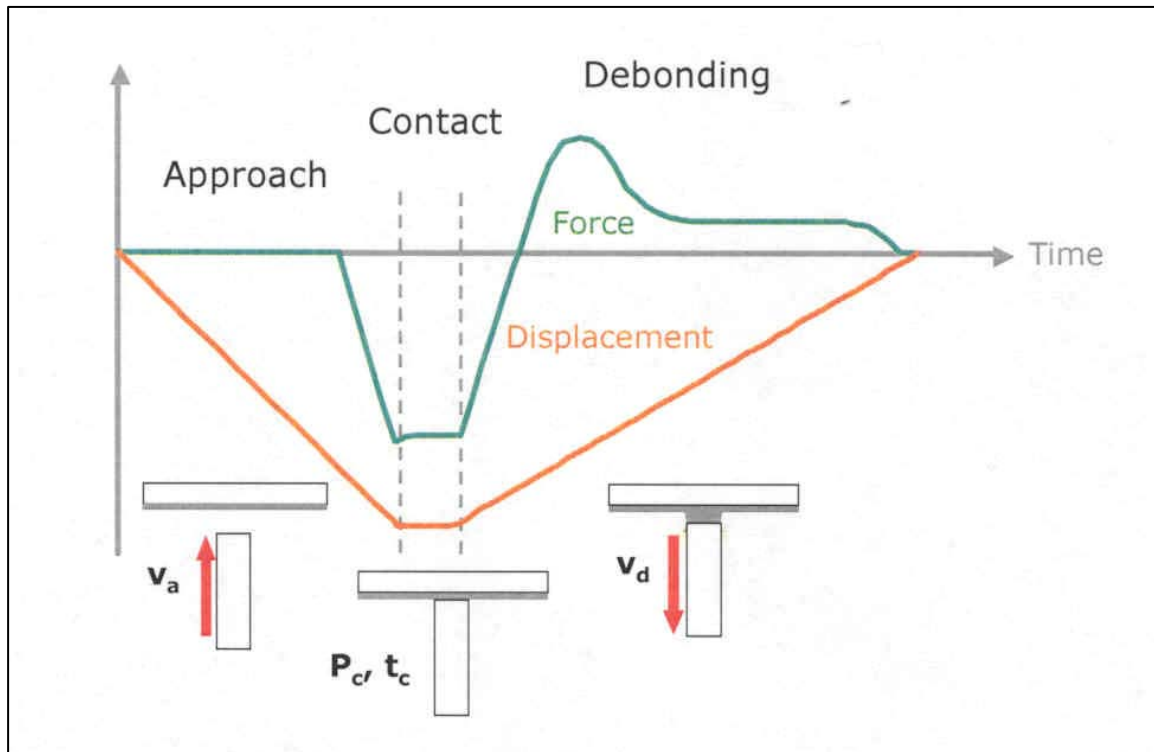


Figure 3.16. Schematic of a probe tack test[178].

As a side note, a drawback to the probe tack test is a misaligned sample can lead to reduced and nonspecific contact area. This can be combated by using a spherical probe at the expense of having a lower overall (but constant) contact area, when compared to a flat probe.

Figure 3.17 shows the steps of progression that lead to debonding of a PSA during a probe tack test. This description presents a good explanation of the debonding process

and will be discussed in later sections detailing how a number of factors affect the levels of tack that are measured for various adhesive systems.

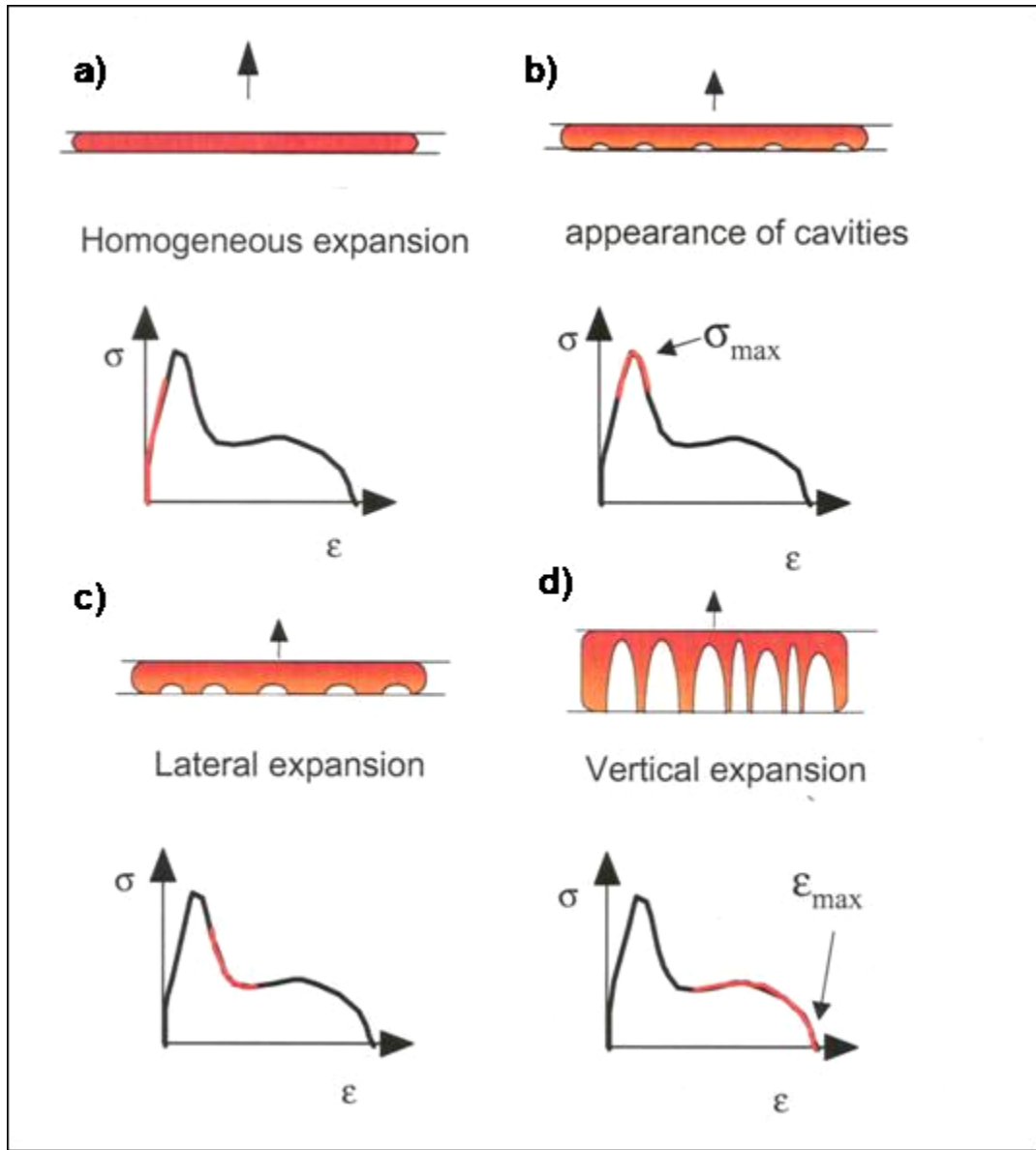


Figure 3.17: Schematic of the deformation mechanisms for a conventional PSA during a probe tack test[178].

The schematic presented in Figure 3.17 is an adaptation of the results from debonding studies that used video capture techniques to determine the progression of debonding during a probe tack test of an adhesive operating in its intended environment[156, 158, 178-181]. Actual pictures from which the schematic are based are shown in Figure 3.18.

The life of an adhesive bond begins with the initial bond formation between the adhesive and the substrate and then continues as shown in Figure 3.17. Beginning with:

- a) The homogenous expansion of the adhesive during which the polymer and probe surface are still in intimate contact.
- b) Cavities begin to appear at the interface between the adhesive and the adherend. The maximum force occurs during this phase of debonding and it is therefore very important to values of measured tack.
- c) The expansion of the cavities, both horizontally and vertically, occurs in this phase. After the formation of the cavities, the adhesive looks like a foam when viewed from below.
- d) During the vertical expansion of the adhesive a significant amount of energy is dissipated as fibrils develop in the adhesive. The cavities continue to expand vertically and horizontally and when they meet, debonding occurs.

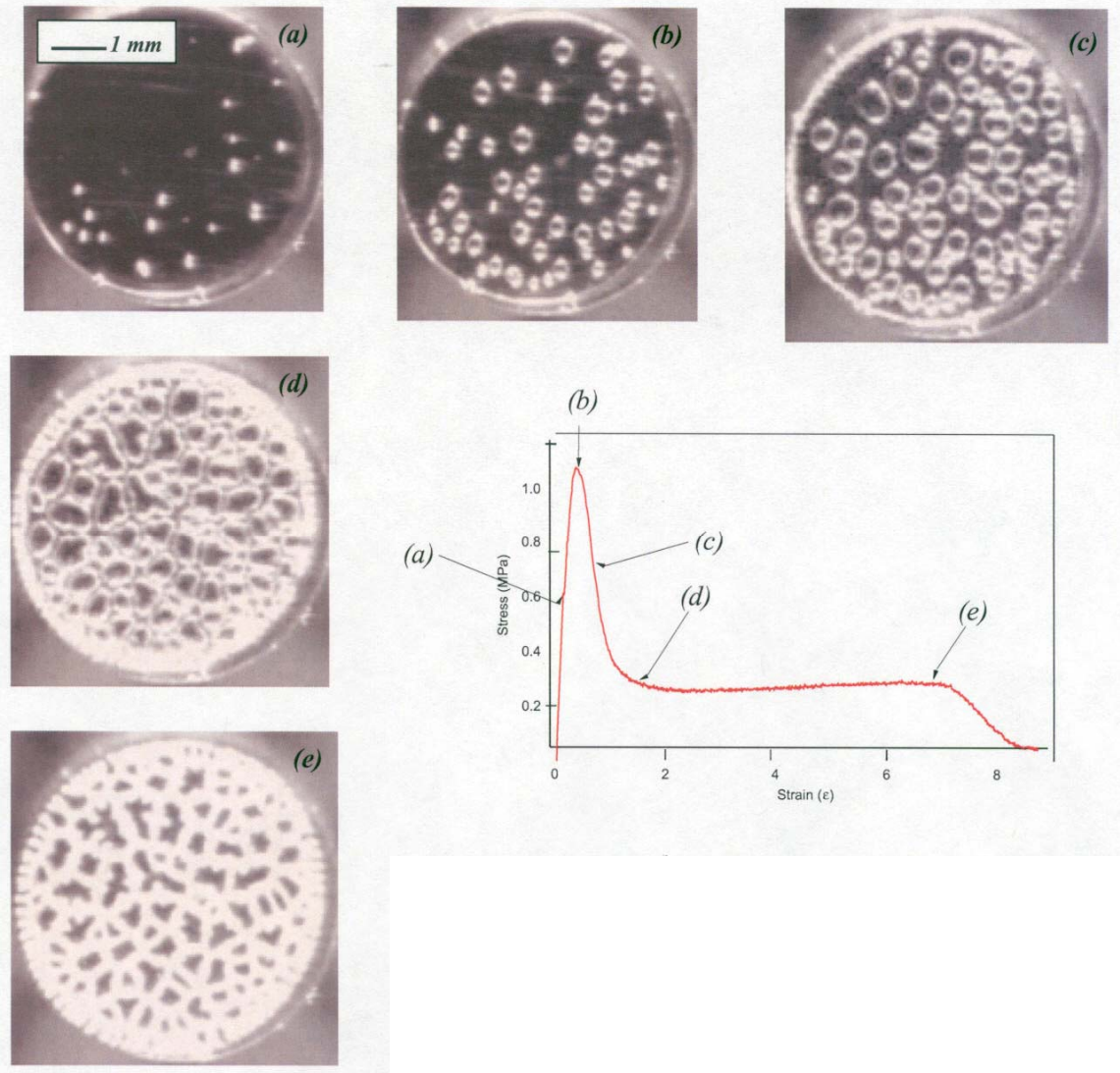


Figure 3.18: Stress-strain curve with optical microscope pictures showing the different stages of the debonding process for an acrylic adhesive[178].

This description of debonding will serve as a foundation for a discussion of how various factors affect tack and how the factors interrupt or accelerate the debonding process.

3.5.2 Factors influencing tack

The measured values of tack depend significantly on a number of experimental parameters that must be considered when designing experiments. The role of temperature, debonding rate (or debonding velocity), contact time, contact pressure and surface roughness are all related to changes in the ability of the adhesive to form a bond with the test probe, which is due to the viscoelastic nature of the PSA material.

3.5.2.1 Temperature

By changing the temperature, the relaxation time (time needed for the adhesive to contact the probe) of the polymer is altered, which changes the adhesive's ability to form a bond with the probe. As shown in Figure 3.19 there is a maximum value for the adhesive bond energy, which occurs above the T_g of the adhesive and before the temperature gets too high causing cohesive failure to reduce the adhesion[49, 171, 182]. The temperature dependence of tack is attributed to changes in the rheology of the polymer and the maximum tack is usually near $T_g + 50\text{ }^{\circ}\text{C}$ [49].

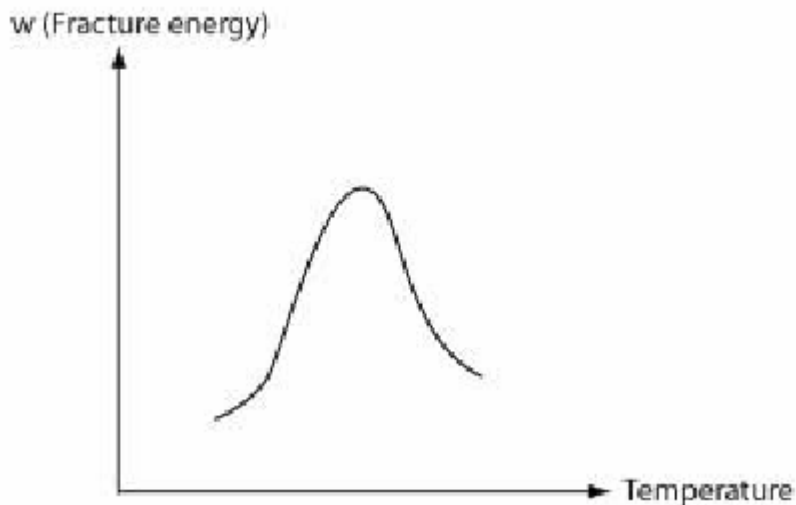


Figure 3.19: Adhesive fracture energy as a function of temperature for a generic adhesive[182].

3.5.2.2 Debonding rate

Similar to temperature, the rate that the probe is debonded from the adhesive alters the rheology of the polymer, which changes the amount of energy the adhesive bond can withstand[49, 183]. As the shear increases, the adhesive is more likely to experience cohesive failure rather than interfacial failure due to the polymer being more fluid-like. The transition from cohesive failure (filled circles) to adhesive failure (open circles) is evident in Figure 3.20.

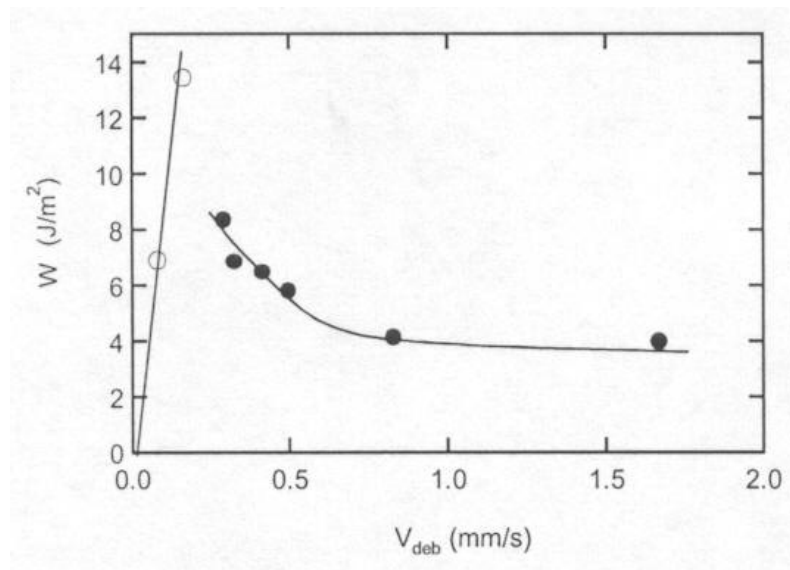


Figure 3.20: Adhesion energy as a function of debonding rate[184].

3.5.2.3 Contact time and contact pressure

Due to the viscoelastic nature of polymers used in PSAs, the effects of contact time and contact pressure will be discussed in the same context since both have been reported to have the same overall effect on adhesion and tack – higher pressures equate to longer contact times if the time scale is greater than the relaxation time of the adhesive[185]. The effect of increasing the contact time (or contact pressure) is to increase the adhesive

energy, as can be seen in the top portion of Figure 3.21. The increase in adhesive energy is due to both a higher peak tack value and a larger amount of dissipation during the vertical expansion fibrillation phase of debonding[49, 183]. This phenomenon is attributed to an increase in the total bonded area that occurs with longer contact times and therefore is more important in systems with higher levels of surface roughness[186].

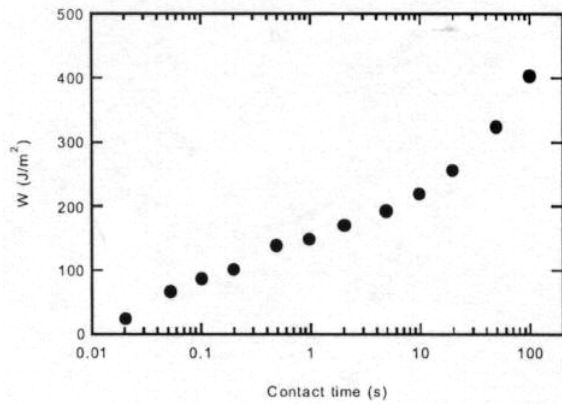


Figure 3.21: Role of contact time in adhesive bond energy[183].

3.5.2.4 Roughness

The detrimental effect of surface roughness on the ability of PSAs to bond is contrary to the effect of surface roughness in typical adhesives where surface roughening is a common surface preparation. Surface roughness has several implications in the bonding of a PSA. First, the asperities present lead to reduced total contact area[161, 187-189]. Second, the asperities serve as nucleation points for the cavities that appear during the debonding process[156]. Figure 3.22 shows a depiction of the effects of surface roughness that illustrate the first point above and also confirms the strong relationship among contact time, contact pressure and surface roughness.

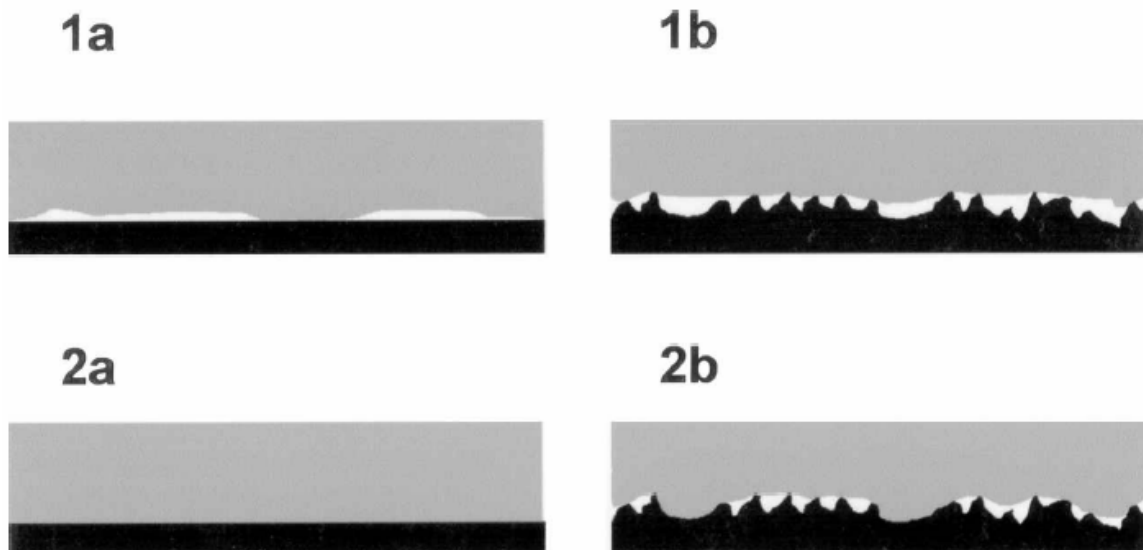


Figure 3.22: Depiction of the effect of contact pressure on rough and smooth surfaces. 1a shows light pressure on a smooth surface. 1b is light pressure on a rough surface. 2a is high pressure on a smooth surface. 2b is high pressure on a rough surface[188].

The surface roughness studies were all performed by varying the roughness of the probe used to measure the tack of the system. Work has also been done by varying the roughness of the polymer film in the form of tape applications. In these cases, the smooth film was made by placing the PSA on smooth film backing and the rough film was deposited on a cloth backing. The smooth film was found to have much larger tack values than the rough film but the role of the different backing materials was not fully investigated[172]. It has also been noted that by adjusting the texture of the polymer surface, the adhesive properties can be tailored to better suit particular applications[190].

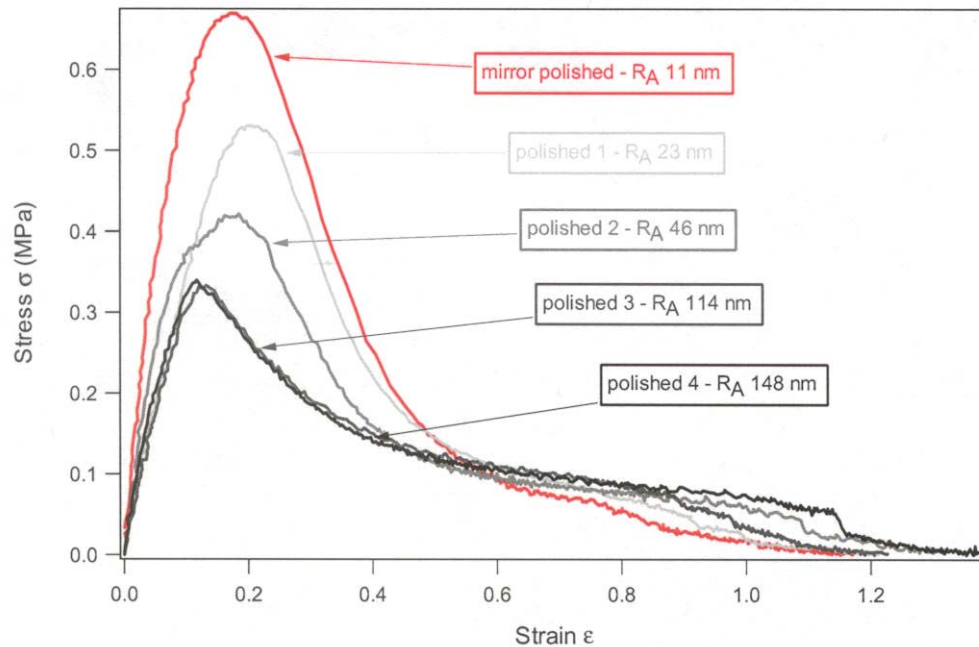


Figure 3.23: Stress-strain curves for the bonding of a PSA to a steel probe with various levels of roughness[157].

3.5.3 Tack summary

The evolution of the study of tack and PSAs has been outlined by providing some historical perspective of the different types of tack measurement and by discussing the benefits of the different types of tack tests. Recent developments have introduced the Polyken probe tack test and the loop tack test, which are now considered the standard tests used to evaluate the tack of PSA materials under variable conditions such as temperature and humidity conditions required for each specific application. While the probe tack tests are well-suited for PSAs used in applications other than tape applications, the loop tack test is best suited for tape applications. Studies have shown that increasing time or pressure of the probe contact with the adhesive will increase the measured tack. Increases in temperature will increase the tack measurement to a maximum before the

measured tack decreases due to enhanced softening of the adhesive. Increases in debonding rate will lower the measured tack, as will increases in surface roughness.

Recent advances in the study of PSAs and tack has greatly improved the understanding of the bonding process. Until recent work brought insight into the mechanisms responsible for tack bonding, the design of PSAs was largely accomplished by trial and error. While work is still necessary to standardize the measurement techniques used for characterizing tack and determining which physical traits relate directly to improved performance in adhesive applications, a good start has been made. Further understanding of the relationships within an adherend-adhesive system will allow PSAs to be used in many more applications than are now considered.

3.6 Experimental and Results

The polyacrylate adhesive was applied to surfaces as a water-based emulsion, which dried to leave a polymer film. The drying was done at both room temperature and at elevated temperatures. The film was applied to coupons of various metals using wire-wrapped coating rods, which produces a uniform film of the emulsion prior to drying and led to a uniform coating of constant thickness. Prior to coating, the metal coupons were cleaned with a variety of organic solvents (acetone, methanol, ethanol and isopropanol) to remove any oils that could have contaminated the surface. Additionally, the roughness of the coupons was measured with profilometry and AFM to confirm that the initial surface topology was the same for both types of bare metal surfaces.

Following application of the emulsion to the metal surfaces, the film was dried in an oven at temperatures ranging from 25 to 130 °C. After drying the film, a number of surface characterization techniques were used to quantify the differences between the two films. The two metals used in this experiment were 1008 carbon steel and 304L stainless steel. The surfaces referred to in the discussion are that of the polymer film on the metal substrates.

The application of the polyacrylate adhesive with the wire-wrapped coating rod (also known as a Mayer Rod) will provide a smooth surface of even thickness where the thickness varies with the solids content and viscosity of the coating and also with the gauge of the wire used for coating[191]. The numbering convention for the rods is that the larger the rod number, the larger the diameter wire used to wrap the rod. To check the compatibility of the system to the coating rods, the film thickness was measured for films produced with a variety of rod numbers. The film thickness was measured using a magnetic thickness probe (CGX Gauge by Oxford Instruments, Elk Grove Village, IL). A linear relationship was expected between film thickness and coating weight and as Figure 3.24 shows, this was observed.

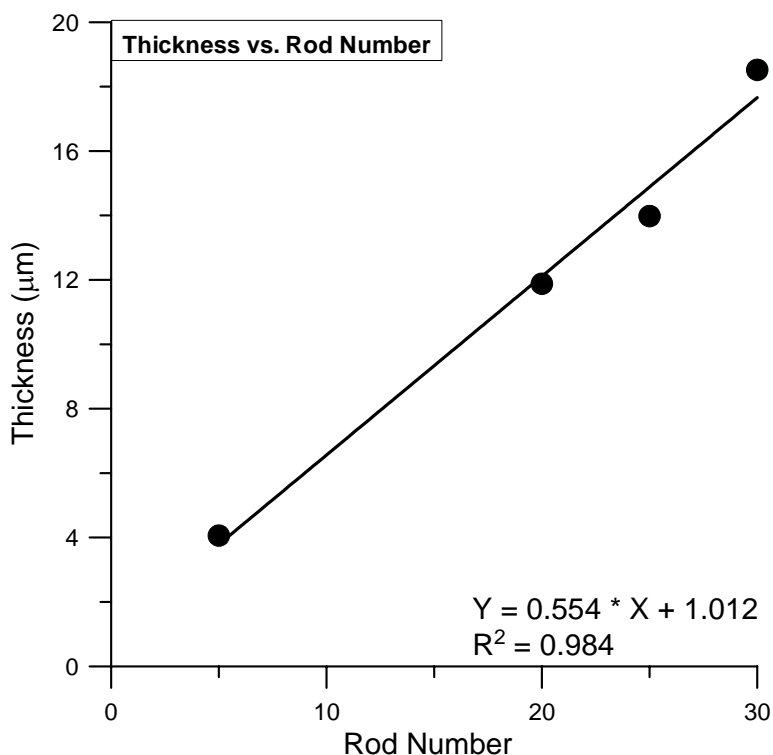


Figure 3.24: Film thickness vs. coating rod number to test compatibility of system with coating rods.

3.6.1 Tack and surface energy studies

The most noticeable and perhaps the most important difference between film on the carbon steel and stainless steel surfaces is the tack of the surface. Qualitatively, the film on the carbon steel surface felt like a piece of hard plastic when touched, as compared to the film on the stainless surface, which was very tacky – as one would expect from a pressure sensitive adhesive. Figure 3.25-Figure 3.27 shows the results of a Polyken probe tack measurement on the films. The measurements were made on the dry film (as opposed to a film heated in water prior to the test) at room temperature with a stainless steel probe. The data confirm the considerable differences in the qualitative examination

of the films. The values for the film on carbon steel at several temperatures are negligible and therefore cannot be seen on the graph.

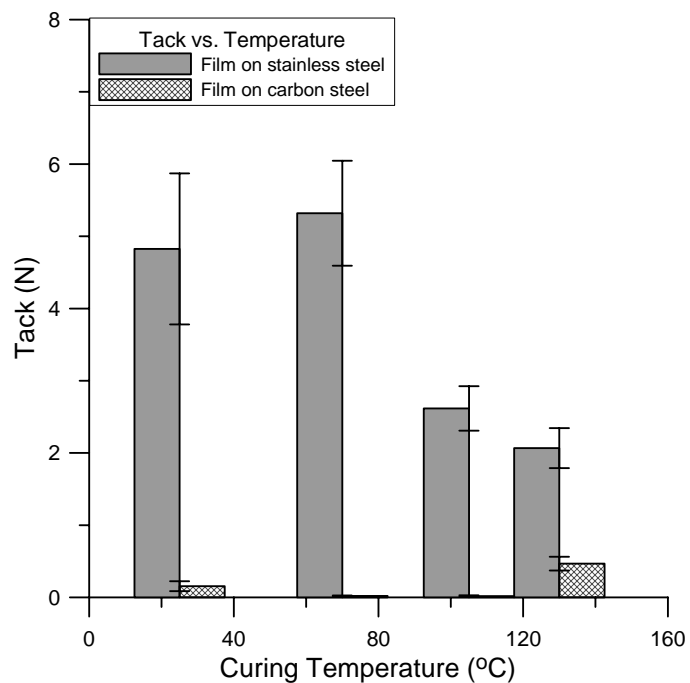


Figure 3.25: Tack measurements of dry film taken at room temperature of polyacrylate films on stainless steel and carbon steel substrates. The temperature axis refers to the temperature of the oven used to dry the film. Film thickness = 25 μm .

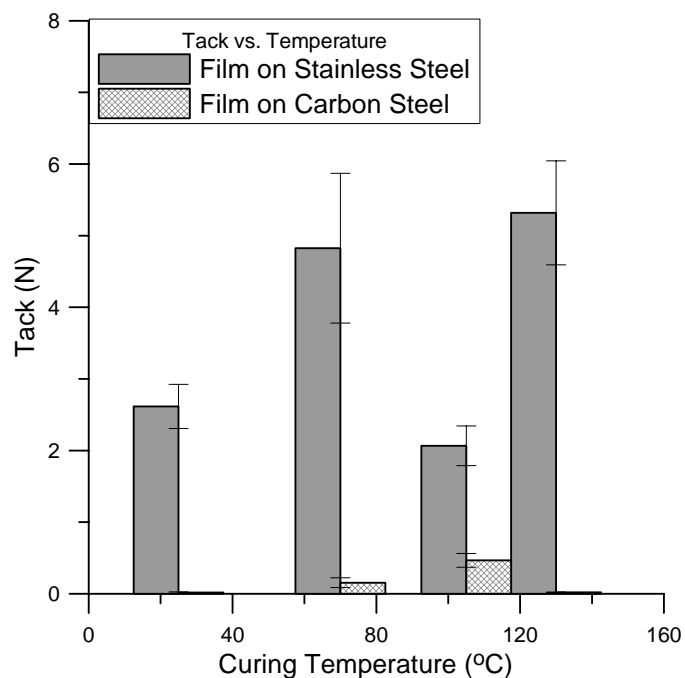


Figure 3.26: Tack vs. Curing Temperature for Carbotac on stainless steel and carbon steel. Film thickness = 17 μm .

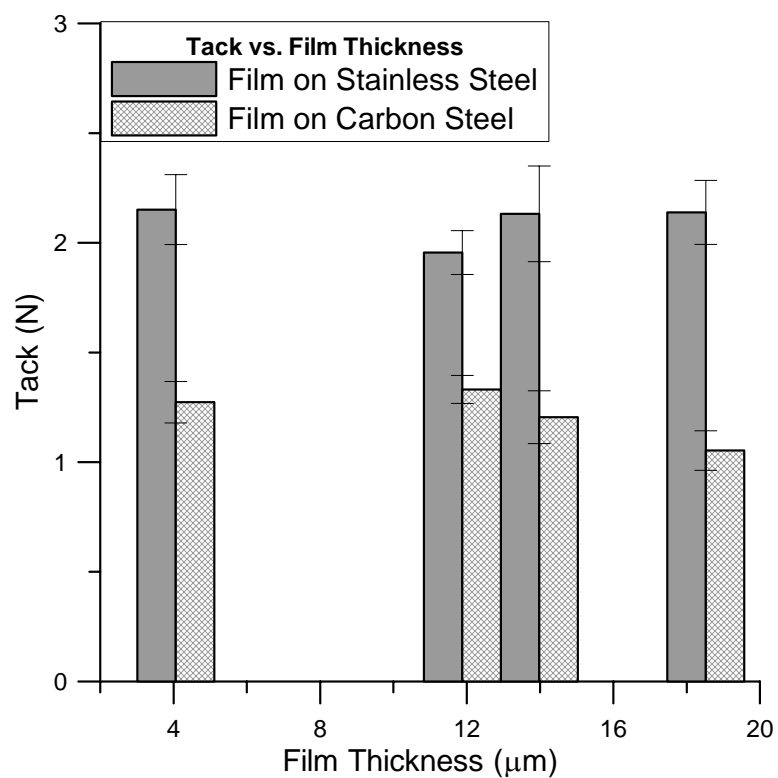


Figure 3.27: Tack vs. Film Thickness for films cured at 105 °C.

Liquid drop contact angles were used next to substantiate the difference between the two films. Reproducibility of the water drop contact angles was determined by preparing five films with thickness near 32 μm and cured at 105 $^{\circ}\text{C}$. The results indicate that the error in water drop contact angle measurements is 2.5%. Figure 3.28 shows the water drop contact angles measured on films of a variety of thicknesses all cured at 105 $^{\circ}\text{C}$.

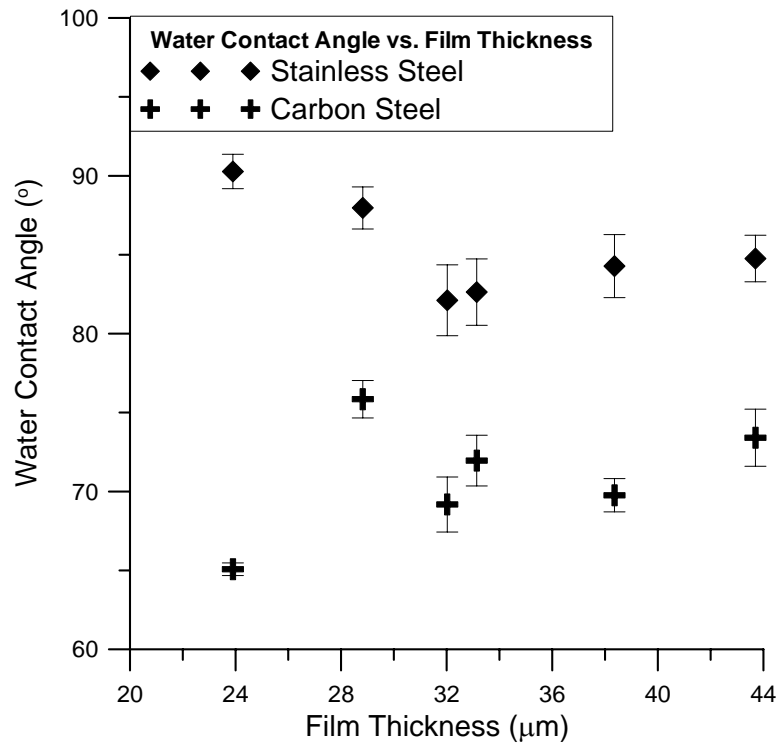


Figure 3.28: Water Drop Contact Angle vs. Film Thickness for films cured at 105 $^{\circ}\text{C}$.

The surface energy of the films was found using the technique developed by Fowkes[93], which uses two different liquids (polar and non-polar) to calculate the polar and non-polar components of the surface energy; water (polar) and methyl iodide (non-polar) were

the liquids used in the study. The results in Figure 3.29 and Figure 3.30 show that the overall surface energies of the two surfaces vary significantly and that the difference has a negligible dependence on curing temperature. The surface energy of the film on carbon steel averages 41 mN/m over the temperature range while the film on stainless steel averages 34 mN/m.

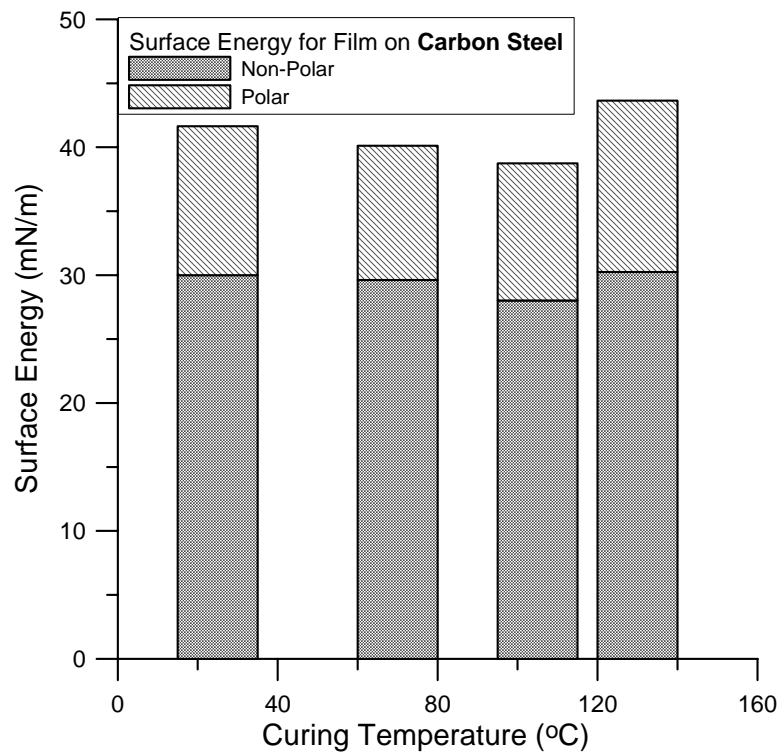


Figure 3.29: Surface energy components for a polyacrylate adhesive deposited on carbon steel at various curing temperatures.

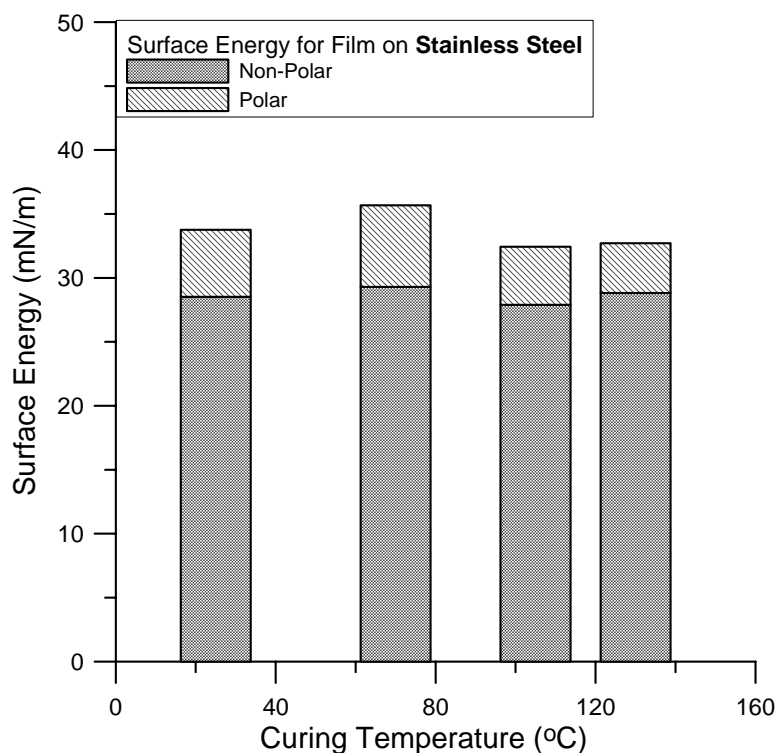


Figure 3.30: Surface energy components for a polyacrylate adhesive deposited on stainless steel at various curing temperatures.

The difference is associated with the polar component of the surface energy, as can be seen in the top portion of the surface energy bars in Figure 3.29 and Figure 3.30. The bottom portion of the bars (solid pattern) represents the non-polar component of surface energy, which is not dependent on the nature of the metal surface or on curing temperature and averages 29 mN/m. The polar component (striped bars) averages for the film on the carbon steel and stainless steel surfaces are 12 and 5 mN/m, respectively.

To study this effect further, films of varying thicknesses were placed on the metal substrates and cured at 105 °C. The film thickness was measured on the carbon steel surface using a magnetic film thickness probe.

Once again, the non-polar component of surface energy remained constant at 29 mN/m for films placed on both carbon steel (Figure 3.31) and stainless steel (Figure 3.32).

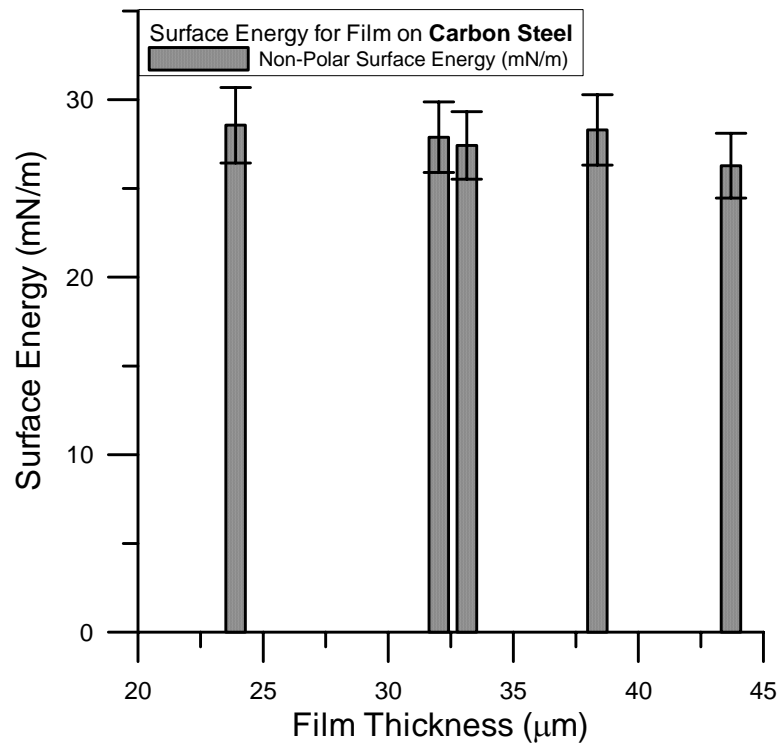


Figure 3.31: Non-Polar component of surface energy of a polyacrylate adhesive on carbon steel as a function of film thickness.

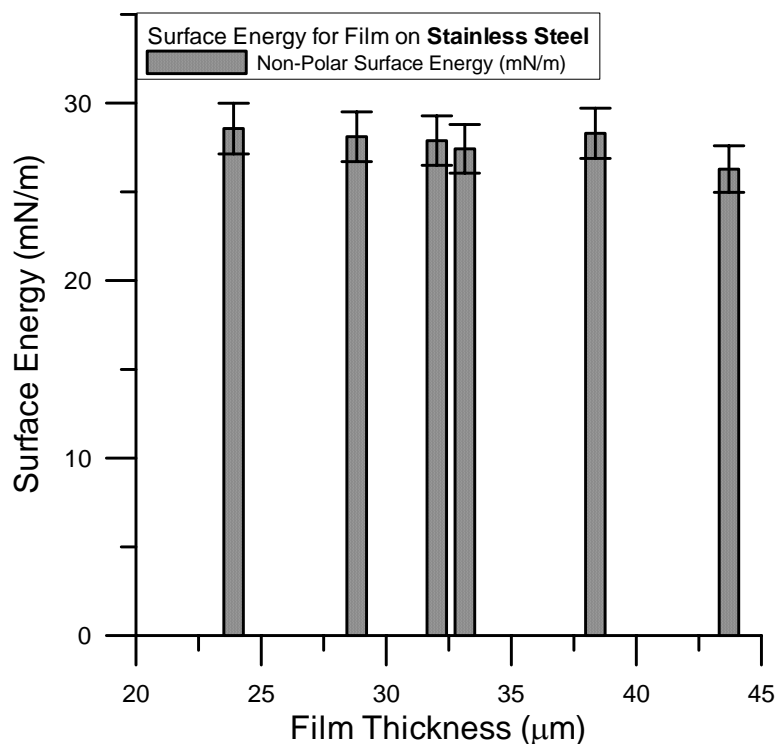


Figure 3.32: Non-Polar component of surface energy of a polyacrylate adhesive on stainless steel as a function of film thickness.

The polar component of surface energy again shows a significant difference when the polyacrylate film is placed on carbon steel as compared to stainless steel. For the film on carbon steel (Figure 3.33), the polar component of surface energy accounts for between 10 and 14 mN/m.

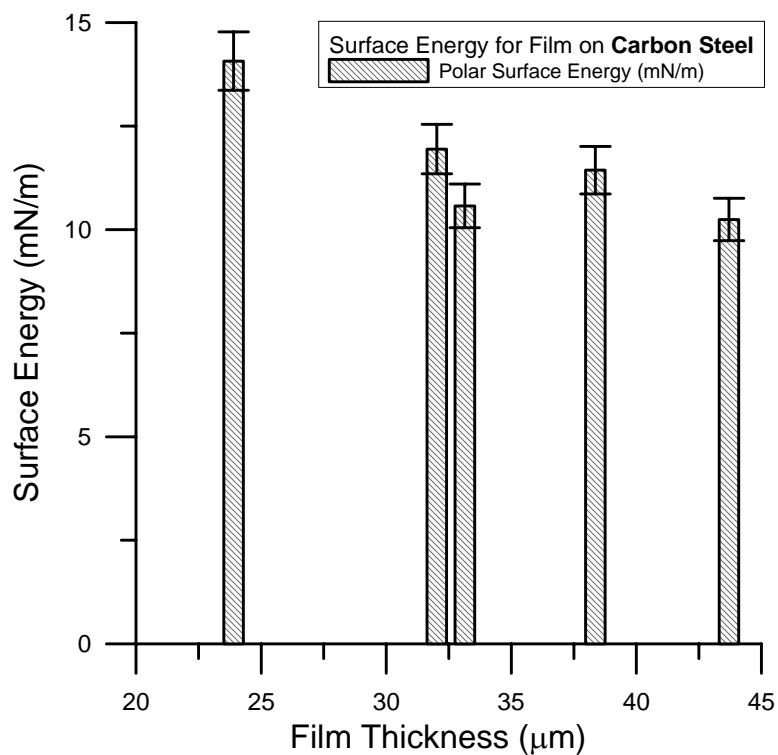


Figure 3.33: Polar component of surface energy of a polyacrylate adhesive on carbon steel as a function of film thickness.

The polar component data for the film on stainless steel is presented in Figure 3.34. Here, the magnitude is much smaller, approximately 5 mN/m. The reason for this difference will be discussed in a later chapter dealing with non-uniformities that develop in the film during drying.

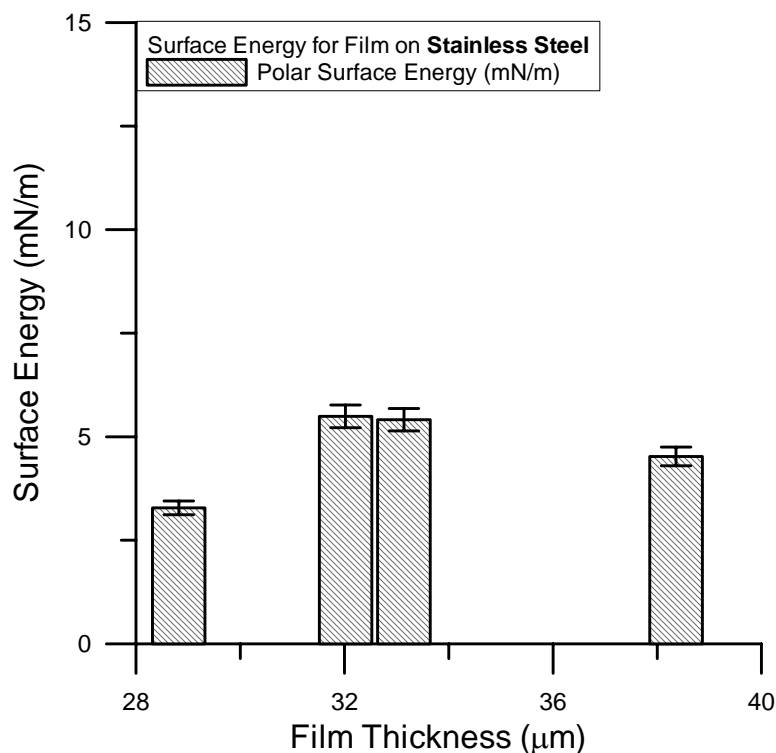


Figure 3.34: Polar component of surface energy of a polyacrylate adhesive on stainless steel as a function of film thickness.

3.6.2 X-ray Photoelectron Spectroscopy (XPS) data

XPS, or electron spectroscopy for chemical analysis (ESCA), can identify the chemical composition of surfaces. Using this technique, polyacrylate films dried on both stainless steel and carbon steel were analyzed. The samples were analyzed at GTRI by Dr. Brent Carter and the results of the analysis were inconclusive in that both films had the same C:O ratio of 3.2. High resolution data was not available for the carbon steel sample due to differential charging.

3.6.3 AFM studies

The next step was to determine the root cause of the unexpected difference in tack and liquid contact angle between the two surfaces. The samples were imaged with AFM, a

technique that allows high-resolution analysis of the surface topology and mechanical properties. Topology data are typically presented as root mean square (RMS) roughness, which is the standard deviation of the height data gathered over the scan. When comparing roughness data it is important to compare data from scan sizes that are equal, with the larger scans being more representative of the sample. Figure 3.35 shows the roughness results on both the carbon steel and stainless steel for a variety of scan image sizes. The roughness of the film on carbon steel is much greater than that of the film on stainless.

Roughness has been associated with reduced tack values in studies of pressure sensitive adhesives[49, 156-158, 161]. Higher roughness values will act to accelerate the debonding process by providing nucleation sites for cavity formation that eventually leads to adhesive bond failure.

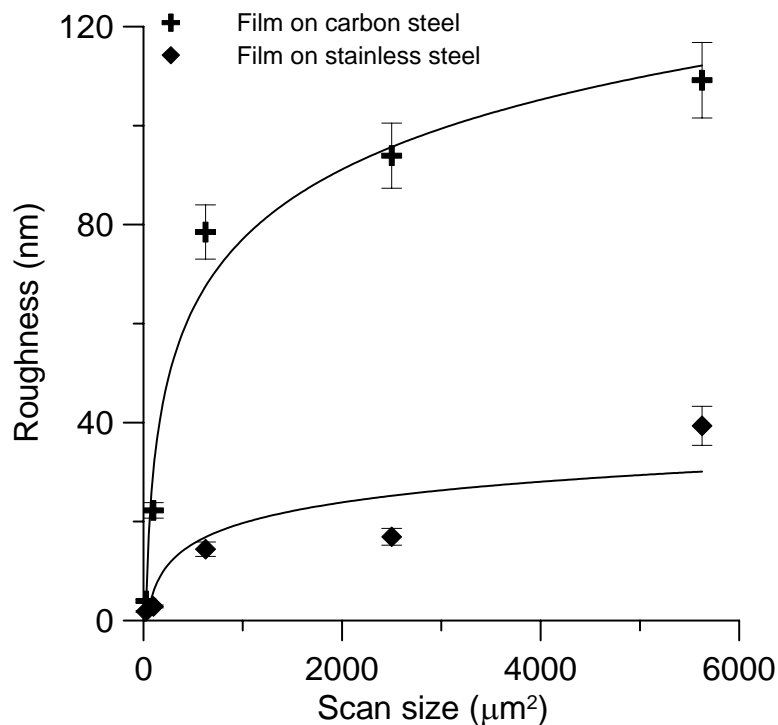


Figure 3.35: RMS roughness values for polyacrylate film on carbon steel and stainless steel at various scan sizes.

AFM uncovered other differences in the films besides roughness. In tapping mode AFM, the phase shift image indicates areas that dissipate energy differently. The darker areas of the phase shift image are regions of the surface that are more attractive to the imaging tip when imaging is accomplished in the attractive region of the force-distance curve.

The image in Figure 3.36 is a phase shift image of the tacky polymer surface on the stainless steel substrate. The scan produces a very uniform image typical of a tacky surface.

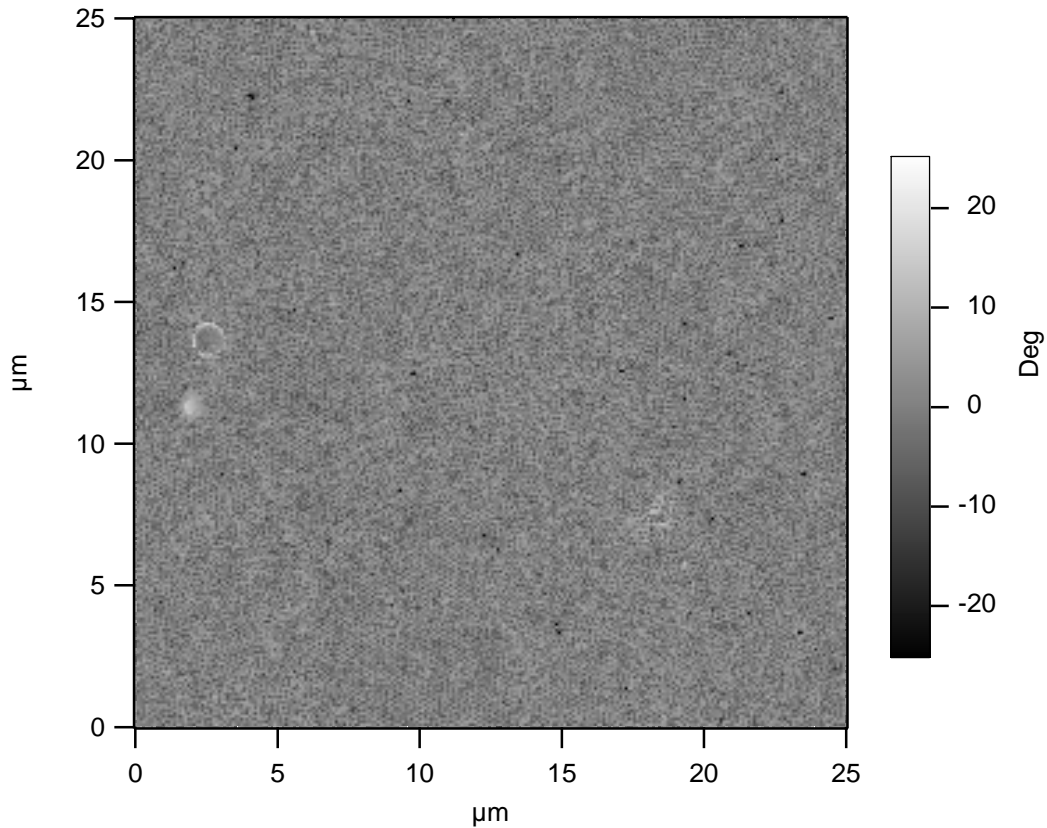


Figure 3.36: 25 μm phase shift scan of polyacrylate film on stainless steel. Very uniform attractiveness.

The data and images of the polyacrylate adhesive on the stainless steel surface are in stark contrast to those from the polyacrylate adhesive placed on the carbon steel surface.

Figure 3.37 shows a phase shift image for the surface that is not uniform in its distribution of the attractive material. The dark areas represent attractive regions of the surface that appear to have collected together, leaving large areas of less attractive material.

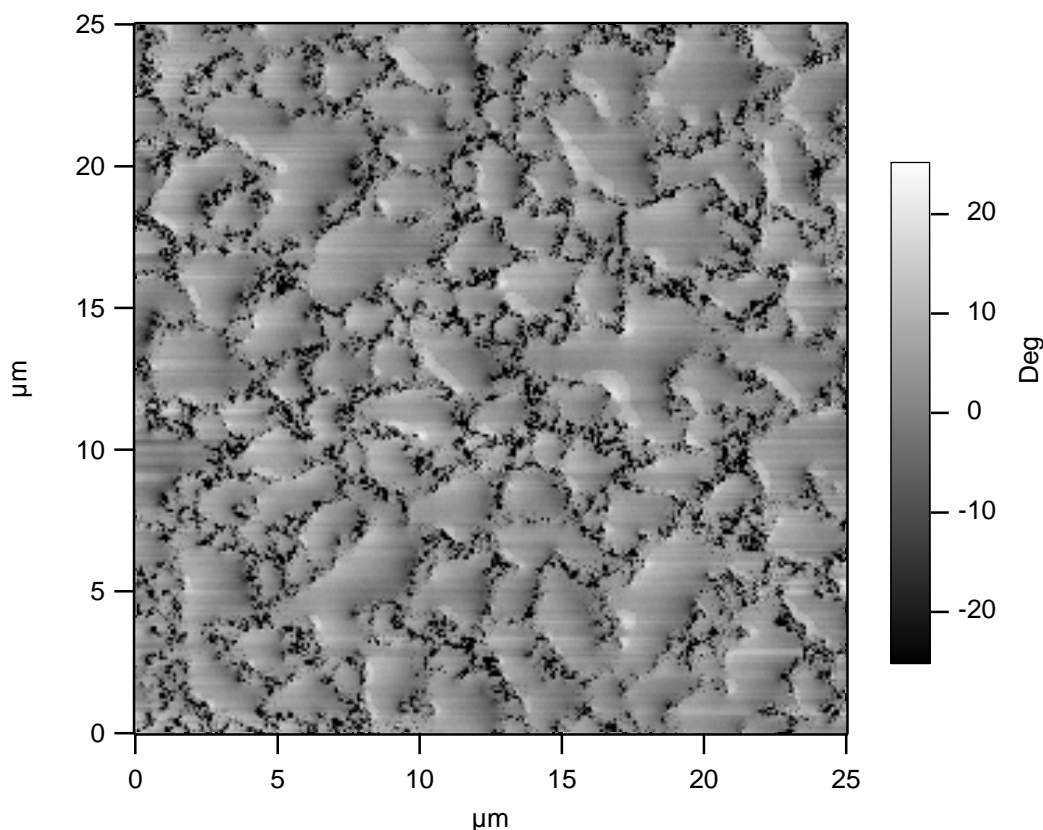


Figure 3.37: 25 μm phase shift scan of polyacrylate film on carbon steel. Uneven distribution of attractive (dark) material.

The image in Figure 3.38 is a combination of the phase shift and topography images for the film on carbon steel. The topography is presented as the vertical axis in the image, showing high points of the surface as peaks and low portions of the surface as valleys. The color scale in Figure 3.38 is taken from the phase shift image shown in Figure 3.37 and the darker colors again represent softer, more attractive portions of the film.

The image presented in Figure 3.38 provides visual support for the non-tacky nature of the film. The attractive, sticky material is segregated in the valleys of the image, which makes it inaccessible to the tack probe as the probe is brought into contact with the film.

As the tack probe touches the surface, it only comes into contact with the lighter colored areas, which are less attractive and tacky.

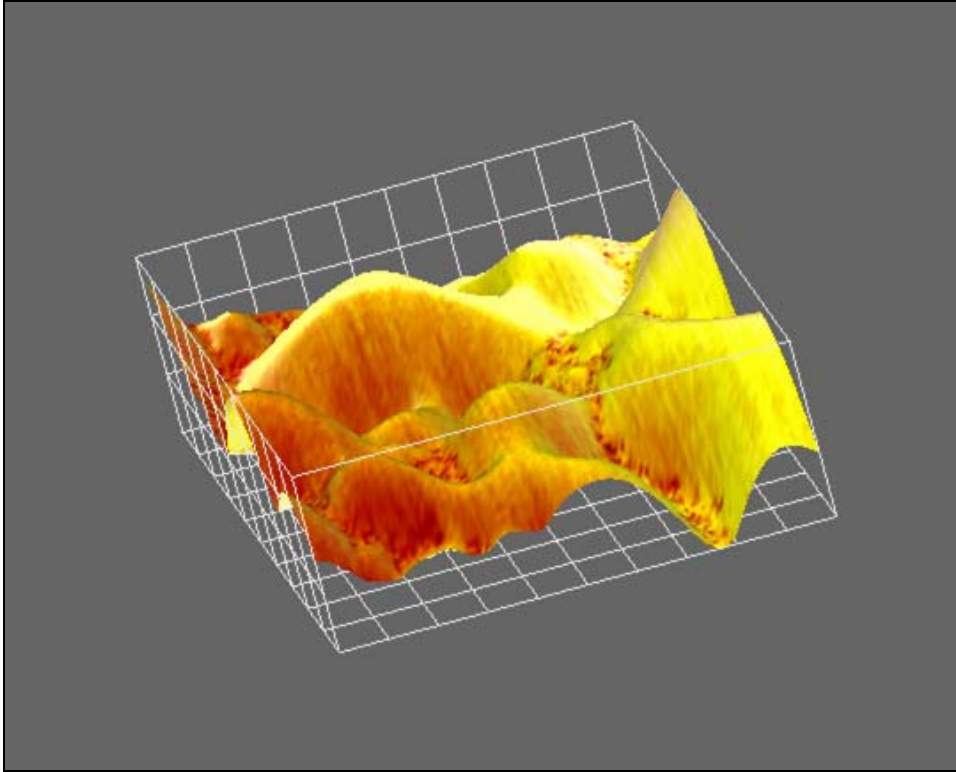


Figure 3.38: 3-D image of polyacrylate adhesive on carbon steel substrate. The surface contour is the height scan and the color scheme is the phase scan. The horizontal axes are 25 microns and the height ranges from -60 to 60 nm.

Contact mode AFM was used to further investigate and compare the nature of the attractive regions (dark colored areas in the images) and the less attractive regions (light colored areas in the images) present in the samples. The same cantilever-tip system was used on all the samples to avoid problems that could arise from using tips with different shapes.

The pull-off force (F_p) as measured by contact mode AFM is basically a tack measurement performed with the tip of the AFM cantilever, which typically has spatial dimensions near 10 nm. The F_p for the less attractive regions present on the high regions of the topography is 21 ± 7 nN. By comparison, the F_p for the attractive regions that are contained in the valleys of the topography is 68 ± 18 nN.

The honeycomb-like features visible on some of the images above and shown in Figure 3.39 and Figure 3.40 reflect the size of the emulsion particles used to carry the polyacrylate adhesive in the water solution.

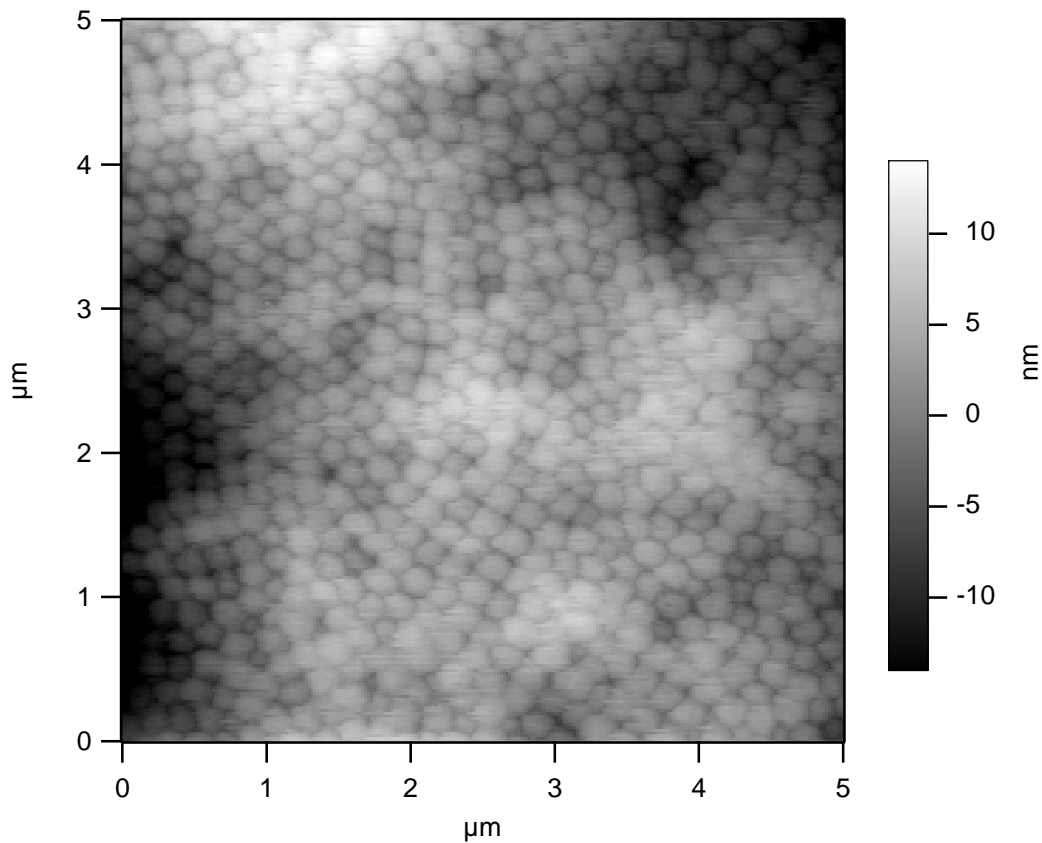


Figure 3.39: $25 \mu\text{m}^2$ AFM height image of a polyacrylate film on carbon steel.

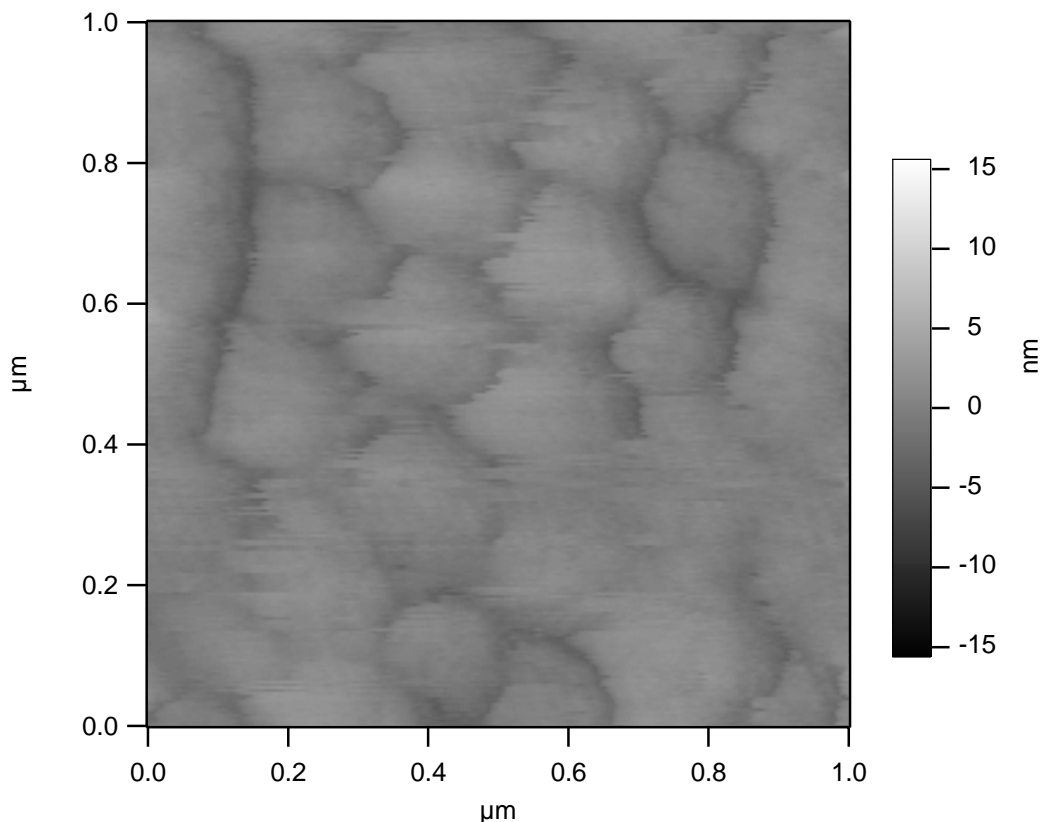


Figure 3.40: 1 μm^2 AFM height image of a polyacrylate film on carbon steel.

The size of these particles, as measured by AFM, after they have been dried onto a surface is 180 ± 40 nm. Dynamic Light Scattering (DLS) studies performed with an instrument from Brookhaven Instruments Corporation. The emulsion particle size, as measured by DLS is 262 ± 13 nm. The difference in size is attributed to the effects of drying on particle size—the particles are more swollen when they are wet.

3.6.4 Thermography studies

Infrared (IR) thermography was also used to distinguish the films as they dried. The technique can discern the relative roughness of the final film by studying the coefficient

of variation (COV) of the film's temperature profile as it dries[192]. The COV is defined as the standard deviation of the temperature divided by the average temperature. A peak occurs in the COV vs. time plot when the liquid film breaks and ceases to be a film. The technique used to find this data is discussed more explicitly in a publication[192] and in a thesis[193].

The results in Figure 3.41 for COV vs. time for the drying of a polyacrylate adhesive on both carbon steel (rough film) and stainless steel (smooth film) at 117 °C show a pronounced peak for the rough film and a less distinguishable peak for the smooth film. The height of the peak points to the film on the carbon steel being rougher during drying.

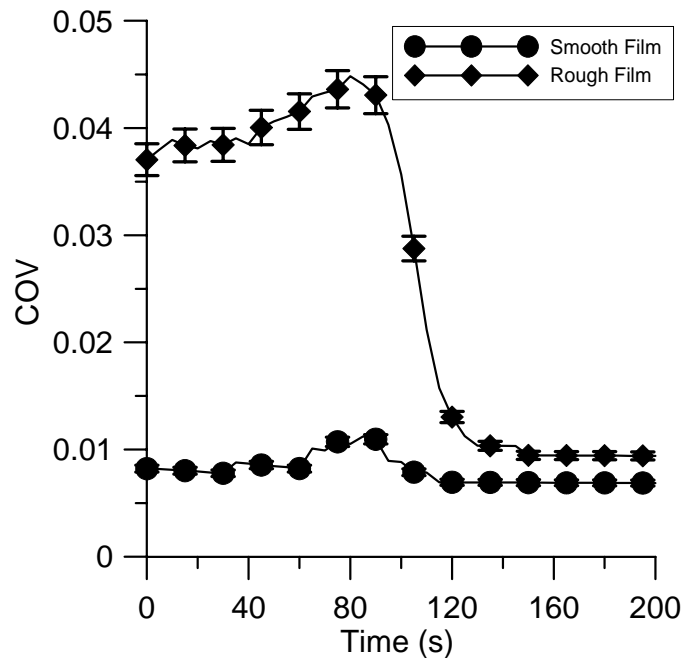


Figure 3.41: COV vs. Time for the drying of a polyacrylate adhesive at 117 °C. The smooth film is on stainless steel and the rough film is on carbon steel.

The data shown in Figure 3.42 are for the drying of the films at a lower temperature of 100 °C. Here, the COV values are much smaller and the smaller difference between the two profiles reflects a smaller difference in roughness values. The peaks occurring at a longer time (~100 s vs. 80 s) points to slower drying, this is expected at lower temperatures.

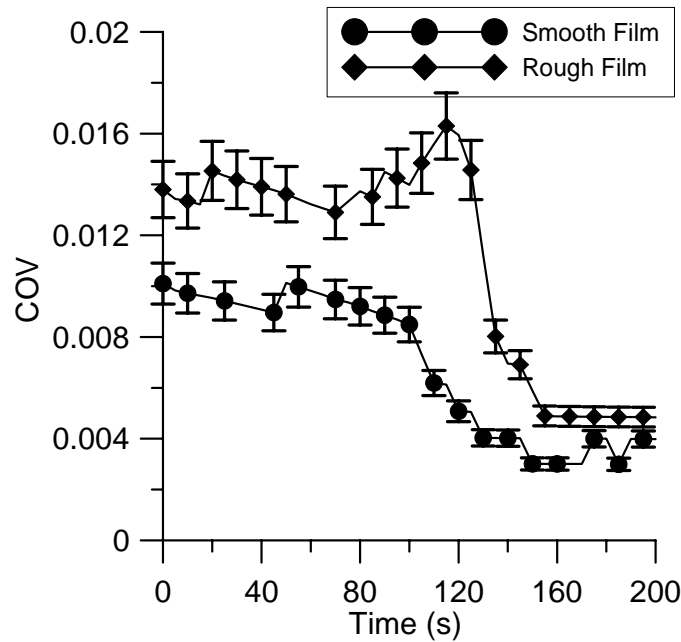


Figure 3.42: COV vs. Time for the drying of a polyacrylate adhesive at 100 °C. The smooth film is on stainless steel and the rough film is on carbon steel.

3.7 Conclusions

The work described here presents the unexpected result of obtaining different surface properties, including tack, by changing only the substrate on which an adhesive is deposited. Tack measurements and surface energy techniques were able to quantify

differences in the film surfaces. AFM analysis proved to be effective in determining the topography of the surfaces and the distribution of soft material on the film. This distribution combined with the topography leads to a visualization of the reasons behind the reduction in tack for the surface. Additionally, an IR technique is presented that further describes the drying of the polymer films and indicates that there are differences in the way adhesives dry.

It was determined that the reduced tack for the film on carbon steel is due to both higher roughness values, which is confirmed in the literature and also due to a less uniform distribution of soft, attractive materials on the surface. The result involving the distribution of the soft, attractive material has not been reported in the adhesives industry literature. The adhesives industry literature shows limited reference to AFM as an analytical tool but more AFM work will likely appear in the future.

This work has focused on finding the properties of the adhesive film placed on carbon steel that result in a much lower tack value. The areas of interest are those of the finished film, which do not give indications as to why the films become different. The IR study mentioned in this chapter provides a starting point to determine the root causes of the differences between the two films. The next chapter will focus on explaining what causes the films to develop differently.

CHAPTER 4 – SUBSTRATE DEPENDENCE OF POLYMER FILM TOPOLOGY

As discussed in Chapter 2, the performance of an adhesive was drastically altered by the substrate on which the film is deposited. It has been determined in Chapter 2 that the topology (both roughness and homogeneity) of the polymer film determines the ability of the adhesive to perform as it is designed. The goal of this chapter is to determine the mechanism responsible for the differences in topology.

Surface driven flow will be introduced and its role in the process will be determined through experimental techniques and analytical models. To support the hypothesis of surface driven flow, a number of background areas will be discussed. The composition of metals and the effects of composition on heat transfer will be presented as well as a background of IR thermography and its relation to measuring metal and polymer films during heating.

Finite element (FE) analysis will be used to confirm the IR data gathered during the heating of metal coupons and the drying of the polymer films. Finally, experimental results will be shown that help to confirm surface driven flow as the mechanism responsible for the differences recognized between adhesive films deposited on different metal surfaces.

4.1 Non-uniformity in metals

The mechanical, chemical, electrical, and thermal properties of metals are largely dependent not only on the primary metal components but also on the alloying constituents and contaminants present in the metals. In many applications it is sufficient only to consider the overall properties of the composite material, but in some cases the individual contributions of specific components are important[194]. This review will focus on the heat transfer characteristics of carbon steel and stainless steel and will consider the uniformity of the measured values. Studies that have incorporated techniques to calculate overall properties based on component contributions will be dissected to elucidate the roles of various chemical compositions and corrosion products on the ability of metals to transfer heat.

4.1.1 Composition of carbon steel

Carbon is added to steel to increase the hardness of the steel because the carbon content affects the material structure. This also decreases the malleability of the material. Carbon steels are commonly classified by the carbon content as low ($<0.2\%$), medium or high ($>0.5\%$) carbon steel but the terminology “ultrahigh-” and “ultralow-” carbon steel is also used. Although many other alloying elements, including manganese, chromium, nickel, molybdenum, copper, nitrogen, vanadium, niobium, titanium and zirconium are present in carbon steel, it is classified by the carbon levels[195-200].

Carbon is rarely present as elemental carbon. Typically, the carbon is associated with iron and forms various ferritic microstructures based on a number of variables such as cooling rate, deformation during cooling and the presence of other alloying elements[201, 202]. Cementite (Fe_3C) is the most common form of carbon in carbon steels and irons and the ferrite-cementite aggregates are known as bainite[198].

Another feature that is important when considering the make-up of carbon steel is the iron-oxides that are present on the steel surface as a result of corrosion. There are nine different iron oxides that have been identified in rust shown in Table 4.1[203-205].

Table 4.1: List of Iron Oxides[205]

Oxide name	Formula
Ferrihydrite	$5\text{Fe}_2\text{O}_3 \cdot 9\text{H}_2\text{O}$
Goethite	$\alpha\text{-FeOOH}$
Akaganeite	$\beta\text{-FeOOH}$
Lepidocrocite	$\gamma\text{-FeOOH}$
Feroxyhite	$\delta\text{-FeOOH}$
Wustite	FeO
Hematite	$\alpha\text{-Fe}_2\text{O}_3$
Maghemite	$\gamma\text{-Fe}_2\text{O}_4$
Magnetite	Fe_3O_4

The corrosive conditions play a major role in determining which of the oxides will be present. For example, magnetite is only formed in high-temperature applications[206]. The thickness of these films can vary significantly and the oxides form layers of various compositions[207]. The literature contains reports of oxide film thicknesses of $30 \pm 7 \mu\text{m}$ [208] and $76 \pm 10 \mu\text{m}$ [209].

The chemical composition, as determined by Metal Samples Company (Munford, AL), of the 1008 carbon steel used in this study is listed in Table 4.2.

Table 4.2: Chemical composition of 1008 carbon steel.

Alloy	Amount %
Carbon	0.07
Iron	99.565
Manganese	0.34
Phosphorus	0.013
Sulphur	0.012

4.1.2 Composition of stainless steel

Stainless steels can be segmented in a variety of ways. Usually, they are classified based on their composition, which is commonly associated with the end uses of the materials.

The four main classifications are: austenitic, ferritic, martensitic and austenitic-ferritic (also known as duplex). Each of these classes of stainless steel requires different welding techniques and result in different resistances to chemicals or temperatures.

The 304L stainless steel used in this study is an austenitic stainless steel and has the chemical composition given in Table 4.3, as provided by Metal Samples.

Table 4.3: Chemical composition of 304L stainless steel.

Alloy	Amount %
Carbon	0.014
Chromium	18.14
Copper	0.142
Iron	71.541
Manganese	1.36
Nickel	8.33
Phosphorus	0.033
Silicon	0.43
Sulphur	0.003
Nitrogen	481 PPM
Titanium	0.0065

The overall thermal conductivity of stainless steel is lower than carbon steels or cast irons. 304L has a thermal conductivity of 15 W/(m-°C)[210], compared to 35 W/(m-°C) for low carbon steel[211]. 304L stainless steel is a spatially homogeneous material since the levels of alloys present that lead to lattice strains are low[212] and also because of manufacturing techniques that take advantage of the softness of the metal[213]. The inclusions found in stainless steels have been found to be on order of 1 μm in scanning electron microscopy (SEM) studies[214].

4.1.3 Localized heat transfer

Because of the non-uniformities present in carbon steel, there are instances, such as in predicting the microstructure evolution, when the spatial uniformity of the heat transfer should be considered[215]. The inhomogeneities arise because of the large differences in thermal conductivity among the components that form carbon steel. A table of thermal

conductivity for many of the structures and oxides that form in carbon steel are presented in Table 4.4 and are gathered from various literature[194, 216-220].

Table 4.4: Thermal conductivity (k) of carbon steel components and oxides.

Component	Formula	Thermal conductivity (W/m-K)
Wustite	FeO	5.0
Hematite	α -Fe ₂ O ₃	1.8-14.7
Magnetite	Fe ₃ O ₄	4.9 - 9.7
Pure ferrite	Fe	78.5
Cementite	Fe ₃ C	8.0
Graphite (parallel)	C	500
Graphite (perpendicular)	C	10
Pearlite	Fe + Fe ₃ C	25

In order to quantify the effect of having a composite material composed of two or more of the components listed in Table 4.4, a two-dimension steady state heat transfer calculation is needed. Fourier's law in two dimensions at steady state can be expressed as follows:

$$\frac{\partial^2 T}{\partial x^2} + \frac{\partial^2 T}{\partial y^2} = -\frac{q'''}{k} \quad [3.1]$$

where T is temperature, x and y are dimensions in the plane of the coupon, q''' is the volumetric heat source and k is the thermal conductivity. Although Equation [3.1] can be solved analytically for a heterogeneous system, it can be solved numerically using a FE technique. The FE method is preferred in this case for several reasons. First, the discontinuities presented by varying the k values make the analytical solution more difficult. Second, in order to evaluate a solution with the large number of nodes that are

used in this study, a numerical technique would be needed to automate the process.

Finally, computer programs are readily available to solve problems similar to the problem presented here.

The FE analysis is accomplished by subdividing the surface of the metal into a number of small volume elements (the z-direction, which is the thickness direction and perpendicular to the x-y plane, is assumed to be uniform). Each volume element can be assigned a different thermal conductivity, which allows the spatial variations in heat transfer of a composite material like carbon steel to be modeled. Equation [3.1] is solved for each element in the calculation grid. The numerical technique used here can be found in Ribando's work (the program is HTT_2dss.exe) with an implementation of a Modified Strongly Implicit iterative method[221].

For the purpose of this study, the surface was divided into nearly 1000 elements (97x99). The grid size was chosen to allow the proper aspect ratio to be attained between the overall size of the material and the areas of lower conductivity. The size of the x-y plane that is being modeled is 2 cm x 2 cm, which makes the size of the areas of low conductivity approximately 200 μm . (The maximum grid size allowed by the program used is 99x99). A diagram of the coupon described by the proposed heat transfer model is given in Figure 4.1.

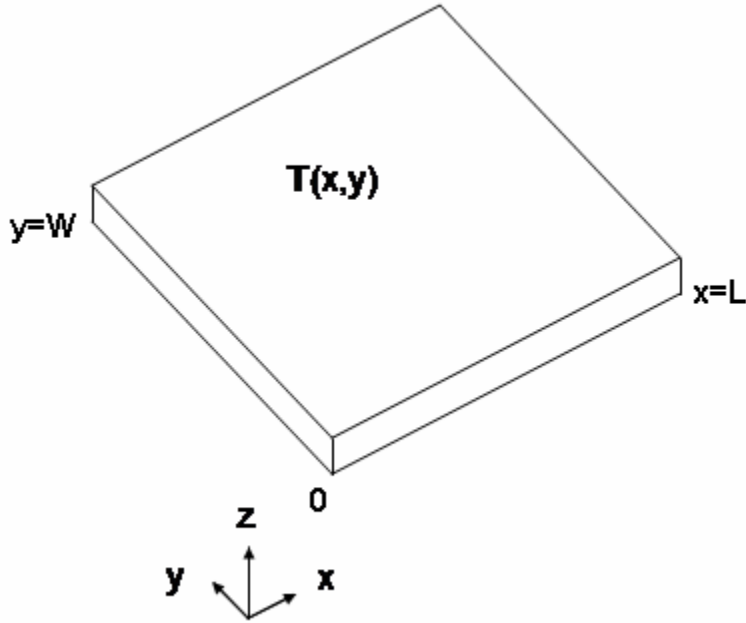


Figure 4.1: Diagram of the coupon described in the heat transfer model.

Boundary conditions can be set at the four edges of the grid and the relative thermal conductivity (λ_{rc} , which ranges from $0 \rightarrow 1$) and initial temperature can be entered for each element. λ_{rc} is calculated with Equation [3.2], where k_i is the thermal conductivity of material i and k_{Fe} is the thermal conductivity of iron.

$$\lambda_{rc} = \frac{k_i}{k_{Fe}} \quad [3.2]$$

The first goal is to determine the possible magnitude of a temperature difference when a low conducting material (cementite or the Fe-oxides) is placed in a composite comprised primarily of Fe. In this simulation, which models the situation where a room temperature coupon is placed into a warm oven, the temperatures at the edges of the coupon are

80 °C. The heating is assumed to occur from the edges of the coupon, which leads to the boundary condition: $T(x=0,L; y=0,W; t) = 80\text{ }^{\circ}\text{C}$. Here, both L and W were set at 2 cm as mentioned above. Applying the FE method to this problem yields a system of equations with the given boundary conditions in a matrix format, which can be solved for all the nodes. The iteration process is applied for changing the volumetric heat source term with respect to relative thermal conductivity. This is continued until the change in temperature is less than 0.001% between iterations.

During the initial stages of the heating, the temperature of the interior is close to its initial temperature, which is 25 °C (generally observed in the laboratory experiments). The temperature profile of the grid containing two low conductivity elements is shown in Figure 4.2. The low-conductivity components were each substituted into the grid at 0.04%. The λ_{rc} of iron is 1 in these simulations since it is the most conductive component in the composite. The λ_{rc} of the material that forms the temperature dip on the top is 0.3, which models the pearlite component in carbon steel and the feature on the bottom has a λ_{rc} of 0.1, which simulates cementite and the Fe-oxides. The pearlite component temperature difference, relative to the neighboring Fe is 2.5 °C (29-26.5 °C) and the cementite component causes a 7.3 °C (29-21.7 °C) difference.

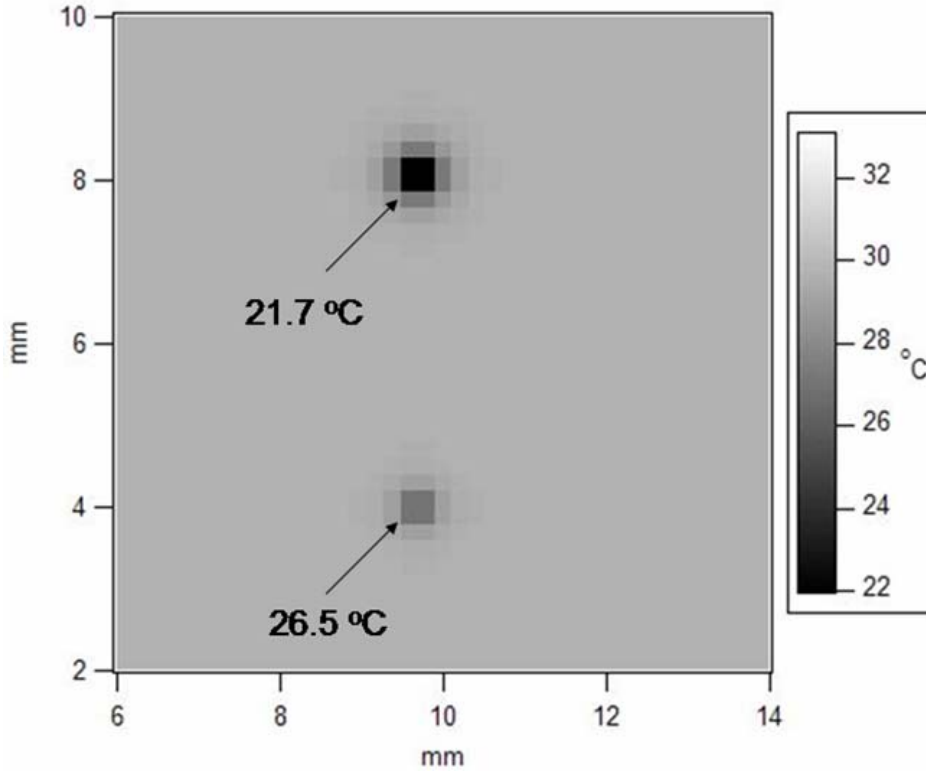


Figure 4.2: Temperature profile of a coupon containing two elements of low conduction. The feature on the top has a $\lambda_{rc}=0.3$ and the feature on the bottom has a $\lambda_{rc}=0.1$. The graph represents an 8 mm x 8 mm square region of the coupon and the average temperature is 29 °C.

Figure 4.3 presents a case where more low-conducting regions are added to the grid, and the conditions are adjusted to simulate a later time in the heating process with the oven temperature equal to 105 °C. Extended heating is simulated by adjusting the volumetric heat generation terms at the edge of the coupon until the average interior temperature is equal to the average temperature of the coupon at a desired time, as measured experimentally. The equal but random distribution of $\lambda_{rc} = 0.1$ and $\lambda_{rc} = 0.3$ regions account for 0.8% of the area and the temperature distribution results in a COV value of 0.11 over the entire surface. The difference between the minimum temperature and the

average is 7.3 °C with the $\lambda_{rc} = 0.1$ regions equal to 71.7 °C and the $\lambda_{rc} = 0.3$ regions equal to 75.6 °C.

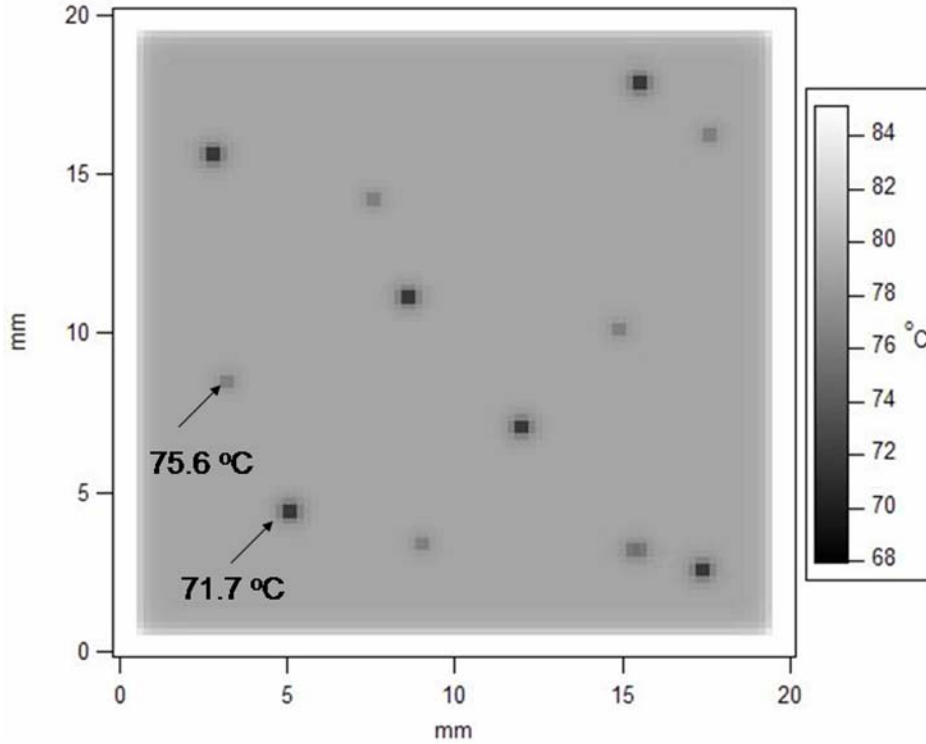


Figure 4.3: Temperature profile of a coupon containing multiple elements of low conduction. The low temperature regions correspond to an equal number of $\lambda_{rc}=0.3$ and $\lambda_{rc}=0.1$ regions. The average temperature is 79 °C.

Measurements of metal coupons during heating were made with an IR camera. The IR camera measures a 2-D temperature profile and does not allow information regarding the z-direction gradient to be determined. Every second a thermal image is recorded, which is comprised of hundreds of pixels, each of which represent a temperature and is approximately 50 μm in size. The minimum temperature of each image is subtracted from the maximum temperature of each image to give the ΔT term for each image. The

average of the first ten ΔT values is used in the calculation and is presented in Table 4.5.

The standard deviation of these values is small—less than 1% in all cases.

Table 4.5: ΔT temperatures ($^{\circ}\text{C}$) measured with an IR camera during the heating of coupons.

	ΔT ($^{\circ}\text{C}$)		
Drying Temperature	Carbon Steel	Stainless Steel	Silicon
75 $^{\circ}\text{C}$	5.3	4.9	3.1
90 $^{\circ}\text{C}$	5.7	4.0	3.4
105 $^{\circ}\text{C}$	7.3	4.9	3.9

The silicon surface results provide a baseline for the measurement because of the uniformity of the silicon substrate. The shiny side of the silicon coupons was measured using the same technique used with the carbon steel and the stainless steel coupons. The measured temperature differences of the carbon steel surface are greater than those of the stainless steel surface, which confirms the results of the 2-D heat transfer model. The non-uniform temperature profile can lead to surface driven flow, which will be described in the next section.

The dependence on the size of the lower-conducting features in the metal surface was investigated by varying the size of the features in the heat transfer model used above.

Figure 4.4 shows the increases in ΔT that are found as the size of the lower-conducting features in the carbon steel composite is increased.

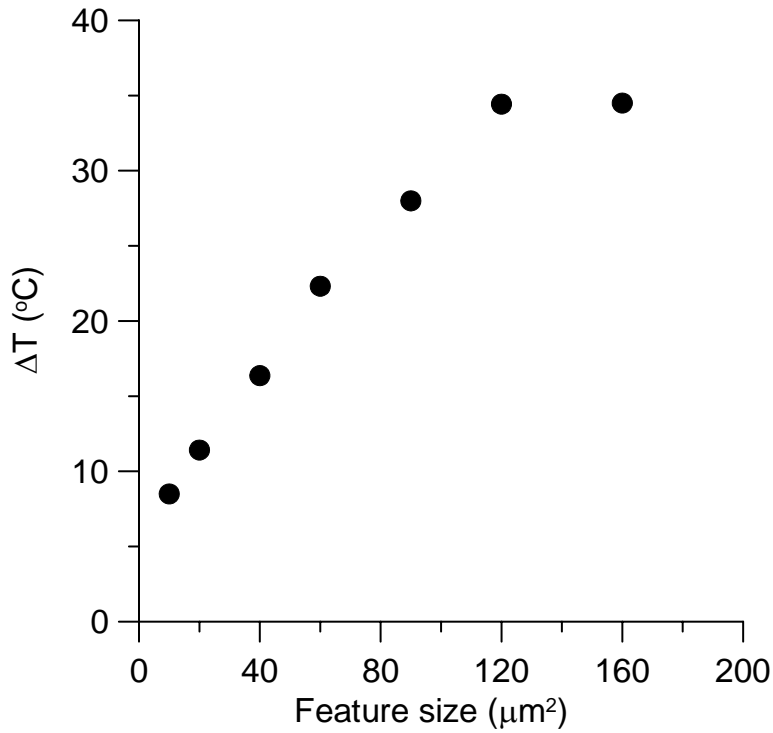


Figure 4.4: Dependence of ΔT on the size of the lower-conducting features in the metal composite.

The sizes of the grain boundaries found within the carbon steel were determined by chemically etching the surface of the metal to reveal the microstructures that comprise the metal. First, the metal was polished to $0.05\ \mu\text{m}$ using a combination of sand paper and polishing clothes. Then, a 2% nitric acid in methanol solution was used to etch the metal, revealing the grain boundaries that were then photographed using 200x with an optical microscope. A representative image is shown in Figure 4.5. In Figure 4.5, the maximum size of a grain is approximately $25\ \mu\text{m}$.

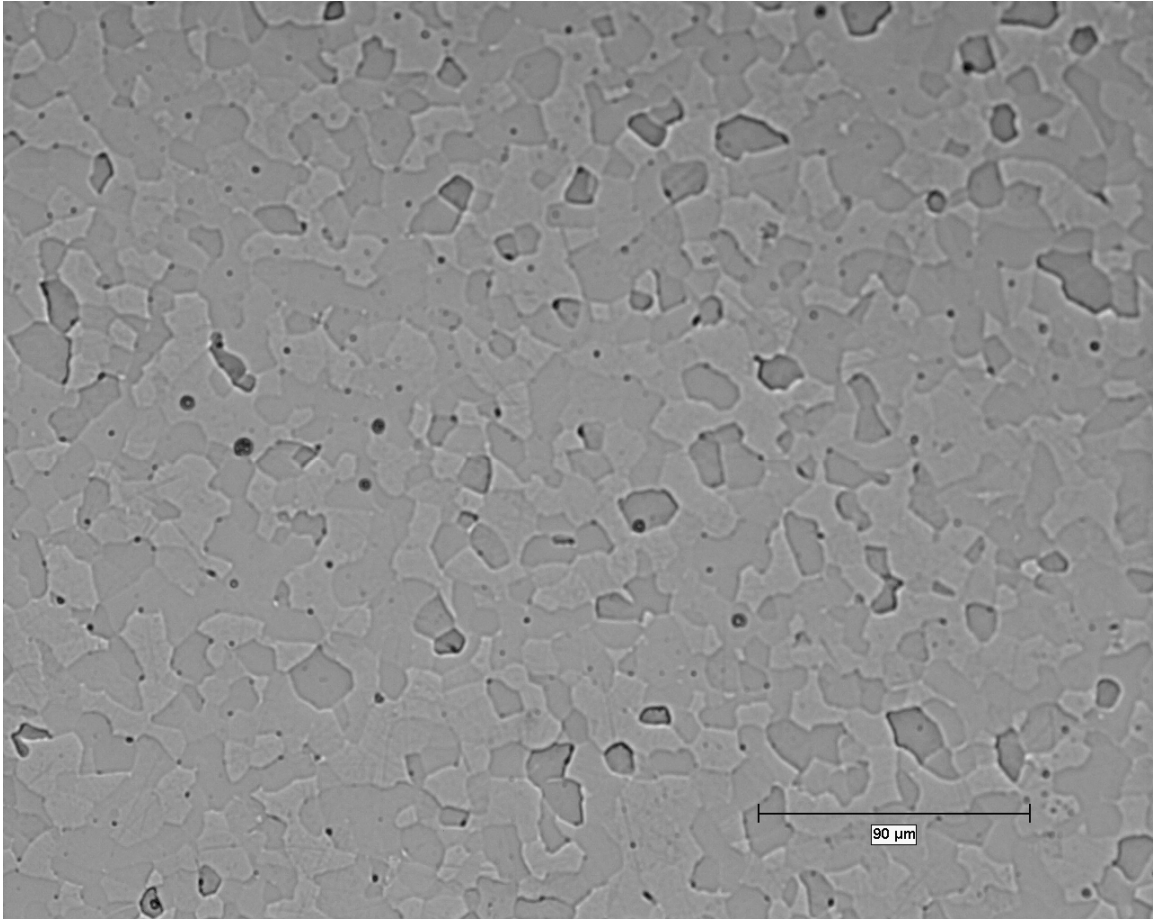


Figure 4.5: Optical image of etched carbon steel at 200x magnification. The size bar is 90 μm .

The microstructure presented in Figure 4.5 is reminiscent in size and shape of the AFM images of the dried polymer films presented in Figure 3.37.

4.2 Surface driven flow

Surface driven flow, also known as Marangoni convection, was reported during in the 18th and 19th centuries but the experiments that piqued curiosity in the area happened in 1901 when Benard reported convection cells that result from heating a liquid from

below[222-224]. It was originally thought by Rayleigh in 1916 [222] that the convection cells were the result of buoyancy effects and the phenomena was named Benard convection. Later, Pearson showed that the convection cells were the result of temperature gradients at the free surface and the resulting surface tension gradients, which are known as Marangoni convection or thermocapillary flow[225-227].

The surface tension differences that are the driving force for Marangoni convection can arise two ways. First, temperature gradients will create surface tension gradients, as recognized by Pearson. For most liquids, surface tension values will decrease as temperature increases. Marangoni convection arising from temperature differences is also called the thermal Marangoni effect[226]. The second way to induce Marangoni convection is to have non-uniform composition at the surface of the liquid. This is most commonly accomplished with concentration gradients of surfactants, which lower the surface tension. The solutal Marangoni effect arises when non-uniform evaporation causes temperature gradients or the evaporation of the solvent leads to areas of concentrated solute, which changes the surface tension and drives surface flow[226, 228]. Often, many of these mechanisms are present and act together. In thick liquid films with a free surface, Benard-Marangoni convection combines buoyancy effects and surface tension effects from temperature gradients[229].

Marangoni convection is depicted in Figure 4.6. The differences in surface tension lead to a wavy surface, which tends toward equilibrium (smooth) through surface driven flow[230, 231].

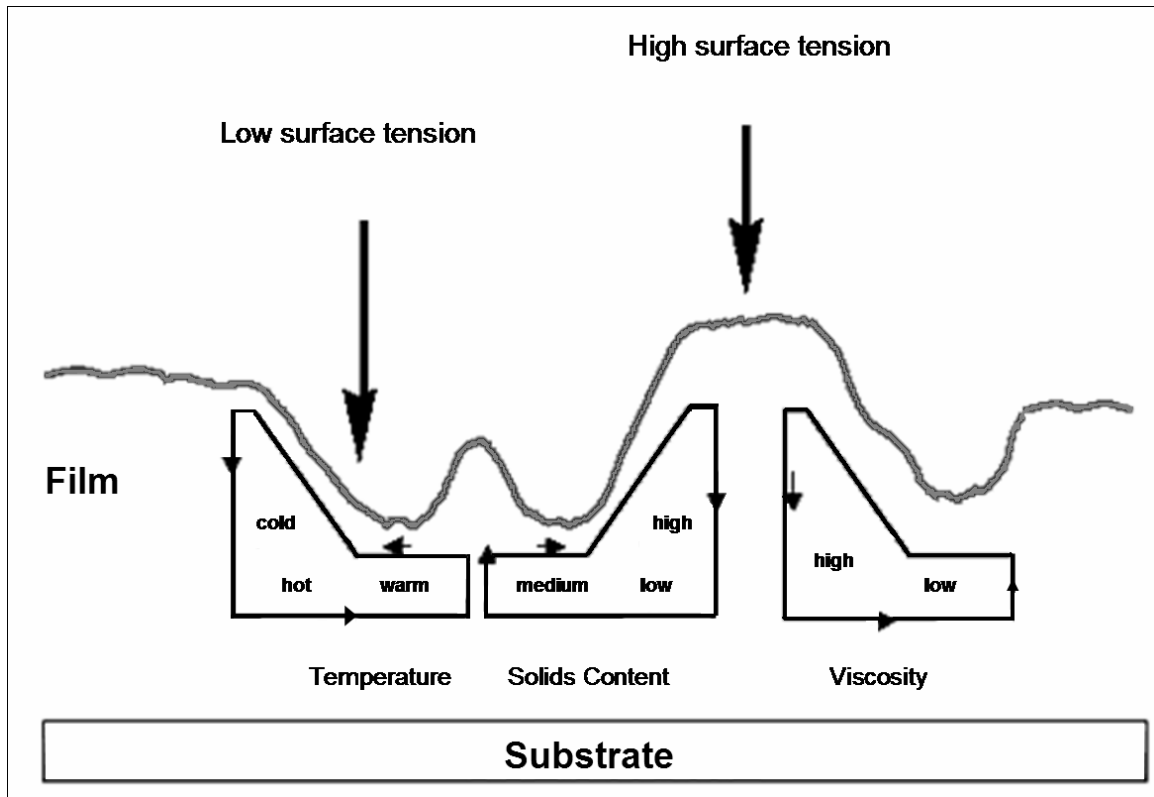


Figure 4.6: Depiction of surface driven flows.

Marangoni convection requires the liquid to be in contact with a free surface, which can be a gas or another liquid. In cases where the fluid is bound on all sides by rigid material, Benard convection can still act but Marangoni convection will not occur. Increasing the viscosity of the fluid will reduce the effects of both Marangoni and Benard convection[232].

As the film thickness becomes thinner, the relative effects of buoyancy are reduced to a point where they become negligible when compared to the surface tension effects[232]. This argument was used by Pearson in his rebuttal to Rayleigh's buoyancy explanation of

Benard's original observation[222, 225]. Pearson shows that the critical film thickness (d_{12}) where buoyancy effects cease to apply is given by:

$$d_{12} = \sqrt{\frac{\sigma}{\rho g \gamma} * \frac{571}{80}} \quad [3.3]$$

where σ is the surface tension, ρ is the density of the liquid, g is the acceleration due to gravity and γ is the coefficient of thermal expansion of the liquid.

Pearson reports in most liquids with thicknesses less than 1 cm that surface tension forces will be “more effective than buoyancy forces in producing instability” and for thicknesses less than 1 mm, surface forces will dominate the buoyancy forces[225].

The Marangoni number (Ma) increases as the instability effects increase and is defined as follows[233, 234]:

$$Ma = \frac{\tau \Delta T D}{\mu \kappa} \quad [3.4]$$

where τ is the negative surface tension gradient with respect to temperature ($\tau = -\frac{\partial \sigma}{\partial T}$),

ΔT is the difference in temperature, D is the thickness of fluid film, μ is the viscosity of the fluid and κ is the thermal diffusivity.

It should be noted that the surface tension gradient for most liquids is negative,

$\left(\frac{\partial \sigma}{\partial T} < 0 \right)$. The surface tension decreases due to the reduced cohesion within the liquid as

the molecular energy increases with increasing temperature. Also note that some

definitions of Ma do not use the negative sign in the surface tension gradient term[222, 234, 235].

Several general themes have developed in studies related to Marangoni convection. Linear stability analysis has been used to model the instabilities created in specific systems that contain limited variables[227, 232, 236-238]. Some of the extensions beyond simple systems have included analysis of two-fluid systems where two immiscible fluids are layered, rather than using a liquid/vapor system[235]. A difficulty of studying Marangoni convection is keeping the thin films from evaporating. A study focused on reducing the effects of Benard convection by placing a liquid in a porous medium with a thin film on top[236]. The porous medium damped the buoyancy convection and allowed a reservoir of liquid.

Most experimental and theoretical studies focus on uniform conduction in the lower heated surface. A recent article presents a theoretical study of Marangoni convection induced by an inhomogeneous temperature profile on the substrate that supports the fluid[239]. The temperature profile is given by a periodic function and the goal of the work is to develop techniques to use Marangoni convection as a control parameter. There are a number of areas where Marangoni convection plays a role in industrial applications. A sampling of these will be presented in the next section.

4.2.1 Importance of surface driven flow in applications

Some of the earliest work regarding Marangoni convection by Pearson in 1958 was initiated by observations made while studying the drying of paint[225]. Since then, the role of Marangoni convection has been studied to understand defects found in coatings including spin coating operations. Marangoni convection has been shown to cause capillary ridges in coatings, which compromises the smoothness of a surface[240]. AFM studies have shown that ring instabilities that lead to holes in coatings are caused by surface driven flow[241]. Marangoni convection has been theorized as a solution to capillary ridges. Heating the fluid where the ridge occurs lowers the surface tension, which causes surface driven flow away from the ridge and reduces the magnitude of the ridge[242].

The role of evaporation has been studied extensively because of the relationship of defects such as striations with evaporation rate[243, 244]. Faster evaporation of the solvent during deposition leads to a rougher surface[245]. This is attributed to both the solutal and thermal Marangoni effect. At higher evaporation rates, the thermal gradients develop due to non-uniform evaporative cooling, which accounts for increases in the thermal Marangoni effect. The solutal Marangoni effect becomes significant as the non-uniform evaporation changes the composition of the liquid, which can cause changes in surface tension[243-245]. In spin coating, striation development due to Marangoni convection occurs after the initial flow of the liquid subsides and the evaporation mechanism begins to dry the film[243]. In a study of polymer films, the characteristic

wavelengths of the defects in a film are reported to scale inversely with the heat flux applied to the polymer film[232].

Slower evaporation rates, which can be attained either by using less-volatile solvents or using lower temperatures will lead to smoother surfaces. Liquids with higher viscosity also are less prone to surface driven flow-defects. Measuring surface driven flow is difficult due to the very thin films involved and the intrusive nature of tracer elements. IR imaging has been utilized successfully in experimental studies of Marangoni convection and will be discussed in the next section.

4.2.2 Surface driven flow imaging with IR thermography

IR thermography has been used to image evaporating water with the primary purpose of understanding ocean movements. During evaporation, non-uniform cooling at the surface leads to instability in the liquid and subsequent flow. Flow derived from the effects of evaporation is called natural convection[246]. Saylor *et al.* have presented images, gathered with an IR camera functioning between 2 and 5 μm in wavelength, which define the convection cells that develop during evaporation. They have also deposited a monolayer of surfactant (oleyl alcohol) on the water films to show the dampening effects of the surfactant on the surface driven flow. The results have also been coupled with a two component laser Doppler velocimeter system to confirm the presence of flow beneath the liquid surface[247, 248].

Figure 4.7 shows the results found by imaging both clean and surfactant covered water surfaces at two heat fluxes. The images represent approximately 15 cm square sections of water in a 15 cm deep tank. The high heat flux-clean water case in (a) shows significant temperature differences at the water surface. Adding a surfactant monolayer (b) reduces the small scale temperature perturbations while the large scale differences remain. At lower heat fluxes, there is less temperature difference for the clean system (c) and the addition of surfactant again reduces the small scale differences (d).

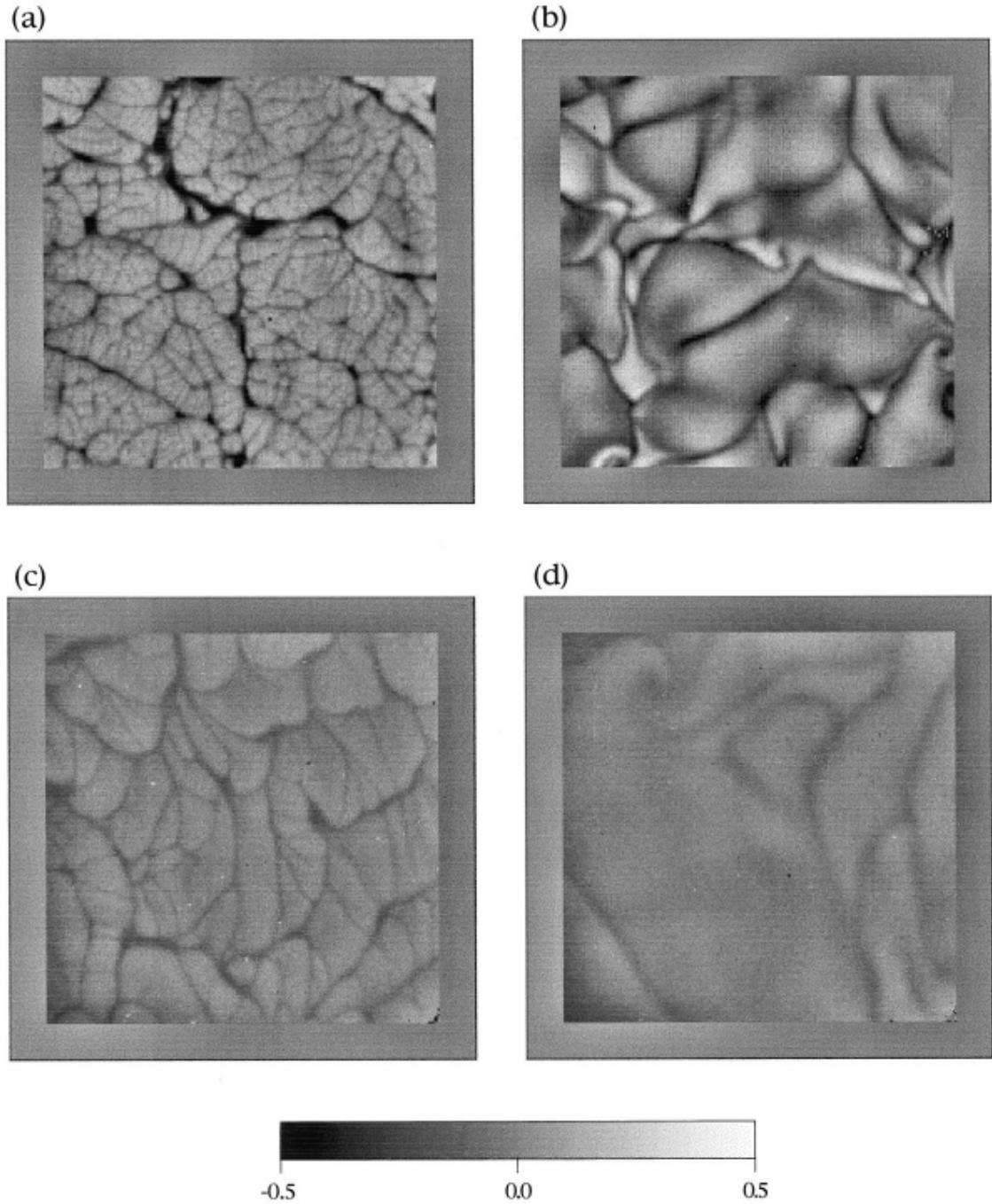


Figure 4.7: Temperature fields measured with IR thermography for evaporating water at various conditions: (a) High heat flux, (b) High heat flux with surfactant, (c) Low heat flux and (d) Low heat flux with surfactant[246]. The temperature scale indicates deviation from the average in $^{\circ}\text{C}$.

The same research group also presented the data shown in Figure 4.8[249]. This depiction better illustrates the progression as the heat flux increases. The root mean square (RMS) of the temperature was also shown to increase linearly with increasing heat flux. These images help to confirm the arguments presented previously that Marangoni convection is bolstered by higher evaporation rates[245].

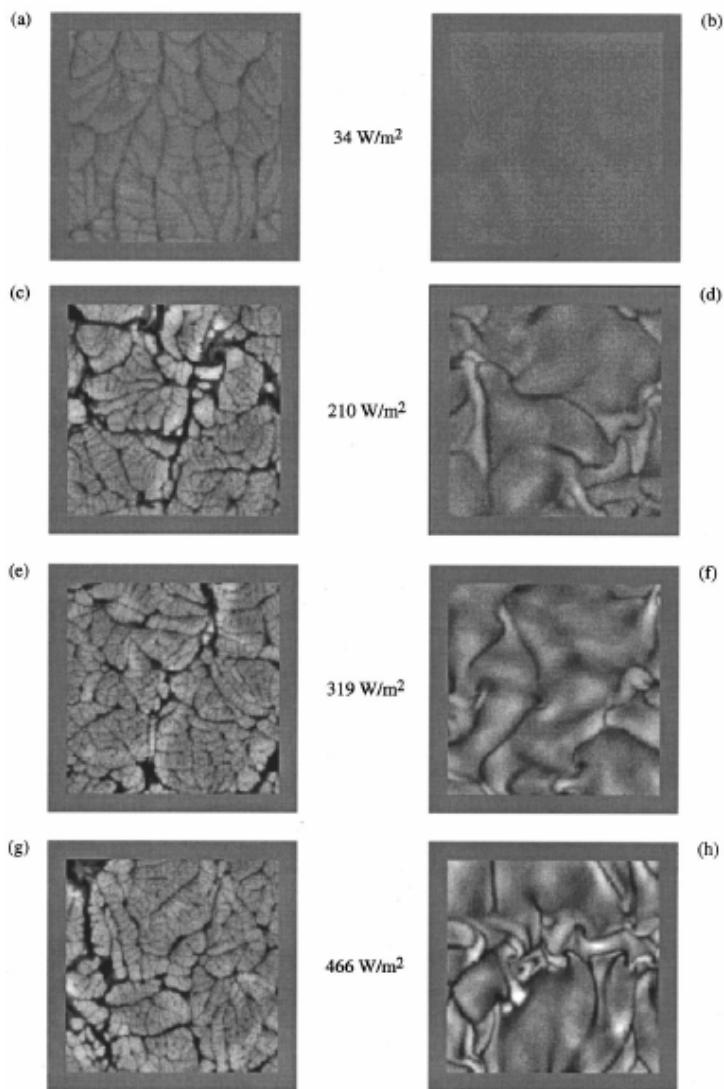


Figure 4.8: Temperature fields at various heat fluxes. The images on the left are clean systems (no surfactant) and the images on the right are systems covered with a monolayer of surfactant[249].

The same technique has been used to measure the spreading of contaminants on the surface of water[246, 250]. In Figure 4.9, the progression of film spreading is shown, starting at (a) when a drop of heptane/oleyl alcohol is shown just prior to being dropped. It is important to note that heptane will evaporate leaving just the monolayer of oleyl alcohol. The expanding ring of contaminant clearly changes the surface of the water beneath by damping the turbulent structure. The IR thermography technique is reported to show the progression of the contaminant more effectively than shadowgraphic techniques previously used[251, 252]. The shadowgraphic techniques measure the curvature that develops on the surface as the contaminant flows across the surface. This technique is error prone for systems that are not extremely smooth.

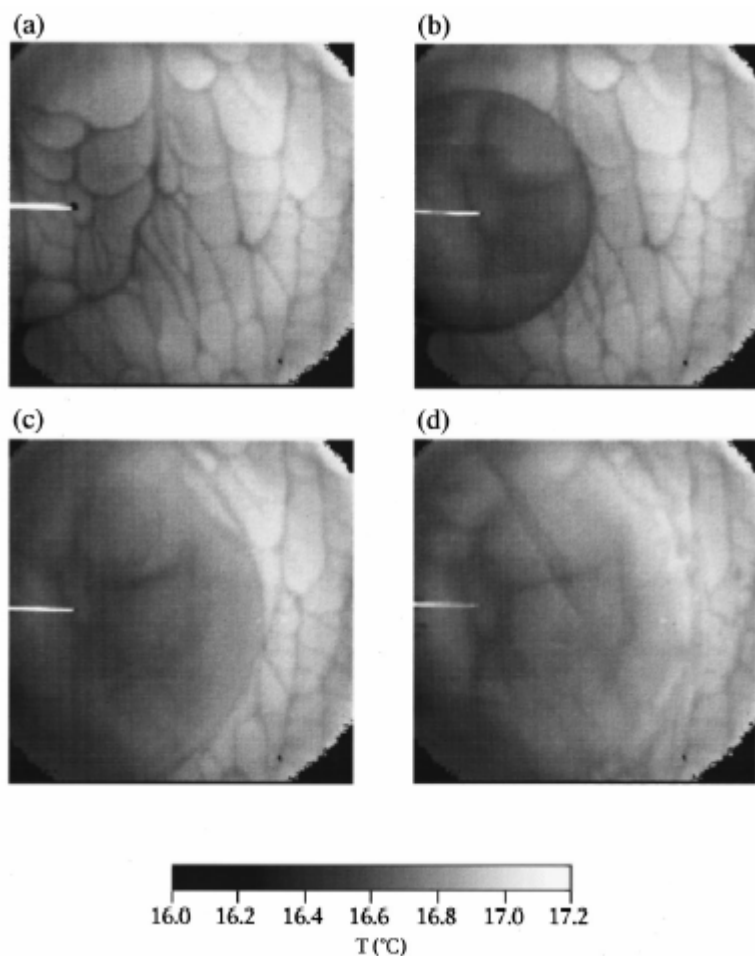


Figure 4.9: IR image showing the spread of surfactant on an evaporating water surface. Time between images is 250 milliseconds[250].

The ability to recognize contaminants with IR thermography has been extended to determining the local surface tension[253]. Surface tension measurements were made using the Wilhelmy plate technique across an image field. The surface tension results were then correlated with the IR images taken during the surface tension measurement and the IR images were found to be more revealing than the traditional surface tension measurement. This result could lead to an improved technique to measure the cleanliness of a liquid surface. In a recent article, Phongikaroon *et al.* report results using this

application to measure the role of contaminants and the temperature profile in the development of a Reynolds ridge wave structure[254].

An IR study of the spin coating process has recognized the evaporative cooling effect that leads to Marangoni convection and discussed the development of mounting chuck surface defects[255]. The paper goes on to explain the presence of “hills” and “valleys” in the film as the result of lateral temperature differences that develop where the chuck contacts the substrate[255].

After presenting background information regarding surface driven flow and how it affects various applications and presenting a technique to identify the potential for surface driven flow, the next logical step is to explore data relevant to the system of interest in this thesis. Therefore, IR data collected during the drying of an adhesive on metal coupons will be analyzed and the propensity of surface driven flow will be presented in the next section.

4.3 Surface driven flow experiments

Experiments were performed at three different drying temperatures, which correspond to three different heat fluxes and the drying of a waterborne acrylic adhesive was monitored with an IR camera. The experimental setup and data collection have been discussed at length in a thesis and publication[192, 193]. The first step is to calculate the critical thickness (d_{12}) for the system in question from Equation [3.3].

4.3.1 Calculation of critical thickness

From Equation [3.3] and the following data from the Carbotac MSDS[256], CRC Handbook[257], and assuming a 10 °C temperature difference: $\sigma = 0.044 \text{ N/m}$, $\rho = 1000 \text{ kg/m}^3$ and $\gamma = 0.2 \times 10^{-3} \text{ }^\circ\text{C}^{-1}$ leads to $d_{12} = 9.7 \times 10^{-4} \text{ m}$. Therefore for the films used in this study (between 10 μm and 80 μm) the surface driven Marangoni effect will dominate over the buoyancy Benard effect based on the work of Pearson[225].

4.3.2 Calculation of heat flux

The heat flux used during drying is calculated to benchmark the drying processes used in this study to others found in the literature. The heat flux was calculated by the following steps:

1. Finding the amount of water that was evaporated from the adhesive by subtracting the wet weight of the coupon plus adhesive from the weight of the coupon and adhesive after drying.
2. Finding the energy required to heat and evaporate the water was accomplished by integrating the heat capacity of the water from room temperature (25 °C) to 100 °C and adding the heat of vaporization. The result of this calculation is J/mol, which can be converted to J by using the weight of water (found in 1) and the molecular weight of water (18g/mol).
3. Dividing this energy by the surface area (m^2) of the adhesive as found with a ruler, which results in J/m^2 .

4. Calculating the amount of time required to dry by analyzing the COV vs. time graphs found with the IR camera. The point at which the COV vs. time graphs flatten to their final value is when the majority of the water has left the film and is a good approximation for the time required to dry the film. The plot indicating the time is shown in Figure 4.10 and the results for drying time are given in Table 4.6.
5. Obtaining the resultant heat flux (W/m^2) is accomplished by dividing the energy per unit area needed to dry the film by the calculated time.
6. Calculating the Convective Heat Transfer Coefficient (commonly denoted by “h”) is done by dividing the heat flux by the difference between the initial coupon temperature and the ambient temperature in the oven.

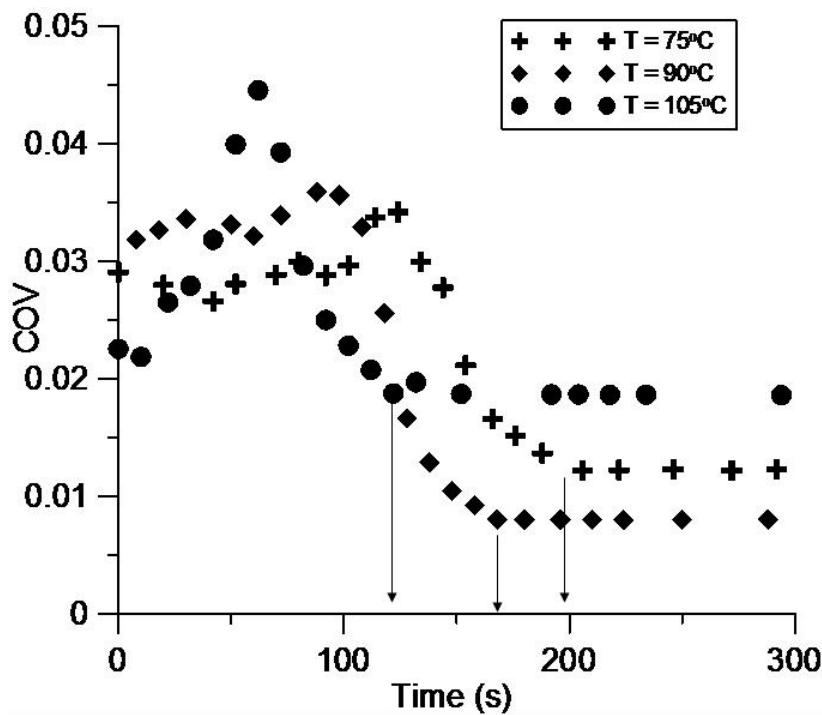


Figure 4.10: COV vs. time plot for the drying of acrylate films on stainless steel. The arrows indicate the point at which the plot flattens, which is the time needed to dry

the film at a given temperature. The error is within the size of the markers and are less than 0.002.

Table 4.6: Heat flux measured at different oven temperatures.

Drying Temperature (°C)	Time to Dry (s)	Heat Flux (W/m ²)	Convective Heat Transfer Coefficient (W/m ² -K)
75	196	200	3.99
90	162	241	3.71
105	122	321	4.01

The range of heat fluxes found in this study are similar to the heat fluxes found by Saylor *et al.* in a water evaporation study[249]. The convective heat transfer coefficient values found here are within the ranges reported by Incropera and DeWitt for similar systems (2-25 W/[m²-K])[258]. The values found here are on the low end of the reported range due to the small volume of air available for convection.

4.3.3 Finding film emissivity

Using IR imaging for temperature measurement requires using a proper emissivity value. A difficulty in measuring the drying of films is that the emissivity is strongly dependent on the moisture content of the film, which makes absolute temperature measurement difficult. For this study the emissivity was determined by heating a stainless steel coupon with a known emissivity (0.70) and applying the temperature to the coupons containing the films. The stainless steel emissivity was found by using a tabulated source [259] and by comparing the reading from a thermocouple to that of the IR camera[192]. The emissivity was calculated by matching the initial temperatures of each coupon that was subjected to the same oven heating conditions. The initial stages of drying are most

important since that is when the surface driven flow can take place, before the film dries and the viscous effects will overwhelm the surface tension effects.

Three types of coupons were used in this study. The first two are the carbon steel and stainless steel coupons—both have been used throughout this body of work. The third type of coupon is a stainless steel coupon, identical to the 304L steel used throughout the study but this coupon is marked with an ink pen with a grid pattern. The ink serves to interrupt the transfer of heat between the film and the metal coupon, which will make the heat transfer less uniform and induce Marangoni convection on the stainless steel coupon that was previously shown to exhibit little instability. The emissivity values of the films associated with each of the three coupons are given in Table 4.7, along with the oven temperature and the heat flux values.

Table 4.7: Table of emissivity values of films on various coupons at different oven temperatures.

Oven Temperature (°C)	75	90	105
Heat Flux (W/m ²)	200	241	321
Stainless Steel Emissivity	0.70	0.70	0.70
Carbon Steel Emissivity	0.36	0.34	0.46
Marked Stainless Steel Emissivity	0.71	0.67	0.73

4.3.4 Calculation of Marangoni numbers

Analysis of the IR temperature data gives information that can be used to calculate a Marangoni number that will describe the instabilities present in the films as they dry. The usual method for calculating the Ma number involves using the temperature gradient through the z-direction of the film as the ΔT term in Equation [3.4]. The IR camera

measures a 2-D temperature profile of the film and does not allow information regarding the z-direction gradient to be determined. Therefore, the ΔT used to calculate the Ma number is the difference between the maximum and minimum temperature measured on the film during the initial stages of drying, which is chosen to be the first ten seconds. (Ten seconds was chosen to encompass the initial stages of heating when surface driven flow is most likely to occur since the viscosity of the emulsion increases during drying. The same results were found by using the data from the first five, ten and 20 seconds of heating. The deviation in the data at five seconds was slightly greater than at ten and 20 seconds (2.8% vs. 1.1%), which made the choice of ten seconds obvious.) Every second a thermal image is recorded, which is comprised of hundreds of pixels, each of which contain a temperature. The minimum temperature of each image is subtracted from the maximum temperature of each image to give the ΔT term for each image. The average of the first ten ΔT values is used in the calculation of the Ma number. The standard deviation of these values is small, less than 2% in all cases.

The remaining data required to calculate the Ma number from Equation [3.4] remains constant in each case discussed here. The values listed in Table 4.8 are used with Equation [3.4] and the ΔT values to calculate the Ma number results presented in Figure 4.11. The film thickness used in the calculation is two times the measured value of the dry film. The viscosity data is from the Carbotac technical data sheet[256]. The surface tension gradient[260] and thermal diffusivity[257] values are specific to water but similar to values in the literature for related aqueous polymer systems[261-263].

Table 4.8: Values held constant in Ma number calculation.

τ	$1.7 \times 10^{-2} \text{ N/m-}^{\circ}\text{C}$
L	$4.0 \times 10^{-5} \text{ m}$
μ	$1.3 \times 10^{-1} \text{ N-s/m}^3$
κ	$1.5 \times 10^{-7} \text{ m}^2/\text{s}$

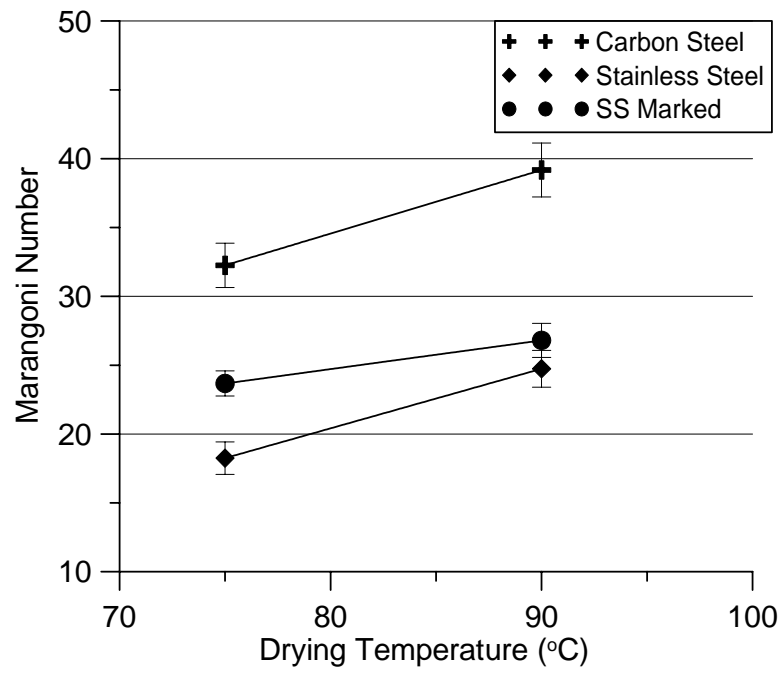


Figure 4.11: Marangoni numbers at various drying temperatures for three coupon types (SS Marked refers to the marked stainless steel coupons).

The drying temperature presented in Figure 4.11 corresponds directly to the heat flux values given Table 4.7. As suggested in the literature, the Ma numbers show a general increase with drying temperature[245, 249]. The films on carbon steel show consistently higher Ma numbers, which would be expected due to the non-uniform heat transfer characteristic of the material. The marked stainless steel coupons lead to slightly higher Ma numbers for the two lower temperatures, compared to the stainless steel coupons. This is expected due to the ink interrupting the heat transfer to the metal coupon.

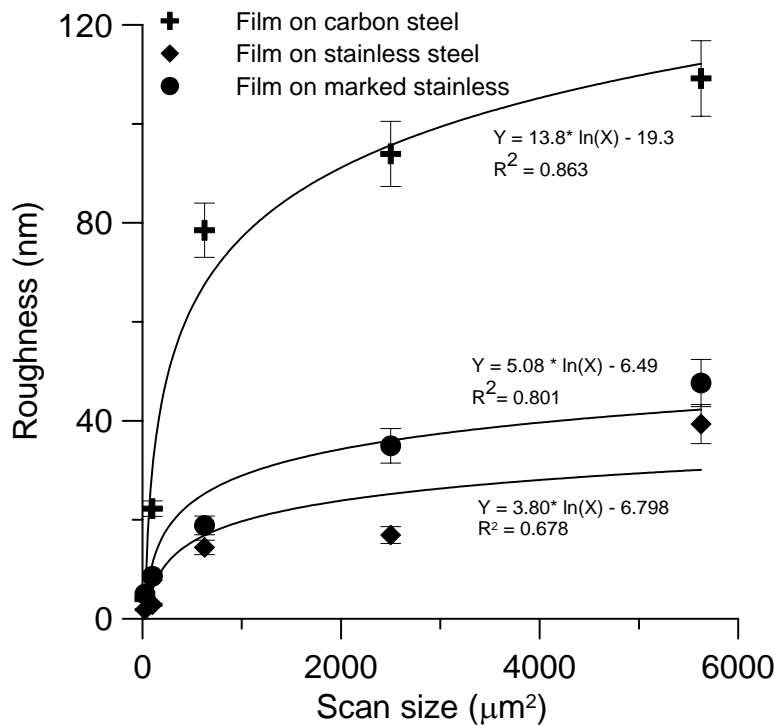


Figure 4.12: Roughness vs. scan size for three coupons dried at 105 °C.

Figure 4.12 shows the results of a roughness measurement performed with an AFM on the films dried on three coupons at 90 °C. The film on the carbon steel coupon resulted in

the highest roughness with the marked stainless steel coupon having a slightly higher roughness when compared to the stainless steel coupon. These results follow the Ma number results.

4.4 Conclusions of heat transfer studies

A literature review has presented appropriate information regarding the importance of substrate properties on the adhesive film development. A 2-D steady state heat transfer model illustrates the effect of having low-conductivity carbon-based constituents in carbon steel and presents spatial variations in temperature due to the low-conductivity components of carbon steel of over 7 °C.

The non-uniform temperature profiles affect the drying of the polymer films by inducing surface driven flow. Surface driven flow is known to cause surface defects in coating operations by causing increases in roughness. Temperature data from an IR camera is used to calculate Ma numbers and the Ma numbers relate well with the roughness of the polymer films. The Ma numbers have the expected dependence on heat flux, which is a direct relationship. It is also confirmed that the films used in this study are much thinner than the critical film thickness, which signifies a transition from buoyancy-dominated convection to surface tension-dominated convection.

By combining the results presented in this chapter, it can be concluded that the most likely mechanism responsible for the rough polymer surfaces presented in Chapter 2 is

Marangoni convection that is a consequence of non-uniform temperature profiles due to carbon-based, low-conductivity areas in carbon steel.

CHAPTER 5 – WADS STUDY OF CONTAMINATION ON DRYER CANS

5.1 Introduction

The production problems associated with stickie deposition in the dryer section of a paper machine and research studies related to those problems have been discussed in section 1.1.3. Another problem that is directly related to the amount of stickie material deposited on the dryer can is the increased force needed to pull the sheet away from the dryer can to move it to the next dryer can. This issue was qualitatively studied by Meinecke by changing the temperature of the dryer can and the incoming solids of the sheet[41]. His results are summarized in Figure 5.1, with the most sticking occurring at the center region of the plot.

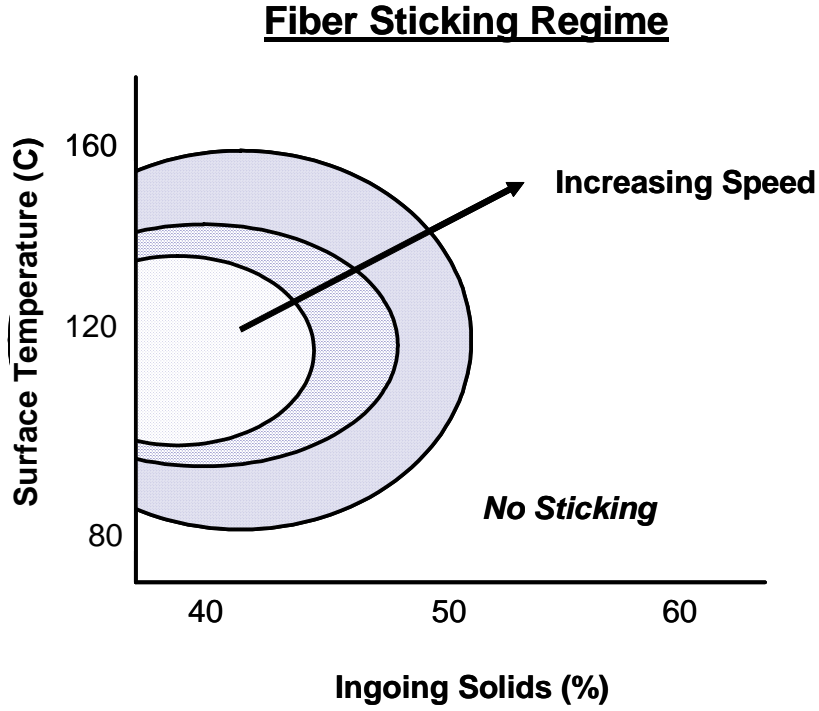


Figure 5.1: Results from the Meinecke study.

Prior to the Meinecke work, Mardon performed peeling studies in the laboratory and developed a relationship to determine the work of adhesion between the sheet and a metal plate using several measurable properties:

$$T^l = \frac{W^{ll}}{1 - \cos \phi} + mV_l^2, \quad [4.1]$$

where, T^l is tension, W^{ll} is the work of adhesion, m is mass per unit area, V_l is the velocity and ϕ is the peel angle.

Mardon's experimental setup did not accurately simulate the drying of paper due to the lack of a heated metal surface[264, 265]. To better replicate the drying of paper,

researchers at IPST have developed the Web Adhesion Drying Simulator (WADS), which has been used in several publications[266-268] and will be described briefly in the next section.

5.2 Description of WADS

The WADS system was designed to simulate conditions of paper drying on a paper machine. The parameters that can be controlled and varied by the machine are listed in

Table 5.1. Additionally, the properties of the sheet being tested can be varied to encompass any type of paper that can be made on a Formette Dynamique.

Table 5.1: Parameters and ranges for the WADS.

Parameter	Range
Surface Temperature	25 - 350 °F
Peel Angle	0 - 90°
Peel Velocity	20 - 400 ft/min
Dwell Time	0.005 - 5 s
Web Pressure	0 - 3 psi
Web Temperature	70 - 200 °F

A schematic showing the WADS is presented in Figure 5.2 and pictures of the system are shown in Figure 5.3 and Figure 5.4.

Web Adhesion and Drying Simulator

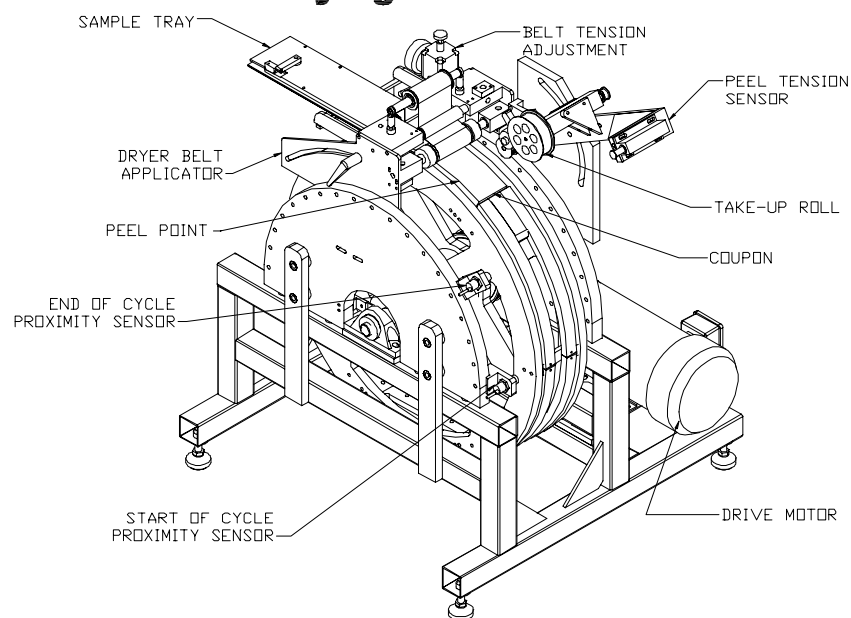


Figure 5.2: Schematic of the WADS unit.

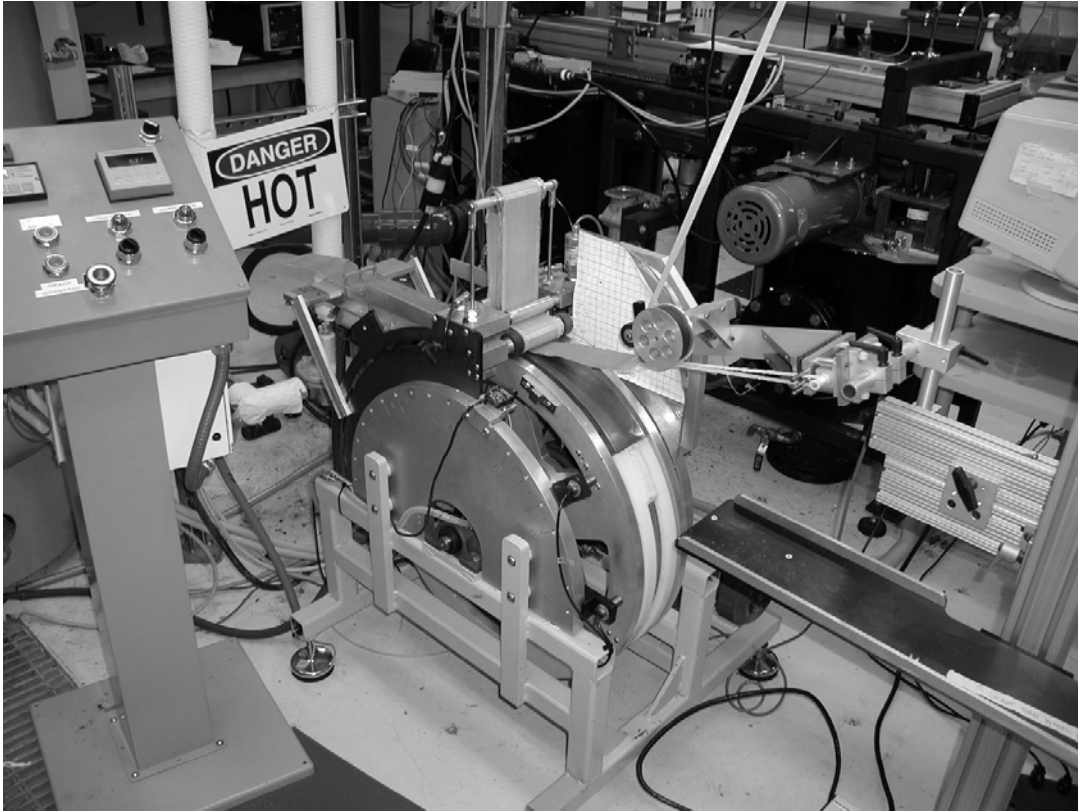


Figure 5.3: Picture of the WADS.

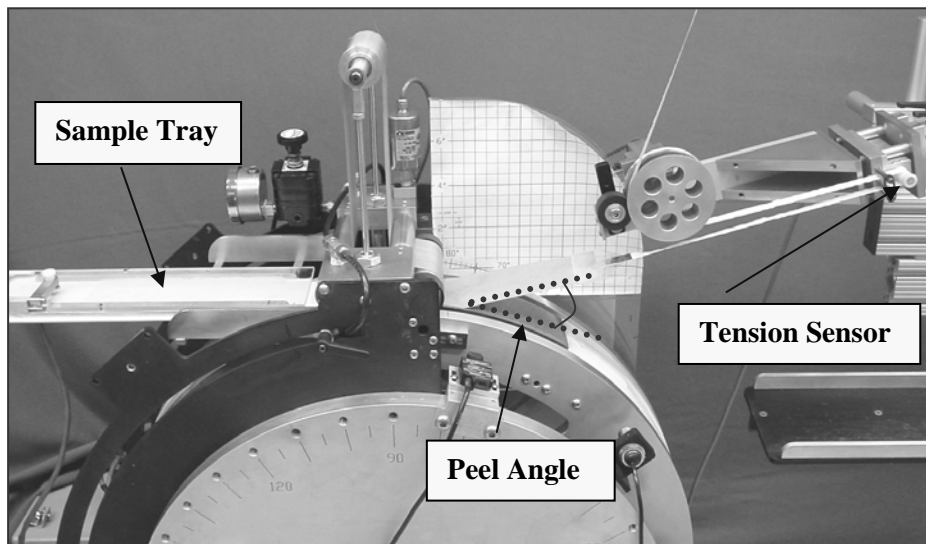


Figure 5.4: Picture of the WADS in operation.

During operation, the sheet is contacted against the metal coupon under a given pressure, and the tension, velocity and peeling angle are measured. Equation [4.1] is then used to calculate the work of adhesion for the system.

The WADS will be useful in determining the relative improvement in operation that can occur when the tack of the metal surface on a dryer can is reduced, as has been show in this thesis. Lower work of adhesion values are beneficial to the operation of a paper machine since it will lead to less picking and sheet flutter.

5.3 WADS experimental results

The WADS study was completed with 100 g/m² bleached virgin softwood that was refined to 550 mL freeness. The variable parameters in the study were the solids content of the sheet, which was set to 40% or 50% solids and the material used for the coupon, which was either carbon steel or chrome-plated steel. An adhesive film was deposited on the coupons in a similar manner as described in Chapter 2. The values listed in Table 5.2 were held constant during the experiments. The resulting films had two distinct levels of tack, as discussed in chapter 2. The film on the chrome-plated coupon was very tacky, as is expected with the Carbotac PSA and the film on the carbon steel coupon was less tacky.

Table 5.2: WADS parameters held constant during experiments.

Parameter	Value
Surface Temperature	194 °F
Peel Angle	15°
Peel Velocity	120 ft/min
Dwell Time	0.125 s
Web Pressure	1 psi
Web Temperature	70 °F

The data analysis includes analyzing the tension data required to pull the sheet off of the hot coupon, and finding the peel angle and the point at which the sheet pulls away from the hot coupon. The process of converting the output of the tension sensor (a voltage) to actual tension data is accomplished by calibrating the system with a series of masses applied to the sensor and by evaluating the impact of the experimental setup on the measured tension values. This information, a sample calculation and additional data from the WADS experiments are in Appendix B.

Figure 5.5 shows a graph of tension vs. time for a run with a sticky coupon on chrome-plated steel mounted in the WADS. The graph shows a maximum tension value of 97 g/cm and an average tension value of 65.5 g/cm during the event. Figure 5.6 shows a video capture from the high-speed video camera (a Vision Research Phantom v4.2 monochrome) that captures the experiment. From this image it can be deduced that the peel point is 69°. The low peel point (<70°) is typical of experimental runs with a sticky coupon. The peel angle is 32° and is measured using the angle tool in ImageJ version 1.32J, an image analysis program developed by the National Institutes of Health.

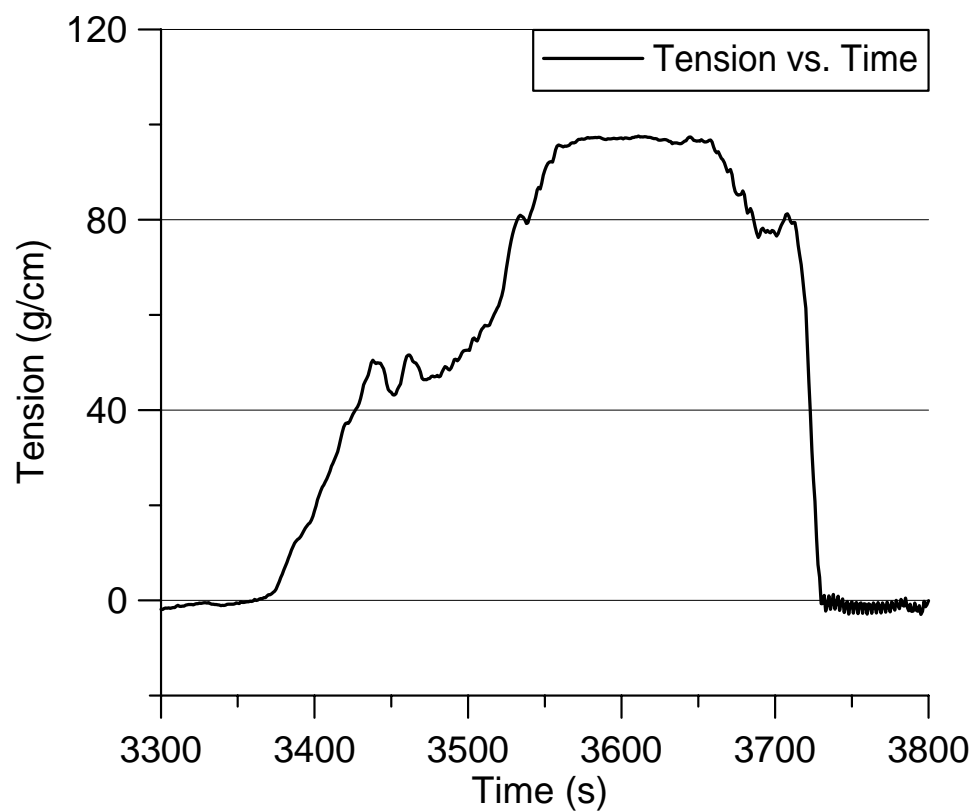


Figure 5.5: Tension data for WADS run with 50% solids sheet and sticky coupon.

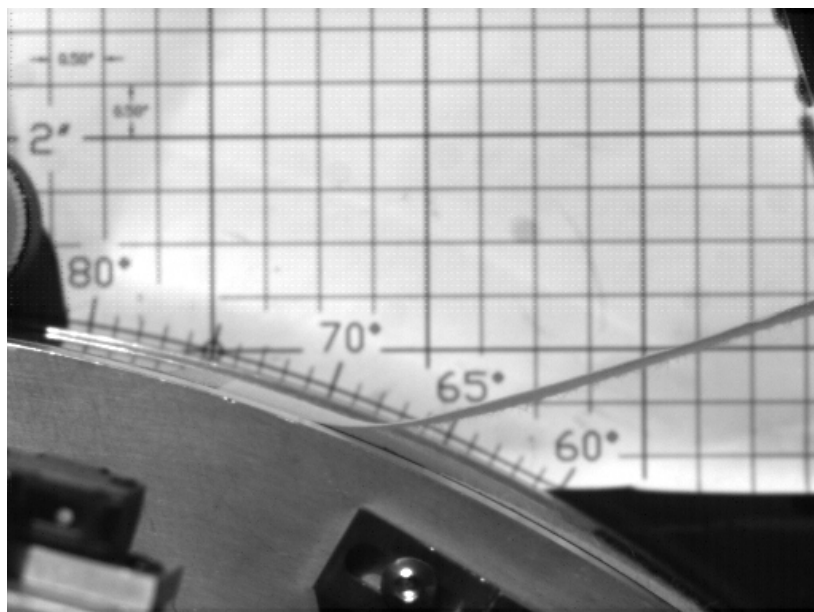


Figure 5.6: Video capture of a peeling event with a sticky coupon mounted on the WADS and a 50% solids sheet.

The work of adhesion was calculated two ways: first, using the average tension value (averaged over the entire experiment) shown in Figure 5.7 and second, using the maximum tension value shown in Figure 5.8.

Analysis of the data shows several trends related to the work required to remove the sheet from the metal surface and also distinctly separates the results from the sticky coupons, when compared to the non-sticky coupons. In addition to the raw data such as tension and peel angle, which are used to calculate the work of adhesion (via the Mardon equation), the peel point is also a good indicator of the operation of the system and can differentiate between sticky and non-sticky coupons.

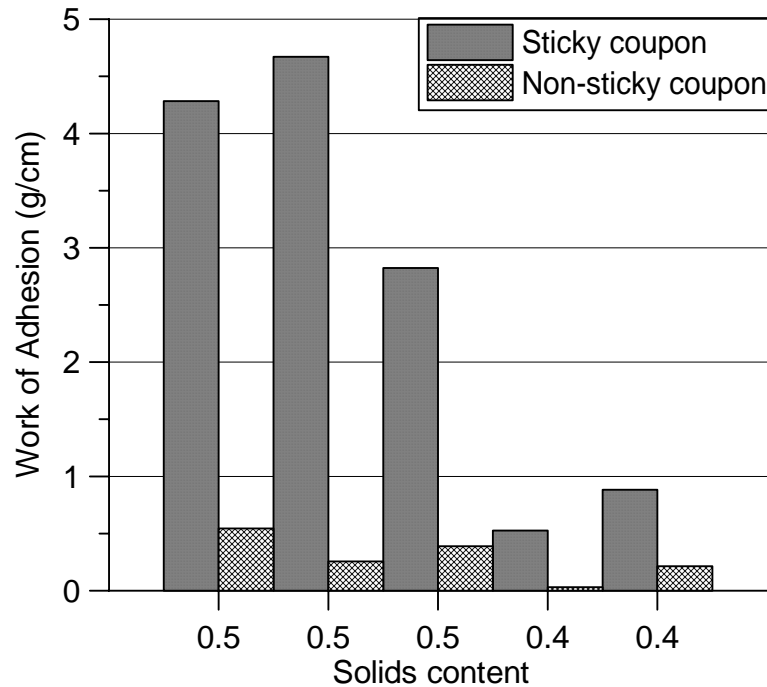


Figure 5.7: Work of adhesion (calculated with the average tension values) as a function of incoming paper solids content for experiments on sticky and non-sticky coupons.

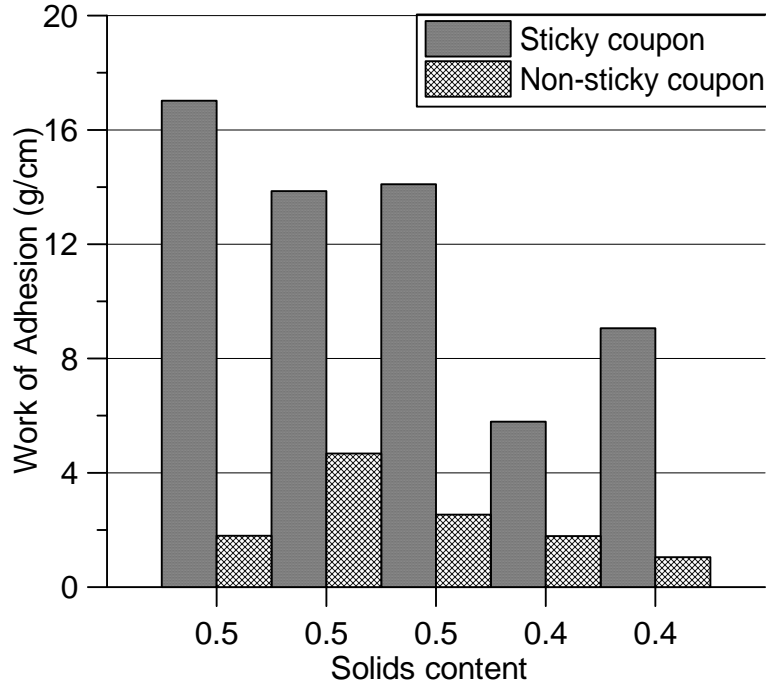


Figure 5.8: Work of adhesion (calculated with the maximum tension values) as a function of incoming paper solids content for experiments on sticky and non-sticky coupons.

As can be seen in Figure 5.7 and Figure 5.8 the work of adhesion values for the sticky coupons on chrome-plated steel is significantly higher than the non-sticky, carbon steel coupons. Also, it is obvious that the higher solids content in the incoming sheet leads to more sticking as was reported in previous work with the WADS machine[266, 267]. The average and standard deviation data for the work of adhesion and peel point are given in Table 5.3.

Table 5.3: Work of Adhesion and Peel Point average and standard deviation data for sticky and non-sticky coupons at 40% and 50% solids.

Work of Adhesion		Avg. Tension	Max Tension	Peel Point
Sticky	50% Average	3.93	14.99	66.2
	50% Standard Deviation	0.97	1.76	5.1
	40% Average	0.70	7.43	72.7
	40% Standard Deviation	0.25	2.31	3.8
Non-sticky	50% Average	1.04	2.77	74.2
	50% Standard Deviation	0.46	1.30	4.4
	40% Average	0.22	2.51	80.4
	40% Standard Deviation	0.15	1.56	1.3

From the data in Table 5.3, a rough relationship can be recognized between the peel point and the work of adhesion. Namely, the lower the peel point, the higher the work of adhesion. This is shown in Figure 5.9.

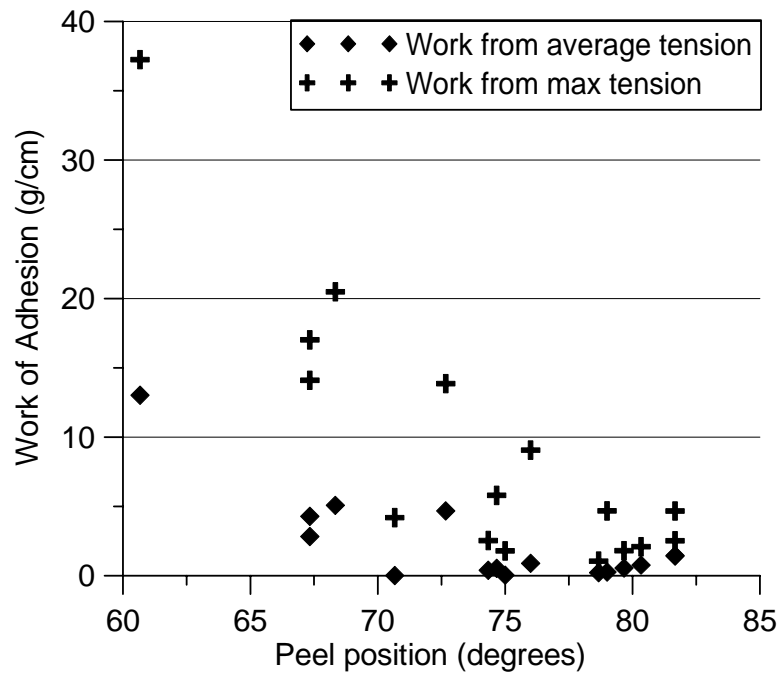


Figure 5.9: Work of adhesion vs. peel point.

The impact of a surface can, in many cases, be realized by watching the sheet peel from the coupon. Figure 5.10 and Figure 5.11 show relatively normal peel events with Figure 5.10 being a low adhesion event with a high peel point. Figure 5.11 is a higher adhesion event with a lower peel point. Both instances reflect a controlled peel event with a relatively constant tension value, which produces less flutter and a more uniform sheet.

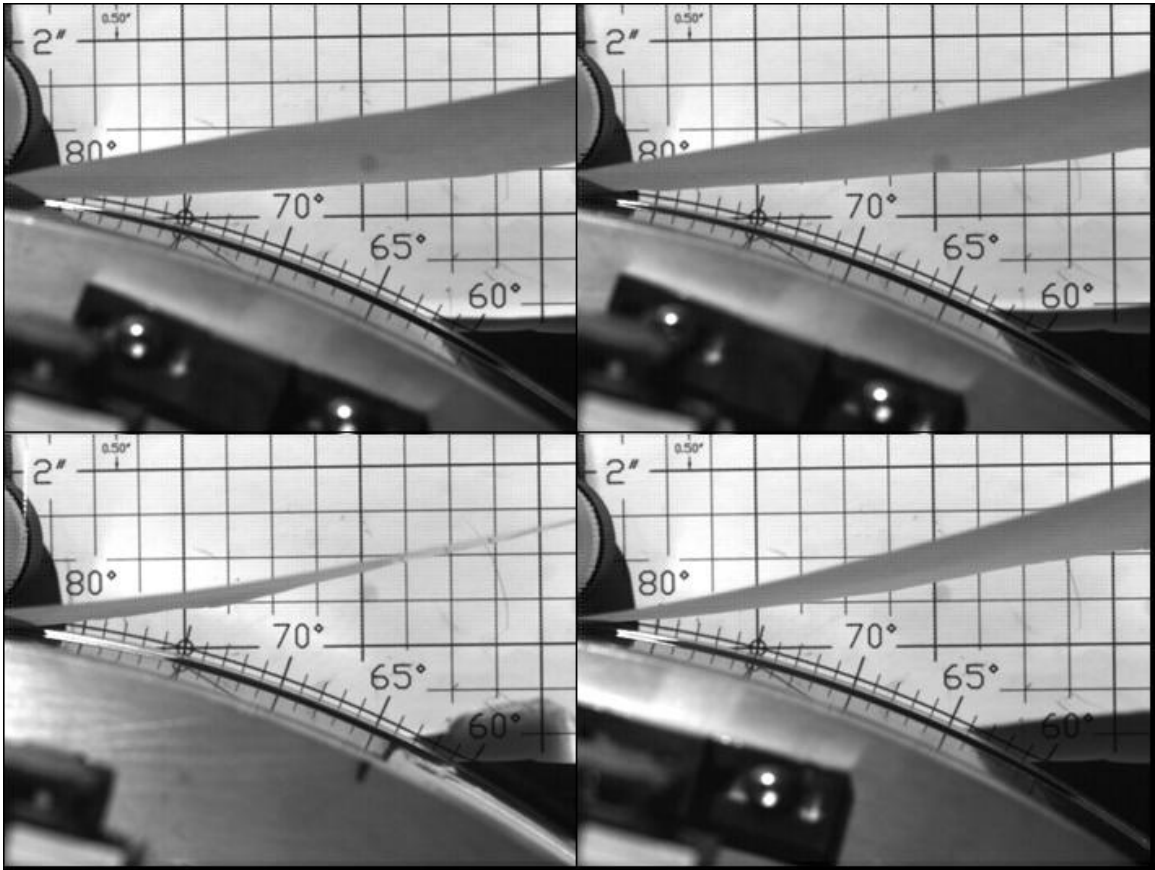


Figure 5.10: Images during the peel event for a 40% solids sheet on a non-sticky coupon.

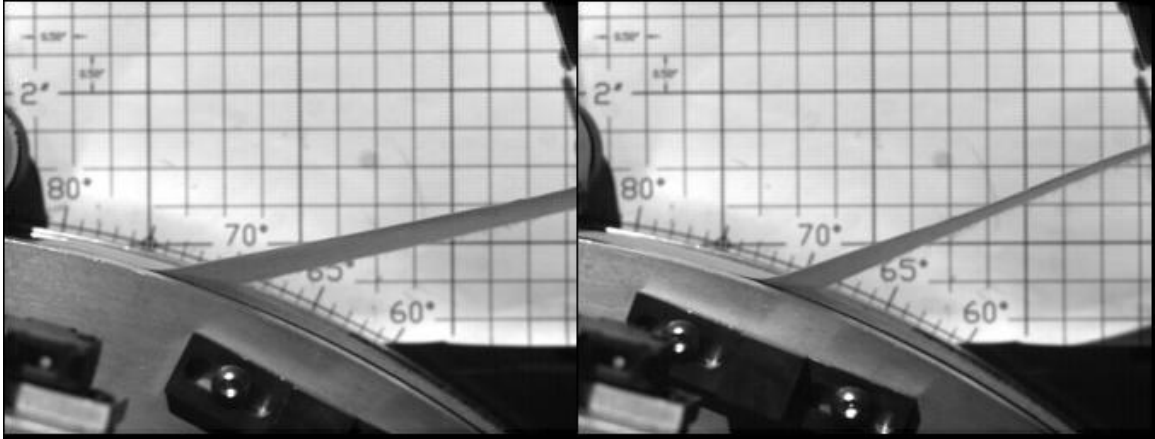


Figure 5.11: Images during the peel event for a 40% solids sheet on a sticky coupon.

Figure 5.12 and Figure 5.13 show images from an atypical peel event that results from a high work of adhesion and a low initial peel point. In this event, the sheet adheres to the coupon very strongly until it experiences a violent release. This violent release produces uneven tension on the sheet, which leads to significant sheet flutter on a paper machine. The sheet flutter and uneven tension can lead to a non-uniformly restrained sheet or at a worst case, a sheet break.

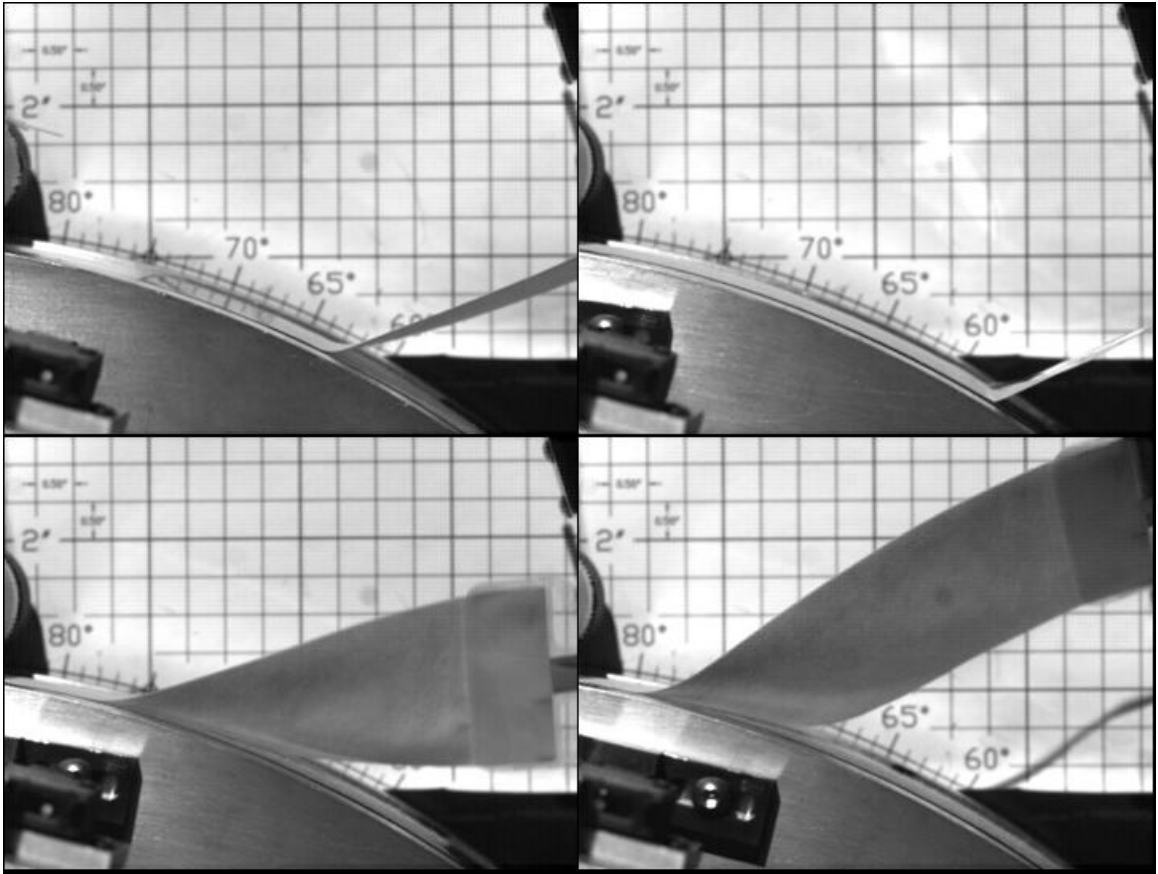


Figure 5.12: Images during the peel event for a 50% solids sheet on a sticky coupon, part 1.

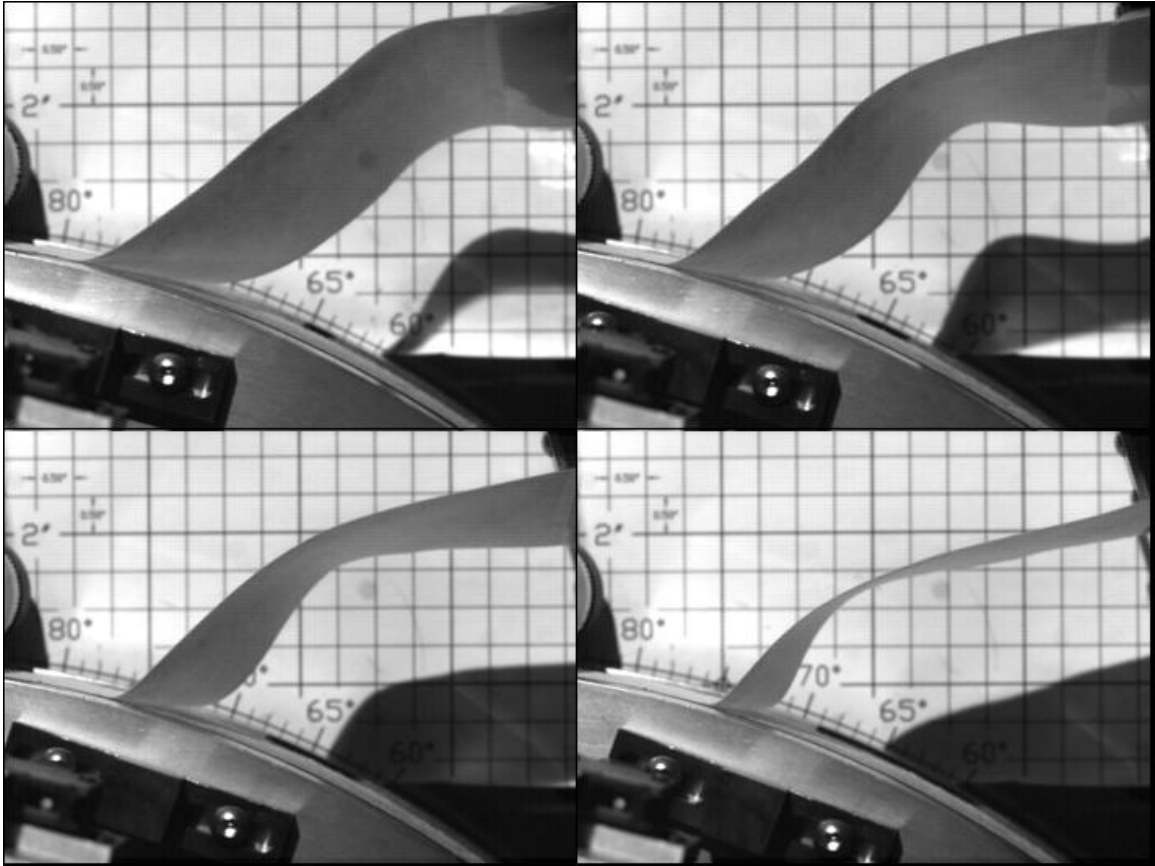


Figure 5.13: Images during the peel event for a 50% solids sheet on a sticky coupon, part 2.

Another problem that is caused by sticky dryer cans is picking, which causes finished product quality issues due to loss of smoothness associated with fibers pulling out of the sheet. Digital images were taken of the coupons after the WADS experiments were complete. Image analysis could be used to quantify the amount of picking by finding the % coverage but due to the very high picking on the sticky samples this analysis was not feasible.

Typical images for picking on sticky and non-sticky coupons are shown in Figure 5.14 and Figure 5.15, respectively. The sticky chrome-plated coupon removes a layer of fiber

across the entire sample. As indicated in the picture of the non-sticky coupon, fibers are removed in small clumps and sporadically across the coupon.

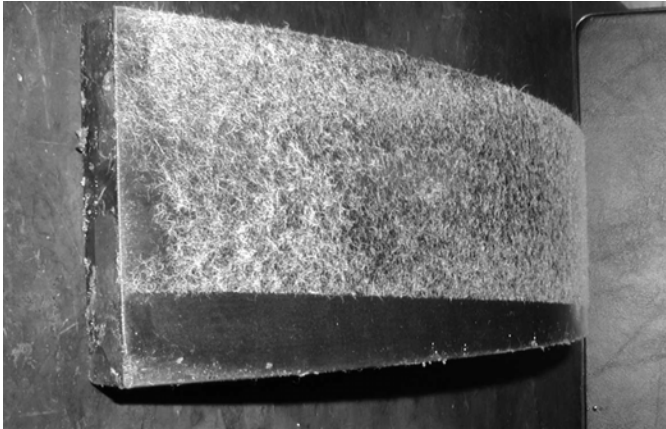


Figure 5.14: Picture of picking on a sticky coupon.



Figure 5.15: Picture of picking on a non-sticky coupon.

5.4 WADS summary

The results found from the WADS show that a significant production improvement can be expected if the tack of the surface of a dryer can is reduced. The reduction in tack

studied here is due to substrate effects that have been characterized in chapter two of this work. It has been shown that a sheet with higher solids content sticks to a metal surface that is contaminated with a polymer film much more than a sheet with lower solids. This is primarily due to the role water plays in disrupting the ability of the sheet to form an intimate bond with the polymer surface.

A relationship between peel point and work of adhesion has also been introduced. A lower value for the peel point indicates a lack of ability for the sheet to release from the metal surface. This coincides with higher work of adhesion values and increased problems in a production environment.

Use of the non-sticky surface in these experiments showed a reduction between 60-80% in the work of adhesion measured for the sheet peel on the WADS. The same coupon change increased the peel angle an average of 10%.

5.5 Conclusions

Literature analysis has determined that polyacrylate-based adhesives lead to problematic stickies in the paper-making process. Additionally, little work has been done regarding the interactions of stickies in the dryer section of a paper machine and specifically how the stickies form polymer films on the metal surfaces of dryer cans.

The work presented in this thesis is based on the unexpected finding that when a polyacrylate adhesive is placed on a carbon steel surface, it is not sticky. This is in contrast to the expected reaction for a pressure sensitive adhesive and does not correspond with placing the same adhesive on stainless steel, which produces a sticky film.

A number of surface characterization techniques were used to investigate the differences between the films. The tack was quantified with a probe-type tack test that shows the film on stainless steel to have 10x the tack of the film on carbon steel. The surface energy is shown to be 15% greater for the film on carbon steel. This difference is due to a much higher (3x) contribution from the polar surface energy components. AFM results show that the film on carbon steel has 3x the roughness of the film on stainless steel. In addition to the very smooth surface on stainless steel, the phase shift distribution is very uniform. The phase shift is sensitive to soft, attractive materials and the combination of the topography and phase shift images show a segregation of soft material in the valleys of the film. The combination of increased roughness, the inaccessibility of the soft material to a contacting surface and the higher surface energy accounts for the lower tack values found on the carbon steel surface.

Carbon-based components present in carbon steel have a much lower thermal conductivity than the iron that makes up the bulk of the material. This difference leads to temperature gradients within the plane of the metal surface. These temperature

differences are measured with IR thermography and are also modeled with a 2-D finite element technique that shows temperature differences of 7 °C are possible.

These temperature gradients often lead to Marangoni convection, which has been reported to cause roughness variations and surface defects in polymer films. The Marangoni numbers for films on carbon steel are 30%-50% higher than those on stainless steel. These elevated Marangoni numbers signify a propensity for increased surface driven flow, which leads to the differences in surface topology between the films as measured by AFM. The films used in this study are two orders of magnitude thinner than films that would experience buoyancy effects from the temperature gradients, which further implicates Marangoni convection as a driving force for the differences in film surface properties.

Marangoni convection was induced in films placed on stainless steel by interrupting the heat transfer at the metal by marking the surface with an ink pen. The resultant non-uniform temperature profile produced a Marangoni number greater than the Marangoni number for unmarked stainless steel. Also, the final film of the marked surface was rougher than the film on stainless steel.

The effect of the reduced tack discussed throughout this thesis on the operation of a dryer can was evaluated with the WADS. The results indicate a six to eightfold increase in the work of adhesion measured as a sheet of paper is removed from a sticky stainless steel surface as compared to the less sticky carbon steel surface. The sticky surface also

released the sheet an average of 8° later, which would lead to uneven tension on the sheet of paper as it dries.

In summary, the non-uniform heat transfer that develops from the various poor-conducting constituents in carbon steel leads to temperature gradients in the drying polymer film. The temperature gradients drive Marangoni convection, which leads to increased film roughness. This increased roughness ultimately results in a reduction of the adhesive's tack. Understanding the role of the substrate properties on film development can lead to improved efficiency of industrial applications.

5.6 *Future work*

The research presented in this thesis could serve as a springboard into new research that can attempt to apply the phenomena discussed in this work to improve current techniques in a number of areas and to further understand the role of surface properties on the development of surface driven flow.

A study to determine the role of the size, composition and spacing of lower-conducting materials in a metal composite on the development of surface driven flow could utilize current etching and deposition technology from the semi-conductor industry. The results of this work could leverage surface driven flow phenomena to develop polymer films with specific structures that would impact the optical, hydrophobic and adsorption properties of the films.

The development of self-leveling films could be realized by taking advantage of the ability of surface driven flow to move material away from the warmer regions of the film. An external heat source such as a laser could provide the heat or the heat could be associated with a chemical or physical reaction taking place in the film.

APPENDIX A – AFM DATA

The images and data contained in this appendix have been gathered with the MFP-3D Atomic Force Microscope (AFM) manufactured by Asylum Research (Santa Barbara, CA). AC240TS silicon tips from Olympus operated in tapping mode were used for all of the AFM work. The images presented in this appendix correspond to the data shown on the page following the images for each sample. The images are the result of a second order flattening, which produces minimal numerical smoothing to the image. Attempts were made to keep the scales of the images as similar as possible to allow direct comparisons of the images, but in certain cases this led to very nondescript images so the scales on the images were adjusted to elucidate the features of the images.

The images were each gathered at over 262,000 pixels (512x512) and the Q factor corresponds to each pixel being the average of nearly 1,000 measurements. The coefficient of variation (COV) values presented for the phase shift data were calculated by dividing the standard deviation (Stdev) of the values of the pixels in the image by the average (Avg) value of all of the pixels. The flatten-0, 1, 2, and 3 correspond to order of the polynomial used in the numerical flattening that serves to eliminate issues with unevenly loaded samples (flatten-0 and flatten-1) and proceeds to perform numerical smoothing to eliminate unnatural features from the image that are commonly attributed to artifacts. Flatten-NF is the original, unprocessed image. The roughness values are the root mean square (RMS) values of the height data found from the scans. Light tapping ($A_{sp}/A_o \sim 0.7$) was used so not to damage the surface of the polymer during the measurement and

also to avoid causing damage to the AFM tip, which could result from sticking to the surface. A_{sp} is the amplitude set point and A_o is the free amplitude of the cantilever and was small for this experiment.

Images are presented for three size scans, which are square images of 5 μm , 25 μm , and 75 μm on a side. Data is presented for the three listed above and also for 10 μm and 50 μm scans in the tables that follow each set of images.

PSA on Carbon Steel – Low Temperature

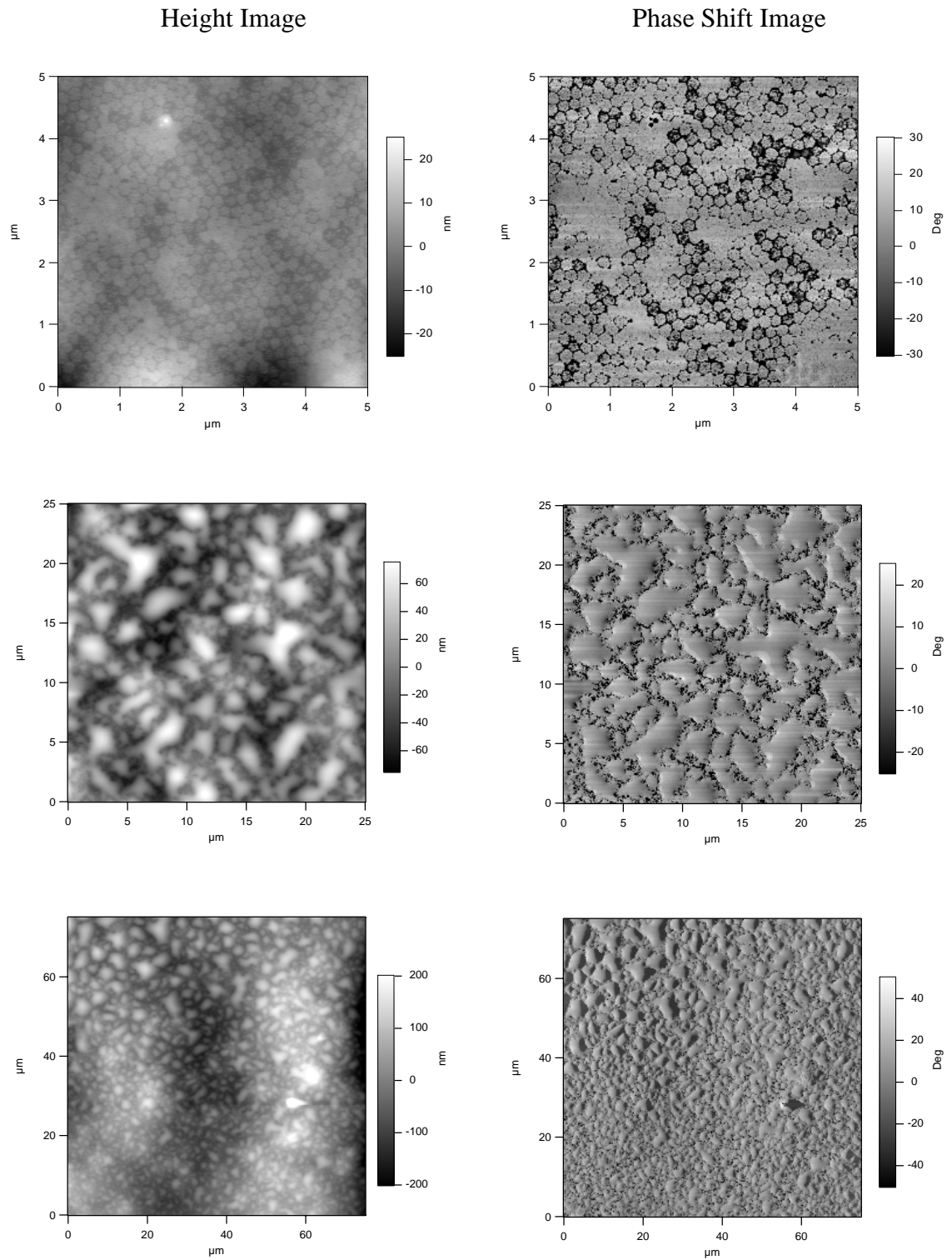


Figure A.1: AFM images of PSA on carbon steel dried at low temperature.

Table A.1: AFM roughness data for PSA on carbon steel dried at low temperature.

PSA on Carbon Steel Low Temperature RMS roughness (nm)						
Scan Size	1	5	10	25	50	75
Flatten -NF	11.0	24.0	30.0	47.9	92.1	125.3
Flatten -1	4.1	14.2	22.4	39.0	66.6	73.4
Flatten -2	2.2	7.9	20.8	23.7	36.9	53.8
Flatten -3	1.9	6.3	14.9	20.1	31.8	45.3

Table A.2: AFM phase shift data for PSA on carbon steel dried at low temperature.

PSA on Carbon Steel Low Temperature Phase Shift (degrees)									
Scan Size	1			5			10		
	Avg	Stdev	COV	Avg	Stdev	COV	Avg	Stdev	COV
Flatten -NF	107.6	13.4	0.1241	107.1	12.9	0.1206	107.6	12.5	0.1164
Flatten -1		12.6	0.1172		12.4	0.1154		12.2	0.1136
Flatten -2		11.8	0.1092		12.3	0.1148		12.1	0.1127
Flatten -3		11.3	0.1048		12.2	0.1140		12.0	0.1110

Scan Size	25			50			75		
	Avg	Stdev	COV	Avg	Stdev	COV	Avg	Stdev	COV
Flatten -NF	106.8	12.2	0.1143	106.2	12.4	0.1171	104.1	13.8	0.1324
Flatten -1		11.8	0.1110		12.2	0.1148		12.0	0.1152
Flatten -2		11.8	0.1104		12.1	0.1143		11.9	0.1143
Flatten -3		11.7	0.1099		12.1	0.1137		11.8	0.1136

PSA on Carbon Steel – Medium
Temperature

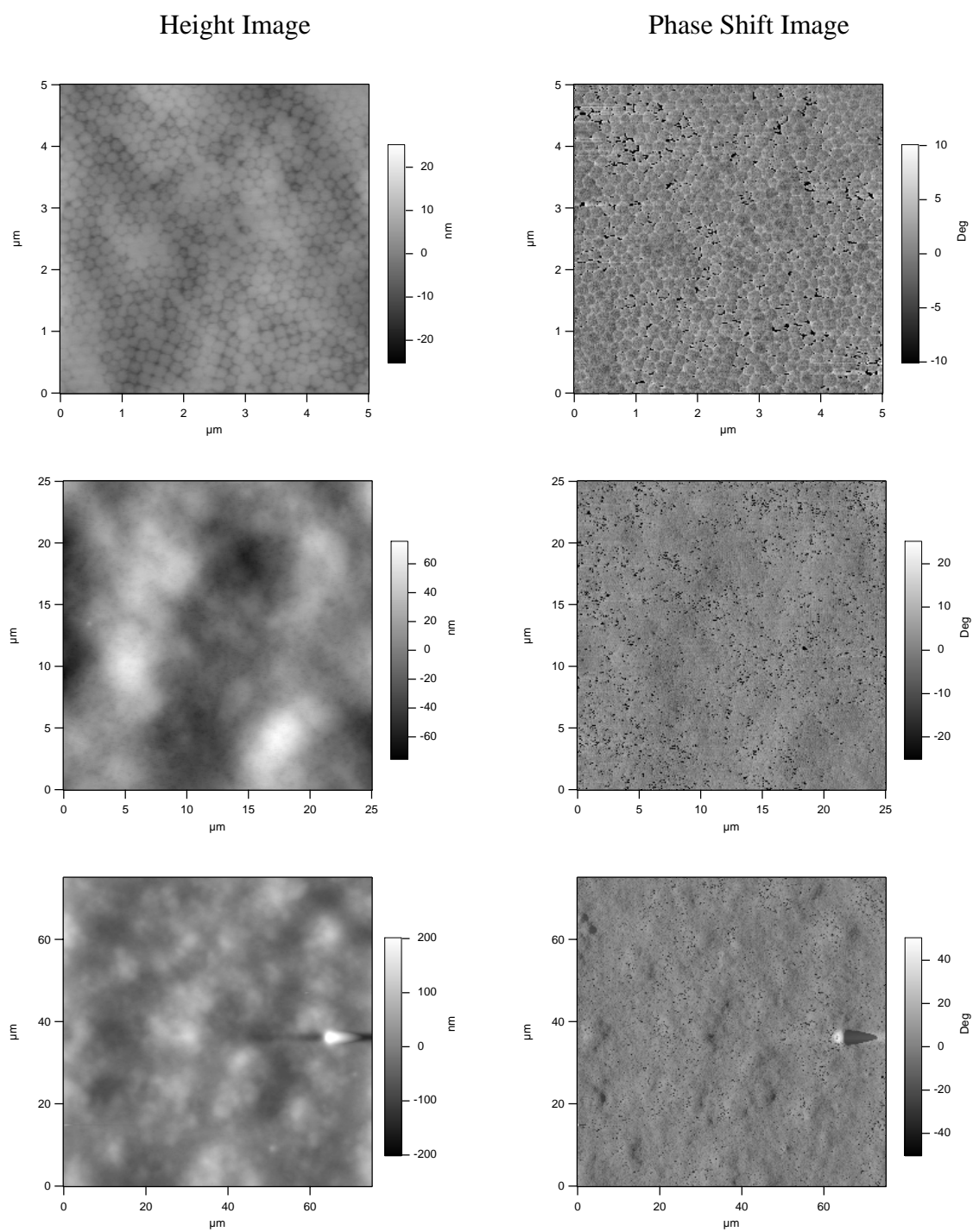


Figure A.2: AFM images of PSA on carbon steel dried at medium temperature.

Table A.3: AFM roughness data for PSA on carbon steel dried at medium temperature.

PSA on Carbon Steel Medium Temperature RMS roughness (nm)						
Scan Size	1	5	10	25	50	75
Flatten -NF	13.3	21.6	19.2	53.4	90.9	132.0
Flatten -1	2.1	7.5	14.0	39.9	50.6	54.4
Flatten -2	1.7	5.7	9.0	19.1	29.8	41.9
Flatten -3	1.4	4.5	7.9	16.9	22.3	32.7

Table A.4: AFM phase shift data for PSA on carbon steel dried at medium temperature.

PSA on Carbon Steel Medium Temperature Phase Shift (degrees)									
Scan Size	1			5			10		
	Avg	Stdev	COV	Avg	Stdev	COV	Avg	Stdev	COV
Flatten -NF	88.6	8.6	0.0967	91.8	9.1	0.0993	93.1	9.0	0.0966
Flatten -1		8.1	0.0916		8.6	0.0932		8.6	0.0928
Flatten -2		7.7	0.0871		8.4	0.0920		8.5	0.0910
Flatten -3		7.3	0.0829		8.3	0.0901		8.4	0.0898

Scan Size	25			50			75		
	Avg	Stdev	COV	Avg	Stdev	COV	Avg	Stdev	COV
Flatten -NF	99.9	15.8	0.1579	98.1	16.3	0.1665	92.9	16.1	0.1732
Flatten -1		15.6	0.1557		16.1	0.1643		15.9	0.1710
Flatten -2		15.5	0.1547		16.0	0.1636		15.8	0.1701
Flatten -3		15.4	0.1541		16.0	0.1629		15.7	0.1691

PSA on Carbon Steel – High Temperature

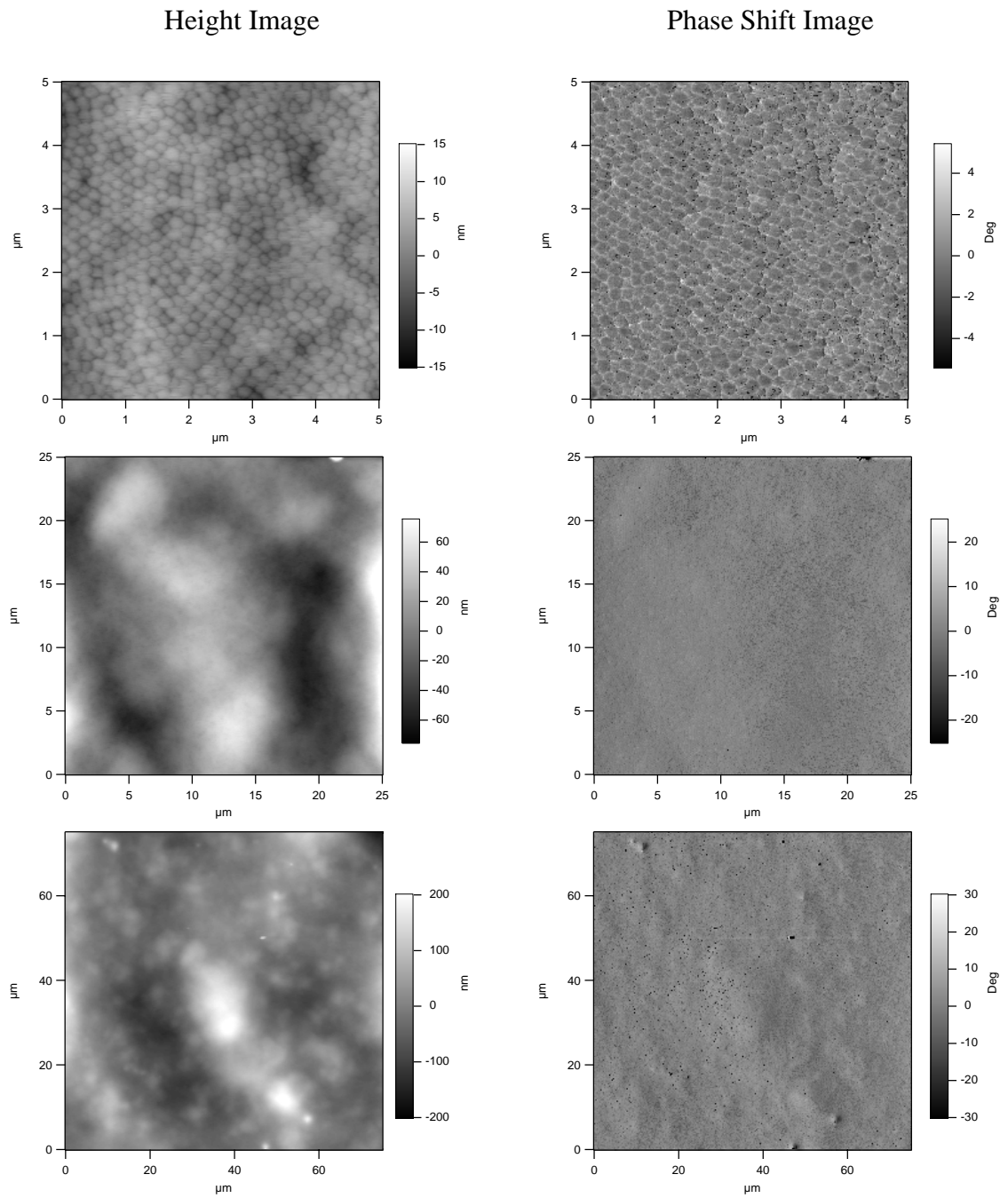


Figure A.3: AFM images of PSA on carbon steel dried at high temperature.

Table A.5: AFM roughness data for PSA on carbon steel dried at high temperature.

PSA on Carbon Steel High Temperature RMS roughness (nm)						
Scan Size	1	5	10	25	50	75
Flatten -NF	7.0	18.7	37.9	111.7	146.1	276.7
Flatten -1	1.8	11.8	25.9	77.2	132.6	204.8
Flatten -2	1.4	4.4	12.8	47.0	47.8	81.4
Flatten -3	1.3	2.5	6.8	32.4	42.0	62.8

Table A.6: AFM phase shift data for PSA on carbon steel dried at high temperature.

PSA on Carbon Steel High Temperature Phase Shift (degrees)									
Scan Size	1			5			10		
	Avg	Stdev	COV	Avg	Stdev	COV	Avg	Stdev	COV
Flatten -NF	126.5	0.9	0.0069	127.0	1.1	0.0083	127.8	1.4	0.0112
Flatten -1		0.8	0.0063		1.0	0.0079		1.3	0.0104
Flatten -2		0.8	0.0061		1.0	0.0078		1.3	0.0102
Flatten -3		0.8	0.0060		1.0	0.0077		1.3	0.0101

Scan Size	25			50			75		
	Avg	Stdev	COV	Avg	Stdev	COV	Avg	Stdev	COV
Flatten -NF	127.7	3.0	0.0237	125.7	4.4	0.0346	125.1	5.1	0.0408
Flatten -1		2.8	0.0221		3.9	0.0308		4.7	0.0376
Flatten -2		2.7	0.0214		3.8	0.0303		4.6	0.0368
Flatten -3		2.6	0.0207		3.7	0.0297		4.6	0.0364

PSA on Stainless Steel – Low Temperature

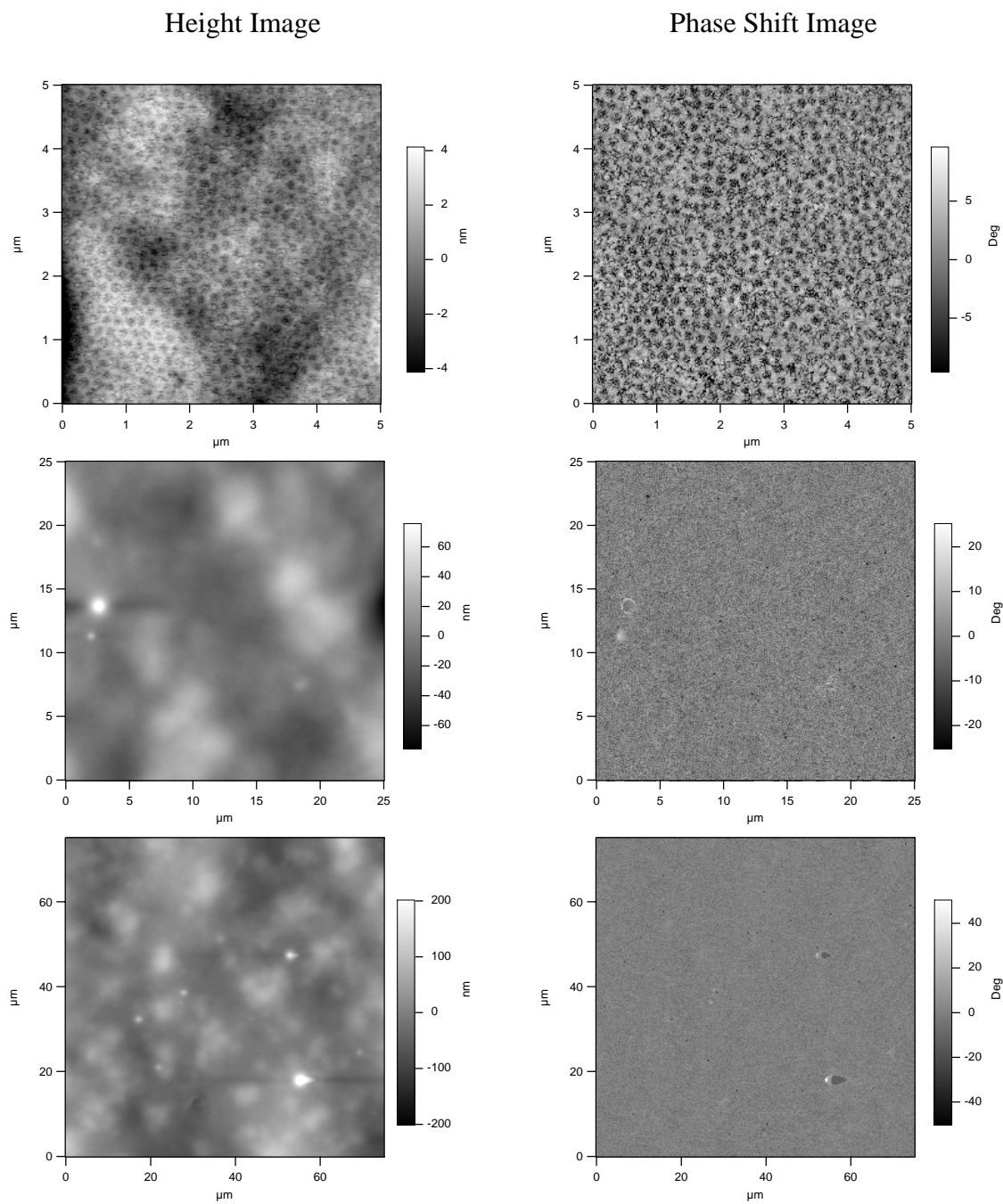


Figure A.4: AFM images of PSA on stainless steel dried at low temperature.

Table A.7: AFM roughness data for PSA on stainless steel dried at low temperature.

PSA on Stainless Steel Low Temperature RMS roughness (nm)						
Scan Size	1	5	10	25	50	75
Flatten -NF	8.2	7.2	14.5	33.7	56.3	80.1
Flatten -1	4.2	3.3	9.3	26.4	38.0	56.6
Flatten -2	2.1	2.1	4.3	18.8	30.3	46.8
Flatten -3	1.5	1.5	3.0	12.7	27.5	40.7

Table A.8: AFM phase shift data for PSA on stainless steel dried at low temperature.

PSA on Stainless Steel Low Temperature Phase Shift (degrees)									
Scan Size	1			5			10		
	Avg	Stdev	COV	Avg	Stdev	COV	Avg	Stdev	COV
Flatten -NF	103.6	7.4	0.0715	118.2	2.5	0.0215	117.8	2.9	0.0246
Flatten -1		6.1	0.0588		2.4	0.0204		2.8	0.0235
Flatten -2		5.9	0.0569		2.4	0.0203		2.7	0.0233
Flatten -3		5.7	0.0547		2.4	0.0201		2.7	0.0232

Scan Size	25			50			75		
	Avg	Stdev	COV	Avg	Stdev	COV	Avg	Stdev	COV
Flatten -NF	114.5	2.7	0.0238	115.0	2.7	0.0230	116.0	3.0	0.0259
Flatten -1		2.6	0.0229		2.6	0.0224		2.9	0.0253
Flatten -2		2.6	0.0227		2.6	0.0223		2.9	0.0251
Flatten -3		2.6	0.0226		2.5	0.0221		2.9	0.0250

PSA on Stainless Steel – Medium
Temperature

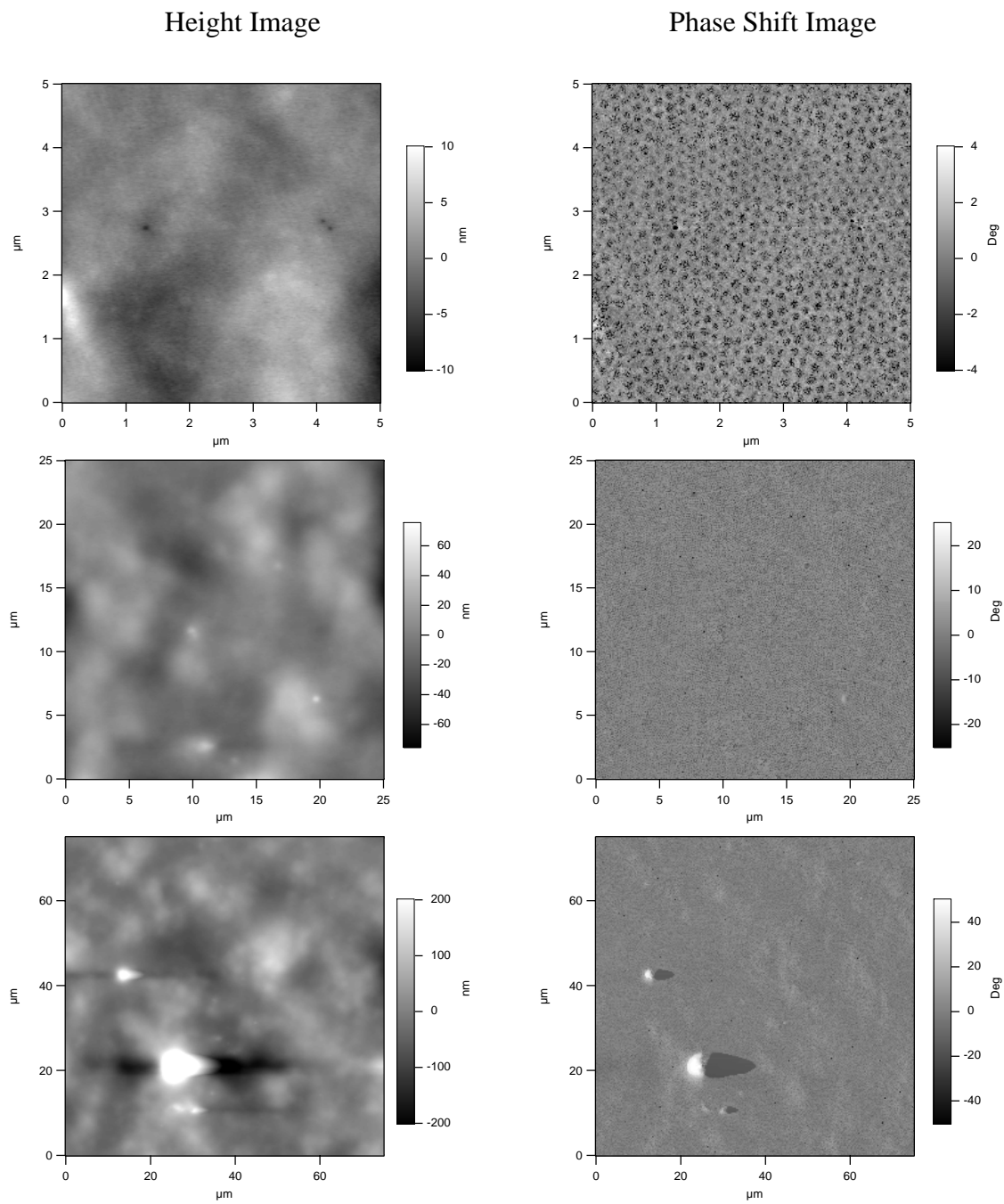


Figure A.5: AFM images of PSA on stainless steel dried at medium temperature.

Table A.9: AFM roughness data for PSA on stainless steel dried at medium temperature.

PSA on Stainless Steel Medium Temperature RMS roughness (nm)						
Scan Size	1	5	10	25	50	75
Flatten -NF	5.2	8.0	15.7	37.3	62.2	73.6
Flatten -1	1.4	3.8	8.2	24.2	51.8	54.6
Flatten -2	0.8	2.1	5.9	12.2	43.8	37.6
Flatten -3	0.5	1.1	3.2	9.7	34.1	34.2

Table A.10: AFM phase shift data for PSA on stainless steel dried at medium temperature.

PSA on Stainless Steel Medium Temperature Phase Shift (degrees)									
Scan Size	1			5			10		
	Avg	Stdev	COV	Avg	Stdev	COV	Avg	Stdev	COV
Flatten -NF	104.0	1.6	0.0154	104.1	1.4	0.0132	104.4	1.3	0.0127
Flatten -1		1.6	0.0150		1.3	0.0129		1.3	0.0124
Flatten -2		1.5	0.0148		1.3	0.0129		1.3	0.0122
Flatten -3		1.5	0.0146		1.3	0.0128		1.3	0.0122

Scan Size	25			50			75		
	Avg	Stdev	COV	Avg	Stdev	COV	Avg	Stdev	COV
Flatten -NF	104.6	2.3	0.0219	90.4	4.8	0.0531	92.4	3.8	0.0406
Flatten -1		2.2	0.0214		4.6	0.0505		3.7	0.0398
Flatten -2		2.2	0.0213		4.5	0.0502		3.7	0.0396
Flatten -3		2.2	0.0212		4.5	0.0498		3.7	0.0395

PSA on Stainless Steel – High Temperature

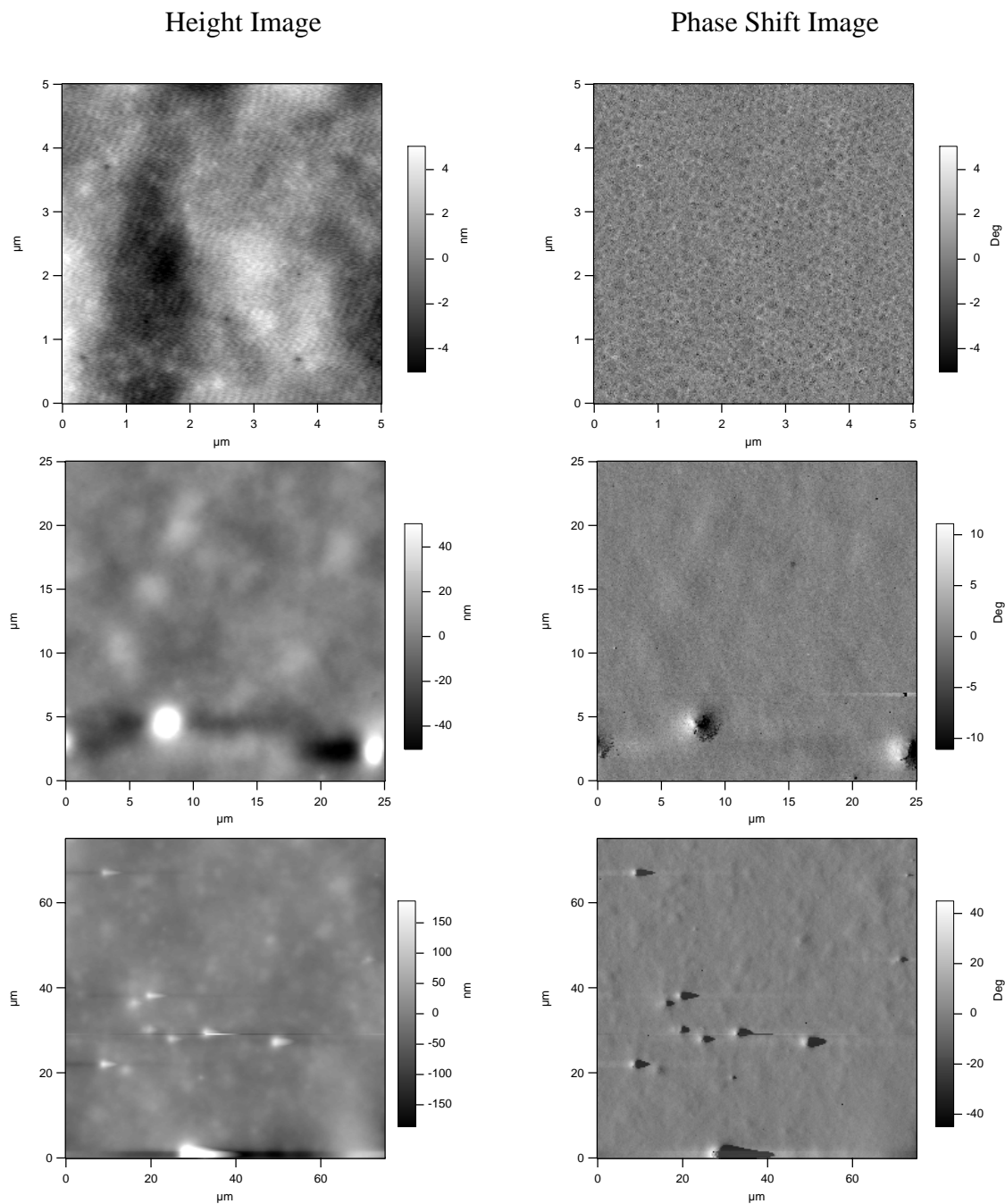


Figure A.6: AFM images of PSA on stainless steel dried at high temperature.

Table A.11: AFM roughness data for PSA on stainless steel dried at high temperature.

PSA on Stainless Steel High Temperature RMS roughness (nm)						
Scan Size	1	5	10	25	50	75
Flatten -NF	7.6	2.8	6.5	21.0	25.5	51.4
Flatten -1	0.5	2.0	4.8	16.1	19.5	35.6
Flatten -2	0.4	1.5	2.3	13.3	14.6	24.2
Flatten -3	0.4	1.1	2.1	11.7	12.6	20.2

Table A.12: AFM phase shift data for PSA on stainless steel dried at high temperature.

PSA on Stainless Steel High Temperature Phase Shift (degrees)									
Scan Size	1			5			10		
	Avg	Stdev	COV	Avg	Stdev	COV	Avg	Stdev	COV
Flatten -NF	104.3	0.8	0.0079	104.3	1.0	0.0096	107.7	1.0	0.0090
Flatten -1		0.8	0.0077		0.9	0.0090		1.0	0.0091
Flatten -2		0.8	0.0077		0.9	0.0090		1.0	0.0090
Flatten -3		0.8	0.0076		0.9	0.0089		1.0	0.0090

Scan Size	25			50			75		
	Avg	Stdev	COV	Avg	Stdev	COV	Avg	Stdev	COV
Flatten -NF	107.5	1.6	0.0150	118.1	2.7	0.0229	117.5	3.1	0.0265
Flatten -1		1.6	0.0144		2.0	0.0169		3.0	0.0253
Flatten -2		1.5	0.0142		2.0	0.0167		2.9	0.0246
Flatten -3		1.5	0.0136		2.0	0.0166		2.9	0.0243

PSA on Marked Stainless Steel – Low Temperature

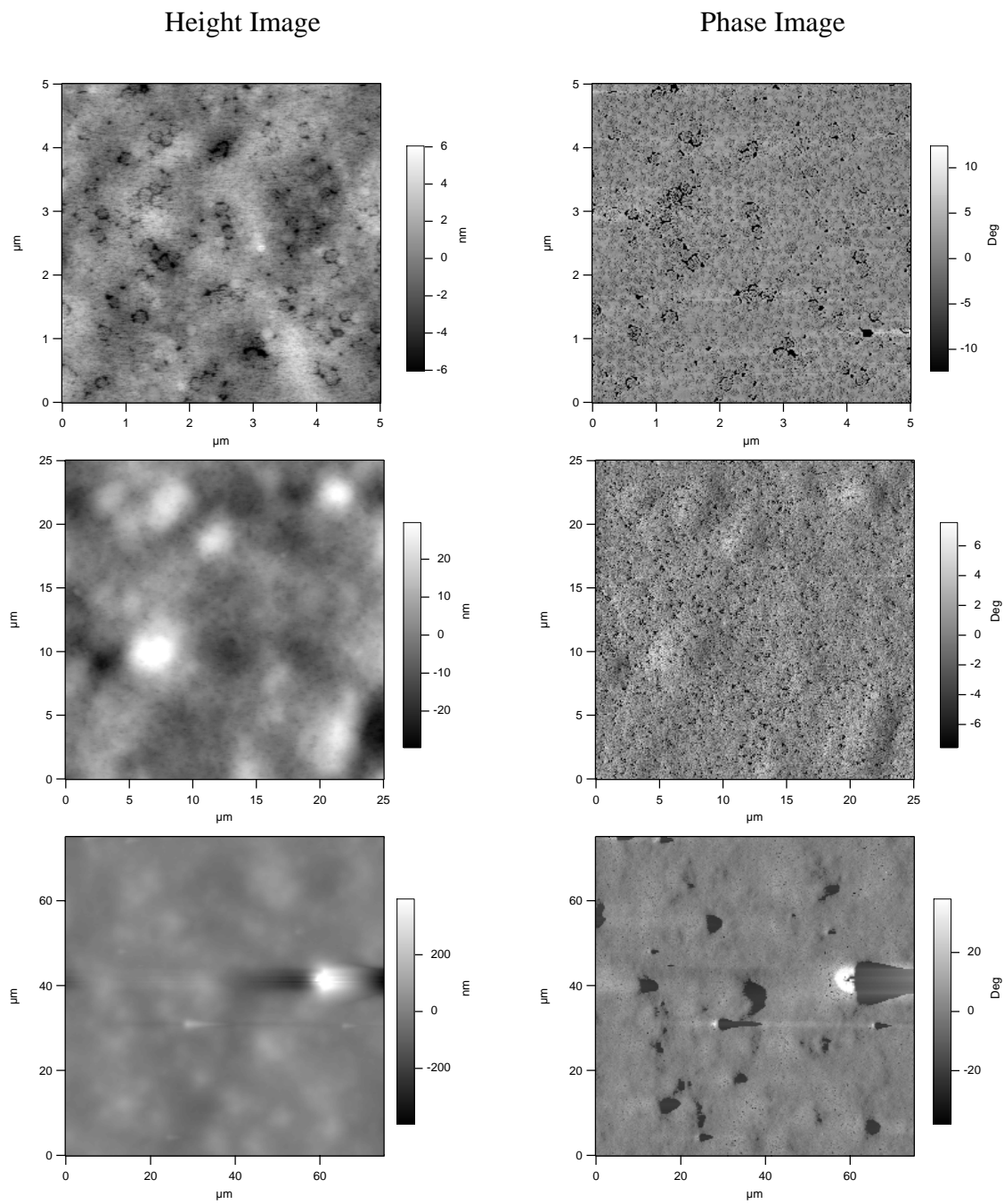


Figure A.7: AFM images of PSA on marked stainless steel dried at low temperature.

Table A.13: AFM roughness data for PSA on marked stainless steel dried at low temperature.

PSA on Marked Stainless Steel Low Temperature RMS roughness (nm)						
Scan Size	1	5	10	25	50	75
Flatten -NF	7.0	4.8	11.8	26.1	92.7	144.4
Flatten -1	1.4	4.1	8.7	19.7	55.3	91.0
Flatten -2	1.3	2.1	5.1	15.7	32.3	84.9
Flatten -3	1.2	1.5	3.1	11.7	21.9	64.7

Table A.14: AFM phase shift data for PSA on marked stainless steel dried at low temperature.

PSA on Marked Stainless Steel Low Temperature Phase Shift (degrees)									
Scan Size	1			5			10		
	Avg	Stdev	COV	Avg	Stdev	COV	Avg	Stdev	COV
Flatten -NF	102.4	5.6	0.0544	103.8	5.4	0.0516	102.1	5.5	0.0534
Flatten -1		5.2	0.0512		5.3	0.0509		5.4	0.0525
Flatten -2		5.1	0.0502		5.3	0.0506		5.3	0.0522
Flatten -3		5.0	0.0487		5.2	0.0501		5.3	0.0520

Scan Size	25			50			75		
	Avg	Stdev	COV	Avg	Stdev	COV	Avg	Stdev	COV
Flatten -NF	104.9	4.1	0.0394	110.3	5.0	0.0449	108.5	7.2	0.0664
Flatten -1		4.1	0.0390		4.7	0.0425		6.9	0.0639
Flatten -2		4.1	0.0388		4.6	0.0422		6.5	0.0601
Flatten -3		4.1	0.0387		4.6	0.0415		6.3	0.0577

PSA on Marked Stainless Steel – Medium Temperature

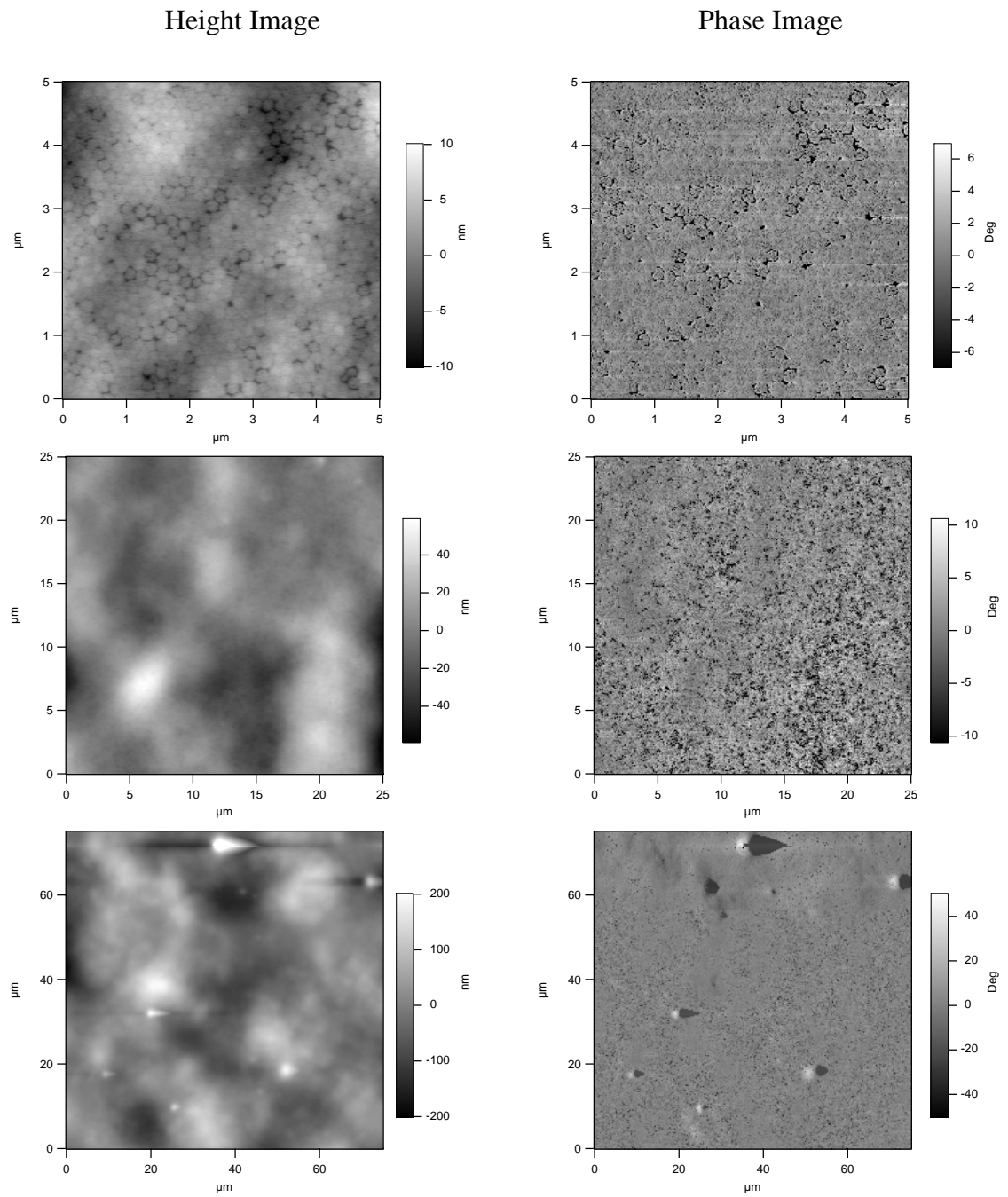


Figure A.8: AFM images of PSA on marked stainless steel dried at medium temperature.

Table A.15: AFM roughness data for PSA on marked stainless steel dried at medium temperature.

PSA on Marked Stainless Steel Medium Temperature RMS roughness (nm)						
Scan Size	1	5	10	25	50	75
Flatten -NF	5.8	9.4	19.3	50.6	75.2	87.9
Flatten -1	1.2	4.8	13.6	30.7	48.2	56.6
Flatten -2	1.1	3.8	9.7	18.2	33.1	45.4
Flatten -3	1.0	1.9	4.6	15.9	28.8	37.6

Table A.16: AFM phase shift data for PSA on marked stainless steel dried at medium temperature.

PSA on Marked Stainless Steel Medium Temperature Phase Shift (degrees)									
Scan Size	1			5			10		
	Avg	Stdev	COV	Avg	Stdev	COV	Avg	Stdev	COV
Flatten-NF	102.2	3.4	0.0337	103.7	3.9	0.0374	104.6	4.3	0.0409
Flatten -1		3.2	0.0318		3.8	0.0366		4.2	0.0403
Flatten -2		3.2	0.0314		3.8	0.0364		4.2	0.0400
Flatten -3		3.1	0.0308		3.8	0.0362		4.2	0.0398

Scan Size	25			50			75		
	Avg	Stdev	COV	Avg	Stdev	COV	Avg	Stdev	COV
Flatten-NF	103.9	4.6	0.0447	105.1	4.4	0.0414	110.8	5.4	0.0490
Flatten -1		4.6	0.0441		4.2	0.0404		5.0	0.0455
Flatten -2		4.6	0.0440		4.2	0.0400		5.0	0.0451
Flatten -3		4.5	0.0438		4.2	0.0398		5.0	0.0447

PSA on Marked Stainless Steel – High Temperature

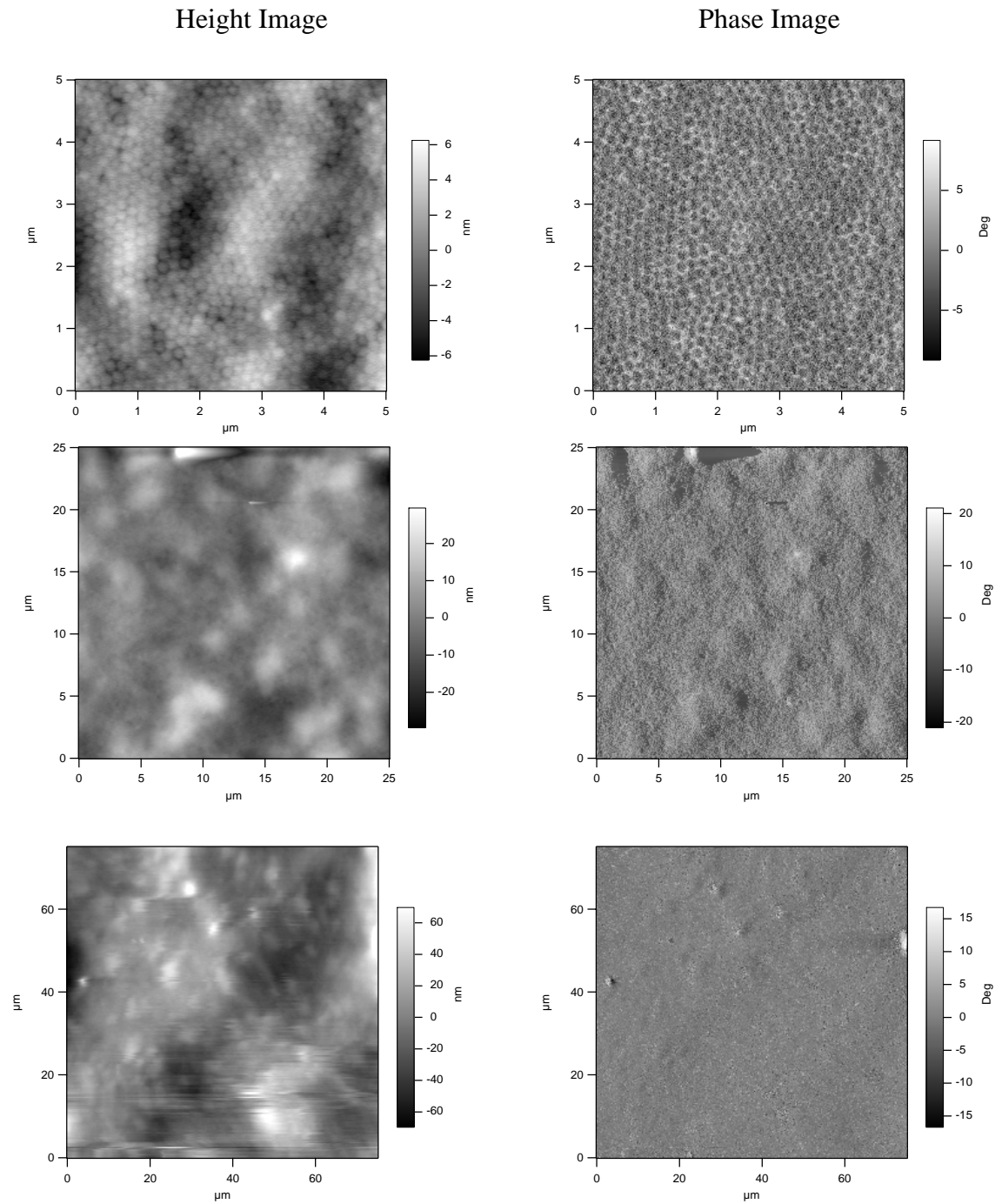


Figure A.9: AFM images of PSA on marked stainless steel dried at high temperature.

Table A.17: AFM roughness data for PSA on marked stainless steel dried at high temperature.

PSA on Marked Stainless Steel High Temperature RMS roughness (nm)						
Scan Size	1	5	10	25	50	75
Flatten -NF	7.2	9.5	9.6	22.7	35.2	52.3
Flatten -1	1.5	3.8	6.7	13.0	25.0	34.9
Flatten -2	0.7	1.6	2.8	6.2	10.9	19.2
Flatten -3	0.4	1.5	2.2	5.2	9.7	13.0

Table A.18: AFM phase shift data for PSA on marked stainless steel dried at high temperature.

PSA on Marked Stainless Steel High Temperature Phase Shift (degrees)									
Scan Size	1			5			10		
	Avg	Stdev	COV	Avg	Stdev	COV	Avg	Stdev	COV
Flatten -NF	92.4	2.2	0.0234	93.5	2.1	0.0223	95.9	2.6	0.0270
Flatten -1		2.1	0.0223		2.0	0.0217		2.5	0.0263
Flatten -2		2.0	0.0216		2.0	0.0216		2.5	0.0261
Flatten -3		2.0	0.0214		2.0	0.0214		2.5	0.0260

Scan Size	25			50			75		
	Avg	Stdev	COV	Avg	Stdev	COV	Avg	Stdev	COV
Flatten -NF	103.4	3.4	0.0331	107.5	3.0	0.0281	106.7	5.0	0.0467
Flatten -1		3.3	0.0321		2.9	0.0273		4.7	0.0437
Flatten -2		3.3	0.0319		2.9	0.0270		4.4	0.0412
Flatten -3		3.3	0.0317		2.9	0.0268		4.3	0.0403

APPENDIX B – WADS DATA

This appendix contains the data found with the WADS in experiments used to determine the effect of reducing the stickiness of a dryer can during operation of a paper machine.

The data includes the average and maximum tension values, graph of the tension vs. time, peel angle, peel point, weight of the sample, pictures from which the peel angle and peel point are found, and the results for the calculations to find the work of adhesion. Also included is a sample calculation.

Sample work calculation for 40% solids, sticky coupon experiment, using the average tension value (experiment 1-21-06):

$$W^{11} = (T^1 - mV_1^2) * (1 - \cos \phi)$$

Where, T^1 = Tension

W^{11} = Work of Adhesion

m = mass per unit area

V_1 = Velocity

ϕ = Peel Angle.

$$W^{11} = \left[\left(33.9 \frac{g}{cm} \right) - \left(0.25 \frac{g}{cm^2} \right) * \left(60.96 \frac{cm}{s} \right)^2 \div 981 \frac{cm}{s^2} \right] * (1 - \cos 30.9^\circ) = 4.67 \frac{g}{cm}$$

B.1 System Calibration

Calibration of the tension sensor was accomplished by measuring the response to a series of weights added to the sensor. The calibration curve is shown below.

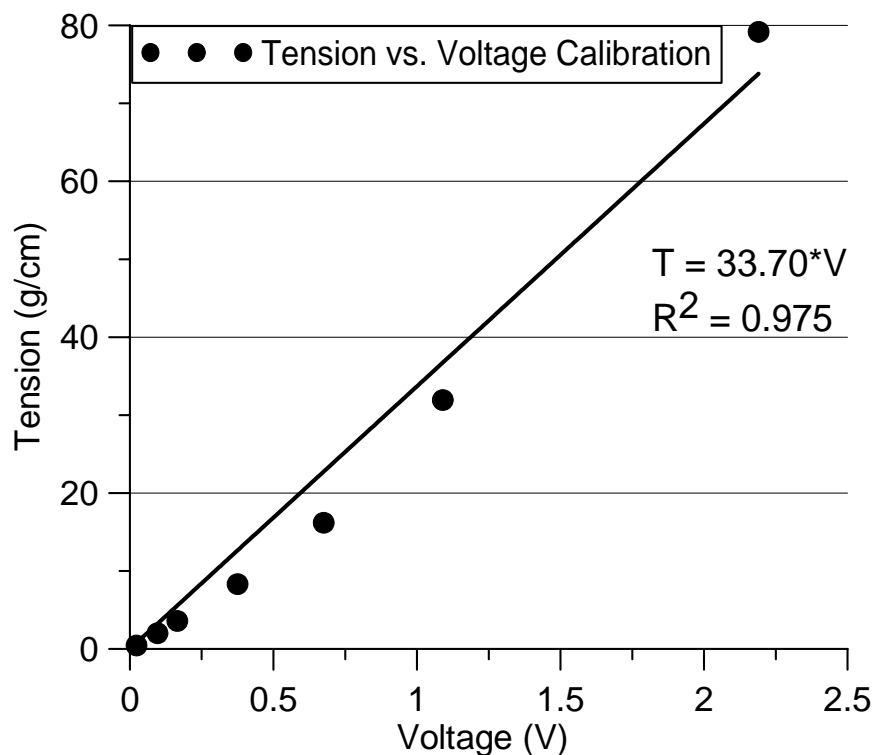


Figure B.1: Tension calibration data for WADS.

The effects of friction and the mass of the ribbon and sample were accounted for by measuring the voltage produced by the cantilever while the sample was retracted through the system. This plot is shown below. The average value found was 0.101 V, which is subtracted from the raw voltage data before the above equation ($T=33.70 * V$) is used.

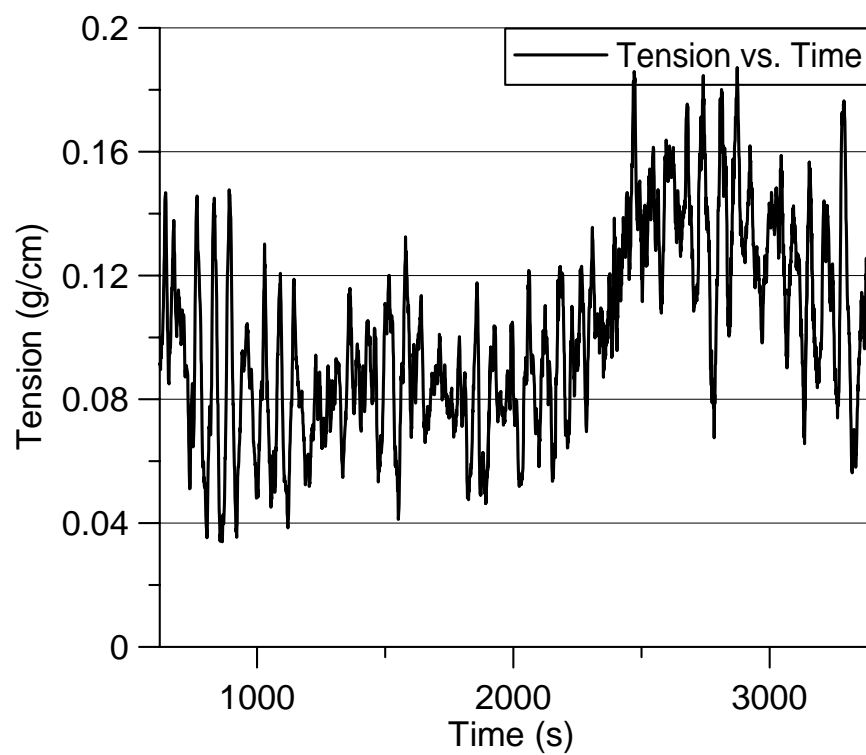


Figure B.2: Tension noise data from WADS.

40% Solids sticky coupon (Experiment #1-21-03)

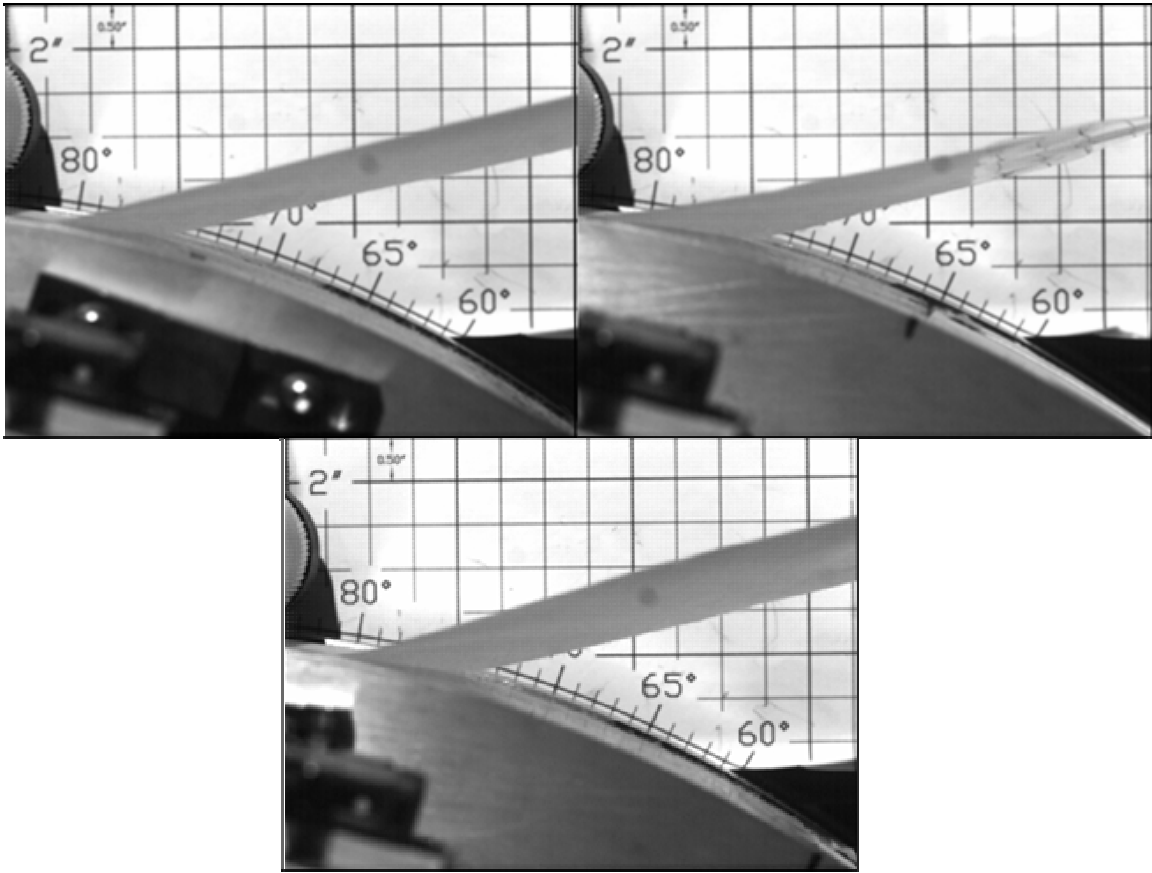


Figure B.3: Peeling images from 40% solids run on a sticky coupon (Experiment #1-21-03).

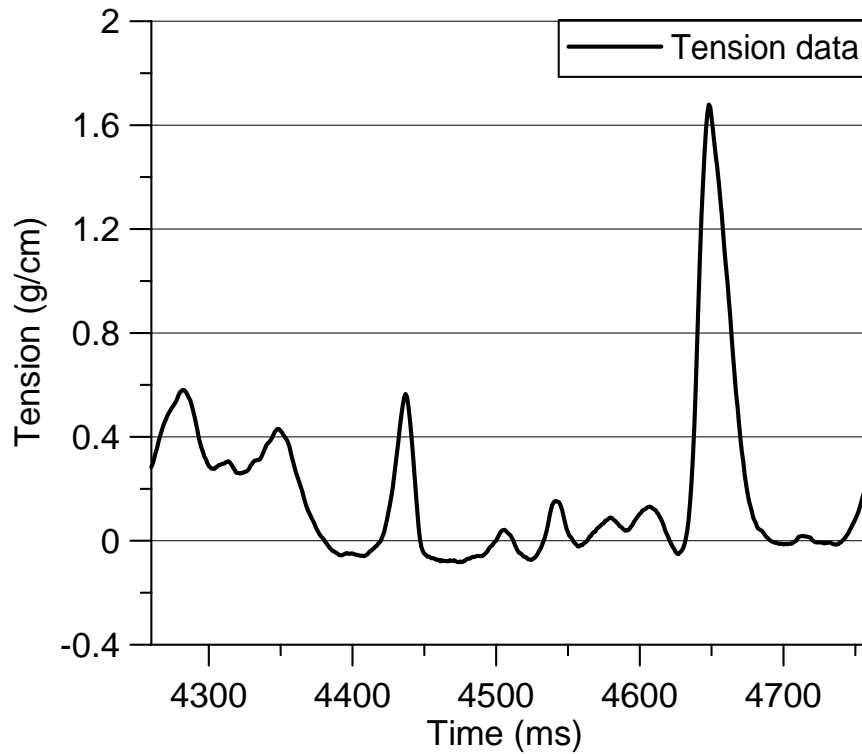


Figure B.4: Tension data from 40% solids run on a sticky coupon (Experiment #1-21-03).

Table B.1: WADS data from 40% solids run on a sticky coupon (Experiment #1-21-03).

% solids	40	WADS peel angle	20.237	Avg. Tension	6.0
weight (g/cm²)	0.25		18.423	Max Tension	56.6
Peel point 1	76		34.152	Mardon work (avg)	0.53
Peel point 2	74		25.334	Mardon work (max)	5.79
Peel point 3	74		28.566		
Peel point avg	74.7		33.473		
			23.844		
			22.688		
			30.616		
		Peel angle avg	26.4		
		Peel angle stdev	5.7		

40% Solids sticky coupon (Experiment #1-21-04)

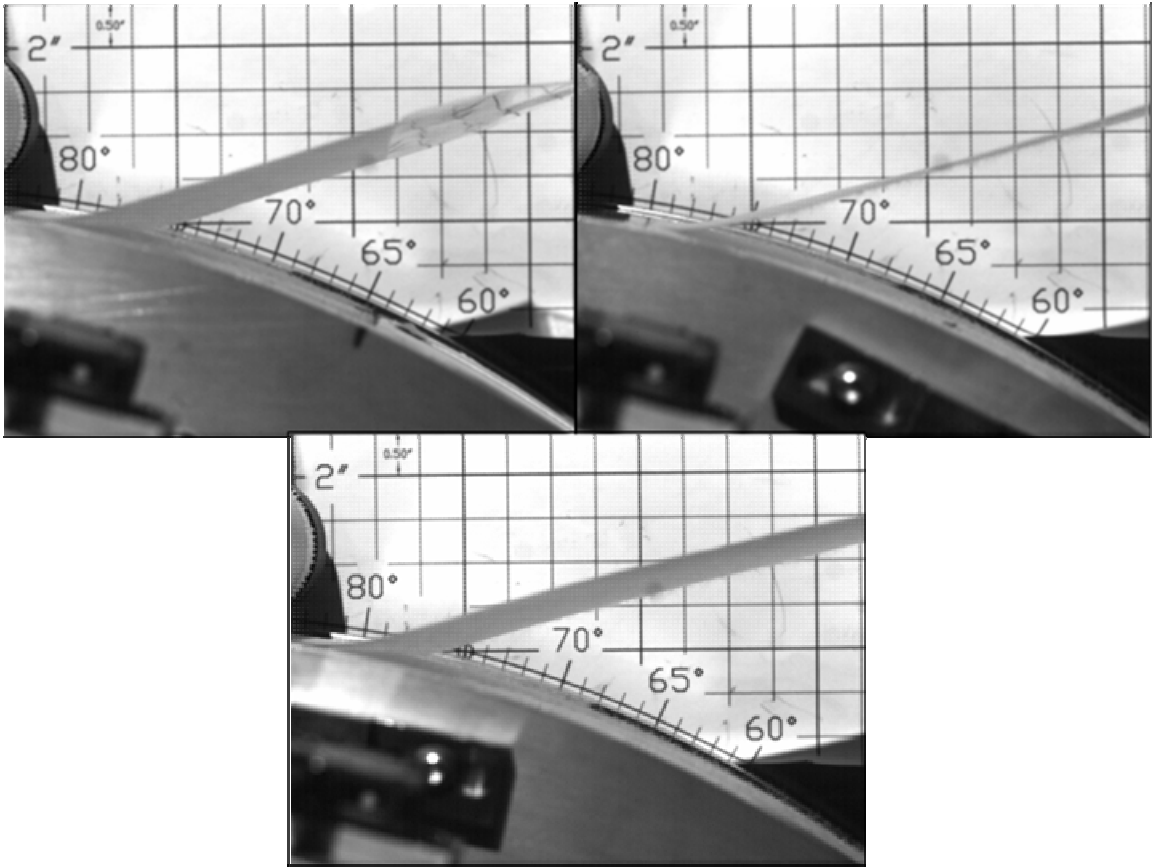


Figure B.5: Peeling images from 40% solids run on a sticky coupon (Experiment #1-21-04).

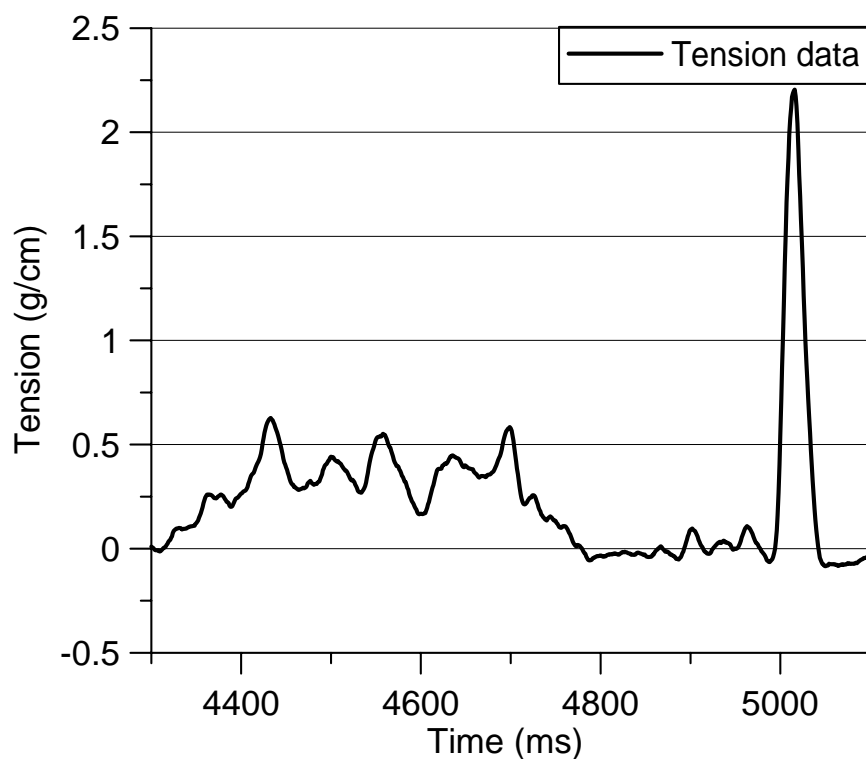


Figure B.6: Tension data from 40% solids run on a sticky coupon (Experiment #1-21-04).

Table B.2: WADS data from 40% solids run on a sticky coupon (Experiment #1-21-04).

% solids	40	WADS peel angle	26.558	Avg. Tension	8.1
weight (g/cm ²)	0.25		28.586	Max Tension	74.3
Peel point 1	75		26.315	Mardon work (avg)	0.88
Peel point 2	76		31.785	Mardon work (max)	9.1
Peel point 3	77		33.488		
Peel point avg	76.0		25.221		
			26.378		
			31.893		
		Peel angle avg	28.8		
		Peel angle stdev	3.2		

40% Solids sticky coupon (Experiment #1-21-05)

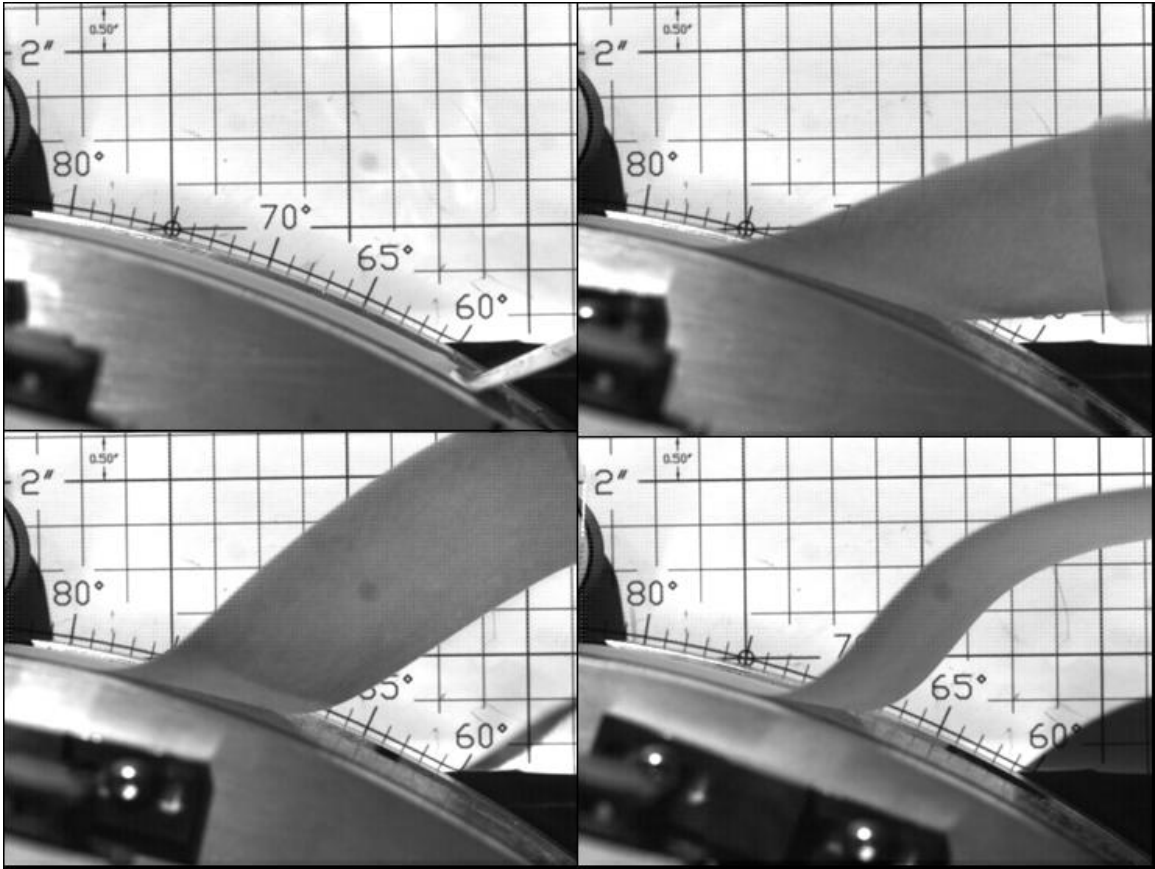


Figure B.7: Peeling images from 40% solids run on a sticky coupon (Experiment #1-21-05), part 1 (continued).

Pictures continued:

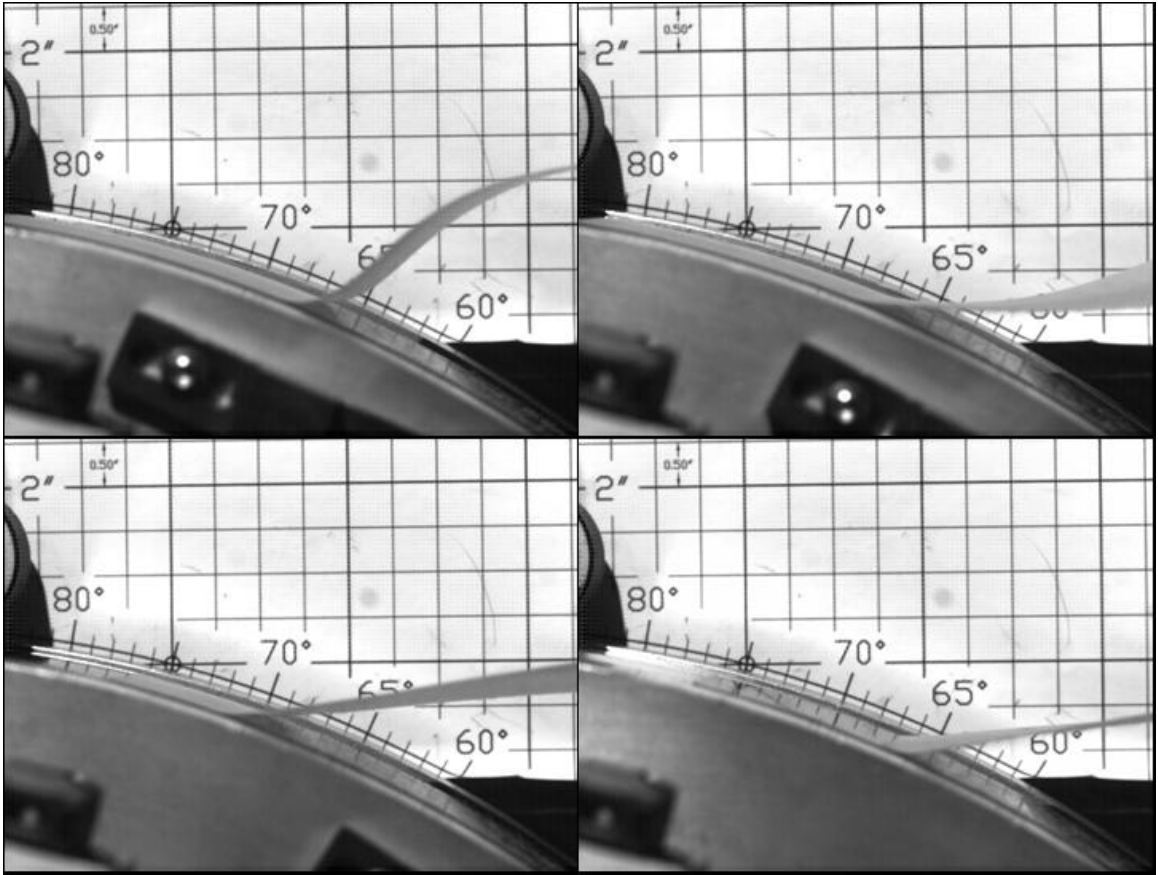


Figure B.8: Peeling images from 40% solids run on a sticky coupon (Experiment #1-21-05), part 2.

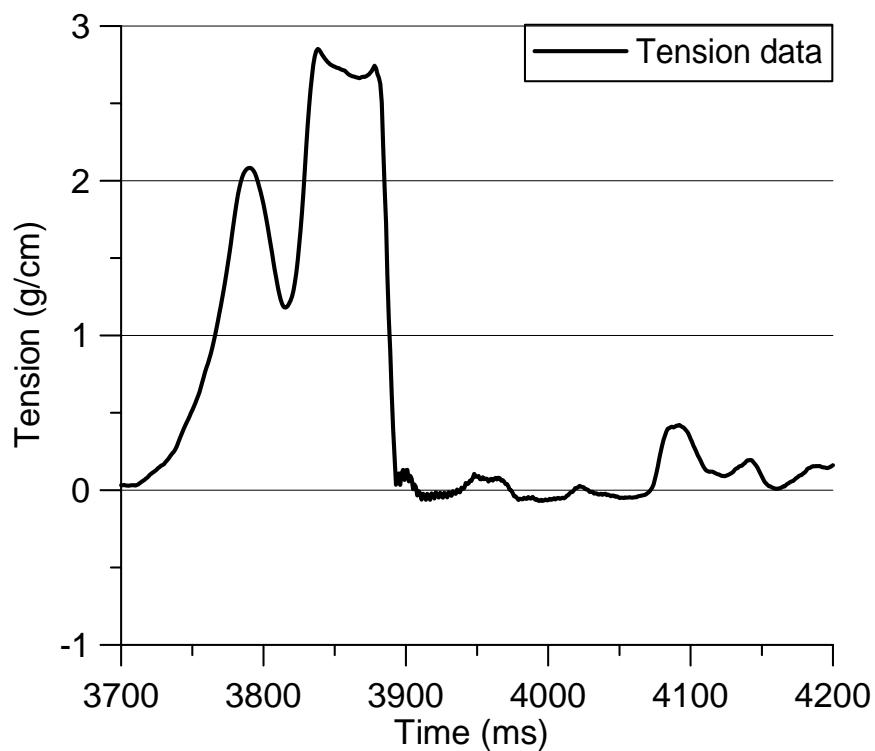


Figure B.9: Tension data from 40% solids run on a sticky coupon (Experiment #1-21-05).

Table B.3: WADS data from 40% solids run on a sticky coupon (Experiment #1-21-05).

% solids	40	WADS peel angle	48.489	Avg. Tension	20.0
weight (g/cm ²)	0.25		34.152	Max Tension	96.1
Peel point 1	66		29.686	Mardon work (avg)	2.82
Peel point 2	68		26.833	Mardon work (max)	14.1
Peel point 3	68		27.523		
Peel point avg	67.3		22.858		
		Peel angle avg	31.6		
		Peel angle stdev	9.1		

40% Solids sticky coupon (Experiment #1-21-06)

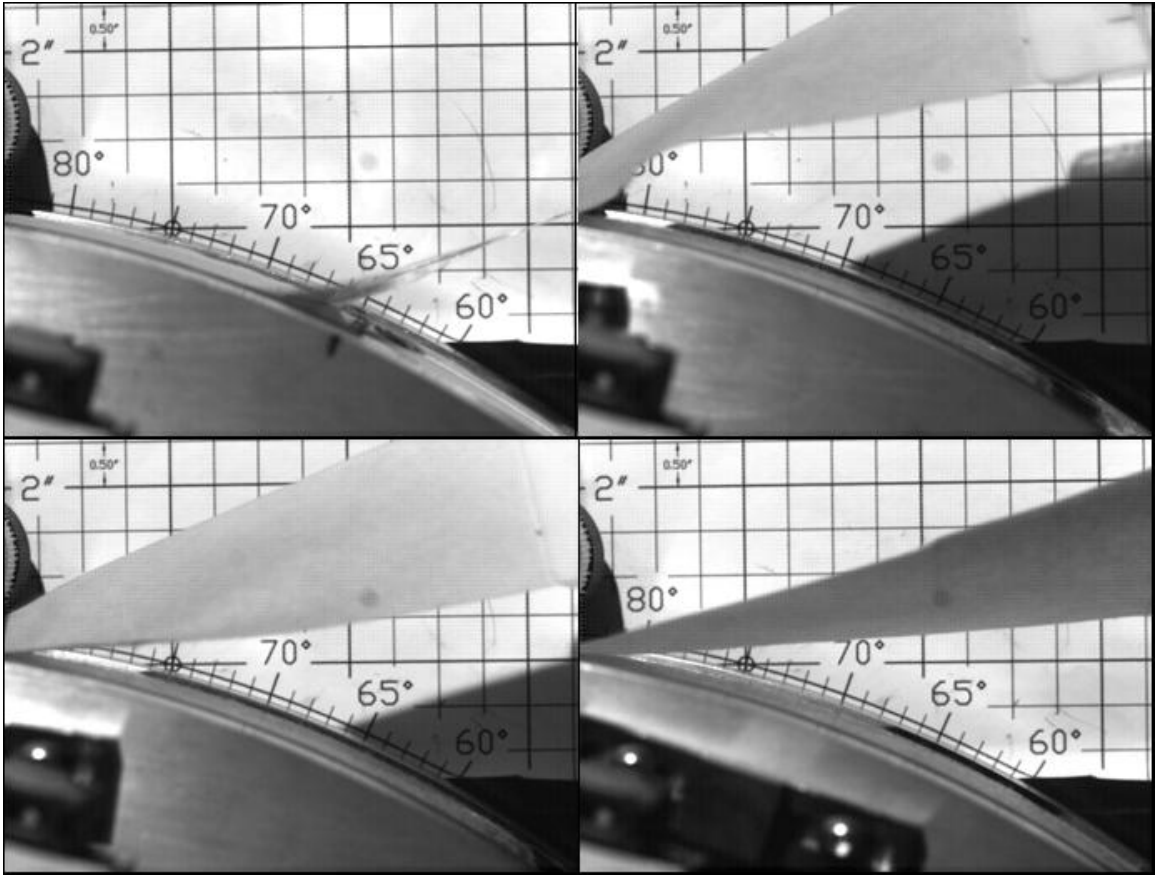


Figure B.10: Peeling images from 40% solids run on a sticky coupon (Experiment #1-21-06).

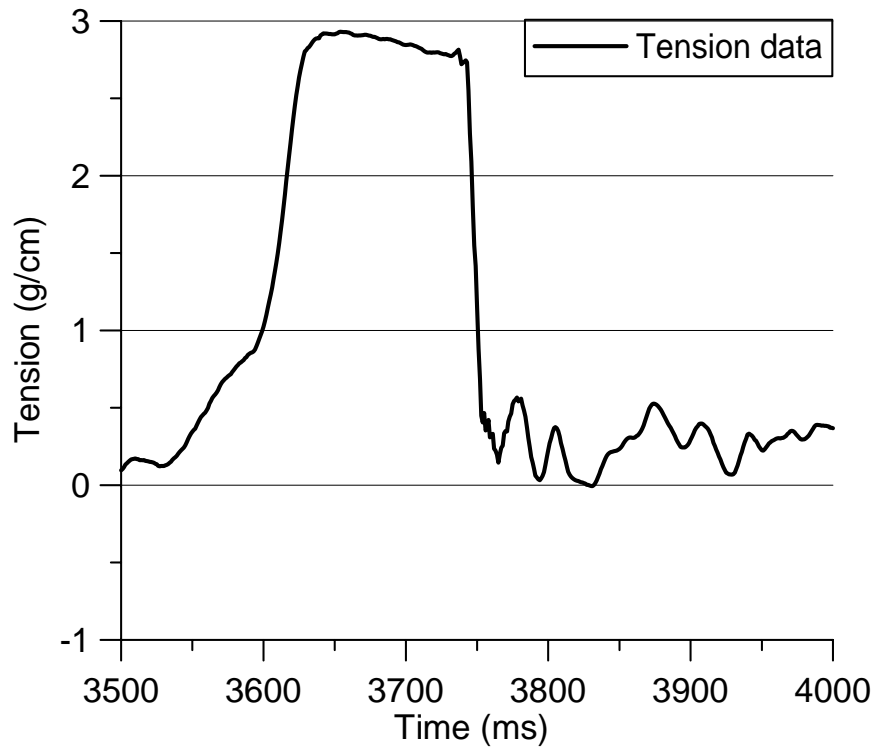


Figure B.11: Tension data from 40% solids run on a sticky coupon (Experiment #1-21-06).

Table B.4: WADS data from 40% solids run on a sticky coupon (Experiment #1-21-06).

% solids	40	WADS peel angle	38.43	Avg. Tension	33.9
weight (g/cm ²)	0.25		27.703	Max Tension	98.7
Peel point 1	66		30.3	Mardon work (avg)	4.67
Peel point 2	75		31.326	Mardon work (max)	13.86
Peel point 3	77		26.654		
Peel point avg	72.7				
		Peel angle avg	30.9		
		Peel angle stdev	4.6		

40% Solids non-sticky coupon (Experiment #1-22-02)

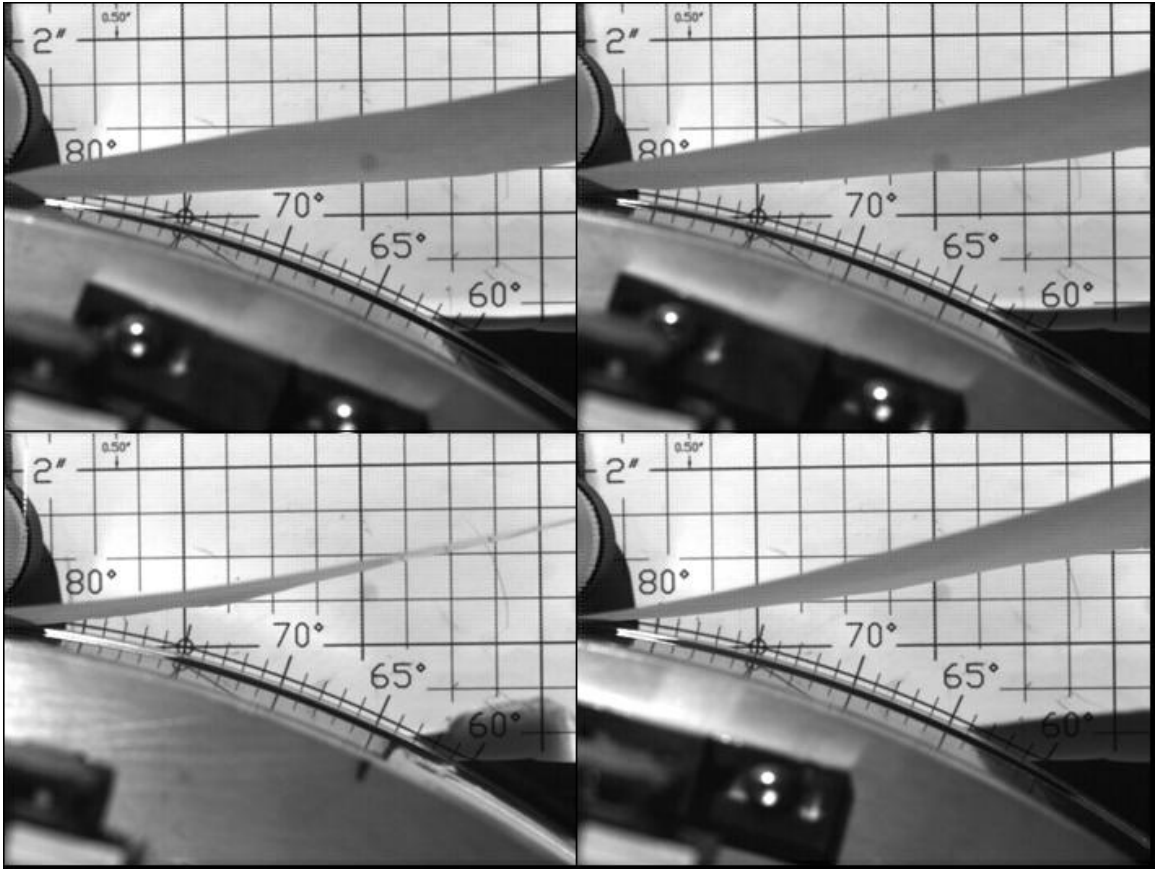


Figure B.12: Peeling images from 40% solids run on a non-sticky coupon (Experiment #1-22-02).

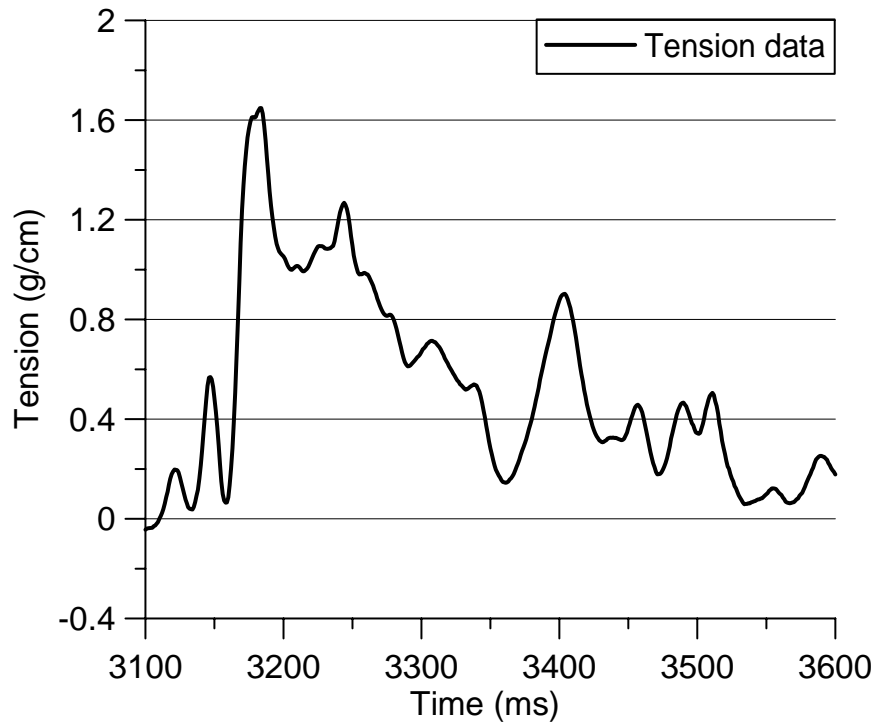


Figure B.13: Tension data from 40% solids run on a non-sticky coupon (Experiment #1-22-02).

Table B.5: WADS data from 40% solids run on a non-sticky coupon (Experiment #1-22-02).

% solids	40	WADS peel angle	26.7	Avg. Tension	17.5
weight (g/cm ²)	0.25		21.758	Max Tension	55.6
Peel point 1	81		25.286	Mardon work (avg)	1.41
Peel point 2	82		16.743	Mardon work (max)	4.67
Peel point 3	82		28.686		
Peel point avg	81.7		17.535		
			31.228		
			27.457		
			19.244		
		Peel angle avg	23.8		
		Peel angle stdev	5.2		

40% Solids non-sticky coupon (Experiment #1-22-03)

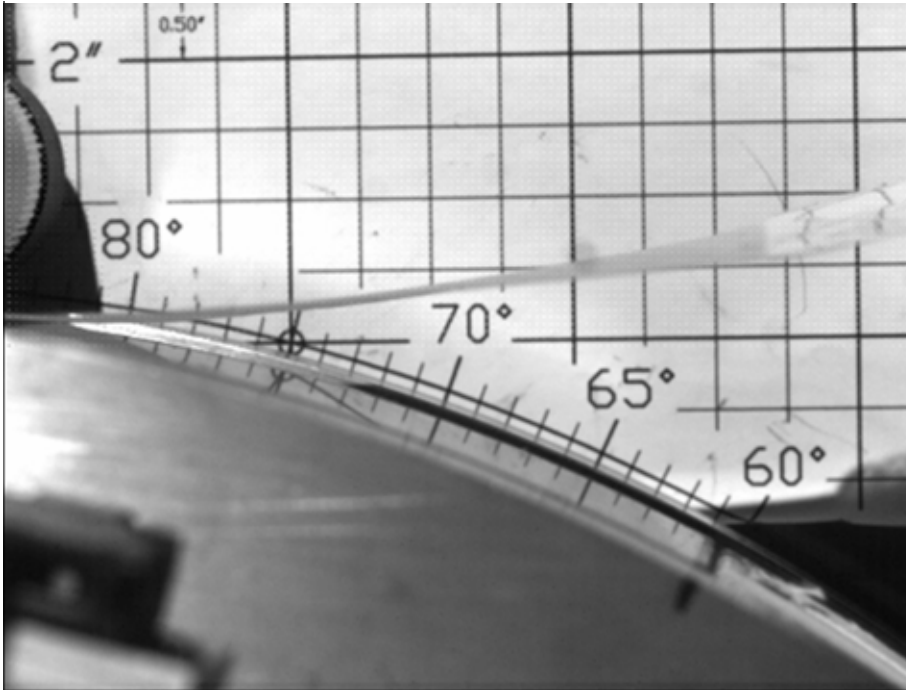


Figure B.14: Peeling images from 40% solids run on a non-sticky coupon (Experiment #1-22-03).

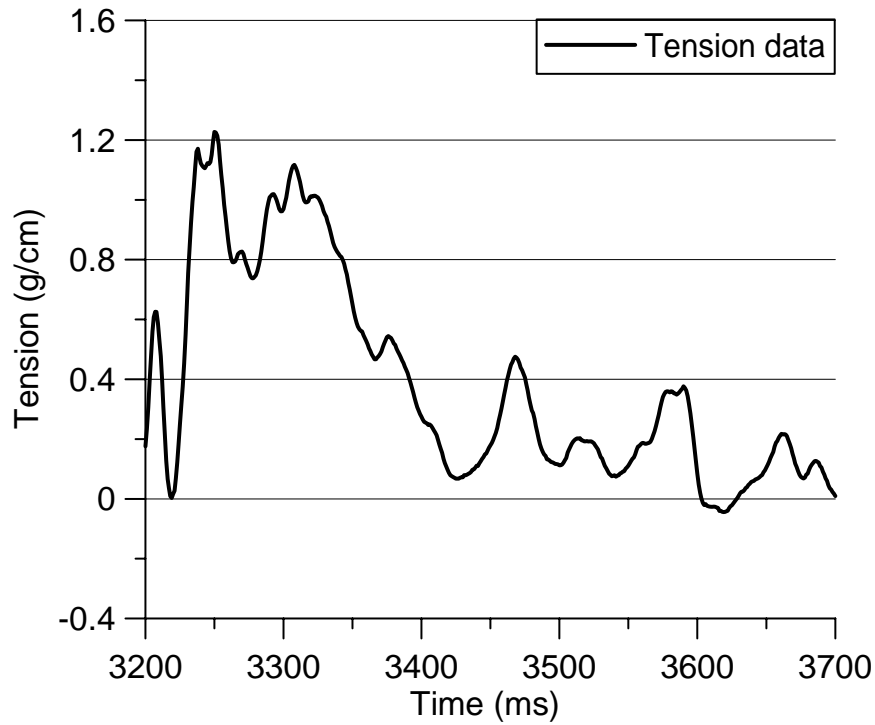


Figure B.15: Tension data from 40% solids run on a non-sticky coupon (Experiment #1-22-03).

Table B.6: WADS data from 40% solids run on a non-sticky coupon (Experiment #1-22-03).

% solids	40	WADS peel angle	17.5	Avg. Tension	13.2
weight (g/cm ²)	0.25		17.094	Max Tension	41.4
Peel point 1	78		14.913	Mardon work (avg)	0.54
Peel point 2	80		18.841	Mardon work (max)	1.80
Peel point 3	81		17.967		
Peel point avg	<u>79.7</u>		16.565		
		Peel angle avg	<u>17.1</u>		
		Peel angle stdev	1.3		

50% Solids sticky coupon (Experiment #1-22-05)

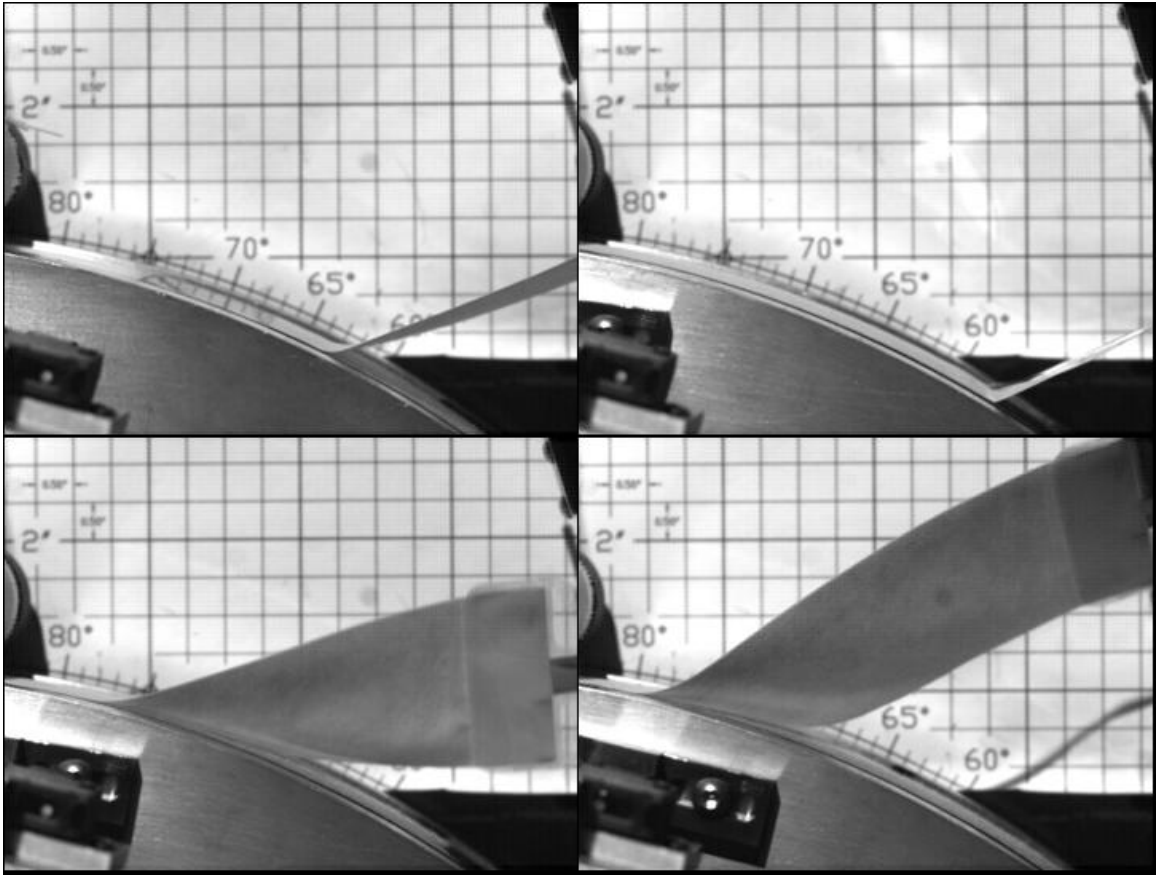


Figure B.16: Peeling images from 50% solids run on a sticky coupon (Experiment #1-22-05), part 1 (continued).

Pictures continued:

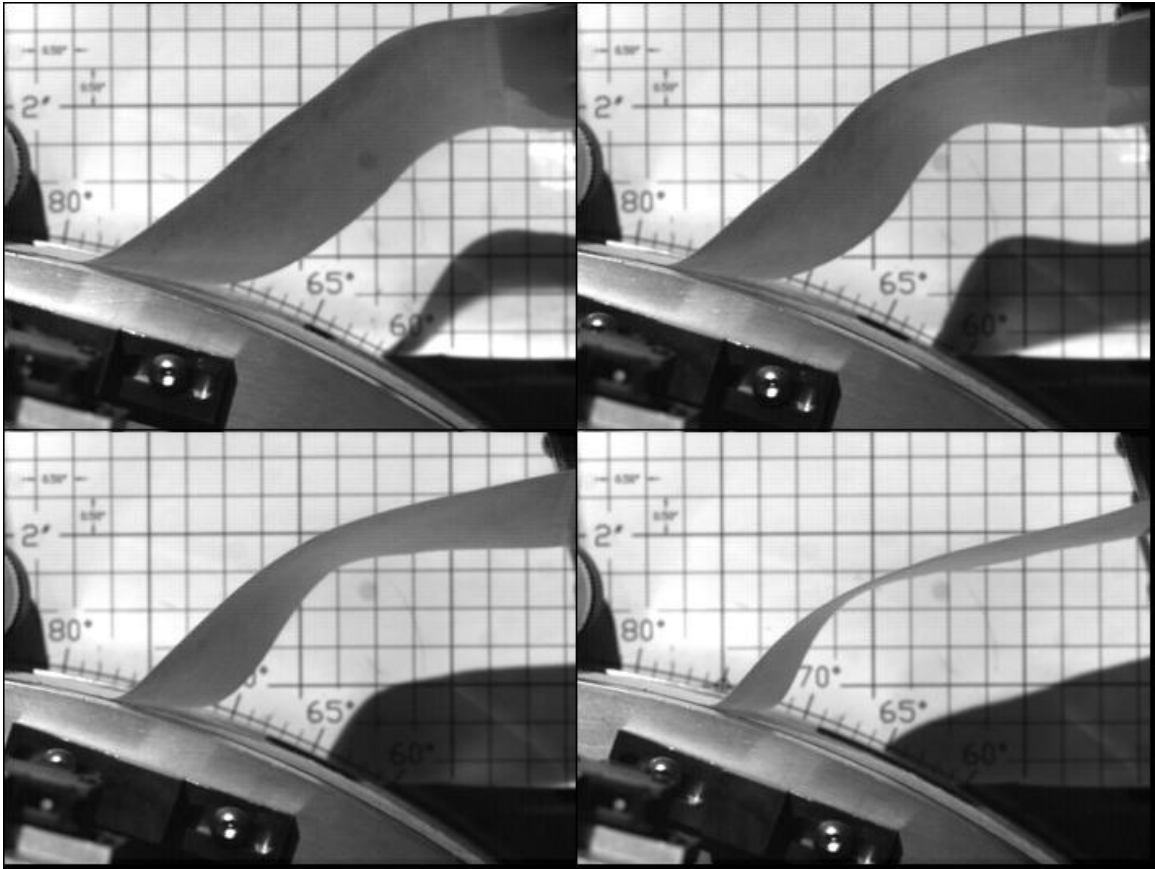


Figure B.17: Peeling images from 50% solids run on a sticky coupon (Experiment #1-22-05), part 2.

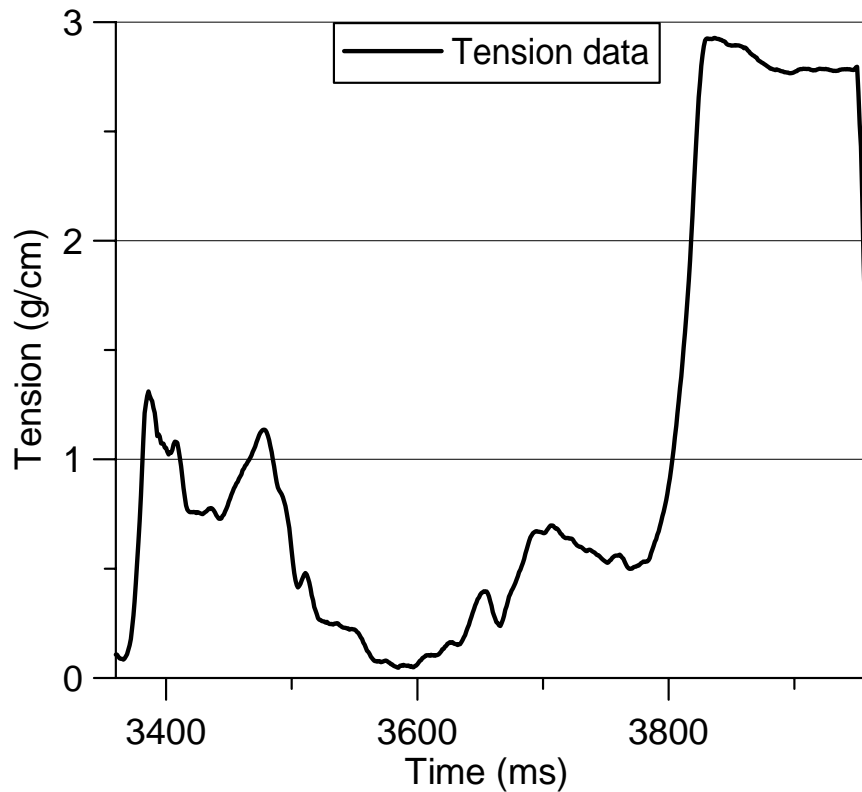


Figure B.18: Tension data from 50% solids run on a sticky coupon (Experiment #1-22-05).

Table B.7: WADS data from 50% solids run on a sticky coupon (Experiment #1-22-05).

% solids	50	WADS peel angle	48.5	Avg. Tension	35
weight (g/cm ²)	0.2		49.221	Max Tension	98.7
Peel point 1	57		45.487	Mardon work (avg)	13.02
Peel point 2	63		54.115	Mardon work (max)	37.25
Peel point 3	62		56.673		
Peel point avg	<u>60.7</u>		56.232		
		Peel angle avg	<u>51.7</u>		
		Peel angle stdev	4.6		

50% Solids sticky coupon (Experiment #1-22-06)

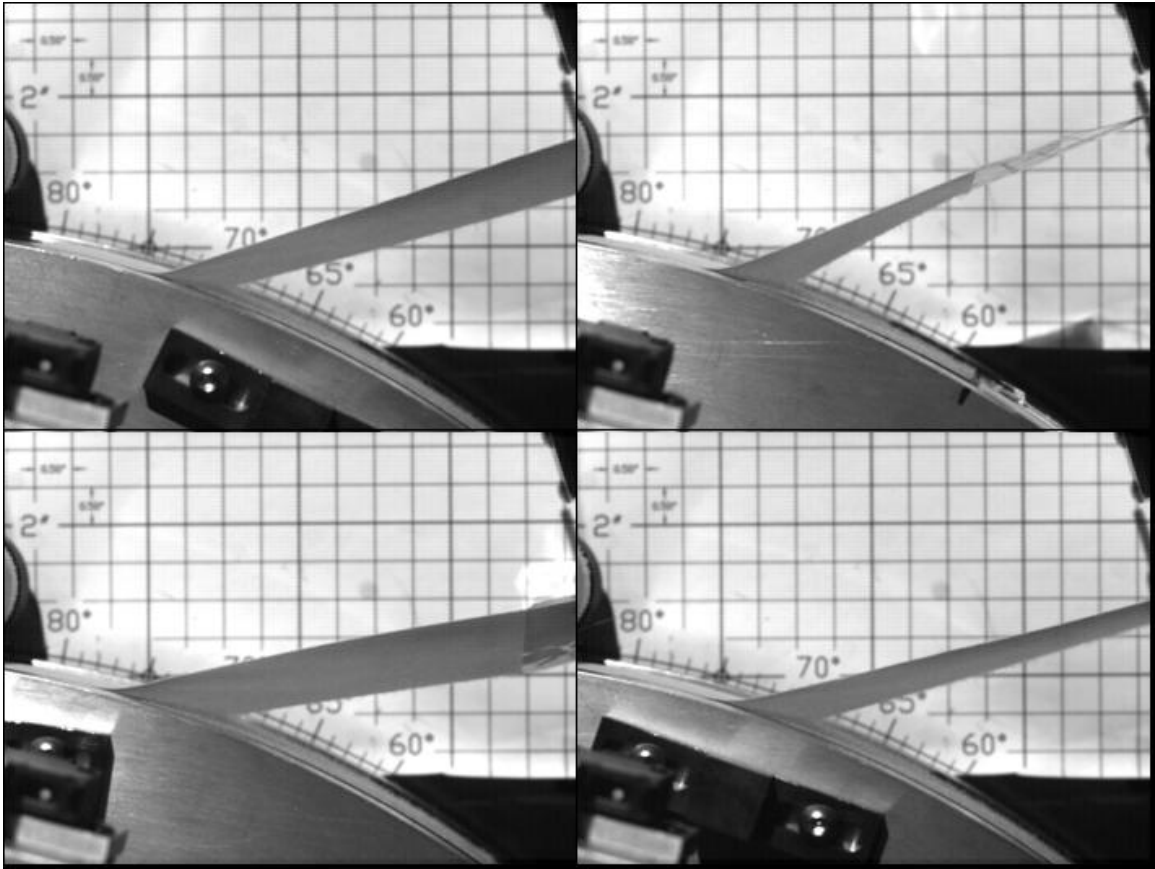


Figure B.19: Peeling images from 50% solids run on a sticky coupon (Experiment #1-22-06).

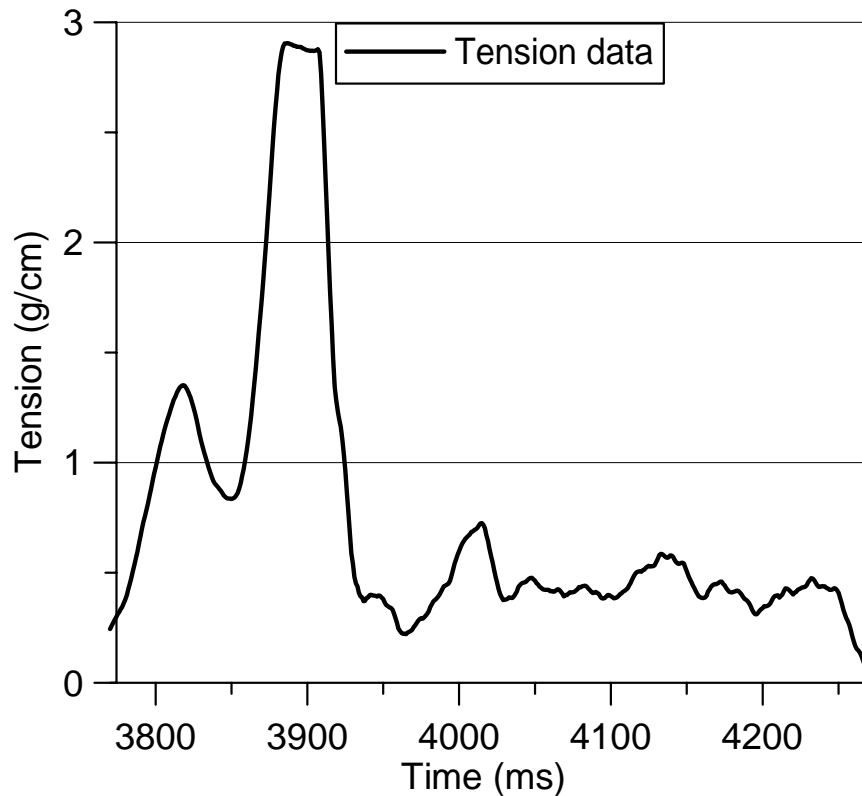


Figure B.20: Tension data from 50% solids run on a sticky coupon (Experiment #1-22-06).

Table B.8: WADS data from 50% solids run on a sticky coupon (Experiment #1-22-06).

% solids	50	WADS peel angle	43.7	Avg. Tension	25.2
weight (g/cm ²)	0.2		30.22	Max Tension	97.9
Peel point 1	67		34.427	Mardon work (avg)	4.28
Peel point 2	67		31.798	Mardon work (max)	17.02
Peel point 3	68		32.858		
Peel point avg	67.3		35.621		
			34.578		
			30.996		
			32.069		
		Peel angle avg	34.4		
		Peel angle stdev	3.7		

50% Solids sticky coupon (Experiment #1-22-07)

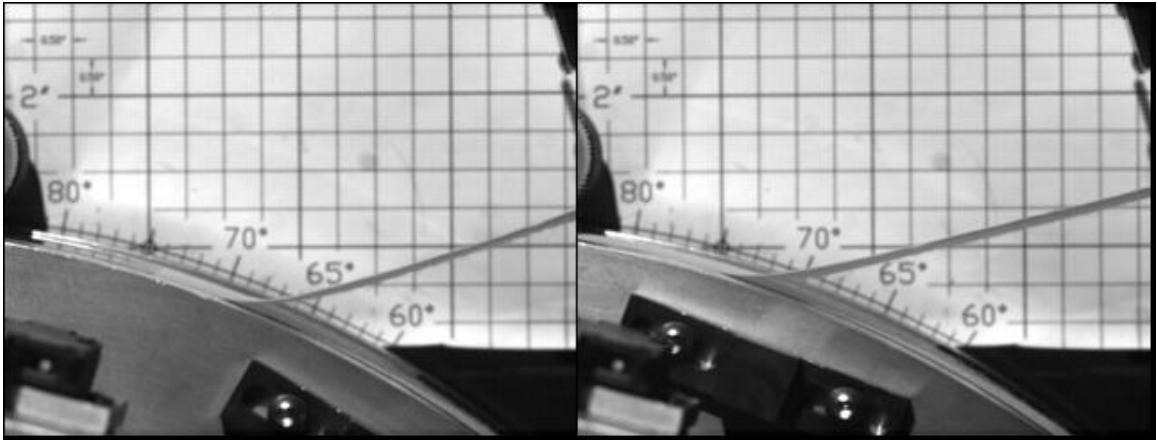


Figure B.21: Peeling images from 50% solids run on a sticky coupon (Experiment #1-22-07).

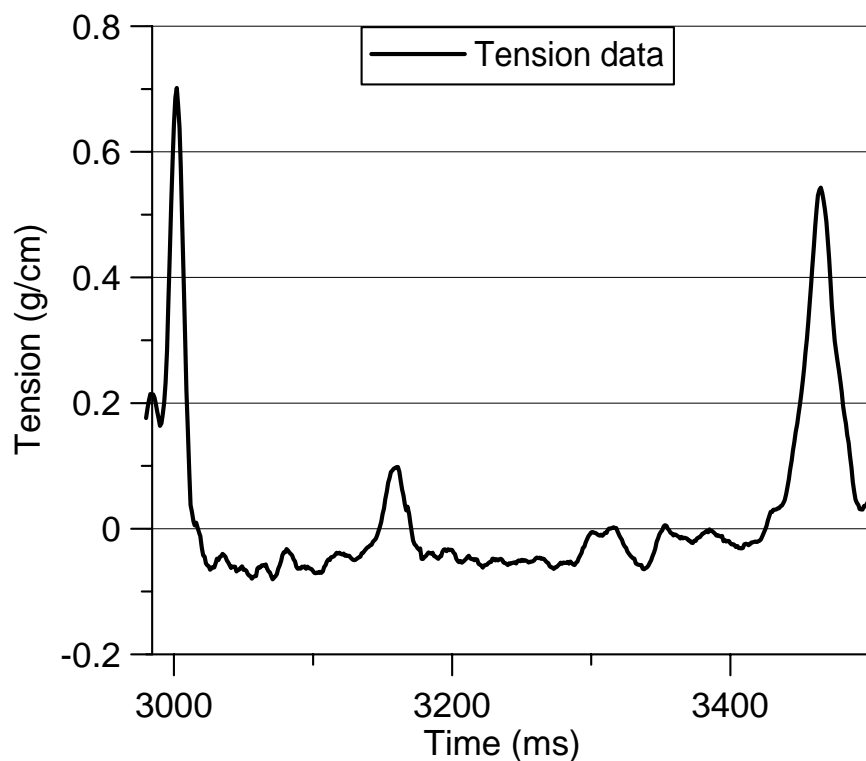


Figure B.22: Tension data from 50% solids run on a sticky coupon (Experiment #1-22-07).

Table B.9: WADS data from 50% solids run on a sticky coupon (Experiment #1-22-07).

% solids	50	WADS peel angle	28.685	Avg. Tension	0.8
weight (g/cm ²)	0.2		31.633	Max Tension	23.6
Peel point 1	72		32.385	Mardon work (avg)	0.01
Peel point 2	72		36.604	Mardon work (max)	4.18
Peel point 3	68		38.894		
Peel point avg	<u>70.7</u>		43.172		
		Peel angle avg	<u>35.2</u>		
		Peel angle stdev	5.3		

50% Solids non-sticky coupon (Experiment #1-22-08)

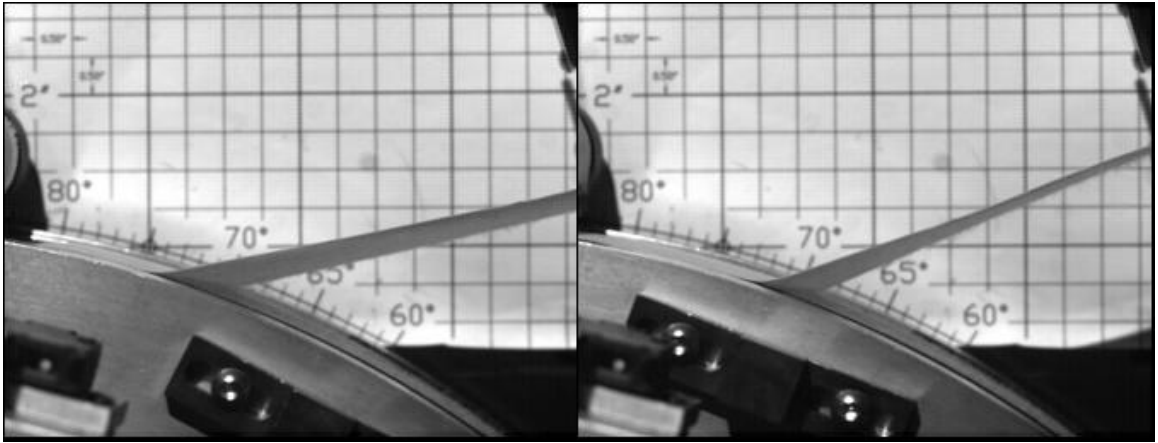


Figure B.23: Peeling images from 50% solids run on a non-sticky coupon (Experiment #1-22-08).

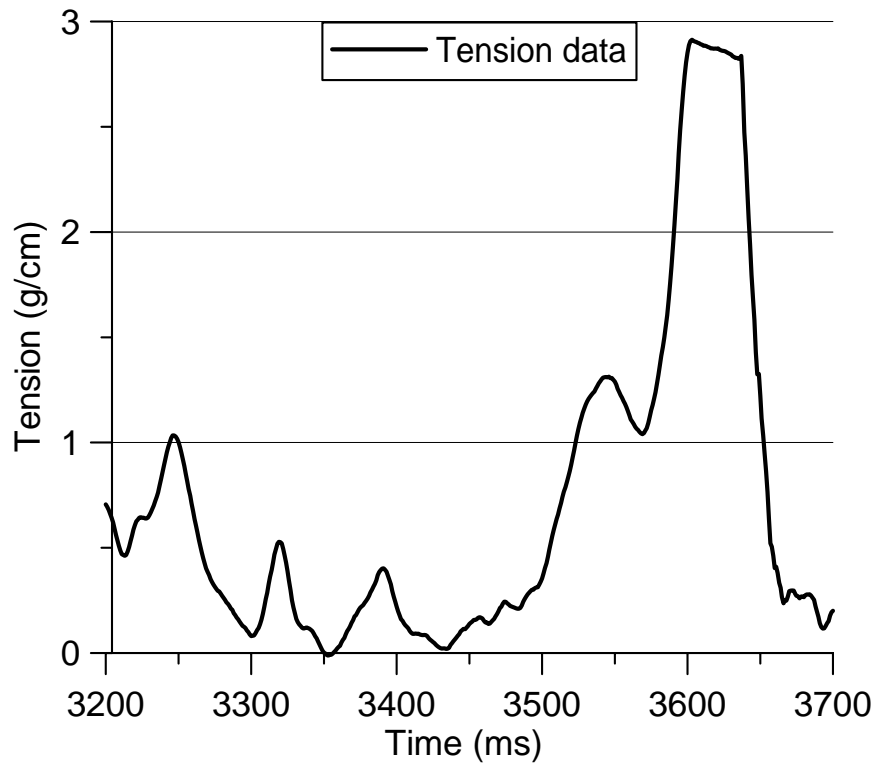


Figure B.24: Tension data from 50% solids run on a non-sticky coupon (Experiment #1-22-08).

Table B.10: WADS data 50% solids run on a non-sticky coupon (Experiment #1-22-08).

% solids	50	WADS peel angle	38.3	Avg. Tension	24.9
weight (g/cm ²)	0.2		46.606	Max Tension	98.2
Peel point 1	69		44.862	Mardon work (avg)	5.08
Peel point 2	68		29.31	Mardon work (max)	20.49
Peel point 3	68		29.81		
Peel point avg	68.3		38.136		
		Peel angle avg	37.8		
		Peel angle stdev	7.3		

50% Solids non-sticky coupon (Experiment #1-22-09)

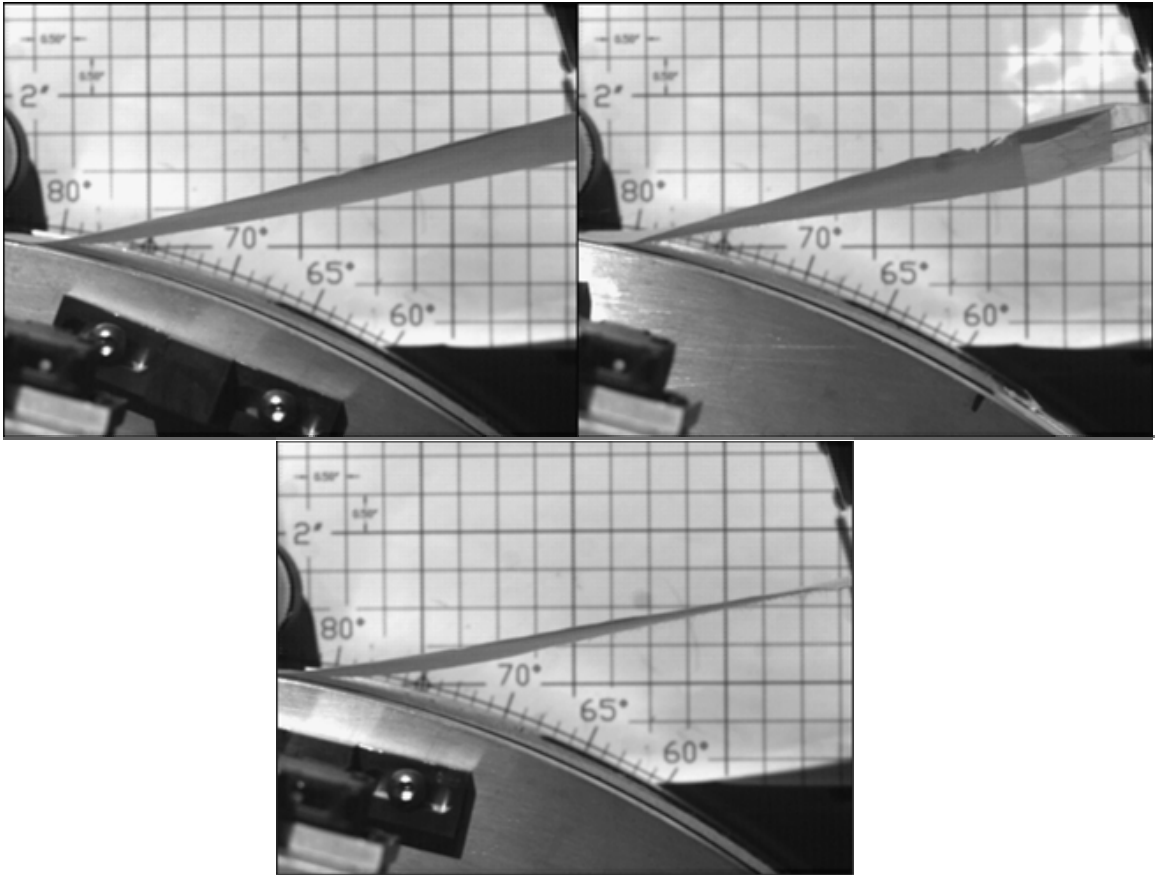


Figure B.25: Peeling images from 50% solids run on a non-sticky coupon (Experiment #1-22-09).

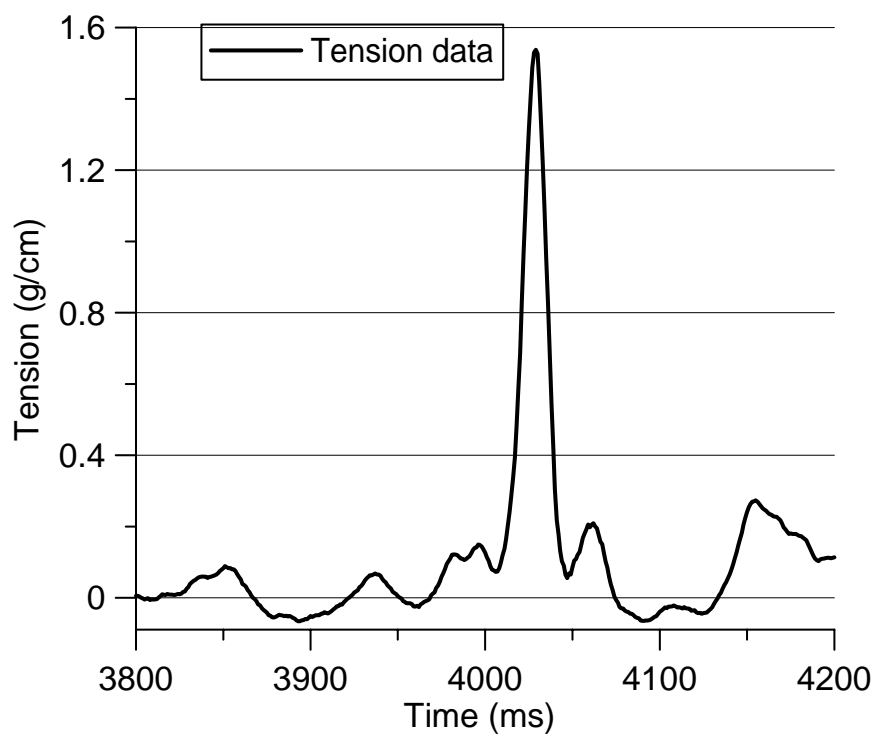


Figure B.26: Tension data from 50% solids run on a non-sticky coupon (Experiment #1-22-09).

Table B.11: WADS data 50% solids run on a non-sticky coupon (Experiment #1-22-09).

% solids	50	WADS peel angle	31.73	Avg. Tension	3.6
weight (g/cm ²)	0.2		27.975	Max Tension	51.8
Peel point 1	77		22.713	Mardon work (avg)	0.26
Peel point 2	80		23.999	Mardon work (max)	4.67
Peel point 3	80		21.127		
Peel point avg	79.0		22.924		
			24.745		
			22.701		
			24.399		
		Peel angle avg	24.7		
		Peel angle stdev	3.3		

50% Solids non-sticky coupon (Experiment #1-22-10)

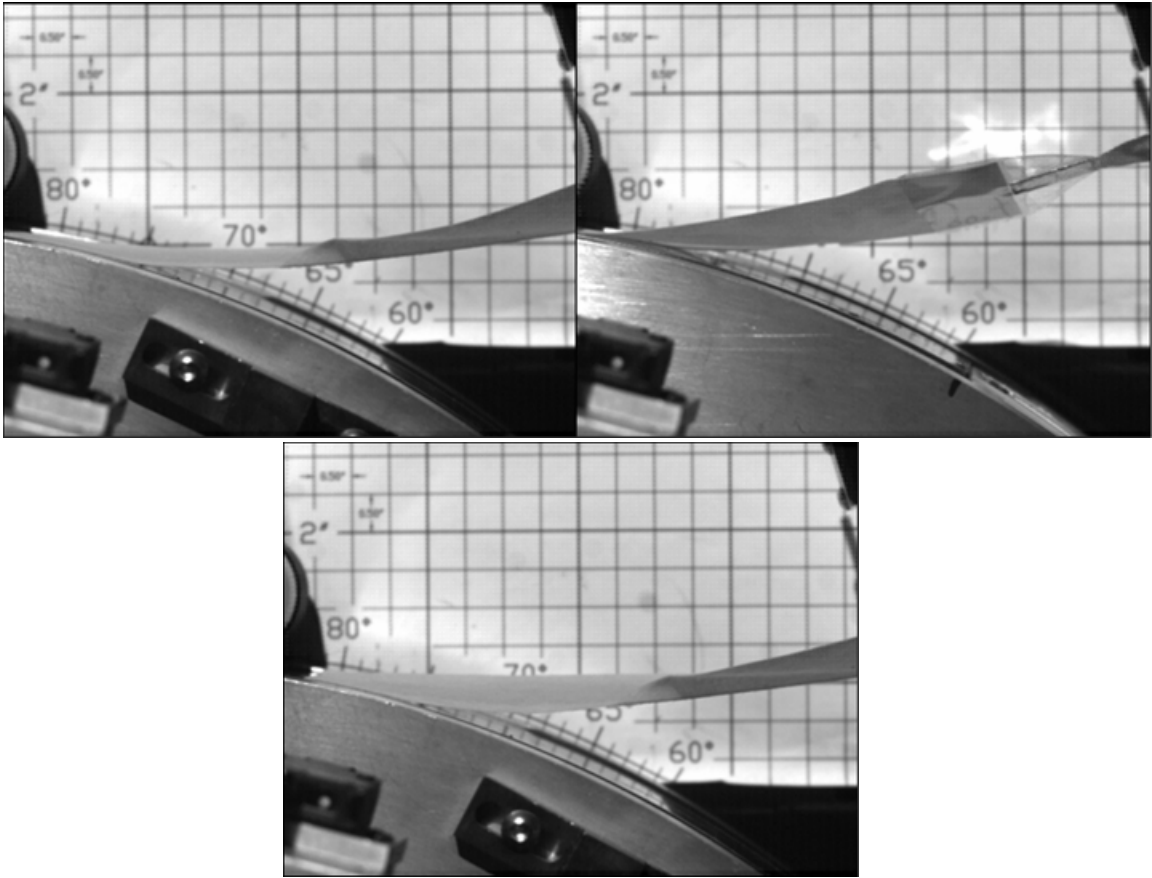


Figure B.27: Peeling images from 50% solids run on a non-sticky coupon (Experiment #1-22-10).

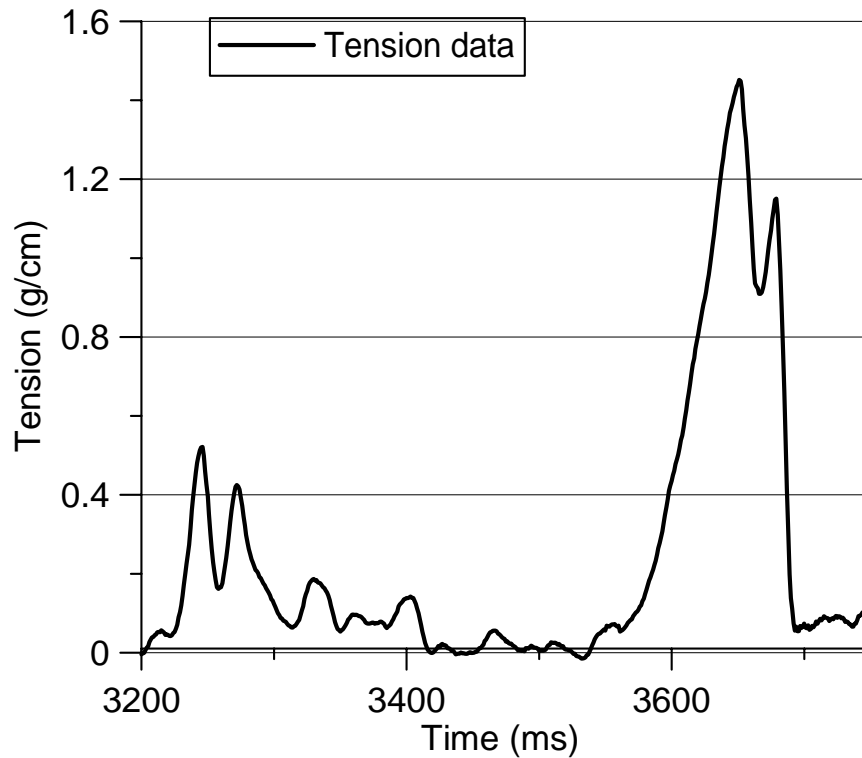


Figure B.28: Tension data from 50% solids run on a non-sticky coupon (Experiment #1-22-10).

Table B.12: WADS data 50% solids run on a non-sticky coupon (Experiment #1-22-10).

% solids	50	WADS peel angle	21.807	Avg. Tension	8.1
weight (g/cm ²)	0.2		19.09	Max Tension	48.9
Peel point 1	74		20.73	Mardon work (avg)	0.39
Peel point 2	74		16.089	Mardon work (max)	2.53
Peel point 3	75		16.002		
Peel point avg	74.3		16.594		
			20.361		
		Peel angle avg	18.7		
		Peel angle stdev	2.4		

50% Solids non-sticky coupon (Experiment #1-22-11)

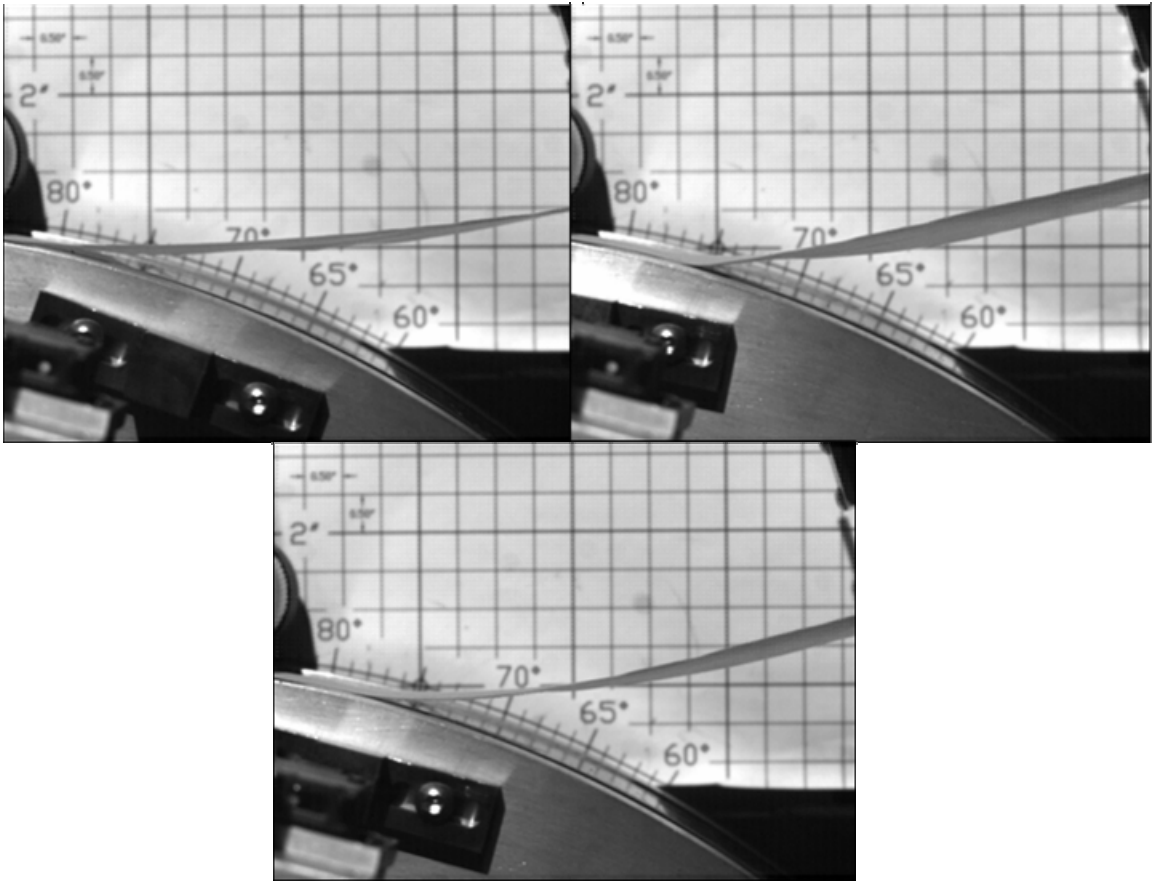


Figure B.29: Peeling images from 50% solids run on a non-sticky coupon (Experiment #1-22-11).

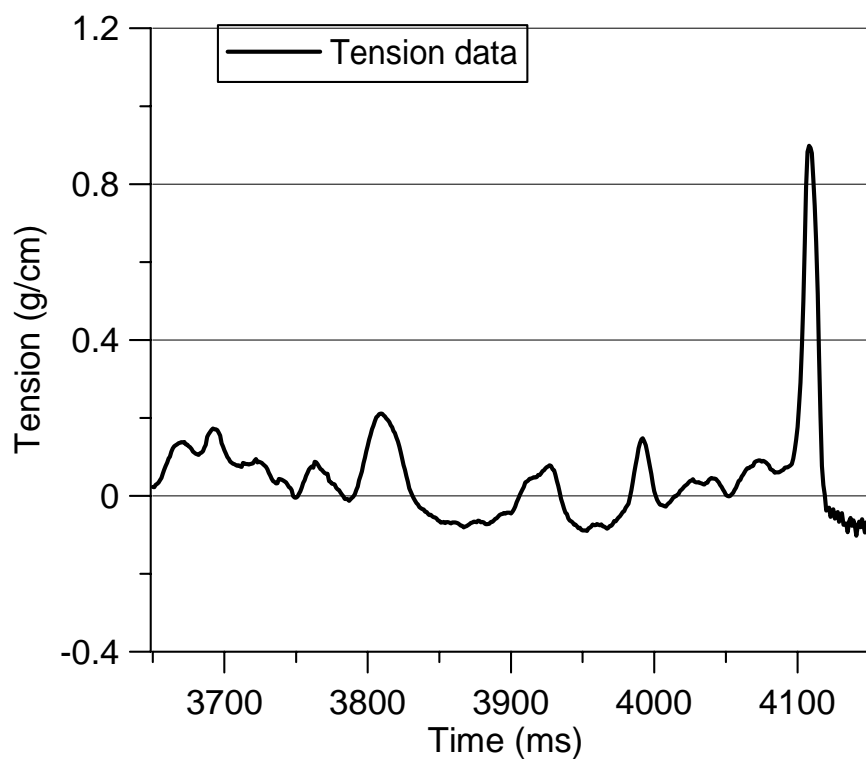


Figure B.30: Tension data from 50% solids run on a non-sticky coupon (Experiment #1-22-11).

Table B.13: WADS data 50% solids run on a non-sticky coupon (Experiment #1-22-11).

% solids	50	WADS peel angle	26.949	Avg. Tension	1.3
weight (g/cm ²)	0.2		24.563	Max Tension	30.3
Peel point 1	75		19.684	Mardon work (avg)	0.03
Peel point 2	74		15.018	Mardon work (max)	1.79
Peel point 3	76		18.108		
Peel point avg	75.0		15.875		
		Peel angle avg	20.0		
		Peel angle stdev	4.8		

REFERENCES

1. Lancey, S., *50% Recovery by 2000 might not be realized, but industry on track*. Pulp and Paper Week, 1998. **20**(17): p. 2.
2. Williamson, P., *Supply of recycled-content business paper outpaces demand*. Paper Industry, 1998. **15**(4): p. 6.
3. Heise, O., M. Kemper, H. Wiese, and E. Krauthauf, *Removal of residual stickies at Haindl Paper using new floatation technology*. Tappi J., 2000. **83**(3): p. 73-79.
4. Friberg, T., *Cost impact of stickies*. Progress in Paper Recycling, 1997: p. 70-72.
5. Cauchon, D., *Paper recyclers unable to lick stickies problem*, in *USA Today*. 1997. p. 3.
6. Doshi, M., *Quantification of Stickies*, in *Paper Recycling Challenge - Stickies*, M. Doshi, Editor. 1997. p. 176-180.
7. Guo, X. and M. Douek. *An Overview of the Chemical Nature of Deposits/Stickies in Mills Using Recycled Fiber*. in *Recycling Symposium Proceedings*. 1997. Chicago, Ill.
8. Chascin, K. *Stickies removal via size and shape development*. in *Pulping Conference*. 1997. San Francisco: TAPPI.
9. Lowe, K., *Contaminants, supply problems hinder secondary fiber usage*. Pulp and Paper, 1973. **47**(13): p. 100-104.
10. Onusseit, H., *Adhesives for the Paper and Packaging Industry -- What Influence Do They Have on Paper Recycling*. Adhesives & Sealants Industry, 2000.
11. Moreland, R. *Stickies Control by Detackification*. in *TAPPI Pulping*. 1986.
12. Bennett, C. *Control of Stickies by Chemical Methods*. in *EUCEPA Symposium Recycling Fibers and Fillers in the Pulp and Paper Industry*. 1989.
13. Hodgson, K., *Surface Science and Process Factors Affecting Removal of Sticky Contaminants*, in *Paper Recycling Challenge - Stickies*, M. Doshi, Editor. 1997. p. 71-75.
14. Alison, P., *Problem Solving Using Specialty Chemicals for Recycled-Fiber Processing*. Paper South Africa, 1992. **12**(5): p. 47-52.
15. Hsu, N., *Stickies - the Importance of Their Chemical and Physical Properties*, in *Recycling Challenge - Stickies*, M. Doshi, Editor. 1997. p. 256-258.

16. Cathie, K., R. Haydock, and I. Dias, *Understanding the Fundamental Factors Influencing Stickies Formation and Deposition*. Pulp and Paper Canada, 1992. **93**(12): p. 157-160.
17. Latimer, J., *Predicting "White Pitch" Problems*. Tappi J., 1979. **62**(5): p. 29-31.
18. Patel, S. and S. Banerjee, *Deposition of Hot Melt and Wax on Surfaces*. Tappi J., 1999. **82**(11): p. 99-103.
19. Wilhelm, D., S. Makris, and S. Banerjee, *Signature of recalcitrant stickies in recycled newsprint*. Tappi J., 1999. **82**(12): p. 63-66.
20. Venditti, R., H. Chang, and H. Jameel, *Overview of Stickies Research at NCSU*. Paper Age, 1999: p. 18-20.
21. Hsu, N., J. Schroeck, and L. Errigo. *Identification of the Origins of Stickies in Deinked Pulp*. in *1997 Recycling Symposium: Proceedings*. 1997. Chicago, IL: TAPPI.
22. Autenrieth, J. and K. Foley, *Resins for Elastomer-Based Adhesives*, in *Handbook of Adhesives*, I. Skeist, Editor. 1990, Van Nostrand Reinhold: New York. p. 556-572.
23. Wake, W., *Adhesion and the Formulation of Adhesives*. 1976, London: Applied Science Publishers.
24. Abarca, S. and L. Mahoney, *Talcs for Pitch and Stickies Control*. Paper Asia, 1996. **12**(12): p. 42-44.
25. Biza, P., *Use of Minerals in Papermaking*. 1998, Surrey, UK: Leatherhead.
26. Holton, J. and C. Moebus, *Control of Pitch, Stickies, Gunk and Trap Organics in Pulp and Paper Mills*. Pulp and Paper Canada, 1982. **83**(4): p. 106-109.
27. Yordan, J.L. and W. G., *Talc for Contaminant Control in Recycled Fiber*, in *Paper Recycling Challenge - Stickies*, M. Doshi, Editor. 1997. p. 76-80.
28. Dykstra, G., P. Hoekstra, and T. Suzuki. *A New Method for Measuring Depositible Pitch and Stickies and Evaluating Control Agents*. in *The Papermakers 1988 Conference*. 1988.
29. Corbel, G. and T. Hassler. *Polymers for Pitch and Stickies Control*. in *1st International Conference and Exhibition on Paper and Board Recycling*. 1994. London.
30. Banerjee, S., *Stickies Control in Recycle Operations*. 1996, Institute of Paper Science and Technology: Atlanta.

31. Nguyen, D., *Prevention of Pitch and Stickies Deposition on Paper-Forming Wires Via Adsorption of a Cationic Polymer Associated with Anionic Species*. Tappi J., 1998. **81**(6): p. 143-151.
32. Hassler, T. *A New Method for Control of Pitch and Stickies Deposition in Papermaking*. in *EUCEPA 24th*. 1990. Stockholm, Sweden.
33. Ahrens, F. and T. Patterson, *Drying Productivity*. 2000, Institute of Paper Science and Technology: Atlanta.
34. Merchant, T. and S. Banerjee, *Stickies Control in Recycle Operations*. 1999, Institute of Paper Science and Technology: Atlanta.
35. Hanecker, E. *Method for the Assessment of Sticky Adsorption in PM Dryer Sections*. in *1st CTP/PTS Recycling Symposium Proceedings*. 1999.
36. Williamson, P., *Sonoco Mill Overcomes Stickies with New Roll Coverings*. Paper Industry, 1997. **14**(5): p. 18-19.
37. Williamson, P., *Roll Technology*. Paper Industry, 1997. **14**(1): p. 12, 16.
38. Hassler, T. and H. Sekiya. *Dryer Section Passivation: A Novel and Effective Method of Preventing Dryer Section Deposition*. in *Papermakers Conference*. 2000. Vancouver, BC.
39. Bierman, C., *Handbook of Pulping and Papermaking*. 2nd ed. 1996, San Diego, CA: Academic Press.
40. Krumenacker, R. and P. Deutsch, eds. *Paper Machine Steam and Condensate Systems*. 5th ed. 1999, Tappi Press: Atlanta.
41. Meinecke, A., T. Chau-Huu, and H. Loser, *New Knowledge on Paper Drying with Drying Cylinders*. Papier, 1988. **42**(10A): p. 159-165.
42. Ahrens, F., *IPST 6153 Class Lecture Notes*. 2000.
43. Ahrens, F., B. Hojjatie, and D. Coffin. *Influence of Drying Variables in Development of Cockle: An Experimental Study*. in *International Paper Physics Conference*. 2003. Victoria, British Columbia, Canada: TAPPI & PAPTEC.
44. Robinson, G. *Understanding and Troubleshooting the Papermachine Dryer Section*. in *PPRIC*. 1990. Montreal, Canada.
45. Ahrens, F. 2000.
46. Gent, A. and G. Hamed, *Fundamentals of Adhesion*, in *Handbook of Adhesives*, I. Skeist, Editor. 1990, Van Nostrand Reinhold: New York. p. 39-73.

47. DeLollis, N., *Adhesion Theory and Review*, in *Handbook of Adhesive Bonding*, Cagle, Editor. 1973, McGraw-Hill: New York.
48. Aubrey, D., *Tack*, in *Handbook of Adhesion*, D. Packham, Editor. 1992, Longman Scientific & Technical: Essex, UK. p. 463-465.
49. Creton, C. and P. Fabre, *Tack*, in *Surfaces, Chemistry and Applications, Vol. I, The Mechanics of Adhesion, Rheology of Adhesives, and Strength of Adhesive Bonds*, A. Pocius and D. Dillard, Editors. 2002, Elsevier: Amsterdam.
50. Russell, T. and H. Kim, *Tack-a Sticky Subject*. Science, 1999. **285**(8): p. 1219-1220.
51. Benedek, I. and L. Heymans, *Pressure-Sensitive Adhesives Technology*. 1997, New York: Marcel Dekker, Inc.
52. Campion, R., *Microstructure and Autohesive Tack*, in *Adhesion I*, K. Allen, Editor. 1977, Applied Science Publishers: London.
53. Comyn, J., *Autohesion*, in *Handbook of Adhesion*, D. Packham, Editor. 1992, Longman Scientific & Technical: Avon. p. 58-62.
54. Packham, D., *Roughness of Surfaces*, in *Handbook of Adhesion*, D. Packham, Editor. 1992, Longman Scientific & Technical: Avon. p. 379-382.
55. Mahoney, C., *Surface Preparation for Adhesive Bonding*, in *Handbook of Adhesives*, I. Skeist, Editor. 1990, Van Nostrand Reinhold: New York. p. 74-93.
56. Matijevic, E., *Surface and Colloidal Science*. 1976, New York: Wiley and Sons.
57. Allen, K., *Mechanical Theory of Adhesion*, in *Handbook of Adhesion*, D. Packham, Editor. 1992, Longman Scientific & Technical: Avon. p. 273-275.
58. Allen, K., *Theories of Adhesion*, in *Handbook of Adhesion*, D. Packham, Editor. 1992, Longman Scientific & Technical: Avon. p. 473-475.
59. Cagle, C., *Handbook of Adhesive Bonding*. 1973, New York: McGraw Hill.
60. Allen, K., *Electrostatic Theory of Adhesion*, in *Handbook of Adhesion*, D. Packham, Editor. 1992, Longman Scientific & Technical: Avon. p. 129-140.
61. Good, R.J. and C.J. van Oss, *Modern Approaches to Wettability: Theory and Applications*, ed. M.E. Schrader and G. Loeb. 1992, New York: Plenum Press. 1-27.
62. Adamson, A.W. and G. A.P., *Physical Chemistry of Surfaces*. 6th ed. 1997, New York: John Wiley and Sons.

63. Janczuk, B., W. Wojcik, and A. Zdziennicka, *Determination of the components of the surface tension of some liquids from interfacial liquid-liquid tension measurements*. J. of Colloid and Interface Science, 1993. **157**(2): p. 384-393.
64. Padday, J.F., *Wetting, Spreading, and Adhesion*, ed. J.F. Padday. 1978, New York: Academic Press.
65. Zisman, W.A., *Chapter 3*, in *Handbook of Adhesives*, I. Skeist, Editor. 1977, van Nostrand: New York.
66. Neumann, A.W. and R.J. Good, *Experimental Methods*. Techniques of Measuring Contact Angles, Surface and Colloid Science, ed. R.J. Good and R.R. Stromberg. Vol. II. 1979, New York: Plenum Press.
67. Fowkes, F.M., *Attractive forces at interfaces*. Industrial and Engineering Chemistry, 1964. **56**: p. 40-52.
68. Fowkes, F.M., J. of Adhesion, 1972. **4**: p. 153.
69. van Oss, C.J., M.K. Chaudhury, and R.J. Good, J. of Separation Science and Technology, 1987.
70. van Oss, C.J., R.J. Good, and M.K. Chaudhury, *Additive and nonadditive surface tension components and the interpretation of contact angles*. Langmuir, 1988. **4**(4): p. 884-891.
71. van Oss, C.J., M.K. Chaudhury, and R.J. Good, J. of Colloid and Interface Science, 1989. **313**.
72. de Gennes, P.G., *Wetting: Statics and Dynamics*. Rev. Mod. Phys., 1985. **57**(3): p. 827-863.
73. Yoon, R.H. and R. Pazhianur, *Direct force measurement between hydrophobic glass sphere and covellite electrode in potassium ethyl xanthate solutions at pH 9.2*. Colloid Surfaces A: Physicochemical and Engineering Aspects, 1999. **144**: p. 59-69.
74. Yoon, R.H. and S.A. Ravishankar, *Long-range hydrophobic forces between mica surfaces in dodecylammonium chloride solutions in the presence of dodecanol*. J. of Colloid and Interface Science, 1996. **179**(2): p. 391.
75. Leja, J., *Surface Chemistry of Froth Flotation*. 1982, New York: Plenum Press.
76. Fuerstenau, D.W., Mining Engineering, Transactions AIME, 1957: p. 1367.
77. Yoon, R.H. and J.L. Yordan, J. of Colloid and Interface Science, 1991. **146**(2): p. 101-108.

78. Bilinski, B. and E. Chibowski, *Powder Technology*, 1983. **31**: p. 39.
79. Spelt, J.K., D. Li, and A.W. Neumann, *Modern Approaches to Wettability: Theory and Applications*, ed. M.E. Schrader and G. Loeb. 1992, New York: Plenum Press. 101-142.
80. van Oss, C.J., R.F. Giese, and R.J. Good, *Reevaluation of the surface tension components and parameters of polyethylene from contact angles of liquids*. *Langmuir*, 1990. **6**(11): p. 1711-1713.
81. Yildirim, I., *Surface Free Energy Characterization of Powders*, in *Mining and Minerals Engineering*. 2001, Virginia Polytechnic Institute and State University: Blacksburg, VA. p. 224.
82. van Oss, C.J., *Interfacial Forces in Aqueous Media*. 1994, New York: Marcel Dekker Inc.
83. van der Waals, J.D., *cited in van Oss*. 1873.
84. van der Waals, J.D., *cited in van Oss*. 1899.
85. Israelachvili, J., *Intermolecular & Surface Forces*, 2nd. 1992, Amsterdam: Academic Press.
86. Keesom, W.H., *Physikalische Zeit.*, 1921. **22**: p. 129.
87. Hiemenz, P.C. and R. Rajagopalan, *Principles of Colloid and Surface Chemistry*, 3rd. 1997, New York: Marcel Dekker, Inc.
88. Prausnitz, J.M., *Molecular Thermodynamics of Fluid-Phase Equilibria*. 1998, Upper Saddle River, NJ: Prentice Hall.
89. Debye, P., *van der Waals' Cohesive Forces*. *Physikalische Zeit.*, 1920. **22**: p. 302.
90. London, F., *Z. Phys. Chem.*, 1930. **11**: p. 222.
91. London, F., *Trans. Faraday Soc.*, 1937. **33**: p. 8.
92. Mahanty, J. and B.W. Ninham, *Dispersion Forces*. 1976, Amsterdam: Academic Press.
93. Fowkes, F.M., *Physicochemical Aspects of Polymer Surfaces*, ed. K.L. Mittal. Vol. 2. 1983, New York: Plenum Press. 583.
94. Packham, D., *Surface energy, surface topography and adhesion*. *International Journal of Adhesion & Adhesives*, 2003. **23**: p. 437-448.
95. Berg, J., *Wettability*. *Surfactant Science*. 1993, New York: Marcel Dekker, Inc.

96. Kwok, D., A. Wu, D. Li, and A.W. Neumann, *Contact angle measurements and interpretation: wetting behavior and solid surface tensions for poly(alkyl methacrylate) polymers*. J. Adhesion Science and Technology, 2000. **14**(5): p. 719-743.
97. Neumann, A.W., *Contact Angles and Their Temperature Dependence: Thermodynamic Status, Interpretation and Application*. Adv. in Colloid and Interface Science, 1974. **4**: p. 105-191.
98. Balkenende, H., A. van de Boogaard, M. Scholten, and N. Willard, *Evaluation of Different Approaches To Assess the Surface Tension of Low-Energy Solids by Means of Contact Angle Measurements*. Langmuir, 1998. **14**: p. 5907-5912.
99. Lam, C., R. Wu, D. Li, M. Hair, and A.W. Neumann, *Study of the advancing and receding contact angles: liquid sorption as a cause of contact angle hysteresis*. Adv. in Colloid and Interface Science, 2002. **96**: p. 169-191.
100. Li, D. and A.W. Neumann, *A Reformulation of the Equation of State for Interfacial Tensions*. J. of Colloid and Interface Science, 1990. **137**: p. 304-307.
101. Li, D. and A.W. Neumann, *Contact Angles on Hydrophobic Solid Surfaces and Their Interpretation*. J. of Colloid and Interface Science, 1992. **148**: p. 190-200.
102. Good, R.J., J. Colloid Interface Science, 1975. **52**: p. 308.
103. Good, R.J., *Contact angle, wetting, and adhesion: A critical review*. J. of Adhesion Science and Technology, 1992. **6**(12): p. 1269-1302.
104. Li, D., M. Xie, and A.W. Neumann, *Vapour Adsorption and Contact Angles on Hydrophobic Solid Surfaces*. Colloid Polymer Science, 1993. **271**: p. 573-580.
105. Morrison, I., *Does the Phase Rule for Capillary Systems Really Justify an Equation of State for Interfacial Tensions?* Langmuir, 1991. **7**: p. 3833-3836.
106. Gaydos, J., D. Li, and A.W. Neumann, *Implications of the Phase Rule for Capillary Systems Containing Surfaces and Three-Phase Contact Lines with Surface and Linear Constraint Relations*. Colloid Polymer Science, 1993. **271**: p. 715-725.
107. Gaydos, J. and A.W. Neumann, *Comments to the Article: I.D. Morrison, Does the Phase Rule for Capillary Systems Really Justify an Equation of State for Interfacial Tensions?*, Langmuir 7, p. 3833-3836. Langmuir, 1993. **9**: p. 3327-3329.
108. Veverka, J., *An Investigation of Interfacial Instability During Air Entrainment*, in *Institute of Paper Science and Technology*. 1995, The Georgia Institute of Technology: Atlanta, GA.

109. Binnig, G., C.F. Quate, and C. Gerber, *Atomic Force Microscope*. Physical Review Letters, 1986. **56**(9): p. 930-933.
110. Albrecht, T.R. and C.F. Quate, *Atomic resolution imaging of a nonconductor by atomic force microscopy*. J. of Applied Physics, 1987. **62**(7): p. 2599-2602.
111. Gould, S.A.C., B. Drake, C.B. Prater, A.L. Weisenhorn, S. Manne, H.G. Hansma, P.K. Hansma, J. Massie, M. Longmire, V. Elings, B.D. Northern, B. Mukergee, C.M. Peterson, W. Stoeckenius, T.R. Albrecht, and C.F. Quate, *From atoms to integrated circuit chips, blood cells, and bacteria with the atomic force microscope*. J. of Vacuum Science and Technology, 1990. **A8**(1): p. 369-373.
112. McGuire, G.E., M.A. Ray, S.J. Simko, F.K. Perkins, S.L. Brandow, E.A. Dobisz, R.J. Nemanich, A.R. Chourasia, and D.R. Chopra, *Surface characterization*. Analytical Chemistry, 1993. **65**: p. 311R-333R.
113. Snyder, S.R. and H.S. White, *Scanning tunneling microscopy, atomic force microscopy, and related techniques*. Analytical Chemistry, 1992. **64**: p. 116R-134R.
114. Albrecht, T.R., M.M. Dovek, C.A. Lang, P. Grutter, C.F. Quate, S.W.J. Kuan, C.W. Frank, and R.F.W. Pease, *Imaging and modification of polymers by scanning tunneling and atomic force microscopy*. J. of Applied Physics, 1988. **64**(3): p. 1178-1184.
115. Magonov, S.N., K. Qvarnstrom, V. Elings, and H. Cantow, *Atomic force microscopy on polymers and polymer related compounds*. Polymer Bulletin, 1991. **25**(6): p. 689-694.
116. Hansma, H.G., F. Motamedi, P. Smith, and P. Hansma, *Molecular resolution of thin, highly oriented poly(tetrafluoroethylene) films with the atomic force microscope*. Polymer Communications, 1992. **33**(3): p. 647-649.
117. Weisenhorn, A.L., P.K. Hansma, T.R. Albrecht, and C.F. Quate, *Forces in atomic force microscopy in air and water*. Applied Physics Letters, 1989. **54**(26): p. 2651-2653.
118. Mate, C.M., M.R. Lorenz, and V.J. Novotny, *Atomic force microscopy of polymeric liquid films*. J. of Chemical Physics, 1989. **90**(12): p. 7550-7555.
119. Burnham, N.A. and R.J. Colton, *Measuring the nanomechanical properties and surface forces of materials using atomic force microscopy*. J. of Vacuum Science and Technology, 1989. **a7**(4): p. 2906-2913.
120. Magonov, S.N., *Atomic Force Microscopy in Analysis of Polymers*, in *Encyclopedia of Analytical Chemistry*, R.A. Meyers, Editor. 2000, John Wiley & Sons Ltd: Chichester. p. 7432-7491.

121. Garnaes, J., A. Kuhle, L. Blunt, and N.B. Larsen. *Comparison of atomic force and interference microscopy*. in *Proc. of the 3rd euspen International Conference*. 2002. Eindhoven, The Netherlands.
122. Boisen, A., K. Birkelund, O. Hansen, and F. Grey, *Fabrication of submicron suspended structures by laser and atomic force microscopy lithography on aluminum combined with reactive ion etching*. *J. of Vacuum Science and Technology*, 1998. **16**(6): p. 2977-2981.
123. MFP 3D Schematic. www.asylumresearch.com/Products/Mfp3D/Mfp3D.pdf. Last viewed on 2-25-05.
124. Lazzaroni, R., *Principles of Atomic Force Microscopy*, in *Laminate short course on Scanning Probes Microscopies*. 2001.
125. Morris, V., A. Kirby, and A. Gunning, *Atomic Force Microscopy for Biologists*. 2001, London: Imperial College Press.
126. Kageshima, M., H. Jensenius, M. Dienwiebel, Y. Nakayama, H. Tokumoto, S. Jarvis, and T. Oosterkamp, *Noncontact atomic force microscopy in liquid environment with quartz tuning fork and carbon nanotube probe*. *Applied Surface Science*, 2002. **188**: p. 440-444.
127. Muller, D.J., D. Fotiadis, S. Scheuring, S. Muller, and A. Engel, *Electrostatically balanced subnanometer imaging of biological specimens by atomic force microscopy*. *Biophysical J.*, 1999(76): p. 1101-1111.
128. Sader, J., J. Chon, and P. Mulvaney, *Calibration of rectangular atomic force microscope cantilevers*. *Rev. Sci. Instrum.*, 1999. **70**: p. 3967-3969.
129. Sader, J. and L. White, *Theoretical analysis of the static deflection of plates for atomic force microscope applications*. *J. Applied Physics*, 1993. **74**: p. 1-9.
130. Burnham, N.A. and R.J. Colton, *Force microscopy*, in *Scanning Tunneling Microscopy and Spectroscopy*, D.A. Bonnell, Editor. 1993, VCH Publishers, Inc: New York. p. 191-249.
131. Boisen, A., O. Hansen, and S. Bouwstra, *AFM probes with directly fabricated tips*. *J. of Micromechanics and Microengineering*, 1996. **6**(1): p. 58-62.
132. Hanley, S. and D. Gray, *Atomic Force Microscopy*, in *Surface analysis of paper*, T. Connors and S. Banerjee, Editors. 1995, CRC Press: Boca Raton. p. 301-324.
133. Markiewicz, P. and M. Goh, *Simulation of atomic force microscope tip-sample/sample-tip reconstruction*. *J. Vacuum Science and Technology B.*, 1995. **13**(3): p. 1115-1118.

134. Russell, P., D. Batchelor, and J. Thornton, SEM and AFM: Complementary Techniques for High Resolution Surface Investigations. www.di.com. Last viewed 2001.
135. Howland, R. and L. Benatar, *A Practical Guide to Scanning Probe Microscopy*, ed. C. Symanski. 2000: Park Scientific Instruments.
136. Kappl, M. and H. Butt, *The Colloidal Probe Technique and its Application to Adhesion Force Measurements*. Part. Part. Syst. Characterization, 2002. **19**: p. 129-143.
137. Nie, H., M. Walzak, B. Berno, and N. McIntyre, *Atomic force microscopy study of polypropylene surfaces treated by UV and ozone exposure: modification of morphology and adhesion force*. Applied Surface Science, 1999. **144-145**: p. 627-632.
138. Irvine, J., D. Aston, and J. Berg, *Use of atomic force microscopy to measure the adhesive properties of sized and unsized papers*. Tappi J., 1999. **82**(5): p. 172-174.
139. A-Hassan, E., W. Heinz, M. Antonik, N. D'Costa, S. Nagaswaran, C. Schoenenberger, and J. Hoh, *Relative Micro-elastic Mapping of Living Cells by Atomic Force Microscopy*. Biophys. J., 1998. **74**: p. 1564-1578.
140. Aime, J., Z. Elkaakour, C. Odin, T. Bouhacina, D. Michel, J. Curely, and A. Dautant, *Comments on the Use of the Force Mode in Atomic Force Microscopy for Polymer Films*. J. of Applied Physics, 1994. **76**: p. 754-762.
141. Karbach, A. and D. Drechsler, *Atomic Force Microscopy--a Powerful Tool for Industrial Applications*. Surface and Interface Analysis, 1999. **27**: p. 401-409.
142. Elsner, N., *Atomic Force Microscopy*. 2003, Max Planck Institute of Colloids and Interfaces: Potsdam, Germany.
143. Raghavan, D., M. VanLandingham, X. Gu, and T. Nguyen, *Characterization of Heterogeneous Regions in Polymer Systems Using Tapping Mode and Force Mode Atomic Force Microscopy*. Langmuir, 2000. **16**: p. 9448-9459.
144. Raghavan, D., X. Gu, T. Nguyen, M. VanLandingham, and A. Karim, *Mapping Polymer Heterogeneity Using Atomic Force Microscopy Phase Imaging and Nanoscale Indentation*. Macromolecules, 2000. **33**: p. 2573-2583.
145. Neumeister, J. and W. Ducker, *Lateral, normal, and longitudinal spring constants of atomic force microscopy cantilevers*. Rec. Sci. Instrum., 1994. **65**: p. 2527-2531.
146. Ducker, W. and T. Senden, *Experimental determination of spring constants in atomic force microscopy*. Langmuir, 1994. **10**: p. 1003-1004.

147. Cleveland, J., S. Manne, D. Bocek, and P. Hansma, *A nondestructive method for determining the spring constant of cantilevers for scanning force microscopy*. Rev. Sci. Instrum., 1993. **63**: p. 403-405.
148. Butt, H., P. Siedle, K. Seifert, K. Fendler, T. Seeger, E. Bamberg, A.L. Weisenhorn, K. Goldie, and A. Engel, *Scan speed limit in atomic force microscopy*. J. Microscopy, 1993. **169**: p. 75-84.
149. Yoon, R.H. and Y. Rabinovich, *Use of atomic force microscope for the measurements of hydrophobic forces between silanated silica plate and glass sphere*. Langmuir, 1994. **10**: p. 1903-1909.
150. Scholl, D., M. Everson, and R. Jaklevic, *In situ force calibration of high force constant atomic force microscope cantilevers*. Rev. Sci. Instrum., 1994. **65**: p. 2255-2257.
151. Gibson, C., G. Watson, and S. Myrha, *Determination of the spring constants of probes for force microscopy/spectroscopy*. Nanotechnology, 1996. **7**: p. 259-262.
152. Torii, A., M. Sasaki, K. Hane, and S. Okuma, *A method for determining the spring constant of cantilevers for atomic force microscopy*. Meas. Sci. Technology, 1996. **7**: p. 179-184.
153. Kirk, M. and M. Tortonese, *Characterization of application specific probes for SPMs*. Proc. SPIE, 1997. **3009**: p. 53-60.
154. Hutter, J. and J. Bechhoefer, *Calibration of atomic-force microscope tips*. Rev. Sci. Instrum., 1993. **64**: p. 1868-1873.
155. Ata, A., Y. Rabinovich, and R. Singh, *Role of surface roughness in capillary adhesion*. J. Adhesion Science and Technology, 2002. **16**(4): p. 337-346.
156. Chiche, A., P. Pareige, and C. Creton, *Role of surface roughness in controlling the adhesion of a soft adhesive on a hard surface*. C.R. Acad. Sci. Paris, 2000. **IV**(1): p. 1197-1204.
157. Chiche, A., P. Pareige, and C. Creton. *Control of the Adhesion Through Surface Roughness in a Flat Probe Geometry*. in *The 5th European Adhesion Conference*. 2000. Lyon, France.
158. Chiche, A. and C. Creton. *Role of Surface Roughness of the Adherent Surface on the Debonding Mechanism of PSA*. in *The 24th Annual Meeting of the Adhesion Society*. 2000. Williamsburg, VA.
159. Assender, H., V. Bliznyuk, and K. Porfyakis, *How surface topology relates to materials' properties*. Science, 2002. **297**(5583): p. 973-976.

160. Mendez-Vilas, A., M. Gonzalez-Martin, L. Labajos-Broncano, and M. Nuevo, *Experimental analysis of the influence of surface topography on the adhesion force as measured by an AFM*. J. Adhesion Science and Technology, 2002. **16**(13): p. 1737-1747.
161. Creton, C. and L. Leibler, *How does tack depend on time of contact and contact pressure?* J. Polymer Science B, 1996. **34**: p. 545-554.
162. Pocius, A., *Adhesion and Adhesives Technology: an Introduction*. 1997, New York: Hanser.
163. Paiva, A., N. Sheller, M. Foster, A. Crosby, and K. Shull, *Study of the Surface Adhesion of Pressure-Sensitive Adhesives by Atomic Force Microscopy and Spherical Indenter Tests*. Macromolecules, 2000. **33**: p. 1878-1881.
164. Crevoisier, G., P. Fabre, J. Corpart, and L. Leibler, *Switchable Tackiness and Wettability of a Liquid Crystalline Polymer*. Science, 1999. **285**: p. 1246-1249.
165. Satas, D., *Acrylic Adhesives*, in *Handbook of Pressure-Sensitive Adhesive Technology*, D. Satas, Editor. 1997, Van Nostrand Reinhold Company: New York. p. 298-307.
166. Williams, N., *Elastic Analysis of the Loop Tack Test for Pressure Sensitive Adhesives*, in *Civil and Environmental Engineering*. 2000, Virginia Polytechnic Institute and State University: Blacksburg, VA. p. 84.
167. Aubrey, D., *Pressure Sensitive Adhesives*, in *Handbook of Adhesion*, D. Packham, Editor. 1992, Longman Scientific & Technical: Essex, UK. p. 335-341.
168. Zosel, A., *The effect of bond formation on the tack of polymers*. J. Adhesion Science and Technology, 1997. **11**: p. 1447-1457.
169. Johnston, J., *Tack--Probe Testing and the Rate Process*. Adhesives Age, 1983. **26**: p. 24-28.
170. Johnston, J., *Tack--Known by Many Names, It's Difficult to Define*. Adhesives Age, 1983. **26**: p. 34-38.
171. Woo, Y., *Inelastic Analysis of the Loop Tack Test for Pressure Sensitive Adhesives*, in *Civil Engineering*. 2002, Virginia Polytechnic Institute and State University: Blacksburg, VA. p. 159.
172. Hammond, F., *Tack*, in *Handbook of Pressure-Sensitive Adhesive Technology*, D. Satas, Editor. 1982, Van Nostrand Reinhold Company: New York. p. 32-49.
173. Pitrie, E., The definition of tack.
http://www.specialchem4adhesives.com/home/editorial.aspx?id=250&key=pressure_sensitive_tape. Last viewed March, 2003.

174. Pizzi, A. and K.L. Mittal, *Handbook of Adhesive Technology*. 1994, New York: Marcel Dekker.
175. Roberts, R., *Review of Methods for the Measurement of Tack--Report 5, Project PAJ1*. 1997, National Physical Laboratory: Teddington, UK.
176. Laureau, C., M. Vicente, M. Barandiaran, J. Leiza, and J. Asua, *Effect of the Composition Profile of 2-Ethyl Hexyl Acrylate/Methyl Methacrylate Latex Particles on Adhesion*. *Journal of Applied Polymer Science*, 2001. **81**(5): p. 1258-1265.
177. Satas, D., *Handbook of Pressure-Sensitive Adhesive Technology*. 2nd ed. 1989, New York: van Nostrand, Reinhold Co.
178. Lestriez, B., H. Lakrout, A. Chiche, A. Roos, and C. Creton. *Probe tack tests as a characterization tool in pressure-sensitive-adhesives*. in *PSTC Technical Seminar TECH XXIV*. 2001. Orlando, FL.
179. Creton, C. and H. Lakrout, *Micromechanics of Flat-Probe Adhesion Tests of Soft Viscoelastic Polymer Films*. *J. of Polymer Science: Part B*, 2000. **38**: p. 965-979.
180. Hooker, J., C. Creton, and P. Tordjeman. *Probe tests investigations of bulk and surface cavitation processes on model PSA's*. in *Proceedings of the 5th European Adhesion Conference*. 2000. Lyon, France.
181. Lakrout, H., C. Creton, D. Ahn, and K. Shull, *Influence of Molecular Features on the Tackiness of Acrylic Polymer Melts*. *Macromolecules*, 2001. **34**: p. 7448-7458.
182. Zosel, A., *Fracture Energy and Tack*, in *Advances in Pressure Sensitive Adhesive Technology*, D. Satas, Editor. 1992, Satas & Associates: Warwick, RI. p. 92-127.
183. Zosel, A., *The Effect of Fibrillation on the Tack of Pressure Sensitive Adhesives*. *International Journal of Adhesion & Adhesives*, 1998. **18**: p. 265-271.
184. Ondarcuhu, T., *Tack of Polymer Melt: Adhesion Measurements and Fracture Profile Observations*. *J. Phys. II France*, 1997. **7**: p. 1893-1916.
185. Zosel, A., *Adhesion and tack of polymers: Influence of mechanical properties and surface tensions*. *Colloid Polymer Science*, 1985. **263**: p. 541-553.
186. Creton, C. and L. Leibler. *How does tack depend on contact time and contact pressure?* in *19th Annual Meeting of the Adhesion Society*. 1996. Kingston Plantation, Myrtle Beach, SC.
187. Hui, C., J. Lin, J. Baney, and E. Kramer, *The Mechanics of Contact and Adhesion of Periodically Rough Surfaces*. *J. Polymer Science B*, 2001. **39**: p. 1195-1214.

188. Ben-Zion, O. and A. Nussinovitch, *Testing the rolling tack of pressure-sensitive adhesive materials. Part II: Effect of adherend surface roughness*. J. Adhesion Science and Technology, 2002. **16**(5): p. 599-619.
189. Kim, H. and T. Russel, *Contact of Elastic Solids with Rough Surfaces*. J. of Polymer Science: Part B, 2001. **39**: p. 1848-1854.
190. Mallegol, J., O. Dupont, and J. Keddie, *Morphology and elasticity of waterborne acrylic pressure-sensitive adhesives investigated with atomic force microscopy*. J. Adhesion Science and Technology, 2003. **17**(2): p. 243-259.
191. Specialties, R.D., Rod FAQs. <http://www.rdspecialties.com/Page.asp?Script=1>. Last viewed September, 2004.
192. Fike, G., J. Abedi, and S. Banerjee, *Imaging the Drying of Surfaces by Infrared Thermography*. Ind. Eng. Chem. Res., 2004. **43**: p. 4178-4181.
193. Fike, G., *Using Infrared Thermography to Image the Drying of Polymer Films*, in *School of Chemical and Biomolecular Engineering*. 2004, Georgia Institute of Technology: Atlanta, GA. p. 55.
194. Helsing, J. and G. Grimvall, *Thermal conductivity of cast iron: Models and analysis of experiments*. Journal of Applied Physics, 1991. **70**(3): p. 1198-1206.
195. Babu, G. and R. Dube, *Processing and Properties of 3-Layer Laminated Composites Based on Ultra High Carbon Steel and Mild Steel*. ISIJ International, 1996. **36**(9): p. 1184-1189.
196. Hosoki, S., *Production and Technology of Iron and Steel in Japan during 1990*. ISIJ International, 1991. **31**(4): p. 315-330.
197. Toroghinezhad, M., A. Humphreys, E. Essadiqi, F. Ashrafizadeh, A. Najafizadeh, and J. Jonas, *Effect of Chromium, Boron and Manganese Additions on the Deformation and Recrystallization Textures of Warm Rolled Low Carbon Steels*. ISIJ International, 2003. **43**(11): p. 1842-1850.
198. Krauss, G. and S. Thompson, *Ferritic Microstructures in Continuously Cooled Low- and Ultralow-carbon Steels*. ISIJ International, 1995. **35**(8): p. 937-945.
199. Kanetsuki, Y. and R. Ogawa, *Improvement of the Torsional Properties of Drawn High Carbon Steel Wire by the Control of Pearlitic Microstructure*. ISIJ International, 1989. **29**(8): p. 687-694.
200. Suehiro, M., T. Senuma, H. Yada, and K. Sato, *Application of Mathematical Model for Predicting Microstructural Evolution to High Carbon Steels*. ISIJ International, 1992. **32**(3): p. 433-439.

201. Tsuchida, N., Y. Tomota, and K. Nagai, *High-speed Deformation for an Ultrafine-grained Ferrite-Pearlite Steel*. ISIJ International, 2002. **42**(12): p. 1594-1596.
202. Grabke, H., *Surface and Grain Boundary Segregation on and in Iron and Steels*. ISIJ International, 1989. **29**(7): p. 529-538.
203. Oh, S., D. Cook, and H. Townsend, *Characterization of iron oxides commonly formed as corrosion products on steel*. Hyperfine Interactions, 1998. **112**: p. 59-65.
204. Cook, D., *In-situ identification of iron-zinc intermetallics in galvanized steel coatings and iron oxides on exposed steel*. Hyperfine Interactions, 1998. **111**: p. 71-82.
205. Cook, D., *Application of Mossbauer Spectroscopy to the Study of Corrosion*. Hyperfine Interactions, 2004. **153**: p. 61-82.
206. Oh, S., D. Cook, and H. Townsend, *Study of the Protective Layer Formed on Steels*. Hyperfine Interactions, 1998. **C3**: p. 84-87.
207. Yamashita, M., H. Nagano, T. Misawa, and H. Townsend, *Structure of Protective Rust Layers Formed on Weathering Steels by Long-term Exposure in the Industrial Atmospheres of Japan and North America*. ISIJ International, 1998. **38**(3): p. 285-290.
208. Balasubramanian, R., D. Cook, and H. Townsend, *Transmission Mossbauer Analysis of Nanophased Oxides formed on High Strength Steels*. Hyperfine Interactions, 2002. **141**(1): p. 369-379.
209. Cook, D., S. Oh, R. Balasubramanian, and M. Yamashita, *The role of goethite in the formation of the protective corrosion layer on steels*. Hyperfine Interactions, 1999. **122**: p. 59-70.
210. Sun, C., Y.Y. Lee, Y.D. Lee, and S. Hwang, *Finite Element Modeling of Thermo-mechanical and Metallurgical Behavior of Type 304 Stainless Steel in Cold Strip Rolling*. ISIJ International, 2003. **43**(10): p. 1572-1580.
211. Mizukami, H., S. Hiraki, M. Kawamoto, and T. Watanabe, *Initial Solidification Behavior of Ultra Low, Low and Middle Carbon Steel*. ISIJ International, 1999. **39**(12): p. 1262-1269.
212. Ohkubo, N., K. Miyakusu, Y. Uematsu, and H. Kimura, *Effect of Alloying Elements on the Mechanical Properties of the Stable Austenitic Stainless Steel*. ISIJ International, 1994. **34**(9): p. 764-772.

213. Salvatori, I., T. Inoue, and K. Nagai, *Ultrafine Grain Structure through Dynamic Recrystallization for Type 304 Stainless Steel*. ISIJ International, 2002. **42**(7): p. 774-750.
214. Mapelli, C. and P. Nolli, *Formation Mechanism of Non-Metallic Inclusions in Different Stainless Steel Grades*. ISIJ International, 2003. **43**(8): p. 1191-1199.
215. Ode, M. and T. Suzuki, *Numerical Simulation of Initial Microstructure Evolution of Fe-C Alloys Using a Phase-field Model*. ISIJ International, 2002. **42**(4): p. 368-374.
216. Lis, J. and P.O. Kellard, *Measurements of the thermal conductivity of thin films of magnetite*. British Journal of Physics D: Applied Physics, 1968(9): p. 1117-1123.
217. Clauser, C. and E. Huenges, *Thermal Conductivity of Rocks and Minerals*, in *Rock Physics and Phase Relations - A Handbook of Physical Constants*, T. Ahrens, Editor. 1995, American Geophysical Union: Washington, DC. p. 105-126.
218. Sun, S. and W.-K. Lu, *Mathematical Modeling of Reactions in Iron Ore/Coal Composites*. ISIJ International, 1993. **33**(10): p. 1062-1069.
219. Sundarmurti, N. and V. Rao, *Thermal Conductivity and Diffusivity of Iron Ore Pellet Having Low Porosity*. ISIJ International, 2002. **42**(7): p. 800-802.
220. Akiyama, T., H. Ohta, R. Takahashi, Y. Waseda, and J.-i. Yagi, *Measurement and Modeling of Thermal Conductivity for Dense Iron Oxide and Porous Iron Ore Agglomerates in Stepwise Reduction*. ISIJ International, 1992. **32**(7): p. 829-837.
221. Ribando, R., *Heat Transfer Tools*. 2002, Boston, MA: McGraw Hill.
222. Nield, D., *Surface tension and buoyancy effects in cellular convection*. J. Fluid Mech., 1964. **19**: p. 341-352.
223. Chandrasekhar, S., *Hydrodynamic and Hydromagnetic Stability*. 1961, New York: Dover Publications, Inc.
224. Gugliotti, M., *Tears of Wine*. Journal of Chemical Education, 2004. **81**(1): p. 67-68.
225. Pearson, J., *On convection cells induced by surface tension*. J. Fluid Mech., 1958. **4**: p. 489-500.
226. Gugliotti, M., M. Baptista, and M. Politi, *Surface Tension Gradients Induced by Temperature: The Thermal Marangoni Effect*. Journal of Chemical Education, 2004. **81**(6): p. 824-826.

227. Perez-Garcia, C., B. Echebarria, and M. Bestehorn, *Thermal properties in surface-tension-driven convection*. Physical Review E, 1998. **57**(1): p. 475-481.
228. Haas, D. and D. Birnie, *Real-Time Monitoring of Striation Development During Spin-On-Glass Deposition*, in *Sol-Gel Commercialization and Applications (Ceramic Transactions)*, X. Feng, et al., Editors. 2001, Am. Ceramic. Soc. p. 133-138.
229. Grigoriev, R., *Control of evaporatively driven instabilities of thin liquid films*. Physics of Fluids, 2002. **14**(6): p. 1895-1909.
230. Myers, T., *Surface Tension Driven Thin Film Flows*, in *The Mechanics of Thin Film Coatings*. 1996, World Scientific Publishing Company: London.
231. Gugliotti, M., M. Baptista, and M. Politi, *Laser-Induced Marangoni Convection in the Presence of Surfactant Monolayers*. Langmuir, 2002. **18**: p. 9792-9798.
232. Schaffer, E., S. Harkema, R. Blossey, and U. Steiner, *Temperature-gradient-induced instability in polymer films*. Europhysics Letters, 2002. **60**(2): p. 255-261.
233. Ismagilov, R., D. Rosmarin, D. Gracias, and A. Stroock, *Competition of intrinsic and topographically imposed patterns in Benard-Marangoni convection*. Applied Physics Letters, 2001. **79**(3): p. 439-441.
234. Char, M.-L. and K.-T. Chiang, *Stability analysis of Benard-Marangoni convection in fluids with internal heat generation*. Journal of Physics D: Applied Physics, 1994. **27**: p. 748-755.
235. Zeren, R. and W. Reynolds, *Thermal instabilities in two-fluid horizontal layers*. J. Fluid Mech., 1972. **53**(2): p. 305-327.
236. Nield, D., *Onset of convection in a fluid layer overlying a layer of a porous medium*. J. Fluid Mech., 1977. **81**(3): p. 513-522.
237. Smith, K., *On convective instability induced by surface-tension gradients*. J. Fluid Mech., 1966. **24**(2): p. 401-414.
238. Perez-Garcia, C. and G. Carneiro, *Linear stability analysis of Benard-Marangoni convection in fluids with a deformable free surface*. Physics of Fluids A, 1991. **3**(2): p. 292-298.
239. Das, K. and J. Bhattacharjee, *Marangoni convection on an inhomogeneous substrate*. Physical Review E, 1999. **59**(5 Part B): p. 5407-5411.
240. Kalliadasis, S. and C. Bielarz, *Steady free-surface thin film flows over topography*. Physics of Fluids, 2000. **12**(8): p. 1889-1898.

241. Masson, J., O. Olufokunbi, and P. Green, *Flow Instabilities in Entangled Polymer Thin Films*. Macromolecules, 2002. **35**: p. 6992-6996.
242. Gramlich, C., S. Kalliadasis, G. Homsy, and C. Messer, *Optimal leveling of flow over one-dimensional topography by Marangoni stresses*. Physics of Fluids, 2002. **14**(6): p. 1841-1850.
243. Haas, D., D. Birnie, M. Zecchino, and J. Figueroa, *The effect of radial position and spin speed on striation spacing in spin on glass coatings*. Journal of Materials Science Letters, 2001. **20**: p. 1763-1766.
244. Strawhecker, K., S. Kumar, J. Douglas, and A. Karim, *The critical role of solvent evaporation on the roughness of spin-cast polymer films*. Macromolecules, 2001. **34**: p. 4669-4672.
245. Birnie, D., *Combined flow and evaporation during spin coating of complex solutions*. Journal of Non-Crystalline Solids, 1997. **218**: p. 174-178.
246. Saylor, J., G. Smith, and K. Flack, *The effect of a surfactant monolayer on the temperature field of a water surface undergoing evaporation*. International Journal of Heat and Mass Transfer, 2000. **43**: p. 3073-3086.
247. Flack, K., J. Saylor, and G. Smith, *Near-surface turbulence for evaporative convection at an air/water interface*. Physics of Fluids, 2001. **13**(11): p. 3338-33345.
248. Saylor, J., K. Flack, M. Schultz, and G. Smith, *The correlation between surface temperature and subsurface velocity during evaporative convection*. Experiments in Fluids, 2002. **32**: p. 570-579.
249. Saylor, J., G. Smith, and K. Flack, *An experimental investigation of the surface temperature field during evaporative convection*. Physics of Fluids, 2001. **13**(2): p. 428-439.
250. Saylor, J., G. Smith, and K. Flack, *Infrared imaging of the surface temperature field of water during film spreading*. Physics of Fluids, 2000. **12**(3): p. 597-602.
251. Dussaud, A., S. Troian, and S. Harris, *Fluorescence visualization of a convective instability which modulates the spreading of volatile surface films*. Physics of Fluids, 1998. **10**(7): p. 1588-1596.
252. Dussaud, A. and S. Troian, *Dynamics of spontaneous spreading with evaporation on a deep fluid layer*. Physics of Fluids, 1997. **10**(1): p. 23-37.
253. Saylor, J., *Determining liquid substrate cleanliness using infrared imaging*. Review of Scientific Instruments, 2001. **72**(12): p. 4408-4414.

254. Phongikaroon, S., K. Judd, G. Smith, and R. Handler, *The thermal structure of a wind-driven Reynolds ridge*. Experiments in Fluids, 2004. **37**: p. 153-158.
255. Birnie, D., B. Zelinski, and D. Perry, *Infrared observation of evaporative cooling during spin-coating processes*. Optical Engineering, 1995. **34**(6): p. 1782-1787.
256. BFGoodrich, *Material Safety Data Sheet and Technical Data Sheet for Carbotac 26171*. 1998.
257. *CRC Handbook of Chemistry and Physics*. 81st ed, ed. D. Lide. 2000-2001, Boca Raton, FL: CRC Press.
258. Incropera, F. and D. DeWitt, *Fundamentals of heat and mass transfer*. 4th ed. 1996, New York: Wiley.
259. *ThermaCAM Researcher 2000 Operating Manual*. 2000, FLIR Systems.
260. *Perry's Chemical Engineers' Handbook*. 6th ed, ed. R. Perry, D. Green, and J. Maloney. 1984, New York: McGraw-Hill, Inc.
261. Hansen, C., *New simple method to measure polymer surface tension*. Pigment & Resin Technology, 1998. **27**(6): p. 374-378.
262. Azab, M., S. Bader, and A. Shaaban, *Nonionic surfactants based on copolymers of dioctyl itaconate with dioxypropylated itaconic acid*. Pigment & Resin Technology, 2001. **30**(6): p. 388-394.
263. Abramson, E., J. Brown, and L. Slutsky, *The thermal diffusivity of water at high pressures and temperatures*. Journal of Chemical Physics, 2001. **115**(22): p. 10461-10463.
264. Mardon, J., *Theoretical and Experimental Investigations into the Peeling of Paper Webs from Solid Surfaces*. Paperi ja Puu, 1976. **11**: p. 797-815.
265. Mardon, J., *The Release of Wet Paper Webs from Various 'Papermaking Surfaces'*. APPTA, 1961. **15**(1): p. 14-34.
266. Mueller, S., T. Patterson, and F. Ahrens. *Peel Testing on Web Adhesion and Drying Simulator*. in *Pressure Sensitive Tape Council Conference*. 2002. Atlanta, GA.
267. Ahrens, F., S. Mueller, T. Patterson, and F. Bloom, *Mathematical Modeling of Web Separation and Dynamics on a Web Adhesion and Drying Simulator*. International Journal of Applied Mechanics and Engineering, 2004. **9**(3).
268. Ahrens, F., T. Patterson, S. Mueller, and B. Hojjatie. *Investigation of Paper Dryer Picking, Web Transfer and Quality Issues Using a New Web Adhesion and Drying*

Simulator. in *Proceedings of the 14th International Drying Symposium*. 2004. Sao Paulo, Brazil.

VITA

Gregory Michael Fike was born on January 6, 1975 in Silver Spring, Maryland to Kenneth and Lynn Fike. He attended Beall High School in Frostburg, MD and proceeded to receive B.S. degrees in Physics and Chemical Engineering from Frostburg State University and the University of Maryland, respectively. He decided to pursue graduate school and enrolled at the Institute of Paper Science and Technology (IPST) in Atlanta, GA. His interest in the study of paper stemmed from his Co-op experience with Westvaco Corporation where he worked both in Laurel, MD and Luke, MD.

When IPST merged with the Georgia Institute of Technology, Greg became a student in the school of Chemical and Biomolecular Engineering at Georgia Tech where he received a M.S. degree in Chemical Engineering and a Ph.D. in Paper Science and Engineering.

His research has led to two publications in peer reviewed journals and three presentations at conferences at the time of his graduation. After graduation he began working for Georgia Pacific in Neenah, WI as a research scientist in the Dixie division.